University of Strathclyde

Department of Electronic and Electrical Engineering

A microfluidic platform for functional assays on tumour biopsy-derived spheroids for precision medicine

Theresa Elisabeth Mulholland

A thesis submitted in partial fulfilment of the requirements for the degree of Doctor of Philosophy

2020

Declaration of Authenticity

This thesis is the result of the author's original research. It has been composed by the author and has not been previously submitted for examination which has led to the award of a degree.

Signed: 

Date: 31st May 2020

Abstract

Precision medicine aims to determine the ideal treatment for each cancer patient through the use of genomic and molecular diagnostics, as well as functional chemosensitivity screening assays. In recent years, the use and development of physiologically relevant patient-derived 3D in vitro cancer models has increased, since 3D ex vivo and in vitro models can replicate many aspects of the tumour microenvironment closely. These aim to provide more predictive tools than cell line-derived models for testing anticancer drug efficacy, particularly in the context of precision medicine in oncology. However, the small number of cells contained in many biopsies, especially in fine needle aspirates, is a major barrier to the use of patient biopsy tissue in 3D functional assays for precision medicine.

Microfluidic technologies have extensive miniaturisation capabilities, which offer increased data throughput while using very small amounts of cells. Therefore, this technology is a good candidate to perform 3D functional assays using patient-derived tissue. However, microfluidic devices frequently require an experienced handler or the use of dedicated fluid actuation equipment, which can create obstacles to its widespread adoption for precision medicine applications.

This PhD aimed to address these issues by creating a microfluidic platform and protocols for medium-throughput screening of tumour biopsy-derived spheroids. The microfluidic system developed in this PhD was used to generate thousands of spheroids from single cell suspensions, which could be cultured in the device for a prolonged period of time. Subsequently, as a proof-of-concept application, prostate biopsy-derived spheroids were exposed to drug concentration gradients, which allowed the establishment of one concentration-response curve per chip, and up to 21 concentration-response curves per patient. This platform offers a novel solution for the functional chemosensitivity testing of biopsy-derived spheroids, maximising the number of conditions that can be tested on patient-derived tissue for the purpose of precision medicine.

Acknowledgements

Firstly, I would like to express my immense gratefulness to my primary supervisor Dr Michele Zagnoni for giving me the opportunity to take part in meaningful multi-disciplinary research which has the potential to affect real change. For the last six years, his unwavering support, guidance and mentorship have steered me throughout this journey, and I will be forever grateful for the opportunities he has afforded me.

A huge thank you is also owed to the University of Strathclyde, the Electronic and Electrical Engineering Department, Medical Research Scotland and AMS Biotechnology Ltd for allowing me to be a part of this project and for making this research possible. In particular, I'd like to thank Medical Research Scotland and AMS Biotechnology for providing the financial support for this PhD.

A special thanks has be given to Alex Sim, my industrial supervisor, for his continued support and enthusiasm for innovation, and his faith in the potential of projects like mine. I would also like to thank Dr Joanne Edwards, for believing in this project and entrusting me with precious patient biopsy tissues for the application of my research. In that breath, a huge thank you is dedicated to the patients who have donated their tissue to the biological research conducted in this project.

I would also like to thank Dr Marie Boyd, Prof David Flint and Dr Annette Sorensen for their help throughout my project, as well as all the people within the Centre of Microsystems and Photonics. In particular, huge thanks are owed to Graham, who taught me almost everything I know about microscopy. Kay and Barbara, who helped and supported me with practical aspects since the very beginning, and especially to Kay, who as my desk mate, endured hours of my chatting valiantly. Throughout the last years, so many people have contributed to making my PhD journey an enjoyable one, with pub evenings, conference trips, summer trips, Christmas lunches and lunch breaks, and I'm so grateful to all the people who shared this adventure with me: Anja, Ralf, Chris, Gordon Humphries, Jonas, Mynie, Karla, Ellis, Daniel, Rozan, Sarah, Samantha, Mick, Gordon F, Jo and Deepak.

I would also like to express thanks to my family and especially my parents, for supporting my move to Glasgow and my crazy endeavours in a different country, and for always being there for me.

Most of all, I'd like to thank my husband Kieran, who has endured the ups and downs of this adventure with me and supported me through all of it.

Table of Contents

List of Figures

List of Tables

Abbreviations

3D	Three-dimensional
AKT	Protein kinase B
ALK	Anaplastic lymphoma kinase
ALL	Acute lymphoblastic anemia
AMACR	Alpha-methylacyl-CoA racemase
AR	Androgen receptor
Bcl-2	B-cell lymphoma 2
CAF	Cancer-associated fibroblast
CAR	Chimeric antigen receptor
CD19	B-lymphocyte antigen CD19
CD28	Cluster of Differentiation 28
CD3zeta	T-cell surface glycoprotein CD3 zeta chain
CRC	Colorectal cancer
CRISPR	Clustered regularly interspaced short palindromic repeats
CT	Choleratoxin
CTL	Cytotoxic T lymphocyte
CTLA-4	Cytotoxic T-lymphocyte-associated protein 4
CXCL12	C-X-C motif chemokine 12
DHT	Dihydrotestosterone
DNA	Deoxyribonucleic acid
DMSO	Dimethyl sulfoxide
ECM	Extracellular matrix
EGF	Epidermal growth factor
EGFR	Epidermal growth factor receptor
EMEM	Eagle's Minimum Essential Medium
EMT	Epithelial–mesenchymal transition
FACS	Fluorescence-activated cell sorter
FAP	Fibroblast activation protein

FASN	Fatty acid synthase
FBS	Fetal bovine serum
FEM	Finite element model
FGF	Fibroblast growth factor
GBM	Glioblastoma multiforme
GOLM1	Golgi membrane protein 1
GLUT1	Glucose transporter 1
HIF1/2	Hypoxia-inducible factor
HNSCC	Head and neck squamous cell carcinoma
HPMC	Hydroxymethylcellulose
HSP	Heat shock protein
IFN-gamma	Interferon gamma
IL-2	Interleukin 2
IPA	Isopropanol
KLK-3	Kallikrein-3
MDSC	Myeloid-derived suppressor cell
MEM	Minimum essential medium
MHC	Major histocompatibility complex
NEAA	Non-essential amino acids
NGS	Next-generation sequencing
NSCLC	Non-small-cell lung cancer
PBS	Phosphate buffered saline
PSA	Prostate specific antigen
PD1	Programmed cell death protein 1
PDGF	Platelet-derived growth factor
PD-L1	Programmed death-ligand 1
PDMS	Polydimethylsiloxane
PDX	Patient-derived xenograft
PGE2	Prostaglandin E2

RNA	Ribonucleic acid
RPM	Revolutions per minute
RPMI	Roswell Park Memorial Institute
RT-qPCR	Reverse transcription quantitative polymerase chain reaction
TGF-beta	Transforming growth factor beta
TME	Tumour microenvironment
TP53	Tumour protein p53
TRUS	Transrectal ultrasound guided
TSP1	Thrombospondin-1
UV	Ultraviolet
VEGF	Vascular endothelial growth factor A

Thesis overview

The following sections introduce the main context and the motivation behind the work carried out in this thesis, as well as the aims and objectives of this research, which is followed by a short novelty statement, the general structure of the thesis and publications.

Motivation

According to the World Health Organization, cancer is the second most common cause of death and was responsible for 9.6 million deaths in 2018 worldwide. Cancer Research UK states that the incidence of cancer has been increasing for years, by 12% since the early 1990s alone, and 1 in 2 people are now expected to be diagnosed with a form of cancer during their lifetime. In the UK the most common types of cancer cases are breast, prostate, lung and bowel cancers, which account for 53% of all new cases and are responsible for almost half (45%) of all cancer deaths. However, as a result of widespread screening of the population, early intervention and improved treatments, the survival rates of all cancer have doubled since 1960, and survival rates for many cancer types, such as breast and prostate have continued to improve over the last four decades (Quaresma et al., 2015). 45% of all patients receive surgery to remove their tumour, with 27% having a form of radiotherapy as part of their treatment, which also includes chemotherapy in 28% of patients, according to Cancer Research UK. Initially, surgery was the first and only modern treatment available to patients, which still provides great benefits beyond the removal of the primary tumour. The removal of a small tumours frequently prevents the future formation of metastatic sites, which improves overall survival and can provide a cure. However, this is not always the case and in some patients the removal of the primary tumour activates the growth of previously dormant sites and metastatic growth flares up (Hanahan and Weinberg, 2011). Novel treatments, which frequently combine several treatment modalities, have changed treatment outcomes completely for many cancers. Vaccines, biologicals and drugs targeting specific tumour attributes, when used

in combination with traditional therapies, have prevented the progression of cancer or produced substantial improvements in cancer outcomes. Cancer research has continued to develop new strategies to fight cancer using oncolytic viruses, nanoparticle drug carriers, hyperthermia and other technologies (Snider et al., 2016; Zugazagoitia et al., 2016; Lawler et al., 2017). Additionally, the modulation of the immune system in order to fight cancer has become a new goal in cancer therapy, resulting in the development of immunomodulatory drugs, such as immune checkpoint inhibitors, and modern CAR-T cell therapies (Schirrmacher, 2019).

However, despite improvements of cancer treatments, the appropriate treatment for patients is frequently determined by the expression of certain biomarkers or genetic mutations, which allows the stratification of patients into groups which will likely benefit the most from a treatment approach. However, only a small fraction of patients possesses mutations which can be targeted specifically using drugs, such as Herceptin (Trastuzumab), which is used in breast cancers which overexpress the HER2 receptor. Despite this stratification, only 40% of patients respond to Herceptin treatment (Pinto et al., 2013). The reasons for this lie in the incomplete understanding of the effects of mutations and their interactions, the impact of epigenetic modifications, and the heterogeneity within tumour types, which prohibits the accurate prediction of treatment responses in patients. As a result, genomic and molecular diagnostics that are currently used to tailor treatments to subsets of patients, cannot yet address every patient and their individual cancers. Therefore, more predictive bioassays are required to improve patient outcome, which has resulted in the increasing use of patient-derived tissues in functional assays (Holton et al., 2017; Powley et al., 2020). These assess the effect of a number of possible treatments on the patient's tumour cells, with the aim of providing the most promising treatment. Patient biopsies and resections have the advantage of retaining the composition and microenvironment of the patient's tumour, providing a more realistic tumour model for functional drug screens. This approach, which establishes the best possible treatment option for a patient using functional assays, has been coined precision medicine (Ashley, 2016). Using patient-derived cells in monolayer cultures for chemotherapy

sensitivity assessment to guide patient treatments has been attempted for decades, but has failed to show significant predictive value (Burstein et al., 2011). The main reason for this is the use of in vitro disease models, which lack the physiological relevance required in order to predict the treatment response of a patient. As a result, more physiologically relevant in vitro models, such as tumour fragment and slice cultures and heterogeneous patient-derived spheroids have been applied to the functional assessment of drug efficacy in patient-derived tissues (Halfter and Mayer, 2017). This has significantly improved the predictive value of in vitro assays, and several studies have demonstrated an accuracy of 80% or more, when patient-derived tissues were used in 3D in vitro assays to predict treatment outcomes (Halfter and Mayer, 2017). However, the widespread use of patient biopsies for precision medicine has been limited by the small number of cells contained in biopsies.

Microfluidic technologies offer an opportunity to miniaturise 3D in vitro assays using patient-derived cells, offering increased throughput and precise control over the culture environment, while requiring only a fraction of cellular materials and reagents with respect to standard culture techniques. So far, several microfluidic platforms have been designed to enable the formation of thousands of spheroids (Tung et al., 2016; Valente et al., 2017; Dhiman et al., 2019), but there remains a lack of miniaturised technologies which can maximise the number of treatments that can be tested on patient-derived 3D in vitro models to achieve precision treatments for cancer patients. Additionally, microfluidic devices frequently require the use of specialised and fluid actuation equipment, which presents a barrier to the adoption of microfluidic devices for precision medicine.

Aims and objectives

The aim of this project was the development of a microfluidic platform, which could be operated without the use of fluid actuation equipment, that is capable of:

1) The generation of thousands of spheroids from single-cell suspensions obtained from patient biopsy tissue

2) The prolonged culture of patient-derived spheroids in a shear-stress free environment
3) The incubation of biopsy-derived spheroids with a customisable drug concentration gradient for at least 12 hours, enabling efficient drug efficacy testing and the generation of one concentration-response curve in each device

For the initial optimisation of the microfluidic platform, the generation of spheroids, spheroid culture conditions, and the application of drug concentration gradients, cell lines were used. In order to demonstrate proof-of-concept for the developed devices, thousands of tumour spheroids were generated from prostate cancer biopsies and the microfluidic device developed in this project was used to determine the efficacy of several drugs in patient-derived 3D tumour models.

Novelty statement

The novel device presented here combines the advantages of using microfluidic technologies and patient-derived 3D tumour models for precision medicine applications. The use of a microfluidic, self-generating concentration gradient allowed the establishment of up to 21 concentration-response curves from a single patient biopsy, utilising hundreds of physiologically relevant 3D patient-derived tumour models per condition. Overall, this provides a 20-fold increase in the number of screens that can be performed for the same amount of starting cellular material. Additionally, the platform does not require the use of external equipment connected to the device and is operated entirely using hydrostatic pressure driven flows, which enables compatibility with robotic dispensing for future up-scaling of the platform.

Publications

The work demonstrated in this thesis contributed to a patent (pending, UK Application No. 1705982.5, PCT Application No. PE958217WO), and was published in the following peer-reviewed journal article:

- Mulholland, T., McAllister, M., Patek, S., Flint, D., Underwood, M., Sim, A., et al. (2018). Drug screening of biopsy-derived spheroids using a self-generated microfluidic concentration gradient. Sci. Rep. *8*: 14672.

And conference proceedings:

- Christ, T., Flint, D., Boyd, M., Zagnoni, M. (2015). Drug Dose Responses of 3D Cancer Spheroids in Microfluidics. FASEB Journal. Proceedings of "Experimental Biology 2015", Abstract 926.17, which was presented as a poster at EB2015 in Boston, USA in March 2015
- Christ, T., Payne, S., Yan, Y., Ren, J., Edwards, J., Boyd, M., Zagnoni, M. (2016). On-chip formation of 3D spheroids for patient-derived tissue screening. In form of a poster presentation at the 20th International Conference on Miniaturized Systems for Chemistry and Life Sciences (MicroTAS 2016) in Dublin, Ireland, in October 2016.
- Mulholland, T., McAllister, M., Patek, S., Flint, D., Underwood, M., Sim, A., Edwards, J., Zagnoni, M. (2018). Drug screening of biopsy-derived multicellular spheroids using microfluidic technology. In: Proceedings of the American Association for Cancer Research Annual Meeting 2018. Presented as a poster at the annual meeting of the AACR in Chicago, USA, in April 2018.
- Christ, T., Robertson, G., McAllister, M., Patek, S., Underwood, M., Sim, A., Edwards, J., Zagnoni, M. (2018). A microfluidic solution to aid precision medicine: Large screening of cancer patient-derived spheroids. Presented as a poster at EACR Goodbye Flat Biology in Berlin, Germany, in September 2018. The poster received the award for the best oncology poster at the conference.

Thesis outline

This thesis starts by summarising in Chapter 1 the key challenges of creating useful and predictive in vitro models for cancer research and how microfluidic technologies can offer solutions to these problems. This is followed by a description of materials and methods used during experimental procedures in Chapter 2. Chapter 3 describes the design, development and operation of the microfluidic platform for the on-chip generation and culture of cancer spheroids. This is followed by Chapter 4, where the generation of a reproducible compound concentration gradient in the microfluidic platform is described and characterised. In this chapter a drug concentration gradient was applied to an array of spheroids, which resulted in the generation of 8-point concentration-response curves with up to 24 replicates from each microfluidic chip. This platform was then applied to the generation of spheroids from prostate biopsy tissue, for which culture conditions were optimised in Chapter 5. In Chapter 6 the microfluidic platform was applied to the screening of spheroids derived from two prostate cancer biopsies, which were exposed to several anticancer drug gradients for drug efficacy testing. Finally, in Chapter 7, a discussion of the results is presented, in addition to conclusions and potential future developments.

1 Background

1.1 The transformation of normal cells into cancer cells

Cancer is a group of hundreds of diseases, which arise from alterations in normal cellular development. Normal human cells can progressively evolve from normalcy through a series of pre-malignant states, ultimately transforming into invasive cancers via a process termed tumourigenesis. These changes are characteristic transformations cancer cells undergo in almost all tumours on their journey to malignancy, resulting in the dysregulation of normal tissue structure and homeostasis, which have been coined the 'hallmarks of cancer' by Robert Weinberg and Douglas Hanahan in 2000 (Hanahan and Weinberg, 2000). Originally, six hallmarks of cancer were proposed, which were amended to include a further two hallmarks and two enabling characteristics of cancer in 2011, in order to account for the impact of the tumour microenvironment (TME) on tumourigenesis (Hanahan and Weinberg, 2011). These proposed 10 hallmarks of cancer will be described in the following section.

1.1.1 Sustained proliferative signalling

The best-known characteristic of cancer cells is their ability to chronically sustain proliferative signalling. Normal cells exert very careful control over the production and release of proliferation-promoting signalling molecules, which become deregulated in cancer cells and allow them to evade the homeostatic control of normal tissue. This sustained proliferative signalling is enabled by a number of molecular changes which occur in cancer cells. Proliferative signalling is activated by the binding of ligand growth factors to growth factor receptors on the cell surface, which conduct these signals through intracellular signalling pathways that regulate the cell cycle and growth, but also survival and cell metabolism. Unregulated proliferative signalling is obtained by cancer cells through several mechanisms. Firstly, many tumour cells have the capability of the production and secretion of growth factors, to which they are able to respond with growth, which is termed autocrine proliferative signalling (Butera et al., 2018). Secondly, they have the capability to induce secretion of growth

factors from stromal cells into the microenvironment (Richards et al., 2019). Additionally, cancer cells may possess increased numbers of growth factor receptors on their surface, which can render cancer cells hyper-responsive to growth factor binding, as seen in prostate cancer cells which can overexpress androgen receptors (AR) resulting in tumour growth (Dehm and Tindall, 2005; Golshayan and Antonarakis, 2013). This hyper-responsiveness can also occur as a result of mutations and structural changes within growth factor receptors or downstream signalling nodes, resulting in ligand-independent constitutive activation of the proliferative signalling cascade (Hanahan and Weinberg, 2011).

These changes in signalling can result in the disruption of negative-feedback mechanisms, which limit excessive proliferation in normal tissue. Observing these adaptations of cancer cells experimentally is complicated by the fact that in vivo growth factor signalling is also transmitted from each cell to its neighbours through paracrine signalling (Nelson and Bissell, 2006). Further, the bioavailability of these growth factors secreted into the extracellular matrix depends on their distribution and their localised, specific activation by proteases and other enzymes (Hanahan and Coussens, 2012). This demonstrates that the tumour microenvironment cannot be ignored in the modelling of cancer, due to its widespread effects on cell behaviour.

1.1.2 Evasion of growth suppression

The second hallmark of cancer cells is their ability to evade growth suppression, by circumventing cellular programmes which negatively regulate cell proliferation. Many of these regulatory mechanisms involve the actions of tumour suppressor genes, which negatively regulate cell growth and proliferation (Payne and Kemp, 2005). The most significant tumour suppressor gene is likely TP53, which responds to intracellular stress signalling and abnormal intracellular changes, such as genomic damage, nucleotide levels, growth-promoting signals, glucose levels and oxygenation levels (Hafner et al., 2019). TP53 then has the ability to stop the cell-cycle progression until intracellular conditions have normalised. However, in the presence of

overwhelming genomic or irreparable cell damage, TP53 can induce apoptosis (Aubrey et al., 2016). Other tumour suppressor genes are active simultaneously in a network of genes and signals responsible for the regulation of proliferation, showing functional redundancy. This has been demonstrated in animal studies using mice, where the loss of a single tumour suppressor gene only resulted in the development of tumours late in life, rather than the immediate progression to neoplasia (Ghebranious and Donehower, 1998; Lipinski and Jacks, 1999).

A further mechanism of limiting excessive non-physiological proliferation is the contact-inhibition observed in vitro and in vivo, through which normal tissue homeostasis is maintained (Ribatti, 2017). Contact-inhibition is frequently lost in tumourigenesis, resulting in continued proliferation even after confluence is achieved.

Similarly, TGF-beta regulates anti-proliferative signalling in normal cells, which in cancer cells can be redirected towards the induction of epithelial-to-mesenchymal transition (EMT), which is a process that confers highly malignant cell traits, such as the ability to migrate, metastasise and evade cell death (Hanahan and Weinberg, 2011; Dongre and Weinberg, 2019).

1.1.3 Apoptosis evasion

Apoptosis, the induction of programmed cell death, is generally seen as the body's defence against cancer development. Physiologically, apoptosis is induced in response to stressful stimuli, which cancer cells experience over the course of tumourigenesis and during cancer treatments. Both the hyperproliferation of cancer cells observed during tumour development that results in genomic damage, and oncogene-induced signalling imbalances, can act as the stressors, which induce programmed cell death (Hanahan and Weinberg, 2011). An extrinsic death-receptor mediated apoptotic programme relays extracellular death-inducing signals to the cytoplasm, where it results in the downstream activation of caspase 8 (Wong, 2011). Intracellular signals of abnormal conditions on the other hand stimulate an intrinsic mitochondrial apoptotic programme which induces the activation of caspase 9

(Wong, 2011). The intrinsic activation of the mitochondrial apoptotic programme depends on a delicate balance of pro- and anti-apoptotic proteins that determines the fate of each cell. Eventually, the extrinsic and intrinsic apoptotic pathways converge on the effector caspase 3, which induces nuclear apoptosis (Hanahan and Weinberg, 2011). Consequently, apoptosis should be induced as a result of tumour growth and after any anticancer treatment, however, research shows that this is not always the case, and that apoptosis is highly reduced in treatment-resistant and high-grade tumours (Wong, 2011).

Instead, cancer cells appear to have evolved numerous ways to evade apoptosis, establishing it as a hallmark of cancer. Cancer cells have been shown to escape apoptosis through increased expression of anti-apoptotic regulatory proteins, or the down-regulation of pro-apoptotic factors, thereby tilting the balance of pro- and anti-apoptotic proteins in favour of survival (Pfeffer and Singh, 2018). Further, down-regulation or loss of certain caspases, as well as impaired death-receptor signalling which induces extrinsic apoptotic cell death in response to stress or cytotoxic agents, can result in attenuated cell death and increased cancer cell survival.

A further mechanism of apoptosis-evasion is mediated by the loss of TP53 in many tumours, where the lack of intracellular damage sensing results in a reduced induction of apoptosis (Aubrey et al., 2016). Several other mechanisms have been proposed to explain the ability of cancer cells to reduce and evade apoptosis, and necrotic cell death as well as autophagy are thought to be intertwined with apoptosis-resistance (Hanahan and Weinberg, 2011; Wong, 2011).

1.1.4 Replicative immortality

The fourth hallmark of cancer cells is their seemingly limitless replicative immortality (Hanahan and Weinberg, 2000, 2011). Normal cells only experience a limited number of cell division cycles before they inevitably enter senescence, a viable but non-proliferative state (Campisi, 2013). Cells which have entered a senescent state rarely re-emerge and eventually face a crisis phase where the majority of a cell population

dies. Rarely, cells will emerge from the brink of extermination with newfound unlimited replicative potential, which has been termed immortalisation (Hanahan and Weinberg, 2000, 2011). The main mechanism of this process is thought to be centred around telomeres.

Telomeres are short tandem repeats at the ends of chromosomes which protect chromosomal DNA from being shortened during a cell division cycle (Okamoto and Seimiya, 2019). Over time and with repeated cell divisions, these telomere DNA segments start to shorten, eventually eroding completely, which results in end-to-end chromosome fusion and threatens the normal karyotype and cell viability. Telomerase is an enzyme which is capable of extending telomeres by adding telomer repeat segments to the ends of chromosome telomeres, effectively extending the life span of a cell (Campisi, 2013). In normal cells telomerase is almost entirely absent. However, telomerase is expressed at significant levels in the majority of immortalised cell lines and cancer cells. By extending the telomere length using telomerase, cancer cells evade both senescence and the eventual fate of apoptosis (Hanahan and Weinberg, 2000).

1.1.5 Angiogenesis

In order to thrive, tumour masses depend on certain levels of nutrients, oxygen, and the ability to clear metabolic waste products and carbon dioxide (Carmeliet and Jain, 2000). In tumour progression, an ‘angiogenic switch’ is frequently found to be activated and remains as such, which results in the chronic induction of new endothelial vessel sprouting of existing blood vessels, in order to increase tumour blood flow and sustenance (Hanahan and Weinberg, 2011).

This process, the sprouting of new vessels from existing ones, is called angiogenesis, and physiologically mainly occurs during embryogenesis and transiently in adult life, in processes such as wound healing (Hanahan and Weinberg, 2011). Normal vasculature remains quiescent for most of our lives, unless required for physiological or pathological circumstances. The activation of an ‘angiogenic switch’ is controlled by

an interplay of signalling proteins, angiogenic regulators, which either induce or inhibit angiogenesis. The most well-known angiogenesis inducer is likely the vascular endothelial growth factor-A (VEGF-A), which encodes ligands for a variety of signalling pathways involved in the growth of new blood vessels (Junttila and De Sauvage, 2013). Both hypoxia, which frequently occurs in tumours, and oncogene signalling can result in the upregulation of VEGF gene expression, which induces angiogenesis (Carmeliet and Jain, 2000).

The fibroblast growth factor (FGF) is an additional pro-angiogenic factor, which supports sustained tumour angiogenesis when it is chronically upregulated (Carmeliet and Jain, 2000). A typical anti-angiogenic signal is thrombospondin-1 (TSP1), which binds to receptors on endothelial cells, inducing anti-angiogenic signals that can counteract pro-angiogenic signalling (Carmeliet and Jain, 2000).

In tumours displaying an imbalance of pro-angiogenic signals, angiogenesis is chronically activated, although the newly formed tumour vessels (neovasculature) are rarely physiologically mature. Neovasculature is frequently inefficient and contains disrupted sprouts, excessive convoluted branching, and vessel distortion, which results in unreliable blood flow and leaking vessels (Carmeliet and Jain, 2000). Nevertheless, the induction of angiogenesis appears to be one of the earliest events in tumourigenesis, enabling continued tumour growth by sustaining the continuous development of new vessels (Hanahan and Weinberg, 2011).

1.1.6 Invasion and metastasis

Once tumours reach a certain state of progression, cancer cells can evolve the ability to leave the primary tumour site and enter the blood stream, which transports cancer cells to distant sites where they can form new tumour sites, so called metastases (Fares et al., 2020). This occurs through the processes of invasion and metastasis. During the invasion-metastasis cascade, cancer cells initially acquire the ability to leave the confines of the original tumour and invade surrounding healthy tissue. Once cancer cells are able to enter the vessels of the lymphatic system and the blood

stream in a process called intravasation, they can spread throughout the body within the circulatory system (Fares et al., 2020).

In order to create a metastatic site, extravasation, the escape of cancer cells from the vessel lumen to surrounding tissue, has to occur. Single cells, as well as cell clusters are involved in this process, which can result in the formation of small tumour nodes, micrometastases, at a new tissue site (Dongre and Weinberg, 2019; Pearson, 2019). These micrometastases can grow into large secondary tumours over time in a process coined colonisation. During the invasion-metastasis cascade, cancer cells undergo changes in cell shape, and in their attachment to other cells and the extracellular matrix (ECM) (Quail and Joyce, 2013). E-Cadherin, a cell adhesion molecule, was found to be essential to cancer cell dissemination and seeding of metastatic lesions (Fares et al., 2020).

The cell adhesion molecule E-Cadherin forms adherens junctions with nearby cells and aids in the formation of immotile epithelial sheets, which are maintained in a quiescent state (Pearson, 2019). Increased expression of the cell-adhesion molecule E-cadherin supresses invasion and metastasis, whilst a reduction in E-cadherin encourages the former two processes (Dongre and Weinberg, 2019; Pearson, 2019). The loss of E-cadherin is observed in a developmental regulatory process called epithelial-mesenchymal transition (EMT), which is currently the centre of invasion and metastasis research (Dongre and Weinberg, 2019; Pearson, 2019).

EMT is initiated by the binding of ligands to transmembrane receptors, such as TGF-beta and Wnt ligands (Pearson, 2019). During EMT, epithelial cancer cells acquire the properties required to invade tissue, evade apoptosis and disseminate (Fares et al., 2020), in a process that can be transiently activated or maintained stably. EMT is controlled by a number of transcription factors, some of which regulate each other, and result in the loss of adherens junctions between cells, repressing cell-to-cell adhesion (Pearson, 2019). Furthermore, during EMT cobble-stone shaped epithelial cells, which are usually immotile, can transform into spindle-shaped motile fibroblast-like cells (Dongre and Weinberg, 2019). Cell motility increases, and the expression of matrix-degrading enzymes is triggered, which allows cancer cells to detach from other

cells and their surrounding extracellular matrix, enabling them to migrate and disseminate (Dongre and Weinberg, 2019). Whilst originally EMT was only thought to be involved in embryogenesis, research in recent years has suggested that cancer cells have co-opted this process to enable invasion and metastasis (Dongre and Weinberg, 2019).

1.1.7 Mutation and genome instability

In 2011, new developments in cancer research were reflected in a second publication by Weinberg and Hanahan, which established four further enabling tumour characteristics and emerging hallmarks. The first of these new features is the genome instability and mutation of tumour cells, which enables the series of changes which cells undergo during tumour progression. Many of the hallmarks described earlier are enabled by the occurrence of mutations in single cells, which confers a selective survival benefit that enables their initial outgrowth and the eventual growth of a tumour (Hanahan and Weinberg, 2011). Some of the hallmark changes of cancer cells are not rooted in mutations, but are instead caused by epigenetic mechanisms (e.g. methylation and histone modifications) which affect gene expression directly (Hanahan and Weinberg, 2011; Nebbioso et al., 2018). The occurrence of such alterations of the genome is monitored by a genome maintenance system, composed of caretaker genes which are able to detect DNA damage (Fanale et al., 2017). This damage surveillance system activates DNA damage repair proteins, which are able to repair most DNA defects and prevent the emergence of mutated cells within normal tissue (Hanahan and Weinberg, 2011). However, cancer cells have developed several mechanisms to evade the control of the genome maintenance system, which results in increased rates of mutation in tumour cells (Bozic et al., 2010). Inactivating mutations and epigenetic repression in cancer cells increase their sensitivity to mutagenic signals and cause a breakdown of the DNA damage repair mechanism (Roos et al., 2016; Nebbioso et al., 2018). Additionally, these changes can disrupt DNA damage surveillance machinery which normally induces senescence and apoptosis when genomic changes are detected (Roos et al., 2016). By interfering at several stages of genome

damage surveillance, at the detection of DNA damage, the activation of DNA damage repair proteins and with damage repair proteins directly, cancer cells are able to progressively accrue countless mutations, resulting in multi-step tumour progression (Roos et al., 2016).

1.1.8 Tumour-promoting inflammation

Tumour-promoting inflammation was established as a further enabling characteristic of cancer cells, in particular as a result of increased understanding of the complexity of the tumour microenvironment. Every tumour is infiltrated by cells of the innate and adaptive immune system to varying degrees, ranging from low level infiltration to massive inflammation (Fridman et al., 2012; Murata, 2018). Originally, it was assumed that the immune response initiated by a tumour was a protective mechanism, which we now know is the case in some tumours where immune cells exert antitumoral effects (Hanahan and Weinberg, 2011; Fridman et al., 2012). However, when an antitumoral immune response is present, a selective pressure is placed on the cancer cells to evade immune destruction, which will be discussed in more detail in section 1.1.10. On the other hand, research has demonstrated that inflammation and immune cells can have extensive tumour-promoting effects (Crusz and Balkwill, 2015; Suarez-Carmona et al., 2017). Immune cells can secrete signalling agents into their microenvironment, such as growth factors, which sustain proliferative signalling, or survival factors, which limit the induction of apoptosis in cancer cells (Suarez-Carmona et al., 2017). Inflammation can also induce the release of pro-angiogenic factors and extracellular matrix-modifying enzymes, which contribute to the induction of angiogenesis, invasion and metastasis (Hanahan and Weinberg, 2011). Inflammation has also been implicated in the induction of EMT, contributing to an invasive tumour phenotype (Suarez-Carmona et al., 2017).

1.1.9 Reprogramming of energy metabolism

The excessive uninhibited proliferation of cancer cells requires the dysregulation of cell proliferation and energy metabolism in order to fuel tumour growth. This is achieved through several adaptations which occur in cancer cells, resulting in the re-programming of their energy metabolism (Hanahan and Weinberg, 2011). In aerobic conditions, normal cells utilise glucose through glycolysis and the resulting pyruvate is utilised in mitochondria. Under anaerobic conditions, glycolysis is upregulated, and less pyruvate is shunted to the mitochondria. In cancer cells on the other hand, glycolysis is always favoured and remains the main cellular metabolic pathway employed, independent of oxygenation (Vazquez et al., 2016). This is the result of the activation of oncogenes, such as RAS, MYC and mutant tumour suppressor genes, especially TP53, which increase glycolytic fuelling (Zong et al., 2016).

Additionally, the upregulation of glucose transport proteins, such as GLUT1, increases the uptake of glucose into the cytoplasm of cancer cells, which sustains a high glycolytic flux (Gatenby and Gillies, 2004). Many tumours experience persistent or transient hypoxia, which induces the activity of hypoxia-inducible transcription factors (especially HIF-1 and HIF-2) (Carnero and Lleonart, 2016). These transcription factors are part of the hypoxia response system, which upregulates glucose transporters and glycolytic enzymes in response to hypoxia and certain cancer treatments, increasing the metabolic shift to glycolysis even further (Zong et al., 2016). This metabolic shift of cancer cells has been termed the Warburg effect, and the reasons for its emergence in cancer cells are not entirely clear, since glycolysis represents a fairly inefficient way for cells to produce ATP. However, it has since emerged that pyruvate and other glycolytic intermediates are instead diverted to biosynthetic pathways, which provide nucleosides and other building blocks for growth of new cells, fuelling tumour proliferation indirectly (Liberti and Locasale, 2016; Zong et al., 2016).

1.1.10 Evading immune destruction

In recent years, interest in the role of the immune system in the prevention or progression of tumours and metastases has exploded due to the advent of CAR-T cell-based therapy, which requires a thorough understanding of all tumour-inhibiting and tumour-promoting effects of the immune system (Schmidts and Maus, 2018). The theory of immunosurveillance suggests that all cells and tissues in the body are constantly monitored by the immune system, in order to detect emerging malignant cells (Galluzzi et al., 2017). The majority of these detected cancer cells are recognised and destroyed by components of the immune system. Therefore, the solid tumours that eventually emerge must have avoided detection by the immune system or managed to suppress the anticancer activity of immune cells, thereby evading eradication by immunosurveillance (Hanahan and Weinberg, 2011; Hanahan and Coussens, 2012; Binnewies et al., 2018). Animal studies have shown that a deficiency in tumour-suppressing immune components, such as CD8+ cytotoxic lymphocytes (CTLs), CD4+ helper T (Th1) cells and natural killer (NK) cells, can result in massively increased development of tumours (Kim et al., 2007; Teng et al., 2008). This has been mirrored in studies of human tumours, where a massive infiltration by CTLs and NK cells improved tumour prognosis, confirming that CTLs and NK cells are part of the tumour-suppressive branch of the immune system (Fridman et al., 2012). However, cancer cells have developed many ways to avoid detection and elimination by immunosurveillance machinery, for example, by interfering with the immune cells recruited to kill them. Cancer cells are able to avoid immunogenic death by secreting TGF-beta into the microenvironment, which paralyses infiltrating CTLs and NKs, and maintains these cells in an anergic phenotype (Fridman et al., 2012). Further, the release of TGF-beta from cancer cells and surrounding stromal cells has been shown to aid in the conversion of Th1 cells into immunosuppressive regulatory T cells (Tregs), that suppress local anti-tumour immune response, which enables continued tumour growth (Konkel et al., 2017; Sanjabi et al., 2017). Tregs found within tumours were determined to be much more immune-suppressive than Tregs found in normal tissue. The recruitment of immunosuppressive inflammatory cells, such as Tregs, to the tumour

microenvironment is mediated by the release of chemokines, and results in a suppression of cytotoxic lymphocytes (Fridman et al., 2012). Additionally, immunoediting provides a selective mechanism, during which highly immunogenic cancer cells (which easily trigger an anti-cancer immune response) are eliminated by the immune system (O'Donnell et al., 2019; Wagner and Koyasu, 2019). The remaining weakly immunogenic cancer cells are then able to continue to colonise the tumour host, undetected and uninhibited by immune surveillance. The management of this complex network of immune and stromal cells is at the forefront of immuno-oncology research, in order to investigate immunotherapy resistance and improve immunotherapy treatment strategies (Binnewies et al., 2018; O'Donnell et al., 2019).

1.2 The tumour microenvironment and its impact on cancer treatments

It is clear from the above sections that other cells types surrounding cancer cells and the ECM between them can vastly contribute to the hallmark characteristics that enable tumourigenesis. Cancer cells are known to interact with many cell types, which surround them within a tumour, such as endothelial cells, pericytes, fibroblasts, immune cells and healthy tissue cells as shown in **Figure 1.1**. These cells can contribute to tumour progression and can be targeted during cancer treatment. However, the tumour microenvironment as a target for anticancer agents is a relatively new concept and most traditional cancer treatments have only targeted cancer cells and their enhanced replicative ability.

Over the last decades, cancer treatment methods may have improved, but its main modalities have remained the same. The majority of cancer patients now are treated with surgery where possible, chemotherapy and radiation, and frequently a combination of treatment methods are used. These treatments have proved to be highly effective in the extension of patient's lives and can result in curative outcomes, which many novel drugs fail to provide (Cheung-Ong et al., 2013).

To prevent the recurrence of tumour tissue, radiotherapy is used in almost 50% of cancer patients to prevent the outgrowth of remaining cancer cells in tumour

margins. Ionising radiation damages DNA strands of rapidly dividing cells, such as cancer cells, and results in the induction of apoptosis. Normal cells are also damaged in radio- and chemotherapy, but they possess the ability to repair themselves and their DNA. On the other hand, many cancer cells contain defects in DNA damage detection and repair proteins and are therefore unable to repair the DNA lesions, which results in differential cell killing of normal and cancer cells. However, after both radiotherapy and chemotherapy, extensive damage in normal tissue can still occur and mutations in normal cells can lead to the development of secondary tumours in long-term survivors (Dracham et al., 2018). The following paragraphs will provide a brief summary of the constituents of the tumour microenvironment, how they interact, how the processes they are involved in affect cancer treatments, and how they can be targeted for anticancer therapy.

1.2.1 Cancer cells and their treatment

Antineoplastic agents target the DNA within cancer cells and can be used in monotherapy, in combination, or used as adjuvant therapy with radiation or surgery, and involves the use of chemical compounds for the treatment of cancer. These cytotoxic drugs include DNA alkylating agents, topoisomerase inhibitors, antimetabolites and microtubule-active agents. All of these cytotoxic drugs act by interfering with DNA synthesis, cell division and cell survival, of both normal and tumour cells.

DNA-alkylating drugs act by modifying DNA bases, which results in interstrand crosslinks. These crosslinks stall the replication fork during DNA replication, which induces double-strand breaks that are followed by cell death by apoptosis. Examples of alkylating agents include cyclophosphamide, temozolomide and mitomycin C. A second class of drugs has a similar mechanism of action (Cheung-Ong et al., 2013) and is described in the following paragraph.

Cisplatin was the first alkylating-like platinum agent to be discovered, which as a class of drugs significantly improved cancer treatments (Cheung-Ong et al., 2013). The platinum component of the drugs binds to DNA nucleotides, where it forms adducts that can result in the formation of intrastrand crosslinks. As described earlier, these

crosslinks interfere with replication, which results in the induction of apoptosis. In fact, cisplatin has been a very successful drug in certain solid tumours, but especially in testicular cancer, where over 90% of testicular cancer cases can be cured using cisplatin therapy (Wang and Lippard, 2005). However, platinum agents have significant side effects due to their high toxicity, which limits the treatment doses that can be administered. Therefore, considerable effort has been made to develop new cisplatin analogues with less nephro- and neurotoxicity, and non-selective tissue side effects (Wang and Lippard, 2005).

Antimetabolite drugs act by mimicking normal metabolites involved with the synthesis of DNA and RNA, in order to interfere with DNA replication. This class of drugs includes pyrimidine analogues, such as 5-fluorouracil (5-FU), which mimic nucleotides during DNA replication and are incorporated into the DNA (Malhotra and Perry, 2003). Once bound, these molecules prevent the extension of the growing DNA strand, which triggers cell death. Antifolates are the second class of antimetabolites discussed here, which inhibit the dihydrofolate reductase enzyme. This inhibits the production of nucleotide precursor molecules needed from folic acid, resulting in the inhibition of DNA, RNA and protein synthesis. The most commonly used antifolate drug is methrotrexate (Cheung-Ong et al., 2013).

A group of drugs termed topoisomerase inhibitors, bind the complex formed between DNA and the enzyme topoisomerase. Topoisomerase causes transient nicks in the DNA, which allow the unwinding of overly coiled DNA during DNA replication, after which the break is reannealed (Minotti et al., 2004). Topoisomerase inhibitors bind this DNA-enzyme complex and prevent the re-ligation of breaks in the DNA. These lesions stall the progress of the replication fork and cause the induction of cell death. A sub-group of topoisomerase poisons, the class of anthracycline antibiotics, which possess further mechanisms of action, such as intercalation, helicase disruption, alkylation and crosslinking of DNA, which render them extremely effective cytotoxic drugs. However, this cytotoxicity is accompanied by severe side effects, such as cardiotoxicity (Cheung-Ong et al., 2013).

Anti-mitotic drugs target the cell division of cancer cells by interfering with the microtubule assembly and disassembly during mitosis (Steinmetz and Prota, 2018). Most of these agents have been derived from marine organisms or plants. They exert their effects by interfering with microtubule dynamics, which are essential for the assembly of the mitotic spindle during cell division, which halts the cell cycle and eventually induces cell death. Microtubule-stabilising agents, such as taxol, stabilise the microtubules of the mitotic spindle, which prevents the separation of chromosomes during mitosis. Microtubule-destabilising agents include vinca alkaloids like vincristine, which prevent the initial assembly of the mitotic spindle (Gascoigne and Taylor, 2009). Although highly effective, microtubule-targeting agents carry severe side effects, such as neurological toxicity.

All of the anticancer drugs described above target the replicative ability of cancer cells. However, they also impact the rapidly dividing normal cells, such as the cells of the bone marrow and gastrointestinal system (Macdonald, 2009). Targeted cancer therapy aims to interact with and inhibit specific pathways that may be dysregulated or that can be exploited in cancer cells, while reducing off-target effects on healthy cells. Tyrosine kinase inhibitors for example, which fall under the class of small molecule inhibitors (<500 Da), target certain receptor tyrosine kinases, which are the initial source of the oncogenic activation of downstream pathways. Gefitinib for example, targets the EGFR receptor, which is mutated in many cancers, but not normal cells, which results in a reduction in downstream signalling mediated for example by Ras and AKT (Seebacher et al., 2019). Gefitinib represented a significant development in the treatment of non-small cell lung cancer, and results in tumour shrinkage in over half of all patients (Seebacher et al., 2019).

Monoclonal antibodies, targeted to one or more tumour specific molecule have been developed in attempts to interfere with specific dysregulated signalling pathways, similarly to small molecule inhibitors. A well-known example of monoclonal antibody drugs is trastuzumab, trade name Herceptin, which targets HER2 receptors in breast cancers with overexpressed HER2 receptors. This results in the abrogation of HER2 signalling, which some tumours crucially depend on (Seebacher et al., 2019).

However, there is an immune component to the efficacy of HER2-inhibitors, as trastuzumab appears to promote tumour infiltration with NK cells and other immune cells (Griguolo et al., 2019). The impact of immune cells on cancer treatments will be discussed in section 1.2.4. Other targeted small molecule inhibitors and monoclonal antibodies inhibit specific proteins involved in angiogenesis (VEGF), matrix metalloproteinases, heat shock response (HSP) and cell death (p53 and Bcl-2) (Seebacher et al., 2019).

The last relevant group of treatments is hormone therapy, which is used in prostate and breast cancer. Many prostate tumours show an excessive activation and dependence on the androgen receptor signalling pathway, which fuels tumour growth in hormone-dependent prostate cancer (Tan et al., 2015). This dependence is exploited by using androgen receptor inhibitors, such as enzalutamide, which prevent the activation of the tumour-driving androgen signalling. Hormone therapy of breast cancer uses a similar approach, where the inhibition of estrogen signalling is used as a strategy in estrogen-receptor positive breast tumours (Dalmau et al., 2014).

These cancer treatments only represent a small number of anticancer agents which target cancer cells, many of which carry significant side effects. This has led to the combination of cancer treatments. By combining two or more drugs, with or without surgery and radiation, during a treatment regiment, the emergence of resistance can be reduced and the administered dose of each drug can be lowered, resulting in less toxicity (Chou, 2010). Frequently, the treatments mentioned above are combined with drugs that target the tumour microenvironment and its components, which will be examined in the following sections.

1.2.2 Fibroblasts and cancer-associated fibroblasts

Fibroblasts and cancer-associated fibroblasts are found in large numbers in many tumour microenvironments. In normal tissue, fibroblasts, are ubiquitous due to their important contribution to the maintenance of tissue structure. Normal fibroblasts can become activated and differentiate into myofibroblasts when a tissue injury is

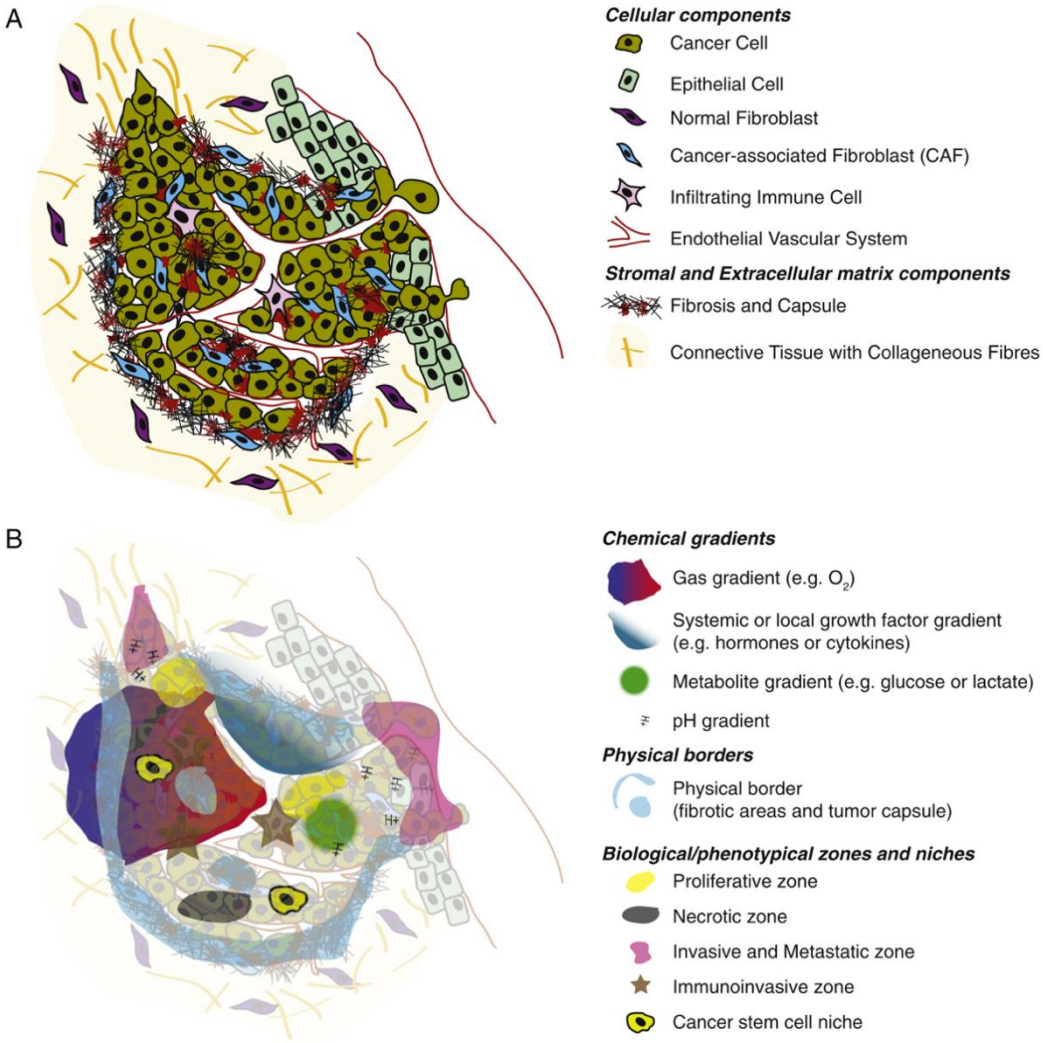

Figure 1.1 Schematic depiction of the components of the tumour microenvironment and the resulting formation of concentration gradients

A) The tumour microenvironment is characterised by the presence of various cell types, beyond cancer cells, which affect the behaviour of cancer cells, tumour progression and treatment response. B) As a result of large inter-vessel distances in combination with diffusion limits of nutrients and gases, concentration gradients of oxygen, glucose and metabolites are established within tumours. These can result in the formation of hypoxic and necrotic zones, which contribute to treatment resistance and tumour recurrence. Reproduced from: Thoma et al. (2014) Advanced drug delivery reviews

registered, in order to repair the injured tissue. These activated fibroblasts are found in many types of tumours and contribute significantly to tumourigenesis and tumour progression (Junttila and De Sauvage, 2013). In tumours, these differentiated fibroblasts, coined cancer-associated fibroblasts (CAFs), can be distributed in fibrovascular

cores which extensively branch throughout the tumour mass (frequently seen in prostate cancer), or as a surrounding fibrotic layer, which secretes extensive amounts of stroma, forming a fibrotic capsule around cancer cells (**Figure 1.1**).

CAFs originate predominantly from normal fibroblasts, which become activated, but can also descend from several other cell types, such as endothelial cells, pericytes, smooth muscle cells and mesenchymal stem cells (Balkwill et al., 2012; Junttila and De Sauvage, 2013). Once CAFS have become activated, significant changes in their behaviour occurs, such as increased proliferation and an enhanced deposition of extracellular matrix proteins. In combination with extensive ECM remodelling due to the secretion of matrix-modifying enzymes from CAFS, such as matrix metalloproteinases, and the induction of angiogenesis due to the liberation or pro-angiogenic proteins in the ECM, CAFs are capable of extensive tissue remodelling in tumours (Junttila and De Sauvage, 2013). CAFs have also been found to secrete various tumour-promoting growth factors and cytokines, such as TGF-beta. As mentioned previously, TGF-beta is involved in the induction of EMT of cancer cells, which promotes an invasive phenotype, but also in the creation of an immune-suppressive tumour microenvironment. This is enhanced by the pro-inflammatory expression signature of CAFs, which promotes tumour growth, stimulates angiogenesis and triggers the recruitment of further immune cells to the tumour.

CXCL12, a chemokine secreted by CAFs, promotes tumour cell growth and survival, but also acts as a chemoattractant for other stromal cells and their progenitors into the tumour microenvironment. However, it is worth noting that both normal and cancer-associated fibroblasts show significant morphological and functional heterogeneity. The origin of this may lie in the unique damage signal experienced by fibroblasts, depending on their location, or the plasticity of their differentiation. CAFs can transition partly or fully between mesenchymal-to-epithelial and epithelial-to-mesenchymal transition, increasing phenotypic heterogeneity. Initially, CAFs were seen as a homogeneous cell population implicated in several pro-tumourigenic processes (Hanahan and Coussens, 2012). However, the discovery of several CAF subtypes, characterised by expression of specific protein markers (since no single overarching

marker exists), has shown that CAFs can also have a tumour-suppressing role in the microenvironment, the mechanisms of which are largely unknown (Gieniec et al., 2019). Their role is thought to be dependent on the specific subtype of CAFs, the tumour location and its stage of tumour progression, however further research is required to elucidate pro- and anti-tumour effects of CAFs and their specific CAF subsets.

CAF have been found to mediate anticancer treatment resistance in several types of tumours, including breast and prostate cancer (Junttila and De Sauvage, 2013). The most prominent mechanism of CAF-mediated resistance is linked to CAF-mediated desmoplasia, which involves the development of a thick stromal layer around tumours. This can be very cell-rich and contain large numbers of CAFs and endothelial cells, or it can consist almost exclusively of ECM proteins such as fibronectin and collagen. The development of this fibrotic capsule around tumours was originally thought to be an anti-tumour response, due to its confinement of the malignant growth (Gieniec et al., 2019). However, it has since been demonstrated that a thick stromal layer presents a significant barrier to the tumour penetration of anticancer drugs, especially since desmoplasia appears to result in a poor vascularisation of the tumour, further decreasing the efficiency of drug delivery (**Figure 1.1**). The failure of cancer treatments to reach the malignant cells within the tumour limits the efficacy of any systemically applied anticancer therapy (Junttila and De Sauvage, 2013). Additionally, the adhesion of cancer cells to the ECM has also been linked to chemotherapy-resistance, likely mediated by the induction of cancer cell EMT by CAFs, due to their release of TGF-beta (Gieniec et al., 2019). The secretion of specific growth factors and cytokines from CAFs results in other treatment-specific problems as well. CAFs release several pro-angiogenic proteins, such as the platelet-derived growth factor C, which were found to mediate resistance to anti-angiogenic therapy (Gieniec et al., 2019), which will be discussed in section 1.2.3.

Due to their extensive tumour promoting effects, CAFs and their regulatory mechanisms have become a target for novel anticancer drugs. Additionally, CAFS are genetically stable in comparison to cancer cells, and are less likely to acquire mutations and

drug resistance, which makes them an ideal target for drug treatments. Animal studies have shown that the ablation of specific CAF subsets, such as FAP-expressing CAFs, result in the induction of tumour necrosis, which could be exploited if these CAF subsets could be targeted specifically (Gieniec et al., 2019). Further, CAFs can play a significant role in metastasis, as they've been shown to accompany disseminating cancer cells, constantly providing them with survival signalling and a growth advantage at the eventual metastatic site (Gieniec et al., 2019). When mouse tumours were depleted of CAFs during metastasis, the number of metastases formed could be reduced drastically (Duda et al., 2010). Although many preclinical studies show a treatment benefit after targeting CAFs, several drugs and small molecule inhibitors of matrix metalloproteinases or CAF signalling pathways have been investigated, but only few clinical trials have targeted CAFs selectively and none of the MMP inhibitors have shown promising results in clinical trials (Chen and Song, 2019). This highlights the need for further research into the pro- and anti-tumour effects of CAFs and their specific subtypes, which are still largely unexplored. Until the role of CAFs can be clarified and their tumour-suppressive effect can be explained, targeting CAFs with drugs will remain difficult, since it could inhibit tumour-promoting or tumour-suppressing CAFs, resulting in potentially opposite effects.

1.2.3 Tumour vasculature

The induction of the neovascularisation of tumours was described earlier as a hallmark of tumourigenesis. Soluble pro-angiogenic factors in the tumour microenvironment secreted by cancer cells and inflammatory cells, such as VEGF, FGF, PDGF and chemokines, stimulate endothelial cells and pericytes via signal-transduction receptors on the cell surface. This stimulation results in the activation of angiogenesis and new vessels sprout in the tumour. However, as mentioned above, the tumour vasculature that is formed as a result is highly abnormal, with extensive chaotic branching, uneven vessel lumen and significant leakiness (**Figure 1.1**). This results in uneven blood flow, gradients of oxygenation, nutrient and drug distribution across the TME, as well as in an increase in interstitial pressure (Carmeliet and Jain, 2000). The raised

interstitial pressure has widespread effects in the TME, since it compresses tumour vessels, which provides a barrier to the movement of drugs across tumour vessels (Junttila and De Sauvage, 2013). Additionally, the intercapillary distance in the tumour vasculature is frequently increased in comparison to normal tissue (averages ranging from 50-100µm) and can range from 50 to more than 250µm (Kolstad, 1968; Wilson and Hay, 2011). These inter-vessel distances can exceed the diffusion limit of oxygen in tissue (approximately 100µm), which results in the formation of hypoxic niches (**Figure 1.1B**) (Brown and Giaccia, 1998; Carmeliet and Jain, 2000). This increased distance to blood vessels in combination with compound diffusion limits results in a decrease in drug delivery to hypoxic tumour regions (Carmeliet and Jain, 2000). Further, the hypoxic niche as been associated as a harbour for cancer stem cells, which are connected to chemotherapy- and radioresistance and can result in the recurrence of tumours after cancer treatment. It appears that the hypoxic niches found in tumours are capable of providing a sheltered protective niche for cancer and cancer stem cells during cancer treatments, which can be the source of tumour regrowth (Wilson and Hay, 2011; Carnero and Lleonart, 2016). Additionally, the lymphatic vessels around and within tumours are altered in their phenotype and function. The high interstitial pressure within tumours compresses the lymphatic vessels so much that they're frequently collapsed and non-functional (Hanahan and Weinberg, 2000). However, at tumour margins and in surrounding healthy tissue, functional, growing lymphatic vessels can be found. These are thought to be the seeding channels for metastasis of cancer cells into the draining lymph nodes.

Overall, the abnormal tumour vasculature, its leakiness and the resulting effects in the TME are thought to present a barrier to the delivery of drugs, thereby aiding in resistance. In order to combat this, the normalisation of vascular beds within tumours, with the intent improve drug delivery, has been attempted by inhibiting signalling molecules involved in the induction of angiogenesis, such as VEGF. This is thought to not only transform tumour vascular beds into normal vascular beds normalising their function, but also to decrease the formation of blood vessels formed to supply the tumour with blood flow (Viallard and Larrivée, 2017).

The most successful attempt of VEGF inhibition has been the development of a humanised monoclonal anti-VEGF antibody, called bevacizumab. Bevacizumab showed very promising results in clinical trials, where its use in combination with chemotherapy appeared to benefit patients and improved progression-free survival (Junttila and De Sauvage, 2013). After the benefit of the inhibition of angiogenic pathways was recognised, small-molecule inhibitors of the VEGF receptor were also tested in clinical trials, but have failed to prove significant patient benefits so far (Junttila and De Sauvage, 2013). Additionally, in some cases, small-molecule inhibitors of the VEGF receptor have resulted in increased invasiveness and metastasis. Not only the class of VEGF-inhibitors appears to affect the response in patients, but also the tumour type. In glioblastoma multiforme (GBM) for example, a subset of patients appears to deteriorate after VEGF inhibition, which was found to be a result of a specific VEGF-mediated down-regulation of the MET receptor, which upon activation worsened treatment outcome (De Groot et al., 2010). However, this shows the potential for combined VEGF and MET inhibition in GBM tumours. This again reinforces the importance of considering the entire TME and the contribution of all of its components and their interaction with each other in drug targeting. Although the mechanisms of the involvement of angiogenesis in tumourigenesis and progression have yet to be fully elucidated, angiogenesis presents a promising target for future combination therapies. Additionally, the receptor expression profiles of tumour-associated endothelial cells and normal endothelial cells may be distinct from each other, making them a potential selective target for cancer treatments, without affecting normal blood vessels (Ruoslahti, 2002).

1.2.4 Immune cells

Initially, the contribution of immune cells to cancer hallmarks was described, entailing both tumour-suppressive and tumour-promoting cell-mediated mechanisms. Several subtypes of immune cells are thought to be involved in the initiation of tumours, tumour progression and the tumour response to treatments, which will be summarised briefly in the following paragraphs. Both the innate and adaptive

immune system can be involved in the promotion or inhibition of tumour growth (Binnewies et al., 2018). And although the body's immune system has the capability of launching anti-tumour responses, through CD8+ CTL cells for example, but immune suppression in the same environment can prevent this. In principle, all immune cells can be found in tumours, however the exact composition of each patient's immune tumour microenvironment varies depending on tumour type, the organ affected, stage of progression and even varies between patients of the same tumour type (Fridman et al., 2012). Despite observed variations in the composition of each patient's immune response, all immune component are found in higher densities in tumours than in normal tissue (**Figure 1.1**) (Fridman et al., 2012).

The distribution of immune cells within the tumour also varies, depending on cancer and CAF-mediated signalling, the permeability of local vasculature, and endothelial cells, which regulate immune cell infiltration. As a result, immune cells can be individual or clustered, and located at the invasive margin, in the tumour core or within tertiary lymphoid structures. The location of immune cells within the tumour frequently affects or indicates changes in cell function. For example, immature dendritic cells are most commonly found in the tumour core, whereas mature dendritic cells concentrate in tertiary lymphoid structures in close contact with naive T cells (Fridman et al., 2012). It is theorised that this interaction educates T cells, generating a form of memory, resulting in the creation of effector T cells, which are then capable of inducing a tumour-suppressing or tumour-promoting response (Fridman et al., 2012).

Overall, the infiltration with lymphocytes, such as T cells, B cells and NK cells has been linked to longer disease-free or overall survival in several cancers, including melanoma, breast, bladder, ovarian, colorectal, renal and prostate cancer (Fridman et al., 2012; Hanahan and Coussens, 2012). In particular, the presence of a high number of Th1 and cytotoxic memory T cells in the tumour core or margins has been a strong prognostic indicator for improved survival and the lack of recurrence (Fridman et al., 2012). Studies have shown that a dense infiltration with CD4+ memory T cells and CD8+ memory T cells can have a protective effect and reduce invasion and tumour

recurrence. T helper Th1 cells secrete cytokines which influence the immune tumour microenvironment, e.g. IL-2 and IFN-gamma, which stimulate CD8+ CTLs, NK cells and macrophages. Both CTLs and NK cells can induce cell death in the cells that they target. Macrophages on the other hand, and especially M2 macrophages, which can be located in the tumour core or the invasive margin, appear to favour the induction of tumour growth and spreading (Fridman et al., 2012).

In some cases, a high infiltration with CD57+ NK cells is predictive of a favourable treatment response in some cancers, such as colorectal, gastric, renal and liver cancers. However, the expression of CD57 is not unique to NK cells and can also be found on cytotoxic T cells (Fridman et al., 2012). Normally, NK cells are found within the stroma of the TME, not in contact with cancer cells directly, however, tumour cell-mediated signalling can affect their function through the secretion of TGF-beta. When found within tumours, TGF-beta signalling of cancer cells has been shown to maintain NK cells in a specific anergic phenotype, which renders them unable to secrete IFN-gamma and kill cancer cells, therefore contributing to an immunosuppressive microenvironment (Fridman et al., 2012). The overall effect of this suppression depends on which type of immune response is being inhibited, and therefore depends on the composition and interaction of the components of the specific microenvironment. Regulatory T cells also appear to have mixed effects on survival and have been reported to have suppressive functions on the tumor immune microenvironment (Binnewies et al., 2018). A high intra-tumoural Treg infiltration correlates with poor overall survival in ovarian, breast and liver cancer, although other studies have not been able to detect an impact of Tregs on survival (Fridman et al., 2012). Meanwhile, an inverse correlation and a positive impact of Treg infiltration on treatment outcome was shown for other cancer types, such as head and neck cancer, ovarian and colorectal carcinoma (Leffers et al., 2009; Frey et al., 2010; Zhang et al., 2010). The effect of Tregs in is still not fully understood and likely depends on the context of the tumour microenvironment. Tregs might exert a harmful effect by inhibiting anti-tumour effector T cells such as CTLs, or have a beneficial effect by decreasing chronic inflammation. This highlights the impact of the tumour

microenvironment and the importance of understanding the mechanisms of its components and how they interact, since opposing effects can occur as a result.

Both radiotherapy and chemotherapy, although not intended, have been shown to result in the production of a robust tumour-specific immune response through the recruitment of CD8+ CTL T cells (Medler et al., 2015). At this point it is well established that a strong immune component and high lymphocytic infiltration is predictive of a favourable chemotherapy and neoadjuvant response in breast cancer (Fridman et al., 2012). In fact, a high number of CD8+ CTLs in the invasive margin of breast cancer tumours predicts a better response to chemotherapies and prolonged survival in a number of tumours (König et al., 2019). There also appears to be an immune component to anti-VEGF therapy using small molecule-inhibitors, such as sunitinib and sorafenib, and the monoclonal antibody bevacizumab. Patients which showed a decrease in Tregs and MDSCs in the tumour margins and core after several treatment cycles, experienced overall longer survival (Fridman et al., 2012).

Since the immune system appears to have a significant effect on tumour progression, modulating the immune system's response to a tumour has become a goal for cancer therapy. The activation of T cells is controlled by finely balanced stimulatory and inhibitory checkpoint signals. The main inhibitory checkpoints are the programmed cell death protein 1 (PD1) and Cytotoxic T-lymphocyte-associated antigen-4 (CTLA-4), which are in place to dampen an active CD8+ T cell response and prevent excessive tissue damage and autoimmune responses (Medler et al., 2015). However, in cancer patients, the inhibition of a potential anti-tumour immune response could worsen prognosis. Therefore, and in order to enhance the anti-tumour immune response, treatments have been developed which target these checkpoints. The first checkpoints to be targeted for cancer therapy were CTLA-4 and PD-1. The first drug to be approved for CTLA-4 inhibition was ipilimumab, a monoclonal CTLA-4 antibody, which upon binding allowed the activation and proliferation of T cells, through the derepression of the CTLA-4 signalling by CD28 (Farkona et al., 2016). CTLA-4 is expressed on CD4+ T cells and functions to dampen the cross-presentation involving T cells in the secondary lymphoid structures, which inhibits education of naïve CD8+ T

cells into activated cytotoxic CTLs. The inhibition of this mechanism increases the recruitment and migration of T cells to the tumour site, and CD8+ CTLs in particular, but also CD4+ memory cells and CD8+ memory cells, which increases the anti-tumour response of the immune system (Medler et al., 2015). Ipilimumab showed promising results in clinical trials for melanoma and advanced metastatic melanoma, improving overall survival significantly (Farkona et al., 2016). However, 35% of patients experienced severe, immune-related and potentially fatal side effects, which left some room for improvement of toxicity of CTLA-4 antibodies (Farkona et al., 2016).

A different target for checkpoint blockade was found in the PD1 receptor expressed on the surface of CD8+ and its ligand PD-L1, which inhibits T cell activation, differentiation and proliferation upon binding (Seebacher et al., 2019). Several anti-PD1 antibodies have been tested in clinic and were approved by the FDA. Both pembrolizumab and nivolumab were able to produce tumour shrinkage and prolong overall survival in melanoma and NSCLC significantly, producing long-lasting remissions (Seebacher et al., 2019). Anti-PD1 antibodies also produced mostly manageable side effects, in stark contrast to the extreme toxicity of anti-CTLA-4 therapy, which is likely due to the more targeted approach of anti-PD1 therapy. PD1 expression is highly upregulated in several cancers, and the targeting of tumour-cell induced immune suppression may be more selective than the non-specific activation of a T cell response through CTLA-4 (Farkona et al., 2016). Several other inhibitors for CTLA-4, PD1 and PD-L1 are currently tested in clinical trials, alone and in combination with other checkpoint inhibitors and chemotherapies.

A problem, which all checkpoint inhibitors share is their limited response rate, since they can produce impressive tumour responses, but only in a fraction of patients, sometimes less than 20% (Seebacher et al., 2019). Several studies now hypothesise that in order for PD-1 blockade to be effective, a reservoir of CD8+ cells has to exist in the tumour already at the time of treatment, in order to “unleash” an already prepared tumour immune response (Dijkstra et al., 2018). This has resulted in the investigation of the level of pre-existing CD8+ T cells before treatment, as a biomarker to predict therapy response to PD-1 blockade (Medler et al., 2015). To improve the

efficacy of existing immunotherapy strategies, significant efforts have been made to establish biomarkers which are able to predict the response to PD-1 and CTLA-4 inhibition. For example, a high mutational tumour burden is thought to generate a more specific neoantigen-specific T cell response, improving immune response to cancer cells after PD-1 or CLTA-4 therapy (Boumber, 2018). Clinically, the number of mutations within tumours appears to correlate with better clinical responses and overall outcomes in melanoma, NSCLC and colon cancer patients (Zugazagoitia et al., 2016). As a consequence, tumour types with a lower mutational burden and less neoantigens, have not benefited from immune checkpoint blockade (Dougan et al., 2019), such as pancreatic cancers, most colorectal and prostate tumours. The success of immune checkpoint blockade relies to some extent on the cross-presentation of cancer cells and the molecules on its surface to T cells, which relies on the major histocompatibility complexes (MHC) 1 and 2. A loss of any of the MHC components through mutation is a common way for tumours to evade checkpoint blockade (Dougan et al., 2019).

An approach to tumour immunotherapy which has gained popularity recently, since its original inception in 1989, involves the use of genetically modified T cells, which are able to recognise tumour antigens without the aid of MHC proteins. These cells are coined CAR-T cells, since they target specific antigens on cancer cells using a chimeric antigen receptor (CAR), which binds to cancer cells and induces a specific immune response against them. CAR-T cells are produced by isolating T cells from a patient, which are then genetically modified by linking the CAR of choice to the signalling domain of CD3zeta and a co-stimulatory domain (for example CD28). The modified CAR-T cells are then expanded and transfused back into the patient. In liquid tumours such as B cell leukemias and lymphomas, targeting CD19 has been highly effective, achieving an unprecedented response rate of almost 80% in patients with acute lymphoblastic anemia (ALL), producing curative outcomes, which revolutionised treatment of ALL (Schmidts and Maus, 2018). However, the success of CAR-T cell therapy in liquid tumour has so far not been able to be replicated in the treatment of solid tumours, although better CAR-T cells with multiple co-stimulatory domains have

been developed since. An additional problem lies in the selection of a suitable tumour-associated antigen which can be targeted. Ideally, this target antigen is highly and uniformly expressed, and only found in tumour cells or shared only with replaceable or nonessential tissue, since off-target CAR-T cell attack can have potentially fatal side effects. The target antigen also has to be expressed on the surface of tumour cells, which only applies to 1% of cell proteins (Martinez and Moon, 2019). This makes the targeting of CAR-T cells problematic, since CAR-T cells are able to attack other cells and tissues which express the target antigen as well. In ALL this is frequently seen as the occurrence of B cell aplasia after CAR-T treatment, since B cells also express CD19, although this side effect can often be managed (Schmidts and Maus, 2018). In solid tumours, off-target effects of CAR-T cells carry severe side effects which are lethal in some cases. This is likely due to expression of the target antigen on normal epithelial cells, which most tumours are derived from. One example of the catastrophic effects of off-target toxicity was displayed in a patient with metastatic colorectal cancer, who received HER2-targeted CAR-T cell therapy and died 5 days later. It was found that epithelial cells in his lungs had expressed low levels of HER2, which were attacked by the administered CAR-Ts (Martinez and Moon, 2019). Finding targets for CAR-T cell therapy which are selective to cancer cells and uniformly expressed presents a tremendous challenge, which isn't helped by current preclinical models used to study CAR-Ts. The main method of testing CAR-T cells preclinically remains in the use of xenografted tumours in immune-suppressed mice, which lack the host expression of the target antigen, and as a result the toxicity of off-target toxicities cannot be assessed sufficiently. A further problem with the use of CAR-T cells for solid tumours rests in the delivery. Intravenous administration of CAR-T cells often results in insufficient trafficking of the CAR-Ts to the tumour site and reduced proliferation, which means that the CAR-T cells cannot persist in the blood stream and the tumour as long as necessary (Schmidts and Maus, 2018). Therefore, the local delivery of CAR-T cells has been investigated as a way to improve CAR-T treatment of solid tumours. When applied locally, for example to the pleural space in pleural malignancies, T cell activation was found to be improved, along with an increased

persistence of CAR-Ts in the blood stream and tumour response, while requiring less CAR-Ts than during IV delivery (Schmidts and Maus, 2018). Several novel CAR-T products are currently undergoing clinical trials, in hopes to improve on results like these in the treatment of solid tumours with cell-based immunotherapy.

1.3 Tumour models for drug efficacy testing and precision medicine

Tumour models are required to perform basic research to aid in our understanding of cancer, for drug efficacy testing in order to discover new anticancer therapies (cell-based or in form of a drug), and to understand how and why drugs exert certain effects in certain patients. We now know that the constituents of the tumour microenvironment and their interaction with each other characterise the behaviour of tumours. Therefore, tumour models have to reflect the tumour microenvironment and its behaviour as closely as possible in order to be a useful and predictive tool for drug discovery, lead optimisation and mechanistic studies.

1.3.1 Overview of tumour models

For a long time, the predominant tumour model used in cancer research and drug development was created by culturing cancer cell lines in monolayers on the flat surfaces of petri dishes, culture flasks and well-plates. These monolayers of cells allowed the observation of cell proliferation and behaviour, and were considered a predictive tumour model since monolayer cultures were developed in 1907 (Breslin and O'Driscoll, 2013). However, over the last two decades, tumour models have slowly drifted away from the use of monolayers for mechanistic studies, because they fail to mimic several features of the tumour microenvironment, which we now know are critical, in order to mimic in vivo tumours closely. This has led to the investigation of differences between cancer cells cultured in 2D and in vivo tumours, which has revealed that cells cultured in 2D undergo changes in morphology, receptor and oncogene expression, and in their interaction with the surrounding matrix (Breslin and O'Driscoll, 2013). Cells grown in monolayers lack the cell-to-cell contact surrounding

them in all directions, any form of tissue organisation, and the tissue oxygen and nutrient gradients which affect cellular behaviours, such as proliferation, migration and angiogenesis. In 2D cultures all cells are exposed to the same concentration of nutrients, oxygen and applied drugs, resulting in a loss of the cellular heterogeneity seen in vivo. Therefore, it was not surprising that meta-analyses suggest that results obtained from drug efficacy testing conducted on cells in 2D, do not correlate with clinical trial outcomes and have poor predictive value (Voskoglou-Nomikos et al., 2003; Burstein et al., 2011). At the same time, the cost for the development of each new approved drug has increased to approximately 2.6 billion USD, and the chance of market approval for a drug entering clinical trials lies at only 11.83%, which has dropped from 20.5% in previous years (DiMasi et al., 2016). The majority of drugs fail during phase 3 of clinical trials, the most expensive stage, with the main reasons being a lack of clinical efficacy or unacceptable toxicity. And while animal studies are undoubtably necessary to assess systemic toxicity, improved in vitro models, which are more predictive of clinical outcomes, could help sieve out ineffective drug candidates earlier on during the development process, preferably before clinical trials and even animal studies (Breslin and O'Driscoll, 2013).

1.3.2 3D tumour models

In order to overcome the drawbacks of monolayer cultures, initial attempts to create a three-dimensional tumour model centred around the creation of multi-cellular tumour spheroids, which are large aggregates of cancer cells that reflect several properties of the tumour microenvironment. 3D spheroids immersed in medium can replicate nutrient, growth factor, gas and compound concentration gradients due to diffusion limits of the gases and chemicals surrounding them (Thoma et al., 2014). These gradients allow the establishment of a proliferative zone of dividing cells around the outside of the spheroid, whilst cells towards the inside of the spheroid gradually become less oxygenated and proliferate less. Oxygen gradients can result in the formation of a hypoxic core in the centre of the spheroid, and even result in necrosis if the spheroid diameter exceeds 500-600µm (Friedrich et al., 2009). The establishment of a hypoxic niche is an interesting feature of spheroids, since hypoxic niches are also

found in tumours in vivo, as described earlier, where they appear to promote angiogenesis, tumour recurrence and harbour cancer and cancer stem cells during cancer treatments. These features of spheroids mimic many features of solid tumours, whilst being particularly amenable to traditional high-content screening techniques (Breslin and O'Driscoll, 2013). Additionally, culturing cells in 3D appeared to alter their expression profiles to closer match those of real tumours, which was determined by comparing the gene expression of mesothelioma cells cultured in 2D and 3D. The expression of 142 genes was found to be altered in mesothelioma spheroids when compared to monolayers, mostly involving genes connected to morphology, proliferation, cell-to-cell signalling and cellular movement. In the 3D mesothelioma spheroids several genes were found to be up-regulated, which were mainly associated with immune response, wound healing, the stimulation of lymphocytes and the cell response to cytokine stimulation (Kim et al., 2012). Down-regulated genes were mainly connected to apoptosis. These changes in gene expression suggest that 3D cultures such as tumour spheroids could be an improved in vitro model with respect to 2D cultures.

1.3.3 Methods for the generation of spheroids

Several methods can be used for the generation of tumour spheroids, the most common one of which currently is the forced-floating method. This involves the use of super-hydrophobic or cell-repellent cell culture surfaces, often in form of a 96-well plate, which prevent the adhesion of cells to the surface, and instead promote the interaction and adhesion of cells to each other, resulting in aggregation and the formation of a spheroid (Ferreira et al., 2018). Spheroids can be created using this method from cancer cells alone or in co-culture with other cell types, such as fibroblasts. Co-culture assays with fibroblasts have shown that fibroblasts affect the treatment response of 3D spheroids, which mimics another feature of in vivo tumours, and shows that 3D spheroids could be a valuable tool to model and investigate CAF-mediated resistance in vitro (Majety et al., 2015).

The hanging drop method utilises a similar approach to the forced floating-method, by providing a non-adherent culture environment. In order to create spheroids using

the hanging drop method, a single-cell suspension is pipetted into wells of a micro-well tray, which is inverted. This results in the floating of the cells within the cell suspension at the bottom of the created droplet, that is only surrounded by an air-liquid interface, which does not allow cell adhesion and promotes aggregation of cells (Breslin and O'Driscoll, 2013). Similar to the forced-floating method, the spheroids produced within hanging drops are fairly uniform in size and are easily accessible for further analysis. However, the small culture volume in the hanging drops, often as little as 20µL, creates problems during medium exchange and the application of drugs, which can disturb cells considerably (Breslin and O'Driscoll, 2013).

In both of these methods, the spheroid size can be controlled by adjusting the cell number in each well and large numbers of uniformly sized spheroids can be produced easily, although medium exchange remains challenging.

Other techniques, such as agitation-based methods, used spinner flasks and rotating vessels, which constantly agitate cells to prevent their adhesion to the culture surface (Thoma et al., 2014). However, this approach requires specialised equipment and produces a diverse range of spheroid sizes, although spheroids of a similar size can be selected after the initial culture (Breslin and O'Driscoll, 2013). As a result, the use of agitation-based methods for the generation of spheroids has declined over the years.

A further method, which remains popular, is the culture of cells on or embedded within a biological matrix, with the goal of mimicking in vivo cell-to-matrix interactions and the cell behaviours which arise from these as a consequence in vivo. As summarised above, the ECM affects cellular organisation and function, which has widespread effects on tumourigenesis and tumour progression (Breslin and O'Driscoll, 2013). As a result of the increased cell-matrix interactions, cells embedded in matrices are able to develop into structures resembling those found in the originating tissue, such as luminated cysts. The most commonly used matrix is likely Matrigel, which consists of basement membrane proteins extracted from mouse Engelbreth-Holm-Swarm (EHS) tumours, containing matrix proteins such as laminin, collagen IV, matrix metalloproteinases and growth factors (e.g. EGF, FGF, TGF-beta),

which are also contained in the tumour microenvironment (Benton et al., 2011). It is worth noting that the ECM found in the body and in tumours is very much tissue-specific, which can be accommodated by commercially available matrices to some extent, since various types are available, and can contain cartilage matrix proteins, high levels of collagen VI or be depleted of specific growth factors (Breslin and O'Driscoll, 2013; Benton et al., 2014). However, since Matrigel and similar matrices are biological substances, their composition can vary between batches, which can result in inconsistencies during matrix-supported 3D culture assays (Breslin and O'Driscoll, 2013). Additionally, matrices are currently very expensive, which makes their use a significant factor in large-scale experiments and high throughput screening, although new matrices and biogels are constantly developed in the hope of producing fully customisable tissue-specific matrices. There are other drawbacks associated with matrix-supported cultures, such as the frequently uneven cell distribution, which can result in the generation of overlapping spheroids that are difficult to process during image analysis.

1.3.4 Advantages of spheroids

Since their inception, spheroids have been generated from numerous cancer cell lines and have found applications as a tumour model to study cancer growth, invasion and drug responses (Härmä et al., 2010). 3D culture appears essential to the replication of in vivo drug responses, as several studies have shown that cell surface receptor function mimics in vivo receptor function more closely when cultured in 3D than in 2D (Howes et al., 2014). Co-cultures of two or more cell types have allowed the investigation of the impact of stromal cells, such as fibroblasts and endothelial cells (HUVEC) on the behaviour and treatment response of pancreatic cancer cultures (Lazzari et al., 2018). Further, since the size of spheroids is easily controlled, they have also become a useful tool for the estimation of tissue drug penetration, which can be a limiting factor in cancer treatments, and the experimental determination of drug diffusion coefficients (Groebe et al., 1994; Kostarelos et al., 2005). Over time the availability of more methods for the creation of spheroids has resulted in the creation

of tumour models of increased physiological relevance. An excellent example of this is the generation of 3D models of breast cancer and normal tissues embedded in gels, which was pioneered by Bissell et al. in 1991 (Bissell et al., 2003). Bissell et al. showed that normal breast and breast cancer cells, when embedded in Matrigel, could create round ductal structures, which were able to secrete casein, a component of breast milk. This undoubtedly showed that a 3-dimensional culture environment could restore cellular organisation and physiological tissue functions, which likely increases the predictive value of 3D culture in comparison to monolayers (Bissell et al., 2003).

All of the methods described above for the generation of 3D tumour models have advantages and disadvantages, some of which depend on the application of the model. The forced-floating method in micro-wells and hanging drop plates is still the most commonly used methods for the generation of spheroids for drug screening purposes, because they produce uniformly sized spheroids and easily interface with imaging and analysis equipment, such as plate readers. However, both ultra-low adhesion and hanging drop plates are somewhat cumbersome and require skilled handling in order to not interfere with the formed spheroids. Further, the liquid-to cell ratio experienced by cancer cells in tumour spheroids generated using these methods does not match the conditions within tumours, which means that spheroid-secreted factors frequently do not reach physiological concentrations (Frimat et al., 2010). All of the methods mentioned for the generation of spheroids require large amounts of cellular material, reagents, some of which are extremely expensive, e.g. Matrigel. Additionally, the matrices used for spheroid assays do not reflect the tissue-specific matrix for each organ and are obtained from a different organism (mice), which limits their physiological relevance.

In many respects, complex 3D models generated from cell lines, such as co-cultures are still not similar enough to target tissues to be of predictive value and require validation, although they can be a valuable tool in the investigation of specific mechanisms. Cell line-derived 3D tumour models lack the diverse set of cell types found in tumours and therefore only mimic incomplete heterotypic interactions. This also

applies to the heterogeneous cancer cell population seen in vivo, which cannot be reflected by cell lines.

Ultimately, only the use of patient-derived tissue can truly replicate a human tumour as closely as possible, since it does not just contain the tumours heterogeneous cell population, but also its extracellular matrix which is an essential contributor to the TME and its function (Kunz-Schughart et al., 2004). This has been demonstrated by Landberg et al., who decellularized breast tumour tissue, leaving only a scaffold of extracellular matrix behind. These patient-derived scaffolds were recellularised using breast cancer cell lines, which induced a series of extensive changes in the cancer cells. They observed the differentiation of cells, epithelial-mesenchymal transitions and an increased number of cancer stem cells. These recellularised patient-derived scaffolds were compared to xenografts of the same cell type and demonstrated similar tissue morphology and gene expression patterns. Additionally, the assay appeared to have predictive value, as the patient-derived scaffolds which initiated EMT in vitro, correlated with disease recurrence in the corresponding breast cancer patients, which highlights the role of the ECM in tumour progression (Landberg et al., 2020). Indeed, many studies have now shown that functional in vitro assays using patient-derived tissue in a 3D context are capable of predicting clinical outcomes for several types of cancer, which is not the case for 2D assays using patient tissue (Kross et al., 2008; Halfter and Mayer, 2017; Shuford et al., 2019). However, the use of patient tissue for high throughput drug screening has been limited by the small quantities of the available tissues, lack of access to patient-derived tissue, and the large cell requirements of the 3D tumour models described above.

1.3.5 3D tumour models utilising patient-derived tissues

Despite the drawbacks of limited quantities available and the high degree of variability between patient tissues, the need for predictive in vitro models and their potential use in precision medicine have fuelled the use of patient-derived tissues in preclinical assays. The lack of predictive value of 2D functional assays using patient-derived tissue (Higashiyama et al., 2008) has led to the development of several functional assays

which could assess the response of tumour-derived cells in a 3D context (Halfter and Mayer, 2017). Functional assays which have involved the use of tumour fragments or suspensions, replicate the resident tumour more closely than xenografts can, since they retain many aspects of the patient's TME. Additionally, 3D assays using patient tissues, independent of their application in patient-derived xenografts or in vitro models, carry the disadvantage of high variability between individual patients. However, this also represents an opportunity for mirroring the intratumoral heterogeneity and the true heterogeneity of tumours of the same type, which is increasingly presumed to affect treatment outcomes (Junttila and De Sauvage, 2013). This information would be valuable for research into novel biomarkers for patient stratification, which could enable more targeted clinical trials, or for predictive markers of the outcome of various therapies, including immunotherapies. As mentioned previously, immunotherapies of various types and other cancer therapies can produce impressive improvements, but since they are only effective in a fraction of patients, it's become important to identify which group of patients will benefit the most by using predictive biomarkers. Simultaneously, predictive 3D patient-derived assays could reveal markers of a negative outcome, which could lead to the development of new drugs or combination therapies which specifically target these non-responding patients. One further opportunity for patient-derived tumour models lies in precision medicine, which could be used to guide individualised treatment, which could increase the number of successful treatment outcomes and reduce the use of ineffective cancer therapies with potentially lethal side effects.

1.3.6 Precision medicine

Precision medicine has become a new goal in the world of cancer treatment and has to be distinguished from personalised medicine carefully. Personalised medicine provides a degree of individualised cancer treatments, tailored to the individual using genetic, molecular or cellular analysis. Modern molecular diagnostics, such as next-generation sequencing (NGS) have identified thousands of mutations which allow the establishment of clinically relevant tumour subtypes. As a result, patients who show

certain genomic changes can be stratified into groups, based on genomic data, which is in fact how most targeted cancer therapies are used currently. For example, if HER2 is overexpressed in breast cancer patients, the standard-of-care treatment is trastuzumab, which targets the HER2 receptor. However, despite producing promising results in this subset of tumours, only 40% of patients with HER2+ tumours respond to trastuzumab treatment (Pinto et al., 2013). Other treatments targeting genomic alterations, for example in EGFR and ALK expression, such as Gefitinib and Crizotinib, have produced similarly low response rates (Friedman et al., 2015). The reasons for this lie in the incomplete understanding of the effect of mutations and their interactions, which prohibits accurate prediction of treatment response, even if known driver mutations are being targeted. Unfortunately, only 9.6% of cancer patients display targetable alterations in their genome and the impact of epigenomic modifications is unclear (Dienstmann et al., 2015). Therefore, despite the predictive power of next-generation-sequencing and other advances in molecular diagnostics in subsets of patients, the molecular classification of the constituents of a tumour cannot yet address every patient, and only small groups of patients benefit.

1.3.6.1 Functional assays using patient-derived tissue for precision medicine

Functional assays, which determine the response of live tumour tissue to a range of available treatment options in an ex vivo setting, could be used as an additional source of information in order to guide patient treatment. The main benefit of functional assays is that patients could be matched to the treatment most likely to produce a successful outcome, even in cancer types where no predictive markers or targeted therapies exist. Therefore, determining the ex vivo sensitivity to available treatment options using functional testing, could provide access to truly individualised cancer treatment, which is termed precision medicine. Indeed, functional assays, in the form of antimicrobial susceptibility tests, have been routinely used for decades in infectious diseases, providing a precision medicine approach in order to match each patient's infection to the most suitable antibiotic for their infection (Jorgensen and Ferraro, 2009). However, the use of functional assays for individualised cancer

treatments has been hampered by the lack of proof of predictive value and clinical utility (Friedman et al., 2015). We now know that this is likely due to the use of 2D tumour models, which do not reflect the tumour microenvironment and its impact well enough to allow for accurate predictions (Nagourney et al., 2012; Halfter and Mayer, 2017). Since this has been recognised, several methods which test drug susceptibility in a 3D context have been published, which show promising correlations with clinical outcomes, although many still require validation in the clinic (Halfter and Mayer, 2017). Examples of these are provided in the following sections.

1.3.6.1.1 Tumour tissue fragments

Nagourney et al. created spheroids of approximately 500 micron size using mechanical and enzymatic digestion of NSCLC tumour biopsies and resections of patients with metastatic inoperable disease (Nagourney et al., 2012). These patient-derived spheroids were then exposed to ten individual and six combinations of chemotherapy drugs for 72 hours, after which the most effective treatment was identified. The most promising drug was recommended and used for patient treatment where oncologists agreed with the treatment choice. The assay provided a significant improvement in treatment response when compared to control patients.

Jung et al. tested 11 chemotherapeutic agents on tumour fragments derived from advanced epithelial ovarian tumours and compared the outcomes to patient responses. The ex vivo drug efficacy testing completed in this case allowed the successful prediction of clinical outcomes with a clinical correlation of 80-90% (Jung et al., 2013). These studies show that functional assay-guided chemotherapy is a viable option for advanced metastatic diseases.

Similar assays utilising tumour fragments of approximately 500 micron size have been used to determine the treatment response of hormone-dependent tumours, such as prostate and breast cancer (Centenera et al., 2018). A different approach to the functional screening of intact patient tissue was found in the use of thin tumour slices, which can be exposed to chemotherapeutic agents. Using 300µm thick tissue slices,

Vaira et al. demonstrated that patient-specific gene expression was retained over the culture duration, and two 3-point concentration response curves could be obtained per patient (Vaira et al., 2010). Majumder et al. also used tissue slices obtained from biopsies of patients with head and neck squamous cell carcinoma (HNSCC) and colorectal cancer (CRC) of approximately 300µm thickness (Majumder et al., 2015). These slices were cultured ex vivo and exposed to four different conditions, and compared to the responses of patients with matched treatments. This data was combined with genomic and pathology data, tumour staging, and other patient variables to train a machine learning algorithm for the prediction of treatment outcome called CANScript. Using CANScript, the "correct" treatment could be identified with an accuracy of 87%, and only 7 prediction errors occurred in the 55 predicted cases.

These studies show that ex vivo culture of patient-derived tissue in its intact form in a 3D context can provide valuable translational information and has the potential to be a highly predictive tool for precision medicine. The maintenance of the tissue architecture in its original configuration, with all of its components, provides an advantage over 2D functional assays of patient tissue, resulting in increased physiological relevance. However, the ex vivo culture of relatively large tissue fragments or slices means that only a small number of drugs and drug combinations can be tested, which limits the use of these platforms somewhat. Improving the number of possible tests on patient-derived tissue could allow the identifications of other drugs which are simply assumed not to be active, and extensive testing of drug combinations, the success of which is frequently entirely dependent on each patient's specific tumour.

1.3.6.1.2 Tumour cell suspensions

In order to increase the number of tests that can be performed on tumour tissue, the tissue can be disaggregated into a single-cell suspension and allowed to reform small spheroids for the use in functional testing. A drawback of this approach is the loss of the patient ECM during the preparation of the single cell suspension due to enzymatic digestion. Despite this, when this approach was applied by Halfter et al. to the functional screening of HER2- breast cancer tissue, the ex vivo culture outcomes

predicted clinical responses in patients with a specificity and sensitivity of more than 80% (Halfter et al., 2016). Ten drugs and drug combinations were tested on patient-derived spheroids, but also on genetically modified HER2- breast cancer cell line spheroids, which showed that cell line-derived spheroids consistently showed a higher sensitivity to the applied drug treatments. This highlights again the benefits of the use of patient-derived tissues and how the fairly homogeneous nature of cell lines can affect drug screening results. Additionally, it suggests that patient-derived cultures which do not contain the patient ECM might be predictive enough to aid in precision medicine, despite the lack of a crucial component of the patient tumour microenvironment. A possible explanation for the predictive value of these patient-derived spheroids, despite the loss of the patient ECM, could lie in the production and deposition of ECM by patient-derived cells in culture.

1.3.6.1.3 Patient-derived organoids and xenografts

Two further methods which can be used in precision oncology are patient-derived organoids and xenografts. Pauli and colleagues published a seminal paper comparing the predictive value of both methods, which were used for the guidance of precision treatments. Patient-derived organoids are self-renewing and self-organising 3D structures, which replicate many features of the tissue they were generated from, such as the formation of lumina in pancreatic and colorectal organoids (Pauli et al., 2017). To generate organoids, patient-derived cells are embedded in Matrigel and exposed to serum-free culture conditions, which closely resemble the stem cell niche. Organoid cultures crucially rely on the maintenance of stem cells in culture, which enables their almost limitless self-renewal capabilities and allows cryopreservation with minimal loss in viability (Sachs and Clevers, 2014). Pauli et al. used 145 tumour samples, obtained from 18 different tumour types to generate patient-derived organoids, some of which were successfully implanted into immunodeficient mice where they formed xenografts. These patient-derived xenografts (PDX) and patient-derived organoids matched the histopathology of the parent tumour, and whole-exome sequencing confirmed a high concordance when PDX and patient-derived

organoids were compared to the original tumour (Pauli et al., 2017). In order to identify the most effective drugs for each patient, a high content screen of 160 drugs was conducted on the patient-derived organoids, which resulted in a shortlist of the most effective drugs. Any safety concerns of combinations, and mutations that were found during whole exome sequencing were taken into account for the selection of a small number of individual drugs and drug combinations, which were then tested on patient-derived xenografts of two patients and monitored in mice in vivo. The PDX model demonstrated a greater effect of targeted anticancer agents and drug combinations than the current standard of care for both patients. These results have yet to be clinically validated, but demonstrate a potential future precision medicine workflow in a clinical environment. Other studies have since been able to demonstrate that drug responses in tumour organoids correlate with patient outcomes (Papapetrou, 2016; Ooft et al., 2019). However, one major disadvantage of both PDX and patient-derived organoids, is the time it takes to establish these models, with estimates ranging from 2-4 months. A time frame of several months is likely too long to provide meaningful guidance for cancer therapy, as most treatment regimens for tumours are determined as quickly as possible, usually within weeks (Halfter and Mayer, 2017). Additionally, the grafting efficiency of patient-derived xenografts varies greatly between tumour types and appears to favour more aggressive tumour types, which means this technology could not be applied to every patient at the moment, although future advances in PDX might increase the grafting efficacy (Dobrolecki et al., 2016). Several studies have also shown that the patient-derived matrix in patient-derived xenografts is replaced by the host stromal components such as the ECM and fibroblasts after the first passage (Cassidy et al., 2015). This limits the extent to which ECM-tumour interactions can be studies in PDX models. Additionally, PDX models are maintained in immunodeficient mice for long periods of time, which requires specialised facilities, time and resources, making this the most expensive method of all patient-derived 3D culture methods reported here, which will remain a barrier to its widespread use (Halfter and Mayer, 2017).

Organoids require reagents for their maintenance, such as growth factors and matrices, and their associated costs in comparison to standard 2D screening are higher, but not inaccessible (Halfter and Mayer, 2017). So far organoids have found widespread acceptance, due to their precise recapitulation of the native tumour and their self-renewing capabilities, which removes the constraints of testing limited quantities of naïve patient-derived tissue. Since then organoids have been created from normal and many epithelial mouse and human tissues, such as colon, prostate, stomach, breast and lung tissue (Drost and Clevers, 2018). A great advantage of organoid technology is that they cannot just be created from cancer tissue, which is the case for cell lines, but also from normal tissues, which could be an immensely helpful tool in drug discovery. By assessing drug efficacy in tumour organoids and corresponding organoids derived from healthy tissue, the therapeutic index of new drugs could be determined, in order to avoid toxicity to the surrounding healthy tissues (van de Wetering et al., 2015). Additionally, genetic modification of organoids through the use of CRISPR has allowed the development of specific physiologically relevant disease models through the introduction or removal of specific oncogenes (Laperrousaz et al., 2018; Lancaster and Huch, 2019). As a result, organoids have been widely adopted in cancer research, drug discovery and precision medicine (Fatehullah et al., 2016; Papapetrou, 2016; Dijkstra et al., 2018). However, despite these advantages, organoid cultures do not inherently mimic the entire tumour microenvironment, since they lack the native ECM, as well as the interaction of tumour cells with stromal cells.

1.3.6.1.4 Suitability of traditional functional assays for precision medicine applications

All of the methods presented here, which can be used for ex vivo drug screening of tumour-derived cells or tissues, share a high degree of similarity to in vivo tumours, which increases their predictive value. However, not all of these methods are suitable for precision medicine in the form of guided patient treatments, where the input of the results of functional testing would be required much earlier than they can be

available in the case of PDX and organoids. This would suggest that the ex vivo screening of tumour tissue in form of patient-derived explants or patient-derived tumouroids could fit the narrow turnover window of time-sensitive patient treatments. For both methods, the amount of tumour tissue available is the main limiting factor, which reduced the number of tests which can possibly be performed on each patient's tumour models. All methods described, when used to perform drug screening on tumour fragments or biopsy-derived spheroids, were only demonstrated for the screening of a limited number of drugs and drug combinations, due to the small amount of tissue available through biopsies in particular. Fine needle aspirates can contain as little as 500.000 cells, which limits the number of possible tests significantly (Rajer and Kmet, 2005). Therefore, more efficient methods have to be developed for the drug screening of patient-derived tissues, which enable a greater number of screens while retaining a high degree of predictivity. A solution to this problem could lie in the use of microfluidic technologies, which hold the possibility of increasing throughput, while consuming less reagents and cells, while retaining precise control over the cellular microenvironment.

1.3.6.2 Microfluidic devices for functional 3D tumour assays

Microfluidics is the discipline which describes the characteristic behaviour of liquids which are confined to small channels of less than 1 mm in size. Microfluidics also encompasses the construction of microfluidic devices that contain micron-sized channels and chambers, which are used to precisely direct the flow of liquids and particles contained in it (Beebe et al., 2002). On the micron-scale, fluids behave very differently than we are used to in our every-day life, and liquids behave in a very predictable and controllable manner. This is enabled by several phenomena which occur in micro-channels, such as laminar flow. Laminar flow occurs in microfluidics because the impact of viscous forces outweighs the effect of inertial forces on this scale. Viscous forces relate to the friction generated between any two layers of moving liquids, or a fluid layer and a solid layer, whereas inertia refers to the resistance

of an object to a change in its movement and is dependent on an object's mass (Brody et al., 1996). This characteristic relationship of forces acting on fluids within micron-sized channels is characterised by the Reynold's number (Re), which is calculated using **equation 1**, where ρ is the density of a fluid, μ is the fluid's dynamic viscosity, v represents the fluids velocity and D_h is the hydraulic diameter of the microchannel. In microfluidic channels with a Reynold's number of <1, the flow of a fluid is dominated by viscous forces, in such a way that two streams of liquids which are in contact with each other, will only mix due to diffusion and not through convective mixing, which does not occur in Re <1 (Beebe et al., 2002).

Equation 1 $$\boldsymbol{Re = \frac{\rho v D_h}{\mu}}$$

Microfluidic devices can be designed to control the flow of the contained fluid in order perform specific bioassays by creating networks of micro-channels, chambers and valves, to direct the flow of cells and reagents. The main reasons for the use of microfluidics for cell-based assays is the extremely precise spatial and temporal control over cell culture conditions, which allows the miniaturisation of complicated assays, while consuming less reagents (microlitres) and cells (Sung and Beebe, 2014). Additionally, since convective mixing is almost non-existent in static microfluidic channels, molecule transport mainly occurs as a result of diffusion, which allows the establishment of gradients of cell-secreted factors around each cell and its surrounding cells, which is enhanced in microfluidic devices when compared to traditional culture methods (Mehling and Tay, 2014). The presence of more realistic cell-to-media ratios could also contribute to the enhanced paracrine signalling observed in microfluidic devices. These devices can be manufactured from hard plastics or other polymers, although the most common polymers used in biological research settings is Polydimethylsiloxane (PDMS), which is permeable to gas and fluids, has a high degree of optical clarity, which enables high quality imaging, and is highly biocompatible (Mehling and Tay, 2014). As a result, microfluidic devices have been applied to almost every area of research, including the culture and drug screening of cancer cell lines and patient-derived tumour models.

1.3.6.2.1 Microfluidic devices for drug efficacy testing of 3D tumour models

Several microfluidic devices were designed to enable cell seeding and promoting spheroid formation in micro-chambers or traps. Patra et al. manufactured a microfluidic device capable of generating five thousand spheroids from HepG2 cells, a liver cancer cell line, in low-adhesion square micro-wells (Patra et al., 2016). These spheroids could be imaged for the monitoring of spheroid health and were then exposed to chemotherapy, the effect of which could be assessed using viability dyes and FACS. This demonstrated that large quantities of uniformly sized spheroids could be generated from cell lines with a high degree of efficiency, improving on traditional approaches such as ultra-low adhesion plates, even when compared to the most advanced 1536-well ultra-low adhesion well plates. The operation of this device was

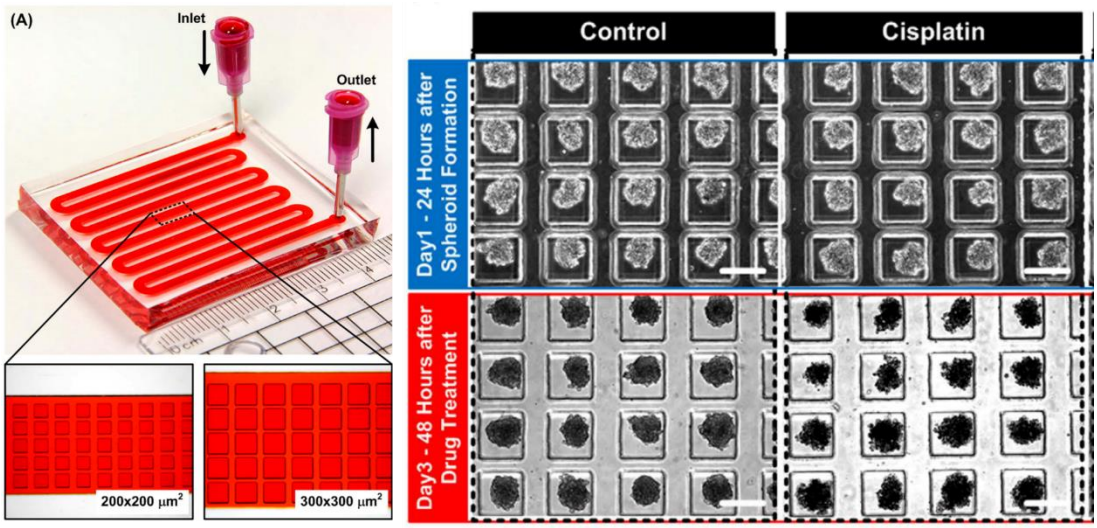

Figure 1.2 Microfluidic device used for drug efficacy testing of cell line-derived spheroids

On-chip generation and culture of 5000 cell line-derived spheroids within micro-wells, which were incubated with fixed drug concentrations. The spheroids could be recovered after drug treatments were complete and further analysis could be conducted using FACS. Reproduced from: Patra et al. (2016) Scientific Reports.

fairly simple, since it relied on the generation of hydrostatic pressure differences between inlet and outlet ports for the generation of flow (**Figure 1.2**).

Additionally, the platform allowed the recovery of spheroids after drug treatments for further analysis, such as FACS. However, the large number of cells required for the operation of this device does not lend itself to precision medicine applications. One further advantage of the device presented by Patra et al. is that it can be operated entirely using micropipettes, without the use of specialised equipment, such as syringe pumps. Syringe pumps and other fluid actuation equipment can be used to precisely control the flow rate or pressure of a fluid entering the microfluidic chip, which can be applied as demonstrated in the following example. Frey et al designed a microfluidic device, which combined a concentration gradient generating tree with a hanging drop array, in which spheroids could be cultured (Frey et al., 2014). Using a concentration gradient generating network of microchannels, four different drug concentrations could be applied to an array four spheroids each, in a reproducible manner on the same microfluidic chip (**Figure 1.3**). This platform presents significant advantages, since no drug dilutions need to be prepared manually, which carries a risk for error, but several assays can be conducted on the same chip. Additionally, the use of the gradient generator means that drug combinations could easily be produced on-chip, which shows potential for drug combination testing in the future. However, the use of syringe pumps adds operational complexity in many labs and in clinical setting. Additionally, in order to scale up this approach for the screening of several drugs using several different patient-derived tumour models in a precision medicine context, presents logistical problems, since each device requires the connection to at least three syringe pumps via microtubing, which carries the increasing risk of errors, for example due to the formation of bubbles within tubes.

It is possible to create drug concentration gradients in microfluidic devices without the use of external fluid actuation equipment, but this requires careful engineering of the microfluidic device. A device designed by Lim and Park in 2018 is a good example of a microfluidic device which incorporated a concentration gradient generator, but could be operated entirely using the hydrostatic pressure generated in open

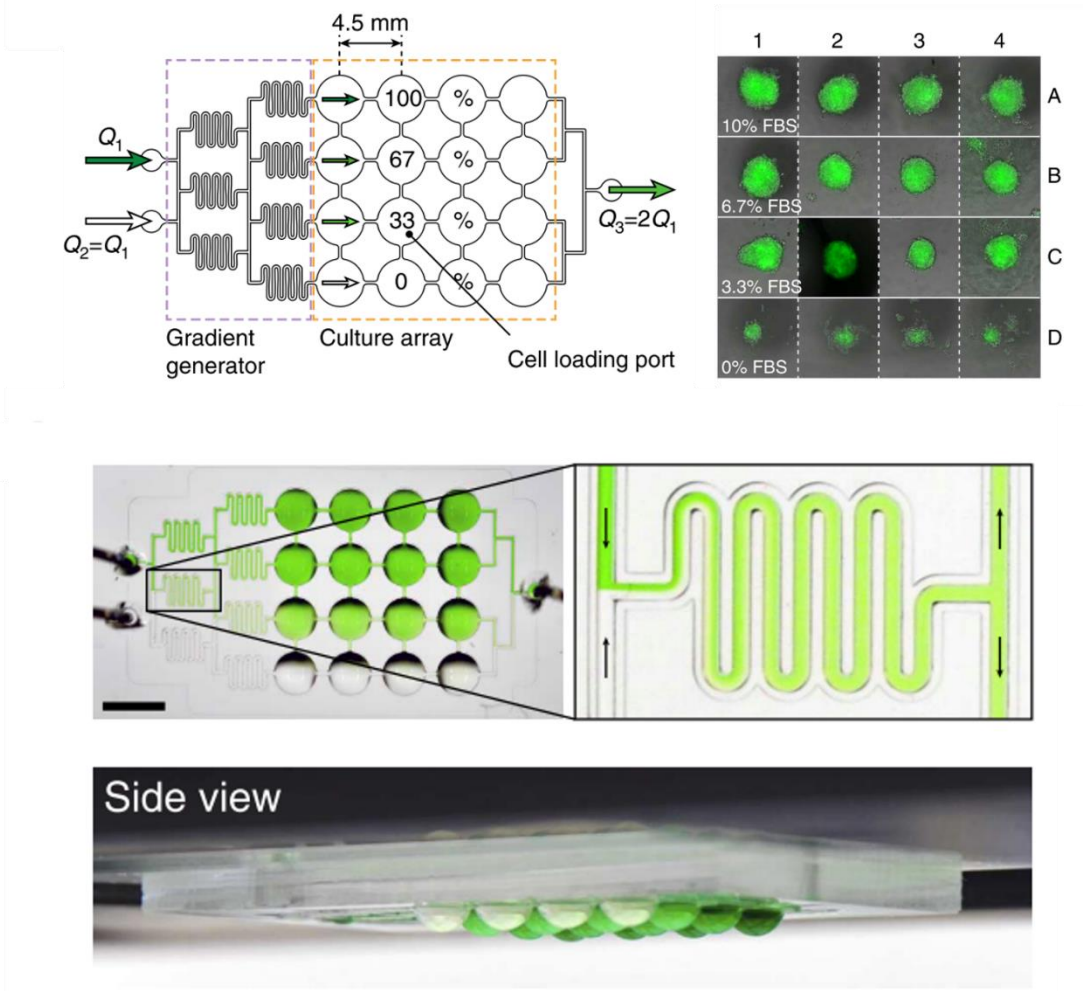

Figure 1.3 Microfluidic device utilising a gradient generator and syringe pumps for drug efficacy testing of cell line-derived spheroids

Frey et al. developed a microfluidic hanging drop platform, which used a gradient generator, that could supply arrays of four spheroids with four different drug concentrations. Reproduced from: Frey et al. (2014) Nature communications

reservoirs (Lim and Park, 2018). In the device, two large reservoirs were connected to a concentration gradient generating tree, which led to 5 channels, each of which contained 10 round spheroid traps that protruded from the central channel (**Figure 1.4**).

As a result, 5 different drug concentrations could be applied to 10 replicate spheroids per concentration in just one device, and a concentration response curve could be established from only one microfluidic device. The device showed great potential for the use with patient-derived single cell suspensions for the formation of spheroids,

since it is accessible using simple pipettes and produced a significant number of replicates to allow for statistically meaningful analysis of cytotoxic drug effects on the spheroids in the device. Unfortunately, cell seeding into the device is conducted by

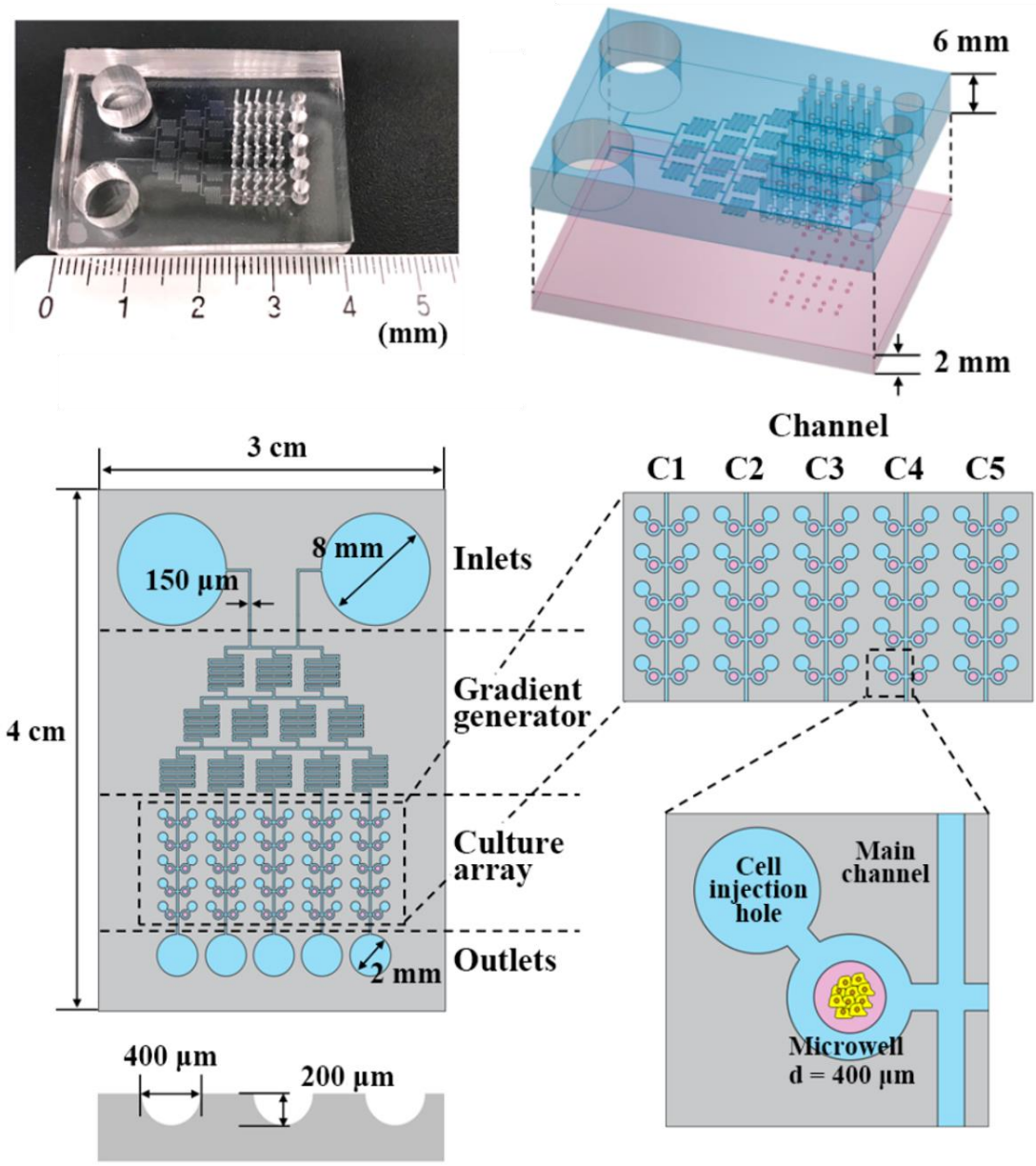

Figure 1.4 Example of a microfluidic device which uses hydrostatic pressure to generate a concentration gradient

Microfluidic device with two large reservoirs, which induce the hydrostatic-pressure driven flow of drug solutions through a gradient generator, which produces 5 different concentrations in the cell culture channels, where 10 spheroids can be cultured. Reproduced from Lim & Park (2018) Molecules

manually pipetting of a cell suspension into 50 cell loading ports on the chip, which could introduce errors and does not lend itself to up-scaling. However, an adapted version of this device provided proof-of-concept for the use of such devices for precision medicine treatment of glioblastoma. Fan et al. seeded patient-derived glioblastoma single-cell suspensions into the microfluidic chip, where they aggregated into spheroids, that could be exposed to seven different drug concentrations or drug combinations while providing 11 replicates per condition (Fan et al., 2016). Three of these devices could be filled using each patient sample, resulting in three tested drugs per patient. Although only a small number of drugs could be tested using this platform, these results suggest that hydrostatic pressure-driven gradient-generating microfluidic devices could be a viable option for application in precision medicine.

1.3.6.2.2 Microfluidic devices for precision medicine application

Although a large number of microfluidic devices have been used for drug screening of cell line-derived spheroids (Valente et al., 2017), only few have applied the benefits that microfluidics can provide to the testing of patient-derived tissues. An impressive example of the increased throughput that microfluidics can provide was presented by Eduati et al. who performed a combinatorial screen of 45 different drug combinations on biopsy-derived cells, in order to identify the most promising drug combination for each patient (Eduati et al., 2018). Tumour biopsies were disassociated into a single-cell suspension, which was encapsulated in water in oil droplets, containing different drugs and drug combinations for a short period of time (16h), after which the toxicity of the applied drugs was determined using fluorescent analysis of caspase 3 activation. The generation of such a large number of droplets with different combinations, was enabled by their microfluidic platform, which allowed the rapid switching between 16 different inlet streams (containing different drugs, that could be combined in droplets) that control the composition of each droplet (**Figure 1.5**). This process was automated using a customised Labview programme and achieved the collection of over 1000 data points in 56 conditions, providing at least 20 replicates for each drug or drug combination applied. However, in order to achieve a

screen of this size only 10 cells could be used per droplet, which meant that many droplets did not in fact contain primary cell aggregates but dispersed single cells. This somewhat deters from the accomplishments of this platform, since a 3D microenvironment appears to be essential for the predictive value of patient-derived tissue screening. Additionally, each chip was connected to 16 different syringe pumps, which suggests that up-scaling this approach for a large number of patients could be problematic. Moreover, droplets are subject to evaporation, which limited the possible drug exposure and culture duration in the device to 16h, which may not be long enough to detect cytostatic or growth-inhibiting drug effects.

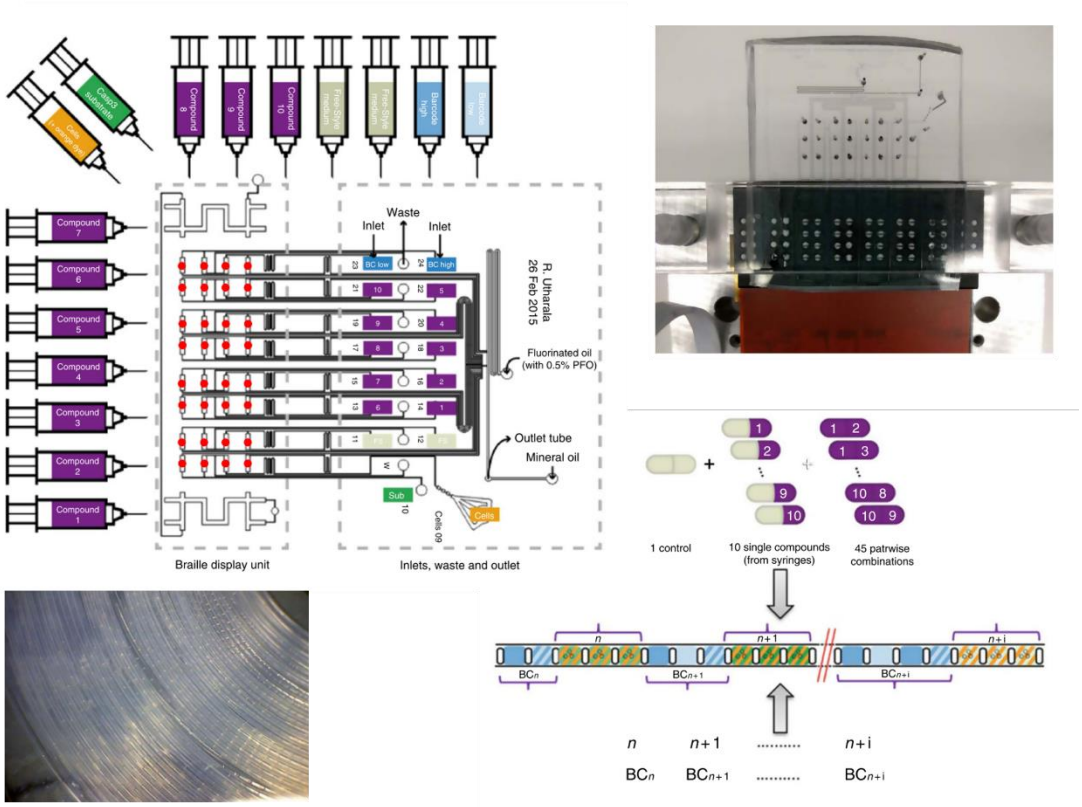

Figure 1.5 High-throughput combination drug screening using a microfluidic droplet generating device

A microfluidic droplet generator, which utilises 16 different syringes in order to create droplets containing 10 patient-derived tumour cells, which can be merged in order to incubate the tumour cells with one drug alone or a drug combination. The droplets containing cancer cells can be stored in the tubing for 16h, after which viability was assessed. The device was used to screen 45 different drug conditions in patient-derived tumour cells for precision medicine applications. Reproduced from: Eduati et al. (2018) Nature communications.

A different approach was used by Ruppen et al., who created a microfluidic device, which used open reservoirs for the seeding of single cell suspensions of patient-derived mesothelioma cells and pericytes (Ruppen et al., 2015). The cells were collected in 8 low-adhesion micro-wells where they aggregated into mono-culture or co-culture spheroids, which were then exposed to 13 different concentrations of cisplatin (**Figure 1.6**). 32 micro-wells could be filled per patient, allowing not only drug toxicity testing, but also the investigation of the impact of pericytes on the tumour cell response. In fact, pericytes appeared to increase the resistance of mesothelioma cells to cisplatin, suggesting a protective effect.

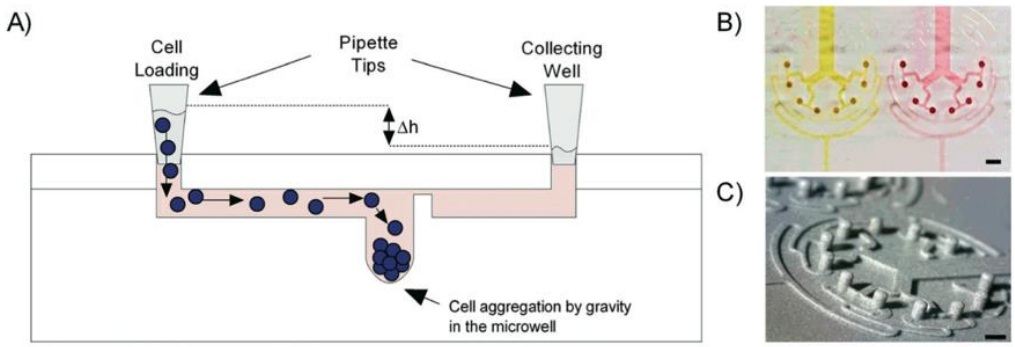

Figure 1.6 A microfluidic device used for the functional testing of patient-derived spheroids

Schematic representation of a microfluidic device developed by Ruppen et al., which was used for drug toxicity testing of mesothelioma-derived spheroids within the device. Reproduced from: Ruppen et al. (2015) Lab on a Chip

Tumour fragments were employed in a different approach to precision medicine by Jenkins et al., who minced melanoma tumour tissues and created small primary tumour clusters by sequentially filtering the tumour fragments through cell strainers of decreasing pore sizes, resulting in the generation of 40-100 micron sized clusters (Aref et al., 2013; Jenkins et al., 2018). The tumour clusters were then resuspended in type 1 collagen and injected into the central gel filling ports, which resulted in the distribution of several tumour fragments within each channel. Two parallel channels were connected to the central channel and used for the perfusion of the tumour tissues in the gel phase with medium or immune checkpoint inhibitors (**Figure 1.7**). The

tumour tissues cultured in the device were found to retain their resident populations of lymphocyte and myeloid cells, which allowed the screening of PD-1 and CTLA-4 checkpoint inhibitors, individually as well as in combination. The effect of PD-1 and CTLA-4 inhibition was determined using immunofluorescence staining in situ and

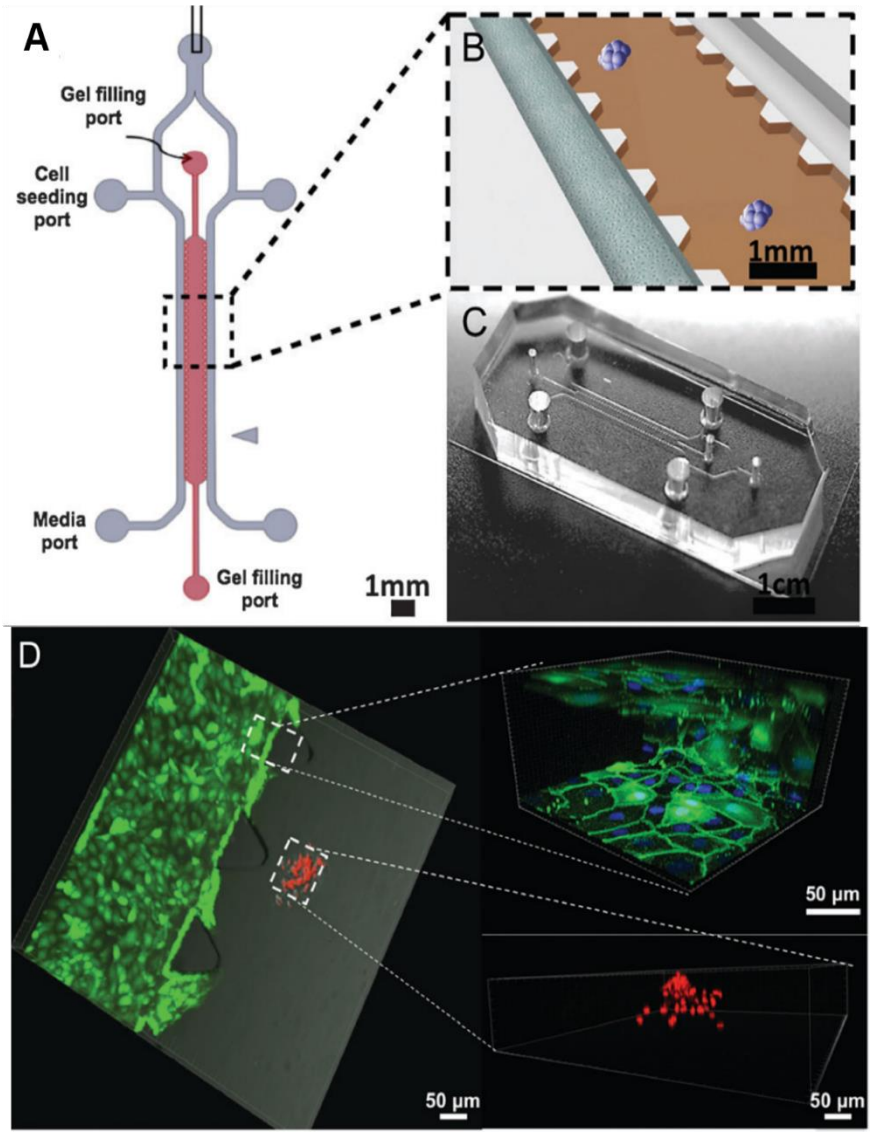

Figure 1.7 Microfluidic device for the functional screening of tumour fragments and slices for precision medicine applications

Patient-derived tumour fragments were suspended in collagen and injected into the microfluidic chip via the gel filling port, which distributes the fragments across the central device channel. Using the two surrounding channels immune checkpoint inhibitors were applied to the tumour clusters to assess the response of the resident immune cells for precision medicine applications. Reproduced from Aref et al. (2013) Integrative biology

FACS sorting, and sensitivity as well as resistance to immune checkpoint blockade could be identified across the patient cohort tested. Although this approach remains to be validated using clinical data, it shows that functional screening of immunotherapy drugs using the patient's own immune cells is possible ex vivo, which could become a valuable tool for precision immunotherapy treatment and the discovery of novel immune targets.

Novel approaches for the screening of patient-derived tissue are continuously being developed and vary in complexity and scalability. Rumaner et al. demonstrated in 2019, how threads, instead of microfluidic channels could be used to transport drug solutions to a tumour tissue slice and enabled the incubation of a tissue slice with3 drugs simultaneously (**Figure 1.8**). The device was operated using hydrostatic pressure driven flow only, which was generated by filling the drug wells with a drug solution. The drug wells are connected to the tumour slice using 6 threads, which span the entire tissue slice and are in gentle physical contact with the tissue. The flow rates generated in threads of different materials, such as nylon, polyester, silk and cotton were quantified, with silk providing the appropriate flow rates for application in this context. These threads guide each of the drug solutions to the tumour tissue, separated by threads containing buffer to prevent the mixing of different drugs assessed. This setup results in the time-dependent perfusion of the tumour tissue with up to three different drugs. Drug effects were assessed using fluorescent viability dyes and provided a quantitative readout of drug efficacy. Although the throughput of this method is fairly low, the use of threads and a plastic frame produced by a standard 3D printer makes this device low-cost and accessible, since it does not require microfabrication. Further, no external fluid actuation equipment is required since reservoirs within the device can be filled using micropipettes, which means that a skilled operator user is not necessarily required, as is the case for other microfluidic platforms.

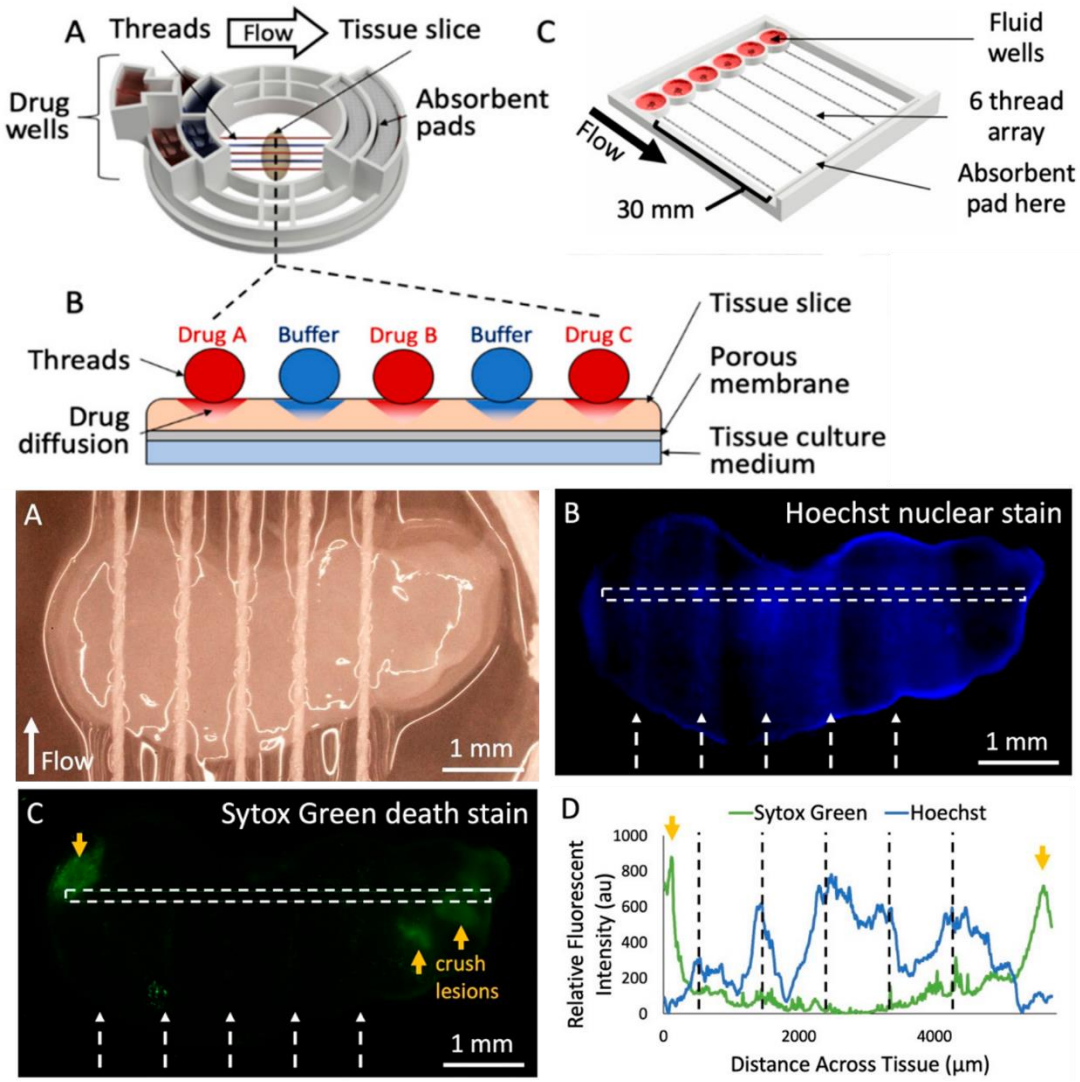

Figure 1.8 Microfluidic devices for functional screening of tumour fragments and slices for precision medicine application

Threads were used to carry drug solutions from reservoirs to distinct areas of tumour slices, where the effect of drugs could be assessed in the native tumour slices. Reproduced from: Rumaner (2019) Micromachines

1.4 Thesis context

The analysis of the literature presented here led to the following conclusions:

- Patient-derived 3D tumour models are suitable for precision medicine applications and offer increased predictive value in comparison to monolayer functional assays.
- The small number of cells contained in tumour biopsies acts as a barrier to the widespread adoption of patient-derived functional assays for precision medicine. It also prohibits the screening of a large number of drugs and drug combinations.
- Microfluidic technologies only require a fraction of the cells required for traditional assays, and can increase the throughput of functional chemosensitivity assays, which has been applied to the screening of patient-derived 3D tumour models. However, these frequently require external actuation equipment, which can introduce errors and prevents the up scaling required for application in precision medicine in a clinical environment.

As such, there is a significant need for a tool that can utilise small quantities of biopsy-derived cells in order to test a large number of drugs on physiologically relevant patient-derived tumour models, for the purpose of providing guidance for the precision medicine treatment of cancer. This thesis aims to demonstrate the development of a microfluidic platform and protocols, including:

- A microfluidic device operated without the use of external actuation equipment, which allows the generation and culture of thousands of spheroids from a single-cell suspension, providing a platform for time-lapse, fluorescence and brightfield-based analysis of live spheroids.
- The formation of a self-generating, long-lasting, repeatable compound concentration gradient across an array of tumour spheroids for drug efficacy testing, which allows the generation of one concentration-response curve per device.

- Proof-of concept application of the platform to the maximised drug screening of thousands of prostate cancer biopsy-derived spheroids, demonstrating its suitability for precision medicine.

2 Materials and Methods

2.1 Design and fabrication of microfluidic devices

2.1.1 Introduction

The microfluidic devices used in this project contained two layers of the elastic polymer polydimethylsiloxane (PDMS, Sylgard 184, Silmid). Both PDMS layers were moulded from patterned silicon master wafers. These were fabricated using standard photolithography techniques, in which the pattern created on each master wafer was determined by the photomasks used. The photomasks were designed in CorelDraw X5 and produced by JD Photodata (UK) on acetate film.

2.1.2 Fabrication of patterned silicon masters using photolithography techniques

In order to pattern silicon wafers in this project, classic techniques of photo- and soft-lithography were used, according to protocols established by David C. Duffy, J. Cooper McDonald, Olivier J.A. Schueller and George M. Whitesides (Duffy et al., 1998; McDonald and Whitesides, 2002).

In preparation for patterning, 4-inch silicon wafers (University Wafers) were cleaned from debris by sequential sonication, for three minutes respectively, in acetone, methanol and isopropanol (IPA). Subsequently, the wafers were dried using nitrogen gas and then dehydrated on a hot plate at 180 °C for at least 45 minutes. The wafer was left to cool down to room temperature. It was then placed on a spinner and approximately 5 ml of negative SU8 photoresist (several varieties, **Table 2.1**) were poured onto the wafer and spun for the time and RPM specified in **Table 2.1**. Spin-coated wafers (**Figure 2.1A**) were then soft-baked briefly at 65 °C and subsequently at 95 °C (specified in **Table 2.1**). Before the next step, a photomask was placed on top of the soft-baked resist and held in place by a glass filter, after which the wafer was exposed to collimated UV light (**Figure 2.1B**). This results in cross-linking of any resist that was exposed to UV light, in the pattern determined by the photomask (see **Figure 2.1C**). Next, wafers underwent a post-exposure baking step and were briefly

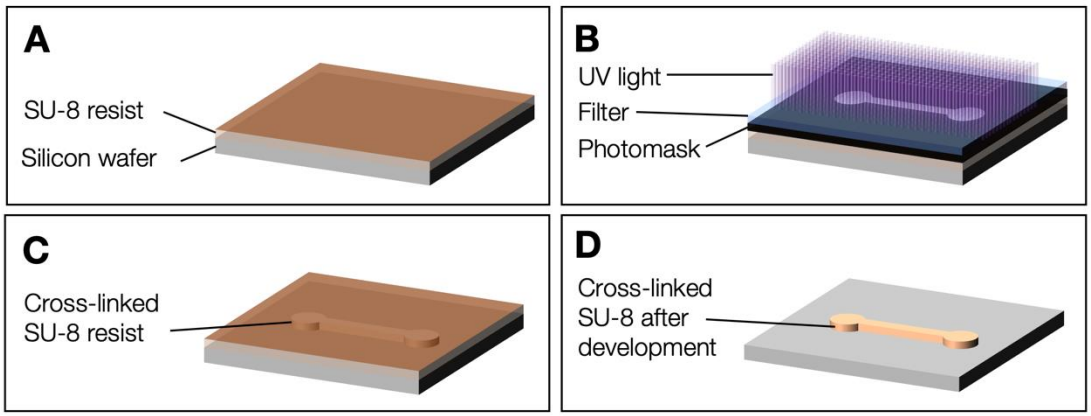

Figure 2.1 Schematic photolithography process

A) SU-8 resist is spin-coated onto a wafer, which is then soft-baked. Once cooled down, the soft-baked wafer was placed on a glass block. B) A photomask was placed on top of the soft-baked resist, followed by a glass filter. The wafer was then exposed to collimated UV light, which resulted in a C) crosslinking reaction in any areas that were exposed to UV light through the photomask. All wafers underwent a post-exposure bake. Following this, any undeveloped resist was removed during the development step with EC solvent, leaving only D) the cross-linked SU-8 behind on the wafer.

placed on a hot plate at 65 °C and subsequently at 95 °C for the times specified in **Table 2.1**.

Once cooled down again, undeveloped resist was removed from the wafer by immersion in MicroPosit EC solvent (time specified in **Table 2.1**, Rohm and Haas, US), and as shown in **Figure 2.1D**, only the cross-linked patterns remained on the wafer. When development was complete, the wafer was rinsed with IPA and dried using Nitrogen gas. All wafers were hard-baked, which involved three baking steps on a hot plate, first at 95 for 5 minutes, then at 150 °C for 5 minutes and finally at 210 °C for 15 minutes. The hard-baked wafer was allowed to cool down. At this point, profilometer (Alpha-Step IQ, KLA Tencor) was used to ensure that the correct height of all patterned features had been achieved. If so, in order to prevent adhesion of PDMS to the patterned features, the wafer was prepared for coating by exposure to oxygen plasma in a Plasma Asher (Pico Plasma Cleaner, Diener Electronic) at 100% for 2 minutes. As a final step, the wafer was coated in Trichloro(1H,1H,2H,2H-

perfluorooctyl)silane (Sigma Aldrich, UK), which was applied by vapour deposition for 45 minutes at room temperature.

Table 2.1 Details of photolithography parameters

Two types of SU8 photo resist were used for the fabrication of master wafers in this project, SU-8-3035 and SU-8-3010 (A-Gas, UK). For required resist thicknesses between 10 and 100 µm, SU-8-3035 was used according to manufacturer's instructions. To achieve resist thicknesses of more than 100 µm, the wafer had to be spin-coated with SU-8-3035 twice, aiming for each layer to reach approximately 100 µm thickness in order to achieve approximately 200 µm in total thickness. For resist layers of less than 10

SU8 resist type	**SU8-3035**	**SU8-3035**	**SU8-3010**
Resist thickness	90 µm × 2	35 µm	8 µm
Spin rate	900	3000	3500
Soft bake time	7 min (65 °C) 27 min (95 °C)	3 min 13 min	2 min 9 min
Exposure time	70 s	35 s	25 s
Post-exposure bake time	1 min (65 °C) 7 min (95 °C)	1 min (65 °C) 5 min (95 °C)	30 s (65 °C) 3 min (95 °C)
Development time	25 min	4 min	3 min
Hard bake times	5 min (95 °C) 5min (150 °C) 15 min (210 °C)	5 min (95 °C) 5min (150 °C) 15 min (210 °C)	5 min (95 °C) 5min (150 °C) 15 min (210 °C)

2.1.3 Production of PDMS casts and assembly of microfluidic devices

To produce PDMS devices from the patterned master wafers, PDMS prepolymer was thoroughly mixed with curing agent in a 10:1 ratio. The mixture was then poured onto

the wafers and degassed inside a desiccator for at least 45 minutes, to remove bubbles from the liquid PDMS mixture (**Figure 2.2A, D**). In some instances, a uniformly flat PDMS layer had to be fabricated to form the base of the device. This was achieved by coating plastic spacers of 1mm height and glass slides with 0.1% hydroxymethylcellulose (HPMC, Sigma Aldrich), which was previously solubilised in phosphate buffered saline (Gitlin et al., 2009; Tropmann et al., 2012). The spacers were then placed on each side of the device pattern on the wafer, so as to support a microscope slide being placed on top. A small amount of degassed PDMS was then poured onto the wafer and was "sandwiched" between the wafer and the HPMC-coated slide, which was secured in place by metal clamps (**Figure 2.2D**).

Once PDMS was cast onto wafers (**Figure 2.2A, D**), it was cured for at least 2 hours at 85°C. After the curing process was complete and the wafers were allowed to cool down, the PDMS casts were peeled off the moulds and cut to size (**Figure 2.2B**). All open wells and overflows were created in the device using surgical punches (Milltex) (**Figure 2.2C**). To assemble the double-layer device, both the device base layer and the top layer containing the fluidic channels were exposed to oxygen plasma for 12 seconds at 70 % power (**Figure 2.2C**; Pico plasma cleaner, Diener electronic) and then permanently bonded. After being placed in contact with each other, covalent bonds are formed at the contact surface, resulting in a strong permanent bond (**Figure 2.2D**). To further enhance the bonding strength, the bonded devices were baked at 85 °C for at least 30 minutes and then stored.

Prior to cell seeding, the devices were re-exposed to oxygen plasma for 2 minutes at 100% power. Immediately after exposure, a solution of 1% Synperonic F108 (Sigma-Aldrich) in deionised water was pipetted into the wells of each device. The devices were incubated at 37 °C and 5% CO2 for 24 hours, when the remaining Synperonic F108 solution was removed by first washing the device with PBS, followed by a second wash with incomplete medium.

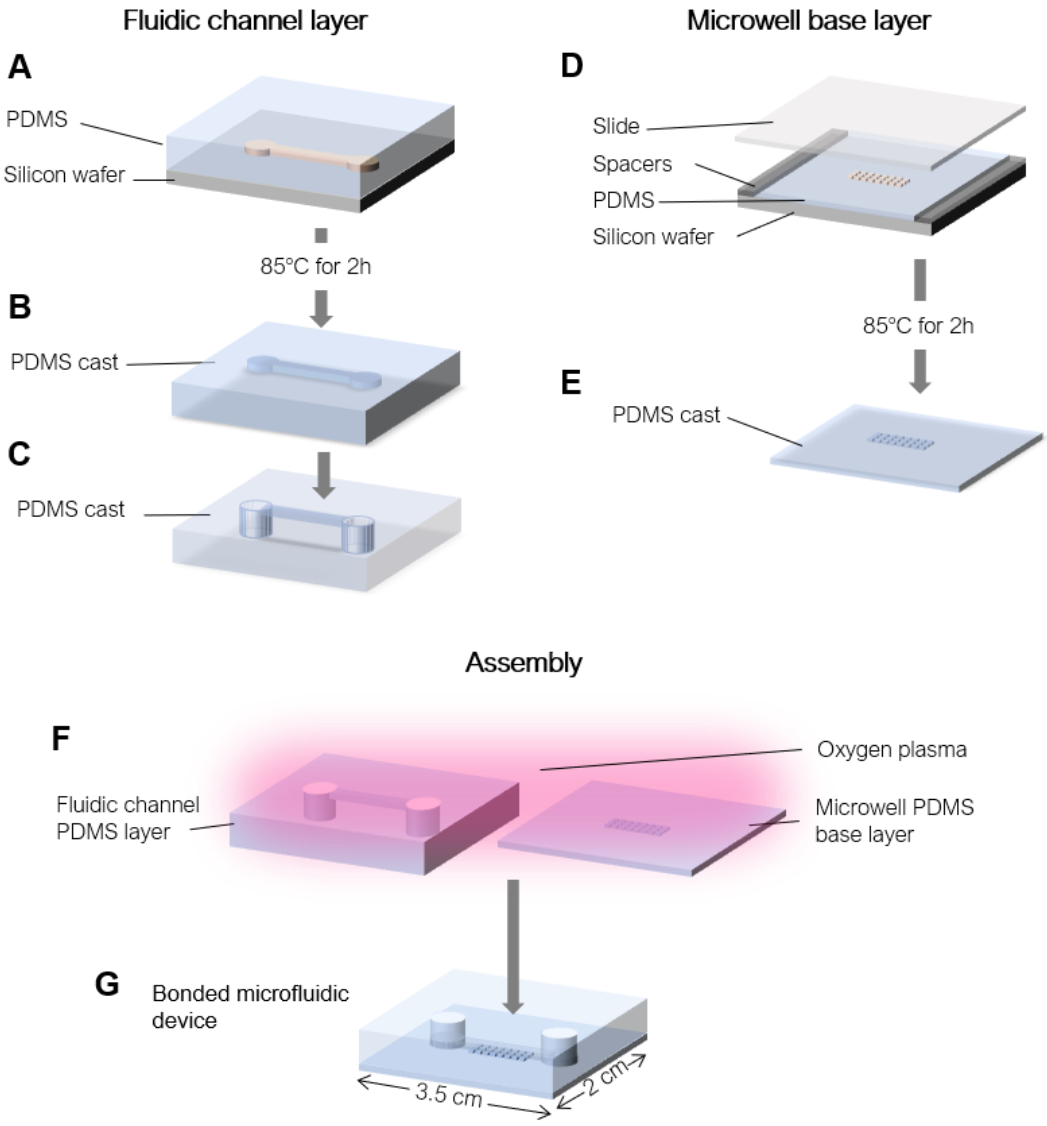

Figure 2.2 Soft lithography process and assembly of microfluidic devices

A) PDMS was poured onto the microchannel-patterned wafer and then cured for 2h at 85 °C. Once cooled down, the PDMS cast was peeled off the wafer (B), and a surgical punch (4mm) was used to create reservoirs in the PDMS cast (C). To create the microwell base layer of the device, two 1mm spacers were placed at the sides of the microwell-patterned wafer and PDMS was poured onto the pattern (D). A microscope slide coated with HPMC was then lowered onto the spacers and held in place using metal clamps for the duration of the curing process (2h at 85 °C). Once curing was completed, the glass slide and spacers were removed from the wafer, and the flat PDMS cast of the microwell layer could be peeled off the wafer (E). To assemble the device, the microwell PDMS base layer and fluidic channel layer were exposed to oxygen plasma at 100% power for 2 min (F), after which the two layers were aligned to each other manually and irreversibly bonded (G).

2.2 Cell culture

2.2.1 Culture of cell lines

UVW cells, derived from a high-grade glioma patient (Boyd, A. Livingstone, L. E. Wilson, 2000), were kindly provided by Dr Marie Boyd (University of Strathclyde). These cells were cultured in T-75 flasks and maintained in MEM (Minimum essential medium, Gibco), supplemented with 10% FBS (Fetal Bovine Serum, Gibco), 2.5 μg ml^{-1} Amphotericin B (Gibco), 100 U ml^{-1} Penicillin-Streptomycin (Gibco) and 2 mmol l^{-1} L-Glutamine (Gibco).

U87MG cells were originally derived from a malignant glioma of a male patient and were purchased from the European Collection of Authenticated Cell Cultures (ECACC). They were maintained in EMEM (Eagle's Minimum Essential Medium, Gibco), which was supplemented with 10% Fetal Bovine Serum (Gibco), 2.5 μg ml^{-1} Amphotericin B (Gibco), 100 U ml^{-1} Penicillin-Streptomycin (Gibco), 1 mmol l^{-1} Sodium pyruvate (ThermoFisher), 1% Non-Essential Amino Acids (NEAA, Gibco) and 2 mmol l^{-1} L-Glutamine (Gibco).

The androgen-sensitive prostate cancer cell line LNCaP, which was originally isolated from a lymph node metastasis, was kindly provided by Prof. Hing Leung (University of Glasgow). LNCaP cells were maintained in RPMI-1640 (Roswell Park Memorial Institute 1640, Gibco) supplemented with 10% Fetal Bovine Serum (Gibco), 2.5 μg ml^{-1} Fungizone (Gibco), 100 U ml^{-1} Penicillin-Streptomycin (Gibco), 1 mmol l-1 Sodium pyruvate (ThermoFisher) and 2 mmol l^{-1} L-Glutamine (Gibco).

All cultures were maintained in a humidified incubator at 37°C in 5% CO_2, at 90% humidity.

2.2.2 Culture of Primary Prostate Cells

All methods and procedure concerning the use of human prostate biopsy tissue samples were carried out in compliance with the relevant guidelines and regulations. In accordance with these guidelines, all regulatory approvals required for the use of

anonymised human tissue and experimental procedures to conduct this work, were obtained by Dr Joanne Edwards (University of Glasgow) from the West of Scotland Research Ethics Service (ref. 16/WS/0015) in collaboration with the surgeon Mark Underwood (Queen Elizabeth Hospital, Glasgow). Informed consent was acquired from all patients prior to any procedures. All biopsy tissue processing was conducted by initially by Samantha Patek and later by Milly McAllister at the University of Glasgow.

Biopsy samples of human prostate cancer were obtained from patients who were undergoing transrectal ultrasound guided (TRUS) biopsies for suspected prostate cancer. Immediately after the procedure, all samples were stored overnight in serum-free RPMI medium (Gibco) at 4°C. The tissue was then minced, re-suspended in serum-free RPMI medium and incubated overnight at standard at 37°C in 5% CO_2. A cell strainer was used to separate loose single cells from the biopsy tissue pieces, which were washed three times in 10 ml PBS (Gibco) and then re-suspended in 5ml of primary prostate cell media. The primary prostate cell medium used in this project (**Table 2.2**) was adapted from Gao et al. (2014), who successfully derived organoid cultures from patient-derived metastatic prostate cancer biopsy pieces. Following re-suspension, the tissue pieces were cultured in T-25 flasks (Corning) coated with basement membrane extract (Matrigel, Corning) at 37°C in 5% CO_2.The flasks were left undisturbed for 7 days, in order to allow the biopsy pieces to attach to the flask. Following this initial incubation, medium was exchanged every 2-3 days. To prevent overconfluence, the cells were passaged at approximately 70% confluence. Firstly, the cells were washed with warmed (37°C) PBS twice, to remove any debris and traces of media. They were then incubated in 3 ml Trypsin-EDTA (0.05%, Gibco) at 37°C in 5% CO_2 for 5 minutes. Since the primary prostate cell medium does not contain serum to inactivate the trypsin, the cells were washed with PBS and centrifuged for 5 minutes to remove the supernatant 3 times, before being resuspended in 10 ml of primary prostate cell medium and cultured in T-75 flasks (Corning). Once again, the cells were cultured up to approximately 70% confluence and all cells were passaged into four T-75 flasks, of which one was used to generate spheroids in

microfluidic devices for this project. The remaining flasks were used for RT-qPCR characterisation by Milly McAllister at the University of Glasgow. Prior to all experiments, cells were detached from T-75 flasks using 0.05% Trypsin, as described above. Trypan Blue (ThermoFisher) was used to stain dead cells for exclusion from cell count. All cell suspensions were prepared in complete primary prostate cell medium.

Table 2.2 Primary prostate medium supplements

Manufacturer and final concentration of each supplement added to advanced DMEM/F12 (Gibco) for human primary prostate cell culture medium, adapted from Gao et al. 2014

Supplement	**Manufacturer**	**Concentration**
EGF	Sigma Aldrich	1 µmol l^{-1}
N-acetyl-cysteine-L	Sigma Aldrich	1.25 mmol l^{-1}
Human R-spondin-1	PeproTech	10 ng ml^{-1}
Human Noggin	PeproTech	10 ng ml^{-1}
DHT	Sigma Aldrich	1 nmol l^{-1}
FGF10	BioVision	1 ng ml^{-1}
FGF2	BioVision	0.1 ng ml^{-1}
SB202190	Sigma Aldrich	10 µmol l^{-1}
Y27632	USBiological Life Sciences	10 µmol l^{-1}
Cholera Toxin	Sigma Aldrich	1 µg ml^{-1}
Amphotericin B	Invitrogen, UK	2.5 µg ml^{-1}
Penicillin/Streptomycin	Invitrogen, UK	50 U ml^{-1}, 50 µg ml^{-1}
L-glutamine	Invitrogen, UK	2 mmol l^{-1}
B-27	Invitrogen, UK	20 ml l^{-1}

2.3 Spheroid culture and operation of the microfluidic device

2.3.1 Spheroid culture in the microfluidic devices

Before devices were used for cell culture, washing steps were carried out using first PBS, followed by a second wash using media. Cells were then seeded into the device as single cell suspensions. In the case of UVW, U87 and LNCaP cells, 16 µL of cell suspension at a concentration of 7×10^6 cells mL^{-1} were seeded. For the primary prostate cells, cell suspensions of 2×10^6 cells mL^{-1} were prepared, and a total of 16 µL were used for each cell culture channel. In order to seed the single cells into the device, 4 µL of cell suspension were pipetted into alternating inlets four times in a row, leaving at least 5 minutes between each step. Once cells were seeded, 30 µL of complete medium was pipetted into both inlet wells. Within 24 to 48 hours, cells typically aggregated and formed spheroids in the non-adherent environment of the microwells. On day 2 of culture, medium was exchanged by simultaneously removing all media in the outlet wells using micropipettes. Excess cells contained at the bottom of the outlet wells were also removed in this step. To exchange medium, 5 µL of media were then pipetted into one inlet well and allowed to equilibrate for 5 minutes, after which both inlet wells were topped up simultaneously with 40 µL of complete medium. After this initial medium exchange, medium was refreshed every 24 to 48 hours, depending on experimental conditions.

2.4 Viability staining in the microfluidic device

Three dyes were used to assess spheroid viability: Propidium iodide (PI, Sigma-Aldrich), Fluorescein diacetate (FDA, Sigma-Aldrich) and Hoechst 33324 (Thermo Fisher). Initially, propidium iodide was solubilised in PBS, to produce a stock solution of 2 mg mL^{-1}, which was stored at 4 °C. Propidium iodide binds DNA as well as RNA by intercalating, but is unable to enter live cells with intact cell membranes, and as a result only stains dead cells red (**Figure 2.3**). FDA was dissolved in acetone, resulting in a stock solution of 5 mg mL^{-1}, which was stored at -20 °C. The use of fluorescein diacetate for cell viability assessment is based on the presence of cytoplasmic

esterases as well as the cell membrane integrity of live cells. Whilst FDA can partition freely into live as well as dead cells, only live cells with functional esterases have the capability to hydrolyse fluorescein diacetate to release the green fluophore fluorescein (**Figure 2.3**). Once released, the accumulation of fluorescein inside of a cell is only possible if the cell membrane is intact. In dead cells, FDA cannot be hydrolysed, and fluorescein cannot accumulate due to a loss of membrane integrity. Hoechst 33324 can cross into live and dead cells, where it binds DNA and fluoresces blue (**Figure 2.3**) and was used as a counter-stain to highlight nuclei present in spheroids.

A staining solution containing all three dyes was made up fresh in serum-free media, containing 20 µg mL^{-1} PI, 8 µg mL^{-1} FDA and 5 µmol L^{-1} Hoechst 33324, and spheroids were incubated in the solution for 30 minutes. Any excess staining solution was washed off by incubating with PBS for 5 minutes, after which spheroids were imaged immediately. After imaging was completed, the experiments were terminated. An example of spheroids stained with PI, FDA and Hoechst 33324 is shown in **Figure 2.3**.

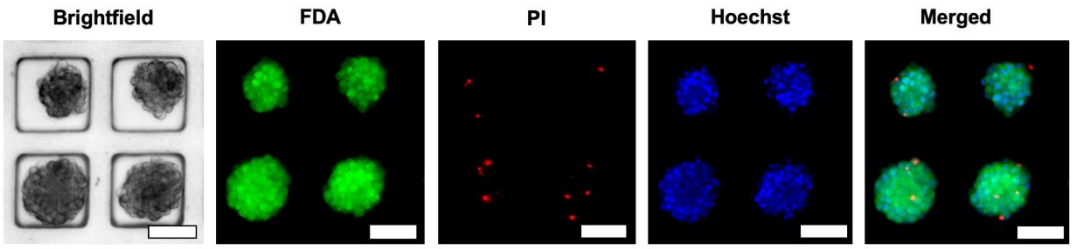

Figure 2.3 Example of spheroids stained using fluorescent dyes for viability assessment.

Fluorescein diacetate (FDA) was used to stain live cells green, propidium iodide (PI) stained dead cells red and all nuclei were stained blue using Hoechst33324. Scale bar = 100 µm

2.4.1 Microscopy and image analysis

Spheroids were monitored every 24 to 48 hours using an inverted microscope (Observer A7, Zeiss), with an Orca Flash 4.0 camera (Hamamatsu) and brightfield images were captured. For long-term imaging of live cells during spheroid formation, the microfluidic device was placed in a microscope-stage incubator (Tokai Hit INUB-WELS-F1, Japan). This allowed the cells to remain in a high humidity environment at 37 °C and 5% CO_2, for the duration of the experiment. To monitor spheroid formation,

brightfield images were acquired every 5 minutes. For the purposes of viability assessment, fluorescent images were also acquired. All images were processed and analysed using Fiji (Schindelin et al., 2012), Zen Blue and Matlab R2017b. A Matlab routine developed by Dr Michele Zagnoni was used to extract spheroid features from brightfield and fluorescent images.

2.4.2 Readouts used to quantify spheroid health

While the images obtained after viability staining provided qualitative information of drug efficacy, the brightfield and epifluorescent images of each spheroid were processed using Matlab to estimate each spheroid's health quantitatively, using the remaining viable fraction, V_F, as well as a shape factor parameter, S_F, described by the following equation:

Equation 2: $$S_F = \frac{P^2}{4A\pi}$$

In **Equation 2**, P is the length of the spheroid perimeter ($P = 2\pi r$) and A ($A = \pi r^2$) is the area of the spheroid cross-section visible in brightfield images. Healthy spheroids maintained a smooth perimeter and a spherical outline ($S_F \sim 1$), whilst unhealthy spheroids showed signs of disaggregation, resulting in a rougher and longer outline and consequently in a higher S_F ($S_F > 1$). This level of disaggregation was quantified utilising **Equation 2**. Similar equations to have been used in the past to quantify the shape of spheroids using various shape factors which determine the circularity of tumour spheroids (Kelm et al., 2003; Friedrich et al., 2009; Grundy et al., 2016).

Additionally, as a measure of drug efficacy, the viable fraction, V_F, was calculated by processing fluorescent images of viability staining in comparison with brightfield images before drug treatment of the spheroids had commenced. To calculate V_F, Equation 3 was used, where $Area_{+FDA}$ is the area of the spheroid extracted from the fluorescent image of viability staining that stained positively for FDA. $Area_{BF\_PD}$ is the area of the spheroid, before any drug was applied, which was extracted from brightfield images.

Equation 3 $$V_F = \frac{Area_{+FDA}}{Area_{BF_{PD}}}$$

The V_F of each spheroid represents its remaining viable area at the time of viability staining, with respect to its area before drug exposure. Values of $V_F \geq 1$ indicate a spheroid that has either grown over time or has remained unaffected by the drug treatment in comparison to its state before exposure, whilst a $V_F < 1$ indicates a detrimental effect of the drug or a deterioration of spheroid health over time. Schematic representations of both the remaining V_F as well as the shape factor S_F can be found in **Figure 2.4**.

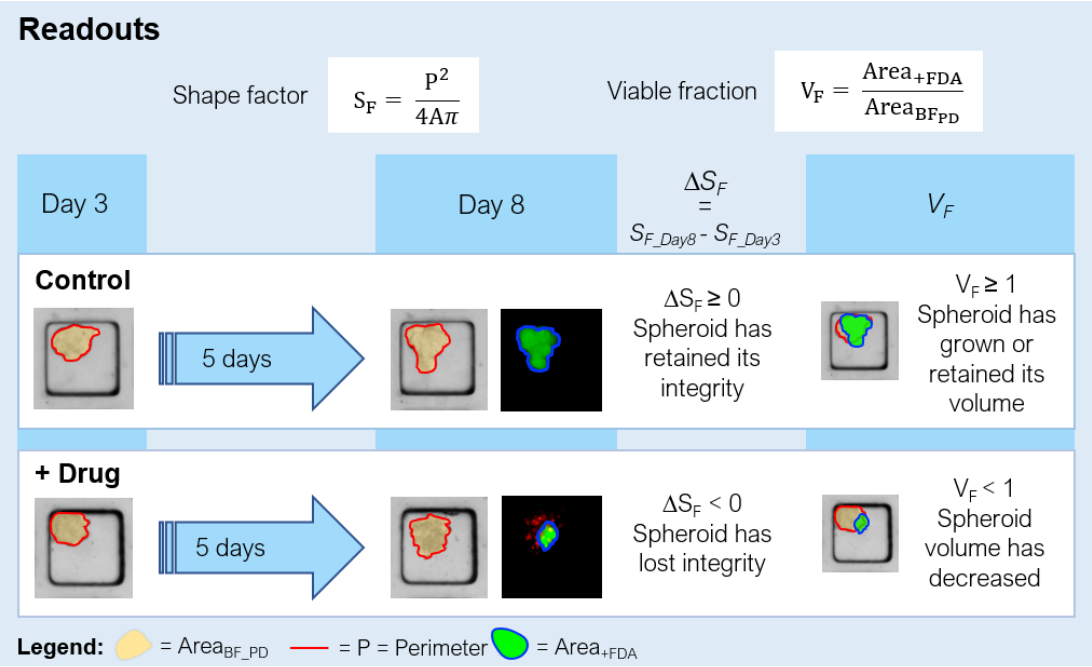

Figure 2.4 Summary of available readouts

Representative brightfield and epifluorescent images of spheroids (UVW cell line) which had been exposed to a drug (cisplatin) in comparison to control conditions. These images were used to obtain the readouts of the viable fraction, V_F, and of the shape factor, S_F. Their determining parameters such as spheroid perimeter, FDA-positive area and the spheroid area prior to drug exposure, $Area_{BF\_PD}$, are highlighted above.

2.4.3 Statistical analysis

Graphpad Prism 7 was used for all statistical analysis and to plot data. All data is presented as mean ± standard error of the mean, using bar graphs or scatter plots with

sigmoidal fitting. Results were compared using two-way ANOVA tests, with differences considered significant when $P < 0.05$. The Pearson correlation coefficient was calculated using Graphpad Prism 7.

2.4.4 Calcein gradient generation

Since the majority of drugs do not fluoresce or are visible, the green fluorescent compound calcein was used to demonstrate and characterise the formation of a microfluidic concentration gradient in the device. First, calcein (Sigma-Aldrich) was dissolved in deionised water to produce a 100 µM L^{-1} solution. The device was then placed in a microscope stage incubator (Tokai Hit INUB-WELS-F1), which was set to create the same conditions used for live cell imaging, i.e. 37 °C, 5% CO_2 and high humidity. These conditions were chosen to allow comparison between the calcein concentration gradient and concentration gradients of non-fluorescent compounds in a drug screening context, which would be maintained in an incubator. Instead of a drug, a 100 µM L^{-1} solution of calcein was used to generate a compound concentration gradient in the device, according to previously established protocols. Epifluorescence microscopy (Observer A7, Zeiss) and a CMOS camera (Orca Flash 4.0, Hamamatsu) were used to acquire images of the area of interest every 5 minutes for over 16 hours, using 25% of the available LED power and an exposure time of 20 ms. The time-lapse images were analysed using FIJI and the average fluorescence intensity in each row of microwells was determined in regions of interest, as outlined in **Figure 2.5**.

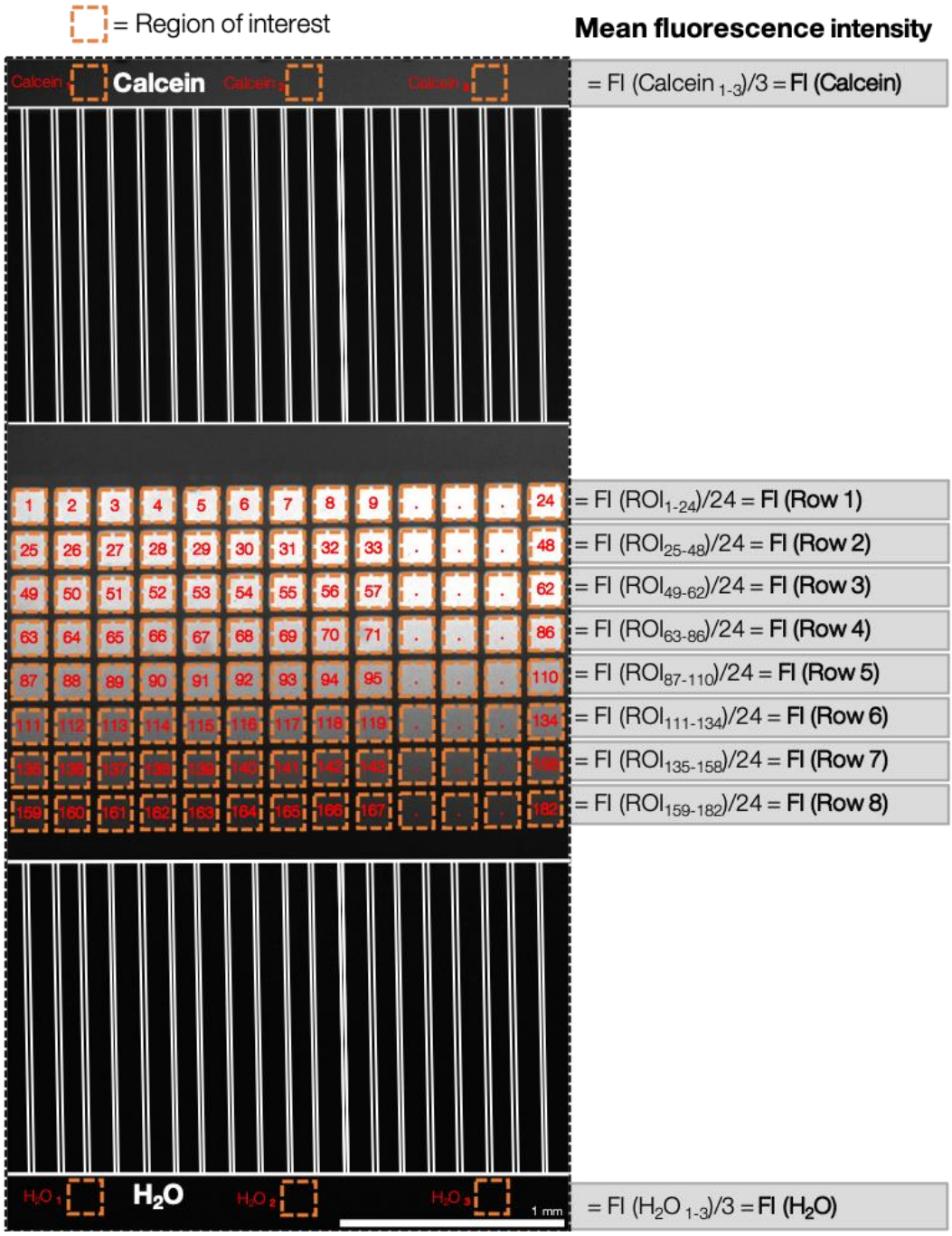

Figure 2.5 ROI map used for quantification of fluorescent gradient generation

Map of regions of interest (ROIs) created for quantification of fluorescence intensity of a 100 µM calcein solution, recorded over a 16-hour timeframe. 3 regions of interest were recorded in each side channel for the mean fluorescence intensity of 100 µM calcein as well as for H_2O. 3 rows of micro-wells at each side of the array were excluded, resulting in a total of 24 ROIs recorded for each row of microwells, which were used to determine the mean fluorescence intensity of each row.

2.4.5 Microfluidic drug screening

To produce a 1.6 mmol L−1 stock solution of cisplatin (Sigma-Aldrich), cisplatin was dissolved in 0.9% NaCl solution (Sigma-Aldrich), which was stored at 4 °C for up to 30 days. A 10 mmol L−1 stock solution of docetaxel (Selleckchem) and a 10 mmol L−1 solution of enzalutamide in DMSO (Selleckchem) was stored at −20 °C. All working drug solutions were prepared in complete medium and used immediately. Spheroids were formed and initially cultured in the microfluidics for a minimum of 3 days. Subsequently, all medium was removed from the devices using a micropipette and replaced by either a drug solution in single-channel micro-well array devices (for comparison against results from drug gradient generating devices) or by both fresh medium and a drug solution in the gradient-generating devices. Drugs were left to incubate in the devices for 12 to 48 hours at 37 °C and 5% CO2. Drug solutions were then washed out using complete medium and spheroid responses were monitored for at least 3 days after drug exposure using brightfield imaging. Finally, viability staining was conducted. Control experiments were performed for each cell line and biopsy culture and for different set of experiments. Concentration ranges for all drugs used in experiments were obtained from the literature, when available for 3D models, or modified from 2D-derived data.

2.5 Numerical simulation of concentration gradient formation

In order to estimate the changes in hydrostatic pressure values over time within each open well during the formation and maintenance of the compound concentration gradient, numerical and analytical models of the fluid behaviour in the device were developed. First, an equivalent electrical circuit of the microfluidic device structure was created using Orcad PSpice by Dr Zagnoni. In this analogue circuit, a distributed resistive network represented the microfluidic channel network, and capacitors represented the open well reservoirs. The initial parameters were set to represent the starting volume of fluids in each well at the beginning of the experiment, which was equivalent to the amount of electrical charge in each capacitor. Values of the

corresponding electrical resistance and capacitance were calculated as previously described (Oh et al., 2012; Robertson et al., 2014). Following this, an analytical expression of the hydrostatic pressure was derived using a simplified equivalent electric circuit, which was used as an input for a finite element model (FEM) simulation. To estimate the temporal evolution of microfluidic concentration gradients, a 3D FEM model of the microfluidic device was built by Dr Zagnoni using COMSOL 3.5. Both active compound transport, as well as diffusion contribute to the compound distribution in the device. Therefore, the Navier–Stokes equations were solved to model pressure-driven fluid transport alongside Fick's law equations to model the compound's diffusive transport. Diffusion coefficients were either obtained from the literature when available or estimated from the compound's molecular weight. This allowed the adjustment of experimental parameters according to each drug's specific diffusion coefficient, based on its molecular weight. Prior to all experiments, simulations for compounds tested were carried out by Dr Michele Zagnoni, in order to estimate variations in the compound concentration gradient due to different diffusion coefficients (estimated in a range 0.2–0.8 × 10−10 m^2s^{-1}). This allowed the adjustment of experimental parameters in order to achieve an ideal compound concentration gradient for every drug tested.

2.6 RT-qPCR

RNA was extracted from biopsy preparations by Milly McAllister and cDNA synthesis was performed. Quantitative reverse transcription polymerase chain reaction (RT-qPCR) was performed to allow comparison between gene expression in the control sample (PNT2 benign cell line), the prostate cancer cell line LNCaP and primary prostate cells. A 96-well optical fast PCR-plate was used and the following quantities were added to each well: 40 ng cDNA from the cell line of interest, 10 µL of master mix (Life Technologies), 5 µL nuclease-free water and 1 µL of gene expression assay. The gene expression assays used in this study were all Taqman Gene Expression Assays and included predesigned primers and probes sets for the androgen receptor (AR), fatty acid synthase (FASN), kallikrein-3 (KLK-3 gene for the prostate specific antigen

protein), golgi membrane protein 1 (GOLM1) and alpha-methylacyl-CoA racemase (AMACR) (Applied Biosystems, cat. no. Hs00171172_m1, Hs01005622_m1, Hs02576345_m1, Hs00213061_m1, and Hs01091292, respectively). Blank control wells containing only the mixture and no cDNA were included in each plate to exclude contamination. Plates were sealed and centrifuged at 1200 rpm for 3 minutes, after which air bubbles were removed using a microlance needle. RT-qPCR was performed using an ABI 7500 real time PCR machine (Applied Biosystems). Samples were heated at 50 °C for two minutes, 95 °C for 10 minutes then 40 cycles of 95 °C for 15 seconds and 60 °C for one minute. Gene expression was normalised to a housekeeping gene (beta-actin, ActB, Applied Biosystems, cat. no. Hs01060665_g1). The comparative cycle threshold (ΔΔCt) method was used to quantify relative gene expression.

3 Development of a microfluidic device for the culture and drug screening of 3D spheroids generated from biopsy tissue

For a long time 2D monolayers were the prevailing culture method for cancer cells, but over the last 20 years, 3D spheroids have emerged as a more physiologically relevant tumour model (Griffith and Swartz, 2006; Pampaloni et al., 2007; Breslin and O'Driscoll, 2013). Spheroids share many properties with in vivo tumours, such as the presence of compound and gas concentration gradients, as well as the increased cell-to-cell contact resulting from a 3D configuration (Griffith and Swartz, 2006). Therefore, spheroids are now seen as a valuable model for drug development and drug screening purposes (Kunz-Schughart et al., 2004). As a further step, spheroids can be generated from primary human tumour tissue, such as tumour resections or biopsy tissue, which are thought to resemble in vivo tumours even more closely, due to the mixed cell population present, which mirrors the cellular heterogeneity seen in human tumours (Weiswald et al., 2015). However, creating large numbers of spheroids of a controlled size without the use of automated equipment remains labour- and cost-intensive. Microfluidic devices allow precise control over the behaviour of fluids and cells and have been used to miniaturise biological assays cost-effectively (Sackmann et al., 2014; Sung and Beebe, 2014). Several microfluidic technologies have emerged as strategies to generate and culture tumour spheroids for drug toxicity testing, providing improved throughput and a highly controllable microenvironment (Kwapiszewska et al., 2014; Sakai et al., 2014; Tung et al., 2016). The main aim of this work was to develop a microfluidic device in which cells derived from biopsy tissue could be cultured in micro-wells as spheroids, and exposed to drug concentrations, whilst allowing monitoring of the spheroid's condition using inverted bright-field and epifluorescence microscopy. The following chapter describes the development of the device and considerations affecting the design of the device and its features, as well as the principles of the drug concentration gradient generation, and preliminary cell seeding and spheroid culture experiments.

3.1 Self-generating gradient microfluidic device

The devices used in this project were produced using soft- and photolithography procedures (Duffy et al., 1998; McDonald and Whitesides, 2002), as described in section 2.1.2 and 2.1.3. The use of square non-adherent micro-wells for the trapping of cells and the culture of cancer spheroids was based on previous micro-well cell trapping devices, first used for oocyte trapping and later applied to cancer cells (Han et al., 2010; Patra et al., 2013). Microfluidic devices have been used to generate concentration gradients using a number of different mechanisms for the purpose of drug screening (Tsui et al., 2013). The gradient-generating device created during this project was composed of two layers: a 1 mm thick PDMS bottom layer, which con-

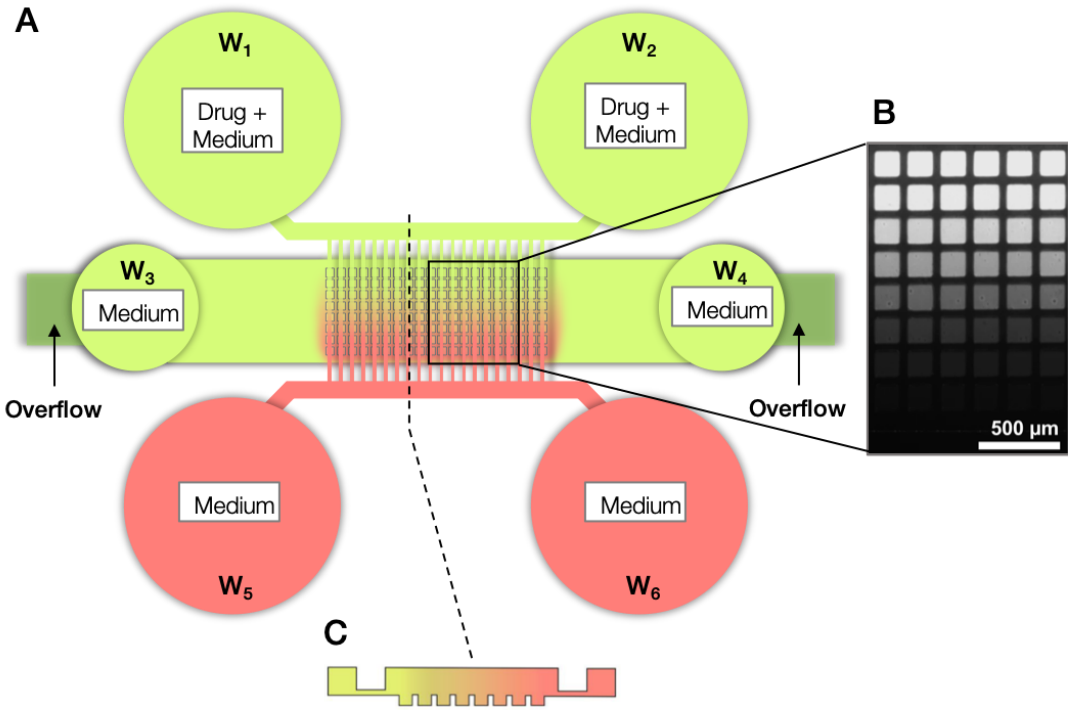

Figure 3.1 Schematic structure of the gradient-forming microfluidic device.
A) 6 reservoirs (W_{1-6}) access the fluidic network. W_1 connects to W_2 via a side channel, as does W_5 to W_6. The side channels are interconnected by a network of microchannels. These microchannels run across an array of micro-wells, which is attached to the bottom of the central channel which connects W_3 and W_4. B) Example of a fluorescent calcein concentration gradient generated in the micro-well array. C) Cross-section of the device, showing both side channels as well as a side-view of the micro-wells at the bottom of the central channel during the formation of a concentration gradient over the micro-well array.

tained an array of 240 square micro-wells (150 × 150 × 180 µm), that were used for spheroid formation and subsequent culture. The second and top PDMS layer of ~5 mm thickness comprised a network of microchannels, which are accessible via open well reservoirs, that were designed for the injection of cells, medium perfusion and formation of a compound concentration gradient. In this top layer, two side channels (35 µm depth) were connected to a central channel, containing the micro-wells, by an array of smaller microchannels (7 µm depth) (**Figure 3.1**).

3.2 Wafer fabrication

As described in 2.1.2, photolithography was used to pattern the master silicon wafer, which is a highly sensitive process. Therefore, each step had to be optimised carefully to accomplish:

1) Good resolution of the high aspect ratio features used to produce micro-wells in the base layer, which was achieved by optimising the soft bake procedure, exposure time and development process. Optimisation of all variables allowed the achievement 180 µm-high square pillars (150 µm × 150 µm) spaced 50 µm apart. This was essential to achieve the highest possible number of micro-wells per imaging field of view, aiding in the optimisation of image acquisition.
2) A micro-well depth of 180 µm was achieved by optimising the resist spin rate. This enabled the fabrication of micro-wells deep enough to allow shear-stress free perfusion of the cells contained within the micro-wells.
3) Strong adhesion of the patterned resist features to the wafer surface was achieved through constant monitoring of wafer temperatures during the soft- and post-exposure baking steps. This allowed the repeated and consistent use of the same master wafer for the fabrication of PDMS devices.

Once the silicon wafer was patterned, silanised and cast, the quality of the replicate moulded features produced was assessed using a scanning electron microscope (SEM, Hitachi S- 3000N) (**Figure 3.2**). A Tencor Alpha Stylus profilometer was used to

measure the height of the SU-8 features on the silicon wafer in at least 6 different places on each wafer to assure that the correct dimensions were achieved.

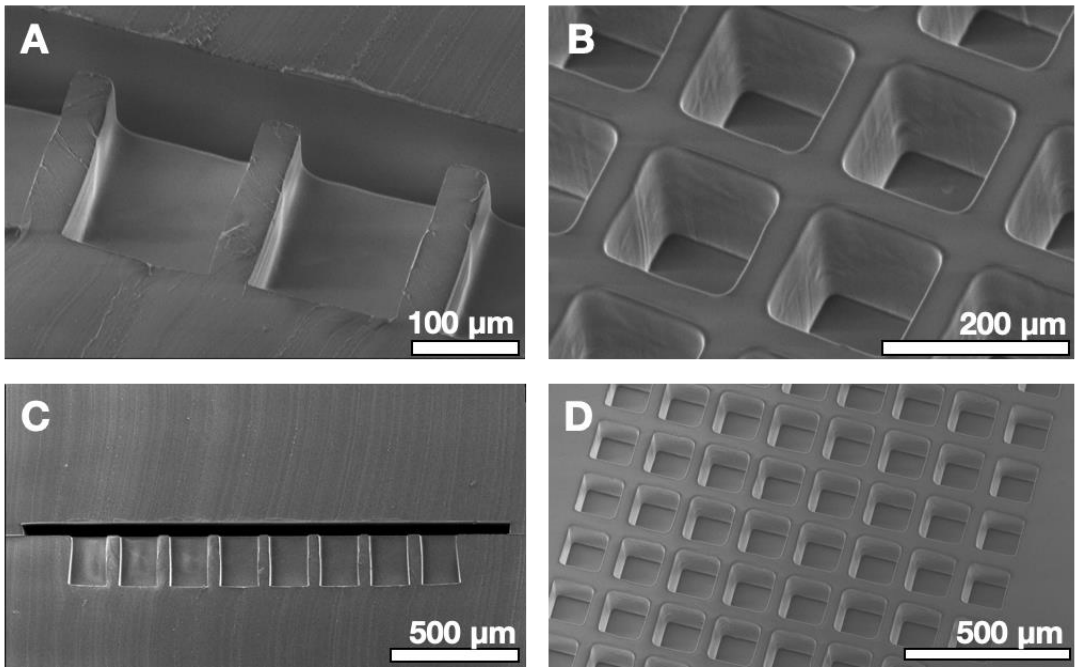

Figure 3.2 Scanning electron microscope images of a PDMS cast.

A) Cross-section of micro-wells. B) Top-down closeup view of the micro-well array. C) Cross-section of the gradient generating device, showing the micro-wells and the central device channel. D) Top-down view of the micro-well array.

3.3 Design considerations

Several microfluidic devices currently exist, which have been used for the drug screening of cell line-derived spheroids for the purpose of drug discovery (Gracz et al., 2015; Cheng et al., 2016; Patra et al., 2016).The main aim of this project was to create a platform, that could be used to generate thousands of spheroids from a cell suspension of a single tumour biopsy (hundreds spheroid/device), in order to screen as many available treatment options and their combinations. The main obstacle to overcome in this pursuit is the small number of cells contained within each needle biopsy. This can range from 500,000 to 1,000,000 cells (Welker et al., 2007), which greatly limits the number of possible experiments using conventional methods, such as ultra-low adhesion plates. In the future, such a device platform could provide valuable insights into which treatment regimen shows the best anticancer activity when

tested on the biopsy-derived spheroids. These insights could provide valuable additional information to oncologists when deciding which treatment best fits each patient, providing a further step closer to truly individualised precision medicine. Therefore, the goal was to develop a platform capable of the following:

1) The generation of thousands of spheroids from a single-cell suspension obtained from tumour biopsy tissue.
2) Prolonged culture of biopsy-derived spheroids for extended periods of time in a shear-stress free environment.
3) Operation of the device is conducted using micropipettes only, without external instrumentation, such as syringe pumps.
4) Exposure of spheroids to a customisable compound concentration gradient lasting at least 12 hours, which enables efficient drug screening in the form of one concentration-response curve per device.

These aims placed a number of constraints on the design of the device, which will be outlined in the following paragraphs.

3.3.1 Micro-well size

The size of the micro-wells produced had to be considered carefully, because it directly affects the size of aggregates created. As a consequence, depending on which tumour stage or area is being mimicked, the appropriate well size has to be chosen. In spheroids with a diameter of more than 500 µm, the large gas and nutrient gradient across the cells can result in the formation of a hypoxic and necrotic spheroid core (Riffle et al., 2017). These spheroids model tumour areas located further than 150-200 µm from vasculature, that contain hypoxic and necrotic zones, which are inaccessible to nutrients, gases and drugs (Brown and Giaccia, 1998; Wilson and Hay, 2011). Hypoxia is thought to play a major role in therapy resistance, invasiveness and tumour recurrence (Wilson and Hay, 2011), hence larger spheroids are a helpful model when investigating hypoxia and necrosis.

Spheroids of less than 500 µm diameter may not always contain hypoxic areas, but still experience a very steep oxygen concentration gradient towards the spheroid

centre. These spheroids replicate the heterogeneous vascularised tumour areas, where cells are exposed to a mixture of oxygen, drug and nutrient concentration gradients (Thoma et al., 2014). For this platform, micro-wells of 250 µm and 150 µm size were chosen, in order to firstly, generate the largest possible number of spheroids, but also to rule out hypoxia-mediated drug resistance (Hanahan and Weinberg, 2011) when determining drug efficacy, so that a definitive conclusion on a therapy's efficacy in dividing cells could be reached.

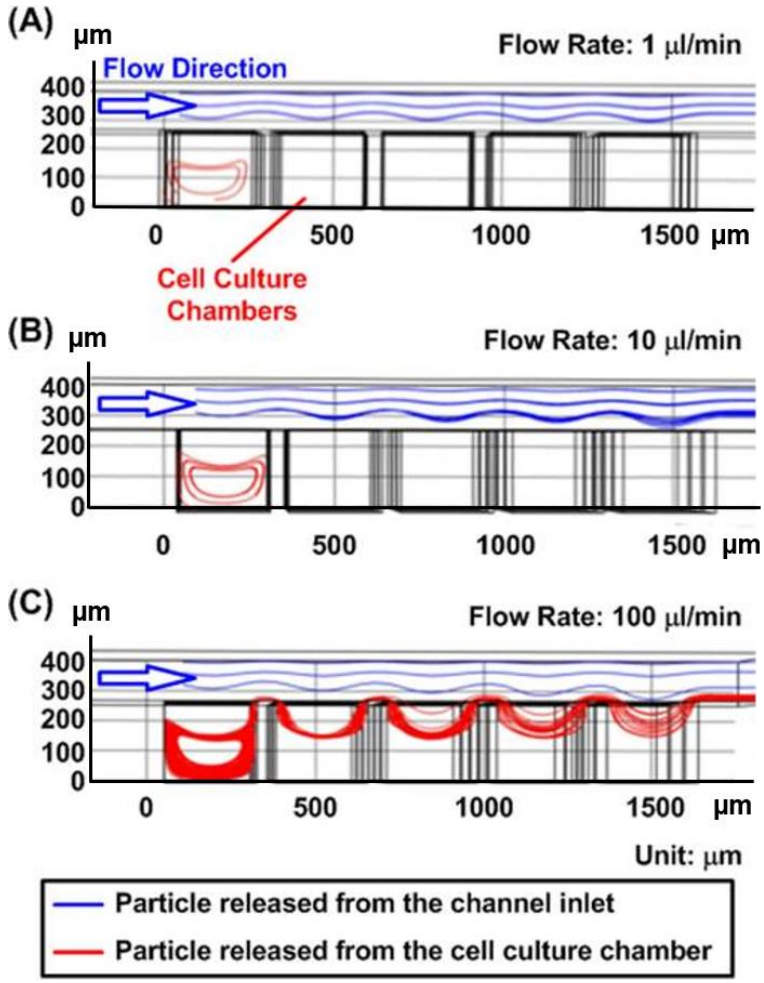

Figure 3.3 Impact of different flow rates on flow patterns

Cells flowing at different flow rates across a micro-array and cells already present in micro-wells, reproduced from Patra et al. 2013

3.3.2 Cell seeding and medium exchange

Since this microfluidic device was to be operated entirely using micropipettes, all active transport in the platform had to be generated using hydrostatic pressure

gradients. Active transport in the device is required for cell seeding as well as for medium exchange of the already formed spheroids. In principle, in order to seed cells into the micro-wells, a cell suspension is pipetted into W_3, which generates a hydrostatic pressure difference between W_3 and W_4, producing a flow of the cell suspension across the micro-well array (**Figure 3.5**). However, the impact of achieving the correct flow rate is crucial, which is illustrated in **Figure 3.3** by Patra et al., 2013.

If the generated flow rate during cell seeding is too high, cells will flow across the array without settling into the micro-wells, which would lower the seeding efficiency. Further, any cells and spheroids already present in the micro-wells during medium exchange are at the risk of being disturbed and washed out. However, if the flow rate generated is too low, cells may only flow across part of the array before the flow stops, resulting in a low seeding efficiency. The following factors affect the flow rate generated inside the cell culture channel and were optimised during this project:

1. **Fluidic resistance.** The volumetric flow rate Q achieved in the central channel connecting W_3 and W_4 (**Figure 3.5**) can be approximated using **Equation 4**, and is proportional to the pressure difference ΔP. The fluidic resistance R_H of a rectangular microchannel is determined by the geometry of the channel as shown in **Equation 5**. **Equation 5** applies to rectangular microchannels with a larger width than height, where W_C is the width of the microchannel, L_C is the channel length, H_C designates the channel height, and η is the fluid dynamic viscosity (Oh et al., 2012). Therefore, the higher the resistance, the lower the flow rate generated in the channel. Moreover, the choice of the channel dimensions was affected by the size of the cells of interest and by the field of view of the camera used, in order to maximise the number of spheroids contained in each image.

   Equation 4: $$\boldsymbol{Q = \frac{\Delta P}{R_H}}$$

   Equation 5: $$\boldsymbol{R_H = \frac{12\,\eta\,L_C}{W_C {H_C}^3 (1 - 0.63\frac{H_C}{W_C})}}$$

2. **Reservoir size.** Since the volumetric flow rate in the central channel between W_3 and W_4 is proportionally dependent on the pressure difference between the two

reservoirs, the choice of the correct reservoir size was crucial. The pressure difference across the channel was determined by the hydrostatic pressures exerted by the columns of liquid contained in the reservoirs, where the hydrostatic pressure P_H (**Equation 6**) is dependent on the density, ρ, of the liquid, the gravitational constant, g, and the filing height, h, of the cylindrical reservoir.

Equation 6*:* $$\boldsymbol{P_H = \rho g h}$$

Since the hydrostatic pressure exerted by the column of liquid in the reservoirs is dependent on the height of the fluid, rather than its volume, it was possible to achieve the desired hydrostatic pressures by optimising the reservoir diameter of the cylindrical reservoir (**Equation 7**, V is the volume, D is the diameter). Further, any volumes used to obtain specific hydrostatic pressures had to be compatible with standard pipettes and were therefore limited to a minimum of 1 µL.

Equation 7*:* $$\boldsymbol{h = \frac{4V}{\pi D^2}}$$

3. **Fluid volume.** Once the reservoir size was fixed, the hydrostatic pressure could still be varied by adjusting the fluid volume, and therefore the fluid height, during experiments. In order to seed cells into the micro-well, the correct volumes and cell concentrations to be pipetted into W_3 and W_4 were determined experimentally. Finally, the parameters required to achieve the highest possible number of filled micro-wells (**Figure 3.4**) were determined experimentally, resulting in almost 100% of micro-wells filled.
4. **Micro-well aspect ratio.** To allow the perfusion of cells and spheroids within the micro-wells without exerting a high degree of shear stress, a high aspect ratio of micro-well width and depth was chosen. In this case, 150 µm square micro-wells were produced with a depth of 185 µm. Cioffi et al. have shown that a high aspect ratio improves recirculation within the well, whilst reducing shear stress and the risk of washing cells and small spheroids out of the micro-wells (Cioffi et al., 2010).

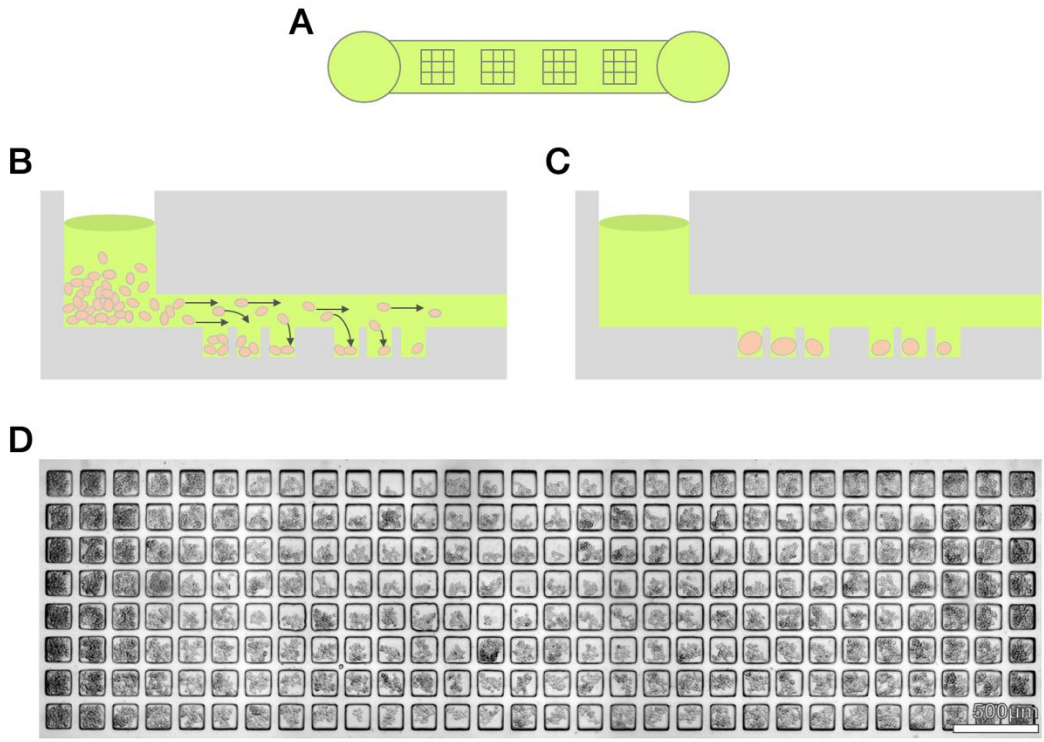

Figure 3.4 Schematic process of cell seeding in the microfluidic device.

A) Top-down schematic view of the structure of the cell culture channel connecting W_3 and W_4 (not to scale). B) Cross-section of a device schematic, showing seeding of a cell suspension from W_3 into the micro-channel, which directs the flow of the cells towards the micro-wells, where the cells aggregate and after 24-48 hours form spheroids (C). D) Top-down view of the micro-well array after cell seeding has been completed (scale bar = 500 µm).

3.3.3 Generation and maintenance of a compound concentration gradient using hydrostatic pressure

As described in the introduction, the majority of drug concentration gradients inside microfluidic devices have been generated using external fluid actuation equipment (Kim et al., 2010; Lim and Park, 2018). However, the aim of this project was to generate a long-lasting drug concentration gradient using hydrostatic pressure gradients only, as the means to create active transport of the chemical compounds. Therefore, a network of microchannels was designed carefully, which would distribute a controlled drug concentration gradient over the array of spheroids within the micro-wells. This network of microchannels could be accessed through the 4 outer connected reservoirs ($W_{1,2,5,6}$, **Figure 3.4**). By creating hydrostatic pressure differences between these reservoirs and reservoirs $W_{3,4}$, a flux was generated from reservoirs $W_{1,2,5,6}$ through the microchannel network and towards the central channel, which, in an interplay with diffusion, generated a concentration gradient over the micro-well array. However, to preserve this concentration gradient for prolonged time periods, a near steady-state flow must be created and maintained. During early experiments

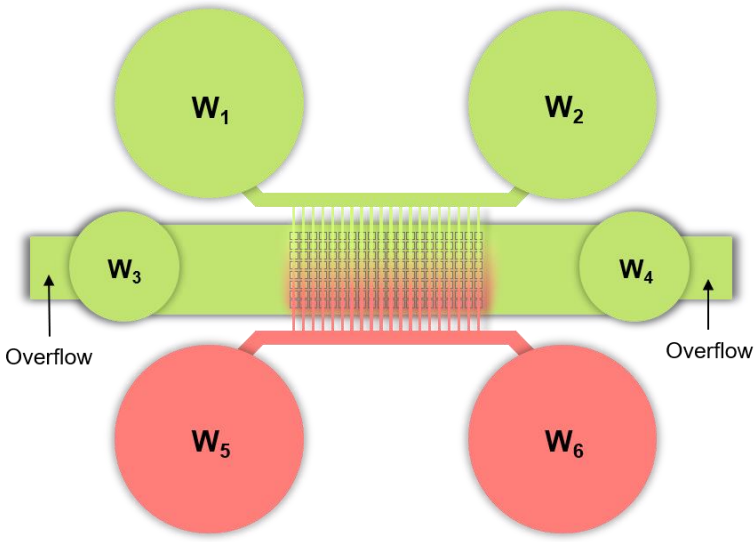

Figure 3.5 Schematic structure of the self-generating concentration gradient device

The four reservoirs $W_{1,2,5,6}$ are interconnected by a microfluidic channel network, which spans the array of micro-wells within the central cell culture channel that links W_3 and W_4.

using the six open reservoirs $W_{1\text{-}6}$, it was established that the concentration gradient obtained initially could not be maintained for long periods of time. The concentration gradient was lost due to the slow equilibration occurring between the six reservoirs, during which the pressure increased in $W_{3,4}$ and simultaneously decreased in $W_{1,2,5,6}$. This resulted in a slow reduction of the hydrostatic pressure gradient ($\Delta P(h)$) between $W_{1,2,5,6}$ and $W_{3,4}$ (**Figure 3.6**). As a consequence, the active transport component contributing to the concentration gradient formation became smaller with respect to the diffusion occurring in the micro-wells. To avoid this early discharge of the hydrostatic pressure gradient, two overflow ports were introduced on each side of W_3 and W_4, which allowed fluid to flow out of the device as it reached the level of the overflows. This effectively limited the fluid height that could be reached during equilibration, which prolonged the maintenance of the pressure gradient ΔP between the outer reservoirs $W_{1,2,5,6}$ and $W_{3,4}$ (**Figure 3.6B**).

3.4 Generation of a concentration gradient over an array of micro-wells

3.4.1 General principles of operation

For the generation of a chemical concentration gradient in the central channel between W_3 and W_4, a near steady-state flow must be maintained. This flow compensates for molecular diffusion across the spheroid array. In the absence of external actuation equipment, such as syringe pumps, this was achieved by carefully designing the resistive and capacitive microfluidic network and by creating overflow ports in both reservoirs connected to the central channel ($W_{3,4}$ in **Figure 3.6**). To create the concentration gradient, a volume of a drug solution was pipetted into both reservoirs of a side channel ($W_{1,2}$ in **Figure 3.5**) and the same volume of complete medium was

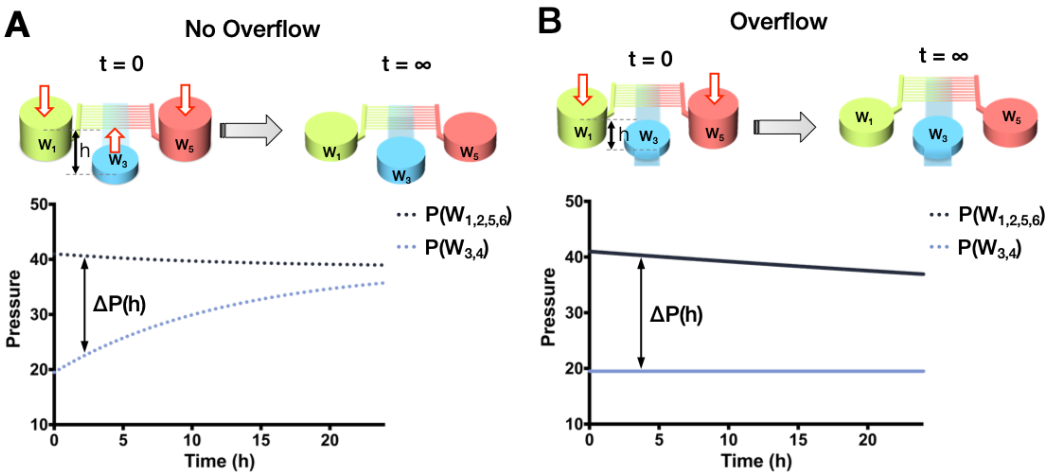

Figure 3.6 Temporal evolution of the pressure gradients within the device

A) Temporal evolution of pressure gradients in the microfluidic device and the (B) impact of the introduction of overflows to the side of W3,4 on the pressure difference between W1,2,5,6 and W3,4 over time (not to scale).

pipetted into the opposite reservoirs ($W_{5,6}$ in **Figure 3.5**), whilst the smaller reservoirs of the central channel ($W_{3,4}$ in **Figure 3.6**) contained a lesser volume of complete medium, with a smaller reservoir filling height. This created a symmetrical hydrostatic pressure-driven flow across the micro-well array that simultaneously transported drug solution and medium from each side channel, respectively, towards the reservoirs of the central channel. The hydrostatic pressure difference, $\Delta P = (P(C_S) - P(C_C))$, between the side reservoirs and central reservoirs of the microfluidic network experienced an exponential decay over time, with C_S and C_C being the capacitance of the side channel and central channel reservoirs, respectively. ΔP was primarily dependent on the fluid height (h) in each reservoir (**Equation 6**) and determined the magnitude of the flow rate in the central channel (Equation 4, $\Delta P = RQ$, where R is the fluidic resistance of the channel network and Q the volumetric flow rate). In the absence of overflow ports (**Figure 3.6A**), the hydrostatic pressure differential caused by the difference in fluid level between inlet and outlet eventually equilibrate. However, when overflow ports were created in the central reservoirs (**Figure 3.6B**), $P(W_{3,4})$ remained constant after the fluid volume had reached the height of the overflow port, whilst the liquid level in the side reservoirs decreased until it eventually reached the level of the $W_{3,4}$, which was determined by the level

of the overflows. In this case, the introduction of two overflow ports and careful microfluidic design allowed fine-tuning of the flow in the central channel to compensate for molecular diffusion, thereby achieving a long-lasting concentration gradient (**Figure 3.6**).

3.4.2 Using analogue circuits to model the active transport of molecules during the concentration gradient formation

In order to enable an estimation of the volumetric flow rates within the microchannel and reservoir network, an analogous electrical circuit of the microfluidic network was created by Dr Michele Zagnoni, following methods demonstrated by Oh, Lee, Ahn, & Furlani, 2012. In this model, all reservoirs were considered as electrical capacitors and the microchannel network as an electrical resistive mesh. As such, C_S and C_c describe the hydrostatic pressure exerted by the initial fluid level in the side channel and central channel reservoirs, which is the equivalent of the initial electrical charge

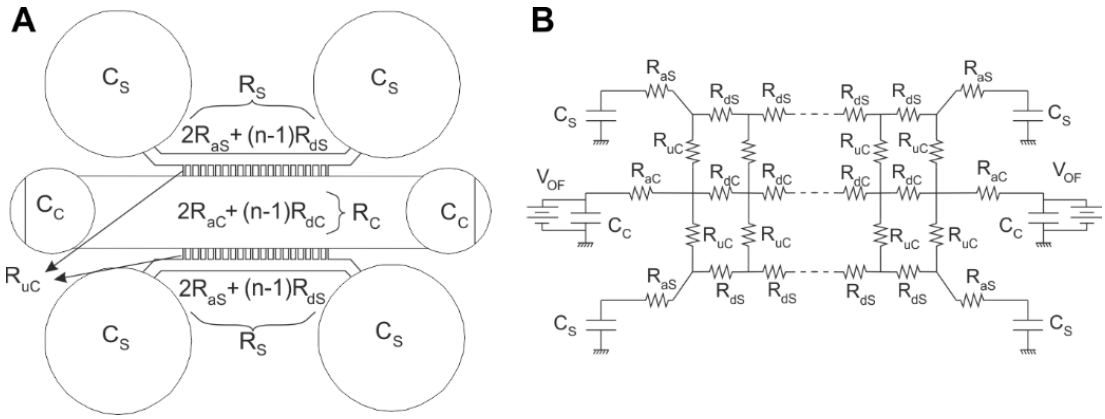

Figure 3.7 Analogue circuit established using the geometry of the device.

By considering the geometrical features of the microfluidic device developed (A), an analogue electrical circuit (B) could be created. The analogue circuit was used in a numerical simulation in PSpice, in order to determine the pressure pattern of each reservoir. In the simulation, the initial fluid level in each reservoir was modelled as the initial electrical charge in each capacitor. C_S and C_C indicate the capacitance of the side and central reservoirs. R_S and R_C represent the resistance of the side and central culture channels, which are equivalent to the sum of the distributed resistances of each channel. R_{uC} indicate the resistance of each microchannel.

in a capacitor in the analogue circuit. The resistance exerted by the side and central cell culture channel, R_S and R_C respectively, is equivalent to the sum of the individual resistances of all contributing channels. For example, the resistance of R_C is composed of the central channel leading from both reservoirs C_C to the micro-channel array, which is equivalent to $2R_{aC}$, and the central channel sections between micro-channels within the array (R_{dC}), which together form the mesh of microchannels, described as $(n-1)R_{dC}$ (**Figure 3.7**). This circuit was simulated in PSpice by Dr Michele Zagnoni (**Figure 3.7**) to estimate the hydrostatic pressure patterns using following set of equations:

Overflow case:

Equation 8: $$\boldsymbol{P(C_S) = \rho g\left(h_{S_{in}} - \left(h_{S_{in}} - h_{C_{in}}\right)\left(1 - e^{-\frac{t}{R_T 4 C_S}}\right)\right);}$$

Equation 9: $$\boldsymbol{P(C_C) = \rho g\left(h_{C_{in}}\right);}$$

No overflow:

Equation 10: $$\boldsymbol{P(C_S) = \rho g\left(h_{S_{in}} - \frac{\left(h_{S_{in}} - h_{C_{in}}\right)}{1+\frac{2A_S}{A_C}}\left(1 - e^{-\frac{t\left(1+\frac{2A_S}{A_C}\right)}{R_T 4 C_S}}\right)\right);}$$

Equation 11: $$\boldsymbol{P(C_C) = \rho g\left(h_{C_{in}} + \frac{2A_S}{2A_S + A_C}\left(h_{S_{in}} - h_{C_{in}}\right)\left(1 - e^{-\frac{t\left(1+\frac{2A_S}{A_C}\right)}{R_T 4 C_S}}\right)\right);}$$

where $P(C_S)$ and $P(C_C)$ are the respective hydrostatic pressure values as a function of time; $h_{S_{in}}$ and $h_{C_{in}}$ are the initial fluid height values in the side and central well reservoirs W_3 and W_4, respectively; R_T is the resistance of the device' fluidic network, and A_S and A_C are the areas of the base of the circular side and central well reservoirs, respectively. Finally, a finite element method (FEM) numerical model (Comsol Multiphysics 3.5) was used to estimate the convective as well as diffusive behaviour of the compound of choice (**Figure 3.9A-C**).

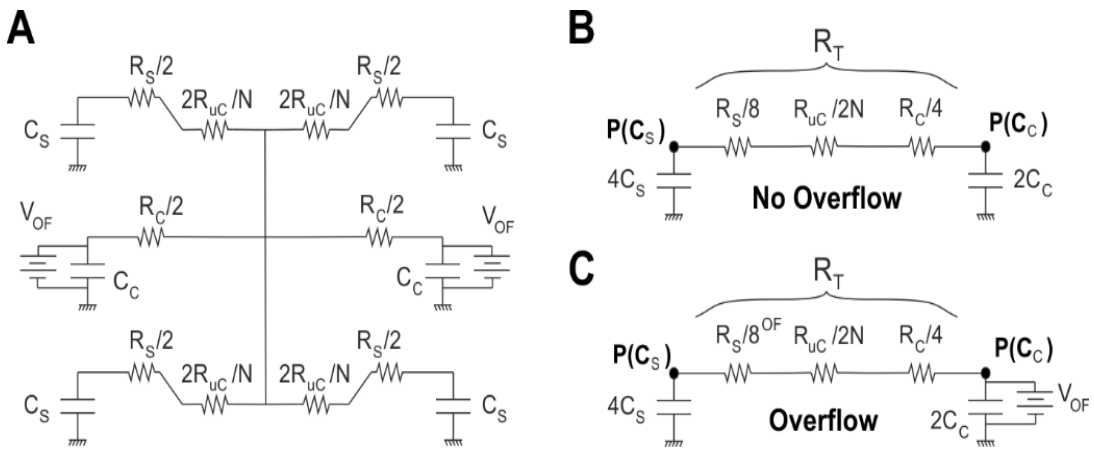

Figure 3.8 Analogue circuit symmetry enables simplification

Due to the symmetrical nature of the analogue circuit in Figure 3.7, it could be further simplified (A) in order to extract an analytical expression of the pressure patterns in each open well reservoir ($P(C_S)$ and $P(C_C)$). These matched those obtained from the numerical simulation conducted in PScpice. (A) could then be further simplified to model the flow from the side reservoirs to the central reservoirs, which depended on the presence (C) and absence (B) of overflow ports created in the central channel reservoirs. The overflow ports were modelled in the analogue circuit as a constant potential generator connected to the central reservoir capacitors.

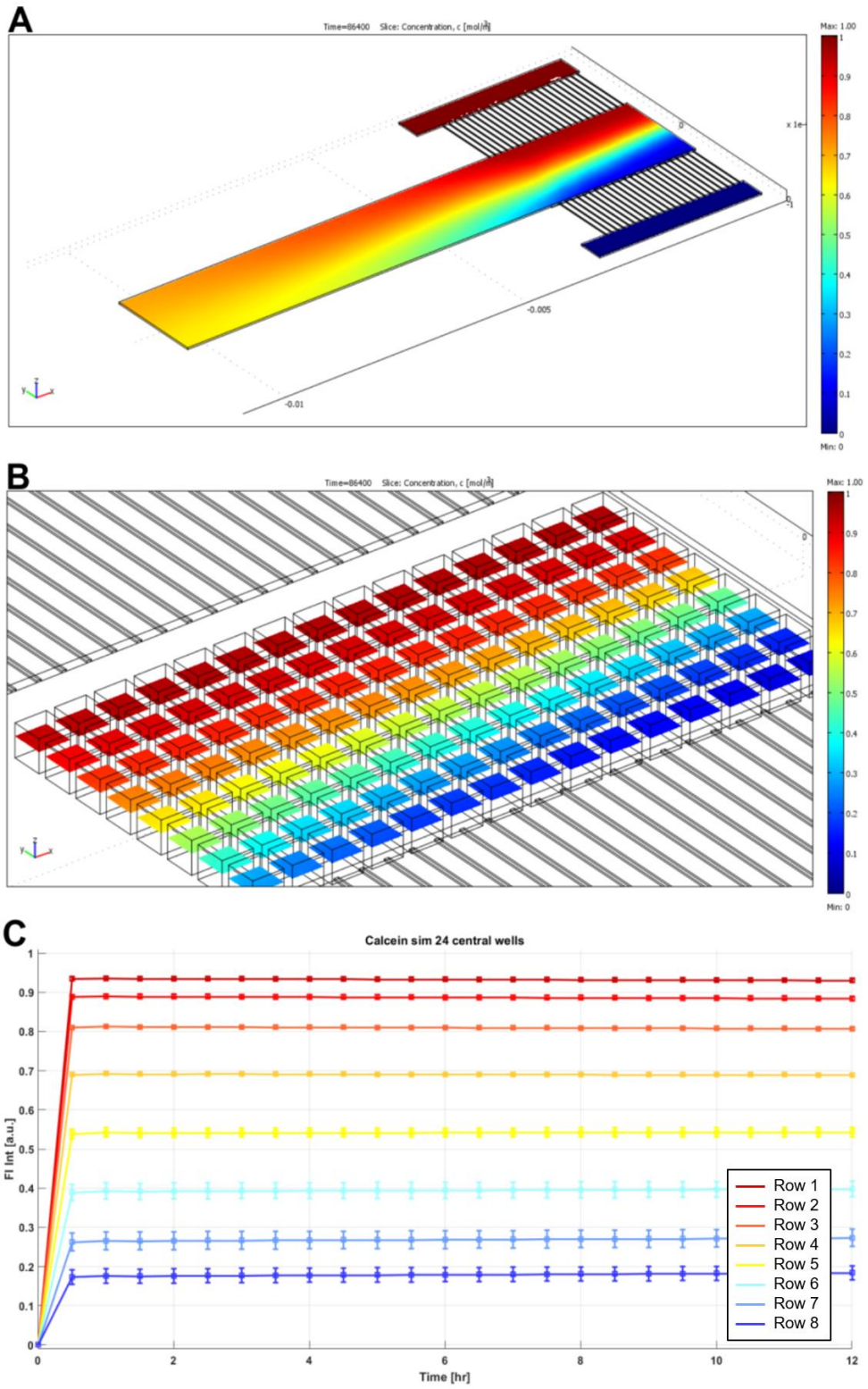

Figure 3.9 Finite element model simulation of the microfluidic gradient generation

A-C) Finite element model (FEM) simulation using COMSOL Multiphysics 3.5 of the active and passive transport of compounds in the microfluidic device and the C) resulting compound concentrations depending on the row position within the micro-well array.

To validate the models developed, a solution of the fluorescent molecule calcein (100 µM) was used to experimentally demonstrate the formation and maintenance of the microfluidic concentration gradient using time-lapse epifluorescence microscopy. The results (**Figure 3.11**) were compared to the numerical simulation (**Figure 3.10**), demonstrating the suitability of this approach and the robustness of the numerical model. In experiments involving chemotherapy, the convective compound transport component of the microfluidic gradient generation and maintenance remained unchanged. However, since the diffusive flux was dependent on each compound's diffusion coefficient, the fluid heights in each protocol had to be adjusted accordingly. For this to occur, the diffusion coefficients for all compounds used were estimated or obtained from the literature and simulations were run to identify the appropriate protocols for each compound.

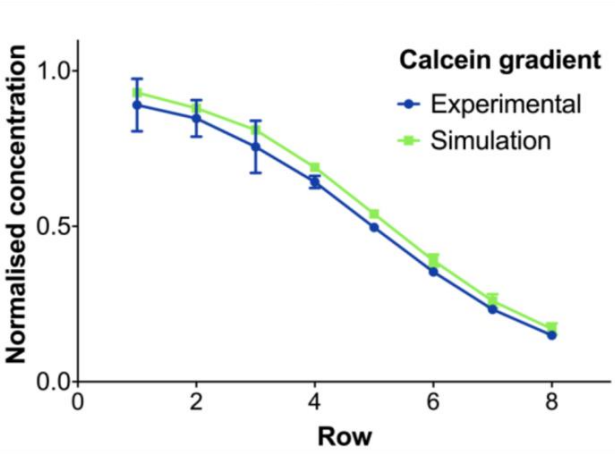

Figure 3.10 Comparison of simulated and experimentally generated calcein concentration gradients

Comparison of the calcein concentrations obtained using epi-fluorescent microscopy experimentally and the concentrations estimated using a FEM simulation in each row of micro-wells. Mean values were determined from all micro-wells in each device row to indicate the calcein concentration in each row of micro-wells, which were normalised to the maximum calcein concentration (100µM) ± S.D.

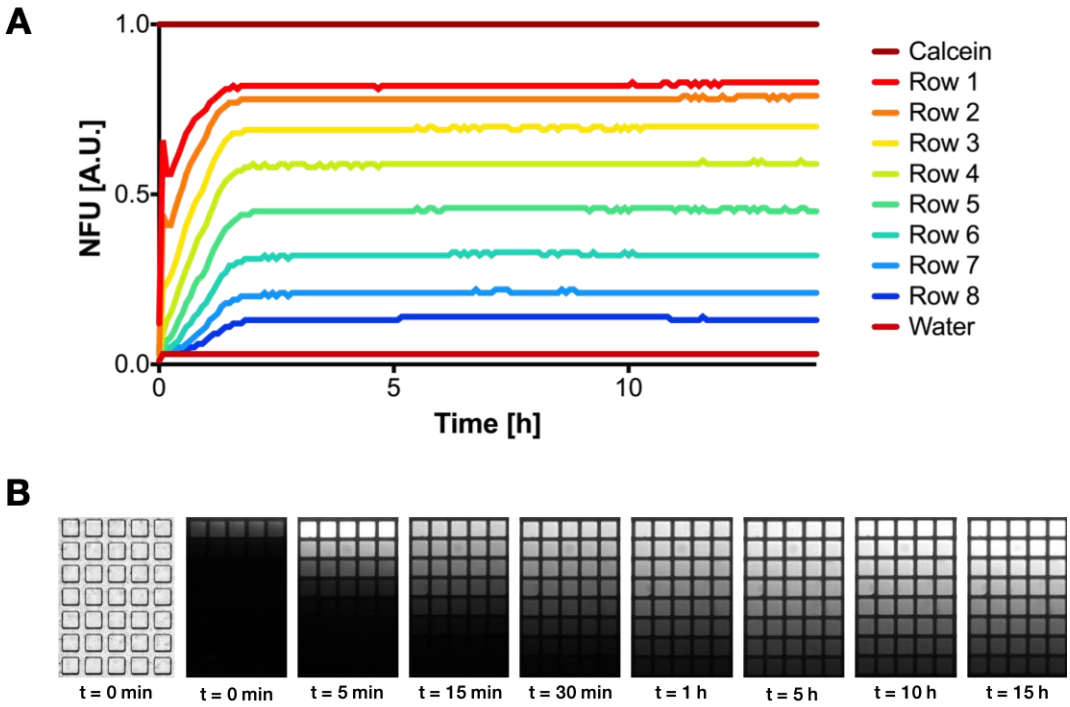

Figure 3.11 Generation of a fluorescent microfluidic concentration gradient

A microfluidic concentration gradient was generated in the micro-well array (micro-well size = 150 µm) using 100 µM calcein, where the fluorescence intensity was quantified in all micro-wells. In A) the mean fluorescence intensity in each row of micro-wells is shown ± S.E.M. over time. B) Representative epi-fluorescent images were chosen at various time points during gradient formation and maintenance

3.5 Cell seeding into the micro-well array

In order to seed cells into the micro-wells, a cell suspension was injected in one of the central wells ($W_{3,4}$ in **Figure 3.5**). This created a volume difference between W_3 and W_4, thereby creating a hydrostatic pressure gradient and as a result a flow the cell suspension along the central channel. This flow was used to spread the cell suspension across the micro-well array, which allowed cells to sediment into the micro-wells, as previously reported (Han et al., 2010; Patra et al., 2013). Due to the non-adherent surface properties of the micro-wells, single cells aggregated to form compact multicellular spheroid within two days of culture and could be cultured viably for as long as 28 days in the case of cell line derived spheroids, and for up to 12 days for biopsy-derived spheroids (**Figure 3.12A**). The seeding protocol involved

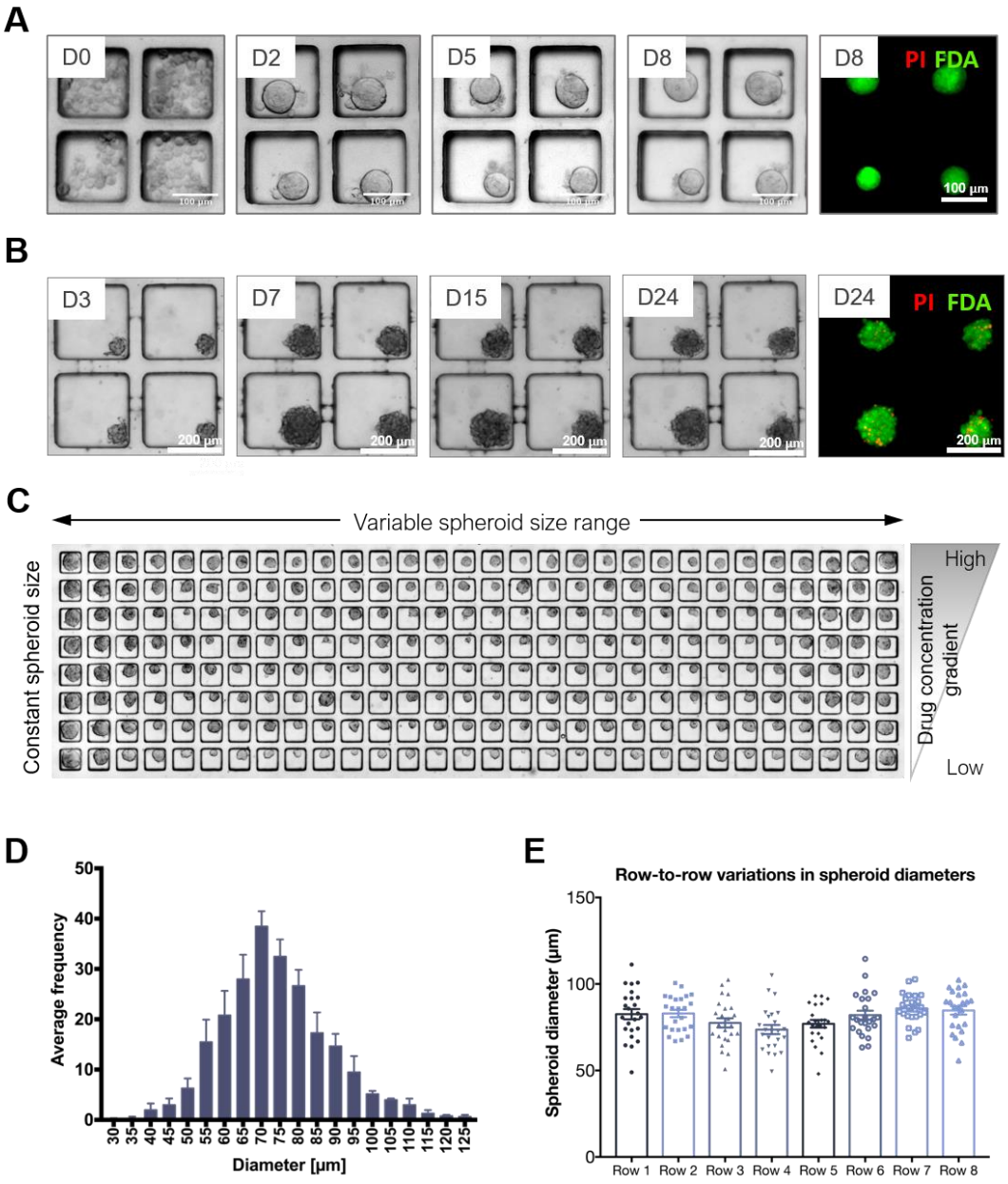

Figure 3.12 Spheroids are generated in the microfluidic device after seeding a single-cell suspension

A) Representative images of human primary prostate tumour cells aggregating in the micro-wells over time (Day 0 of culture to Day 8), showing full viability after staining using PI and FDA on day 8. B) Representative brightfield images of UVW cells aggregrating in the micro-wells over 24 days in culture, followed by viability staining on day 24 using PI and FDA. C) Example of formed UVW spheroids on day 3 within the micro-well array, displaying both the variable spheroid size range between rows and the constant size within each row. C) Histogram plot of the distribution of spheroid sizes between 6 different devices (error bars represent standard error). D) Comparison of spheroid sizes in each row of a representative gradient device, showing mean ± standard error of the values, as well as individual distribution of points.

four separate injections of a small volume of cell suspension into alternating inlet reservoirs ($W_{3,4}$), resulting in the formation of a gradient of the number of cells seeded in each row of micro-wells, which decreased the further the micro-wells were positioned away from W_3 and W_4. Using UVW cells, a glioma cell line, for the optimisation of cell seeding, this created a range of spheroid sizes (50–150 µm**, Figure 3.12C, D**) that could be tested simultaneously, to investigate spheroid size dependent drug effects. This proved to be an especially valuable feature when used in combination with a stable, long-lasting drug concentration gradient. In this context, all spheroids in the same row were exposed to the same concentration, whilst an almost linear concentration gradient was achieved along the columns of the micro-well array **(Figure 3.12C**). This feature provided the means to obtain one concentration response curve per device, where each point (eight points in total, one for each row) is the mean of the readouts of all the spheroids belonging to the same row. Additionally, the variable range of spheroid sizes allows for the selection of the spheroid size of interest when quantifying and analysing drug effects.

3.6 The single-channel micro-well array device

Since most anti-cancer agents are not visible and their concentration within the gradient-generating device cannot be measured directly, the concentration response curves obtained using the self-generating gradient device had to be validated. Therefore, a second microfluidic device was designed and produced, with the aim of mimicking the spheroid generation and culture capabilities of the self-generating gradient device, while allowing the incubation of the created spheroids with a solution of a known compound concentration. As a result, the device designed for this purpose, referred to as 'single-channel micro-well array device', only contained two reservoirs, the central cell culture channel between W_3 and W_4, and the micro-well array of the self-generating gradient device (**Figure 3.13**). In these devices, spheroids could be exposed to a drug solution of a known concentration for any period of time. This allowed the comparison of concentration response curves generated using the self-generating gradient device with those obtained using the single-channel micro-well

device. To enable this comparison, all geometric features of the main central cell culture channel, such as height, length and width remained unchanged between the two devices. Since the dimensions of the central channel were retained, cells could be seeded into the micro-wells using the same protocol established for the gradient device.

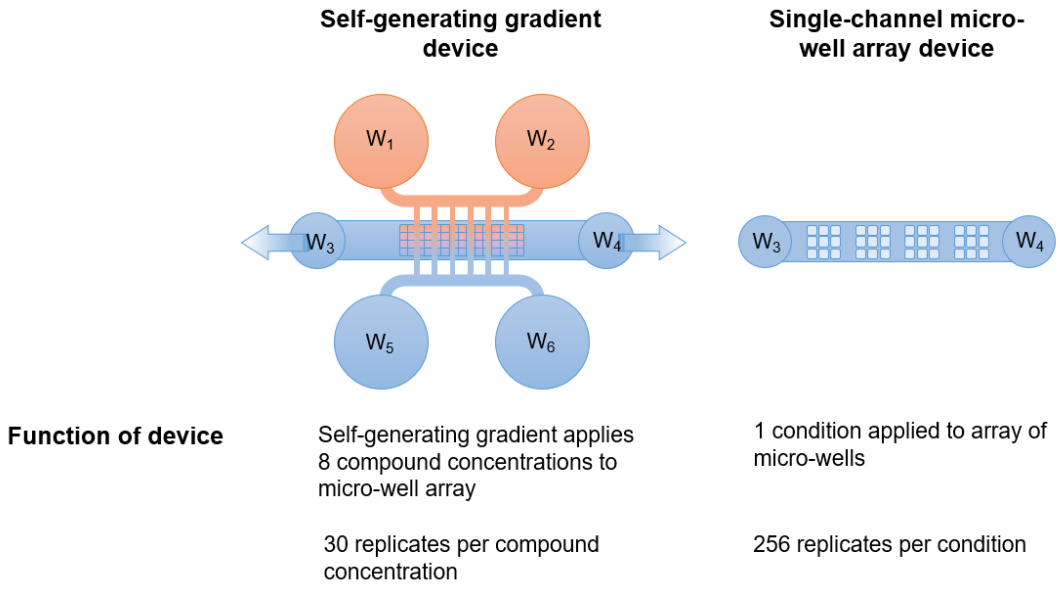

Figure 3.13 Comparison overview of schematic device structures

Both designed devices contained an array of micro-wells used for the generation and culture of multi-cellular tumour spheroids. Whereas the self-generating gradient device enabled the simultaneous application of up to 8 drug concentrations, the single-channel micro-well array device exposed the entire array of spheroids within to a known concentration of a drug. As such, the single-channel micro-well array device can act as a control for concentration response curves obtained from the self-generating gradient device.

4 Application of a microfluidic concentration gradient generating device for drug efficacy testing

4.1 Application of a cisplatin concentration gradient to UVW spheroids

The microfluidic device described in this work is capable of self-generating a chemical concentration gradient across an array of cancer spheroids. One aim of this project was to use this microfluidic device as a tool for the quantitative assessment of the efficacy of drug treatments in biopsy-derived spheroids, finding application in both drug screening and precision medicine.

In order to demonstrate that a drug concentration gradient can be established repeatedly and produce reproducible information on drug efficacy, spheroids were formed from UVW cells and exposed to a concentration gradient of the cytotoxic drug cisplatin. Cisplatin is widely used in the clinic against a number of solid tumours; its cytotoxic effects are thought to be produced by the creation of cisplatin-DNA adducts, which result in intra-strand crosslinks. DNA damage repair proteins detect these crosslinks, which induces apoptosis (Siddik, 2003).

4.2 Experimental procedure

UVW cells, a glioma cell line which easily generates spheroids, were seeded into three gradient-generating devices and allowed to form spheroids, as described in Chapter 2, and were cultured for 5 days. On day 5 of culture, all medium was removed from the device reservoirs and replaced with the appropriate volumes of a drug solution (**Figure 4.1A**). Prior to each experiment, the exact volumes required for the six reservoirs ($W_{1\text{-}6}$, in **Figure 4.1B**), in order to produce a specific concentration gradient, were determined using the model simulation described in Chapter 3. The shape and duration of the drug gradient was dependent on the diffusion coefficient of each drug. Cisplatin's diffusion coefficient D was reported to be 0.77×10^{-10} m^2 s^{-1}. To start the generation of the cisplatin gradient on day 5 of the experiment, 210 μL of a 222 μM cisplatin solution were pipetted into $W_{1,2}$ and 210 μL of medium were added to

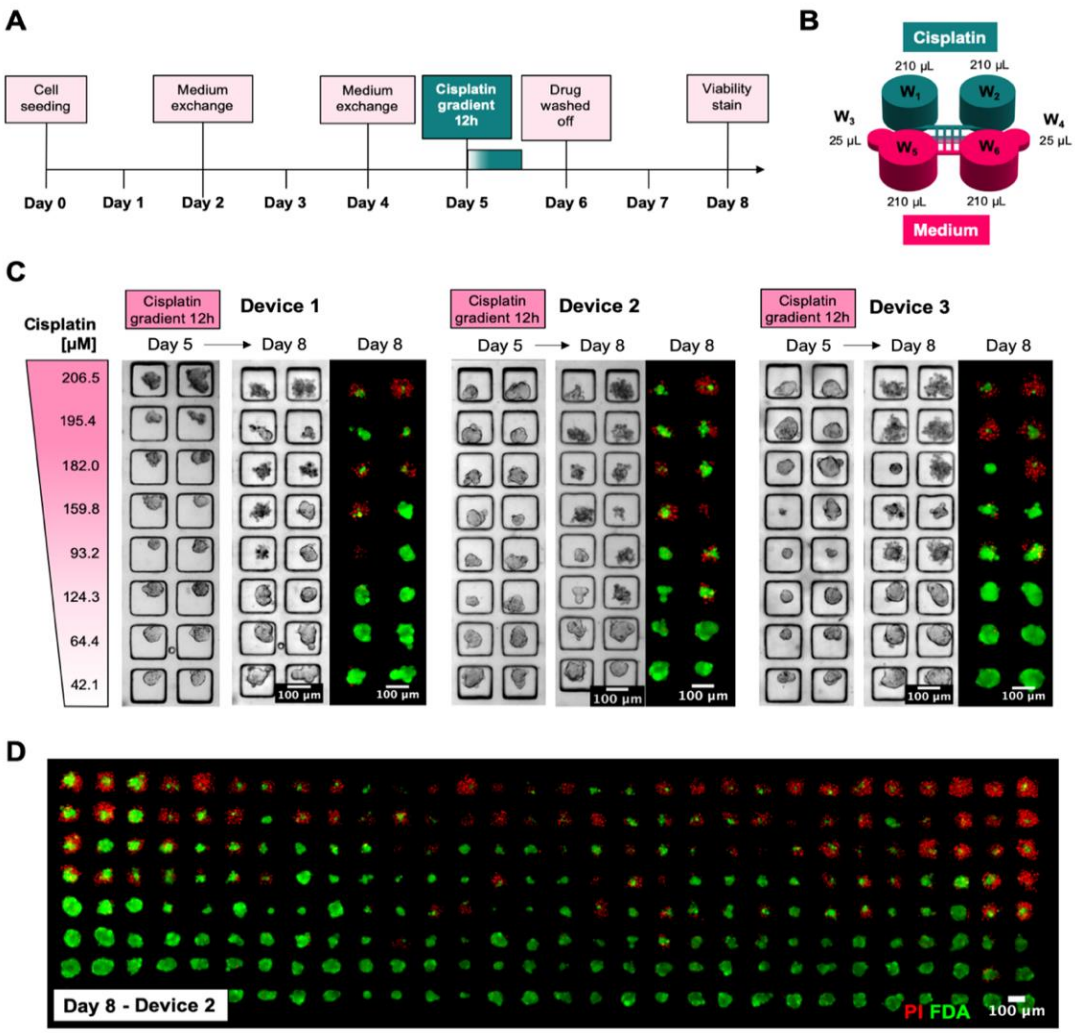

Figure 4.1 Application of cisplatin concentration gradients to UVW spheroids

within the gradient-generating platform

A) UVW cells were cultured for 5 days prior to the application of a cisplatin concentration gradient ranging from 42.1 – 206.5 µM for 12 hours (Row 1 = 206.5 µM, Row 2 = 195.4 µM, Row 3 = 182.0 µM, Row 4 = 159.8 µM, Row 5 = 93.2 µM, Row 6 = 124.3 µM, Row 7 = 64.4 µM, Row 8 = 42.1 µM). After 12 hours the drug was removed and the spheroids were cultured for a further 3 days, before viability staining was conducted. B) Schematic representation of the initial filling heights and respective volumes of medium and cisplatin solutions in all 6 reservoirs, $W_{1\text{-}6}$, at the start of the gradient generation. C) Brightfield images were taken every 24-48 hours and representative brightfield images of 2 columns of each device are shown on day 5, before the application of cisplatin, and on day 8 when viability staining was conducted using PI (dead cells) and FDA (live cells). D) Epifluorescent image of the entire array of spheroid in device 2 after staining with PI and FDA on day 8. Scale bars = 100 µm

$W_{5,6}$. The side reservoirs $W_{3,4}$ were filled with 25μL of medium. The cisplatin concentrations applied to the spheroid array as a result were estimated using the numerical simulation (Chapter 3) to range from 206.5 to 42.1 μM (Row 1 = 206.5 μM, Row 2 = 195.4 μM, Row 3 = 182.0 μM, Row 4 = 159.8 μM, Row 5 =124.3 μM, Row 6 = 93.2 μM, Row 7 = 64.4 μM, Row 8 = 42.1 μM, **Figure 4.1C**). After the reservoirs were filled, the devices were placed in the incubator at 37 °C for thirteen hours. Thirteen hours of exposure time accounted for approximately one hour to establish the concentration gradient, which was determined experimentally (Chapter 3), and 12 hours of drug exposure at the target concentration range. After 13 hours, all solutions contained in reservoirs W_{1-6} were removed and weighed to determine their volumes. The experiment was conducted in three devices to assess the repeatability of gradient generation and the consistency of results (**Figure 4.1C**). Once the cisplatin gradient application was complete and the drug was removed by washing steps, the spheroids were cultured for a further 3 days before viability staining using PI and FDA was conducted, as described in Chapter 2 on day 8 (**Figure 4.1C, D**).

4.3 Characterisation of the size and morphology of UVW spheroids generated in microfluidic devices

The fluorescent images obtained from the PI/FDA staining, as well as the brightfield images acquired every 48 hours throughout the experiment, were processed and analysed using custom Matlab software to quantify the spheroid area, length of perimeter and the FDA-positive spheroid area. These parameters were used to calculate the shape factor and the remaining viable fraction. On day 5, before the cisplatin concentration gradient was applied, the spheroids generated and cultured in the 3 devices were visually similar (**Figure 4.1C**). The majority of the micro-wells in all three devices were filled with spheroids (>99%), and more than 90% of spheroids ranged from 30 to 70 μm in diameter, and were smooth in appearance (Device 2 on day 5, **Figure 4.2A**). The mean spheroid diameter in the three devices was comparable (Device 1 = 52.8 ± 0.7 μm, Device 2 = 54.2 ± 0.8 μm, Device 3 = 58.4 ± 0.8

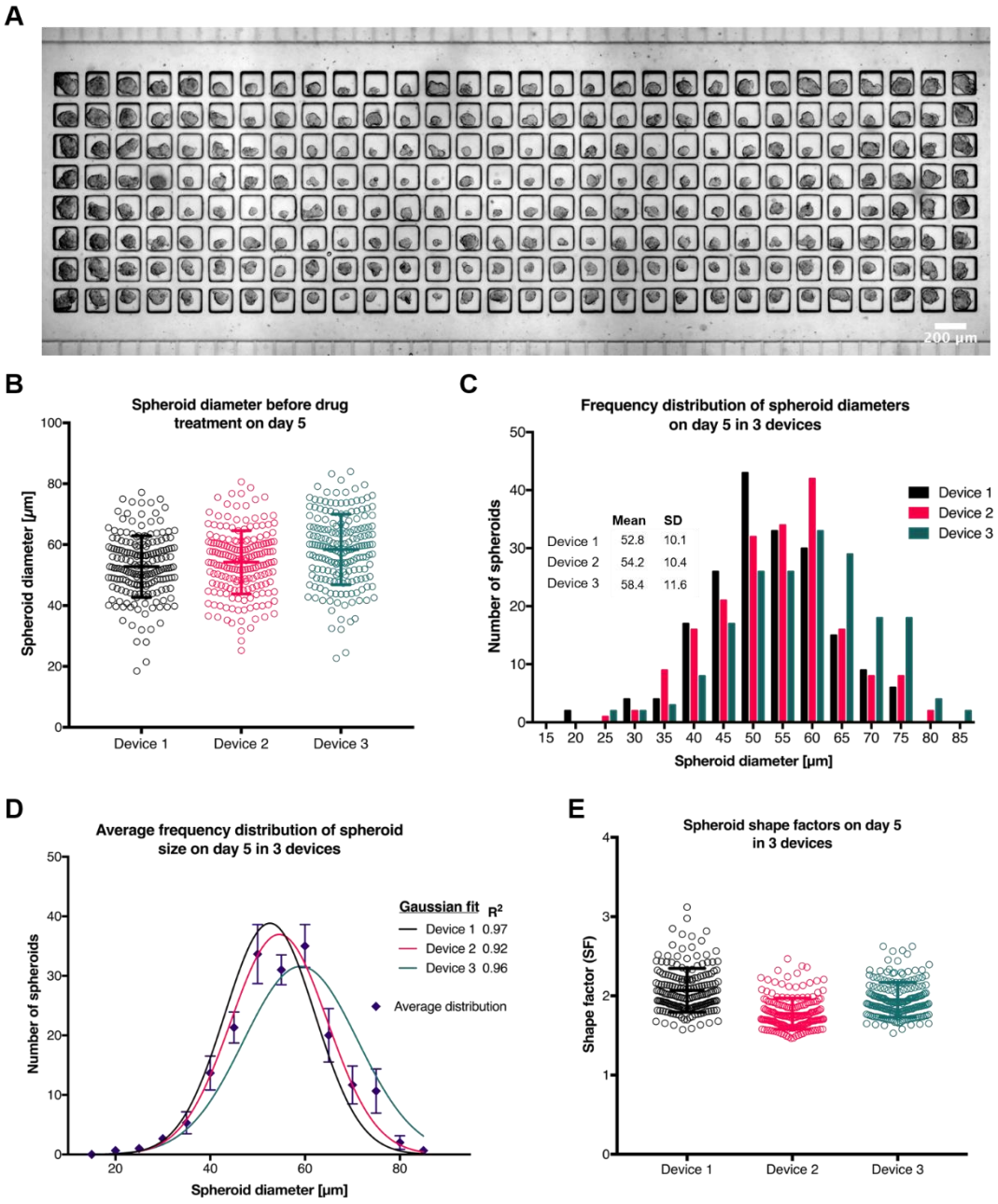

Figure 4.2 Characterisation of shape and size properties of spheroids generated in the microfluidic platform

A) Brightfield image of the full UVW spheroid array on day 5 in device 2 (scale bar = 200 µm). B) Distribution of spheroid diameters on day 5 of culture in three different devices, values displayed are means ± S.D. C) Frequency distribution of all spheroid diameters in the devices using a 5 µm bin size. D) Gaussian curves were fitted to the spheroid diameter frequency distribution in the different devices and compared to the mean diameter distribution (n=3). Values represent mean ± S.E.M. E) Distribution of the shape factors of all UVW in each device on day 5, where values represent means ± S.D.

μm) and did not differ significantly (**Figure 4.2B**). Further, the Brown-Forsythe test for normality suggested that the variability and standard deviations of spheroid diameters on day 5 were consistent between devices. **Figure 4.2C** shows the frequency distribution of spheroid diameters on day 5 in the three devices in greater detail. The frequency distribution is of some importance, since the application of several statistic tests (e.g. ANOVA) rely on Gaussian distribution of the data in order to produce reliable results. A Gaussian curve could be fitted to the spheroid diameter distribution in all three devices with $R^2 > 0.90$, indicating that the distribution of spheroid diameters is near normal in all three devices (**Figure 4.2D**). When the Gaussian curves were compared to the mean diameter distribution of the three devices, shown in Figure 2D, no significant difference was found (p=0.11). The extent of disaggregation of each spheroid in the array was quantified using a shape factor, which was determined using each spheroid's area and length of perimeter (Chapter 2). On day 5, the mean shape factor in the three devices was 1.93, and the three devices showed a similar distribution of spheroid shape factors (**Figure 4.2E**).

4.4 Temporal evolution of UVW spheroid shape after cisplatin incubation

During the experiment, brightfield images were acquired every 24-48 hours, enabling a quantitative label-free readout of spheroid integrity over the course of the experiment. 24 hours after the application of the concentration gradient, concentrations ≥ 159.8 μM cisplatin had produced a significant increase in shape factor. Over the following 3 days, the shape factor increased significantly in a concentration-dependent manner in all device rows with concentrations of ≥ 93.2 μM cisplatin ($p < 0.001$, **Figure 4.3A**). By day 8 the mean shape factors in all rows with cisplatin concentrations ≥ 124.3 μM (Row 1-4) had increased significantly ($p \leq 0.005$) compared to the control, as well as in all three devices (**Figure 4.3B**). **Figure 4.3B** shows the effects of a range of cisplatin concentrations, generated using a microfluidic gradient, on the shape factor changes observed between day 5 and day 8 (SF_{D8}/SF_{D5}) in all three devices, as well as the device mean. The shape factor changes were normalised to the shape factor

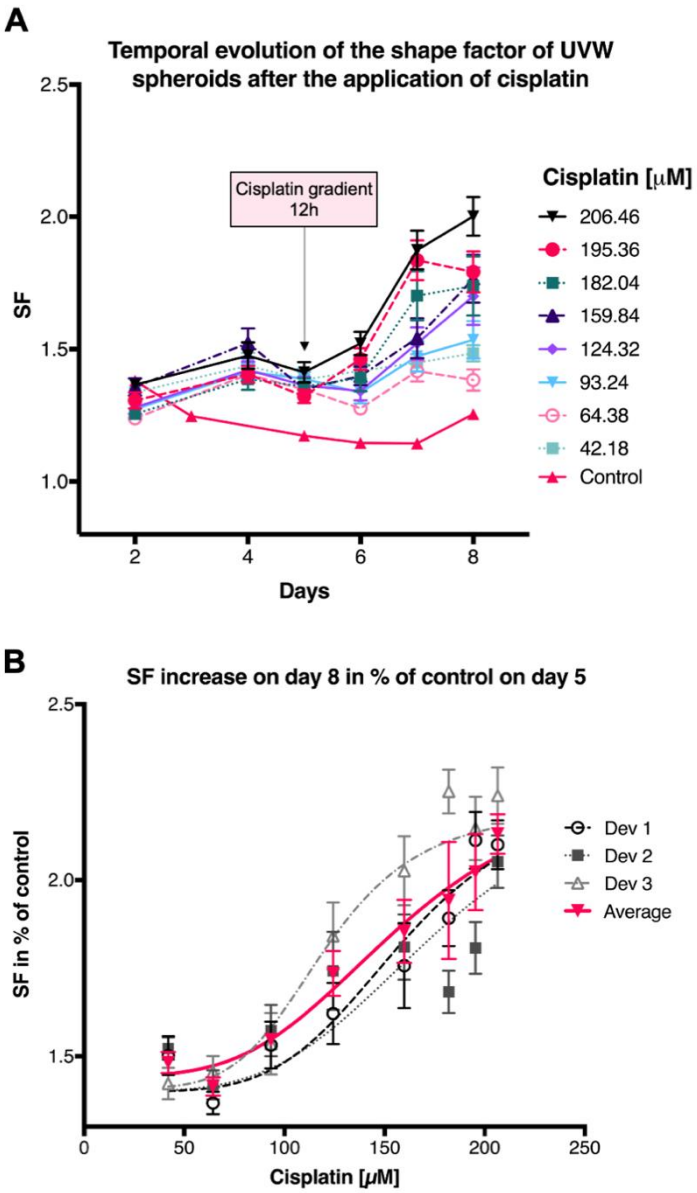

Figure 4.3 Changes in UVW spheroid shape after cisplatin exposure

A) The shape factors of all spheroid in the example of device 2, were determined every 24-48 hours over the duration of the experiment. A cisplatin concentration gradient was applied across the array on day 5 for 12 hours, and the resulting shape factors in each row of spheroids (with concentrations ranging from 42.18 to 206.46 μM) are displayed as means ± S.E.M. B) The experiment was terminated on day 8 and the normalised shape factor changes since the application of cisplatin on day 5, as well as the mean shape factor changes (n=3), were displayed as means ± S.E.M.

changes observed in the control device, and EC_{50}s were determined from the fitted concentration response curves of all 3 devices (**Table 4.1**). The EC_{50}s reported in **Table**

4.1 were comparable, and the average EC_{50} obtained from the three devices for cisplatin was 141.76 μM. A two-way ANOVA test was performed to determine if the effect of cisplatin on the spheroid shape factors was consistent between devices (n=3). For the majority of cisplatin concentrations applied (Row 1 and 4-8, 206.5 μM and 159.8 - 42.1 μM) the shape factor change in the three devices was very similar, and no significant difference between the devices could be found. However, at higher concentrations in Rows 2 and 3 (195.4 μM, 182.0 μM), some variability between the devices was found. The shape factor changes in row 2 (195.4 μM) were consistent between device 1 and 3, but device 2 showed a significantly smaller shape factor increase, whereas for row 3 (182.0 μM) device 3 had a significantly larger shape factor change. However, the shape factor change observed in Row 1 (206.5 μM), which contained the highest cisplatin concentration, did not differ significantly between devices.

4.5 Temporal evolution of spheroid size after exposure to a cisplatin concentration gradient

All spheroids were monitored over the course of the experiment using brightfield microscopy, which was later used to extract spheroid features such as their size. **Figure 4.4A** shows that the treatment with a gradient of increasing cisplatin concentrations resulted in increased spheroid areas. 24 hours after the application of the cisplatin gradient, the spheroid areas had significantly increased for cisplatin concentrations ≥ 124.3 μM in a concentration-dependent manner. After this initial increase in spheroid area, from day 6 on the spheroid size started to decrease for all cisplatin concentrations, until day 8, when the experiment was terminated for viability staining.

In order to compare the efficacy of the drug concentration gradient between the devices and generate concentration-response curves, images acquired on day 5, before cisplatin was administered, and on day 8, when the experiment was terminated, were evaluated and the spheroid areas were extracted (**Figure 4.4A**). The overall change

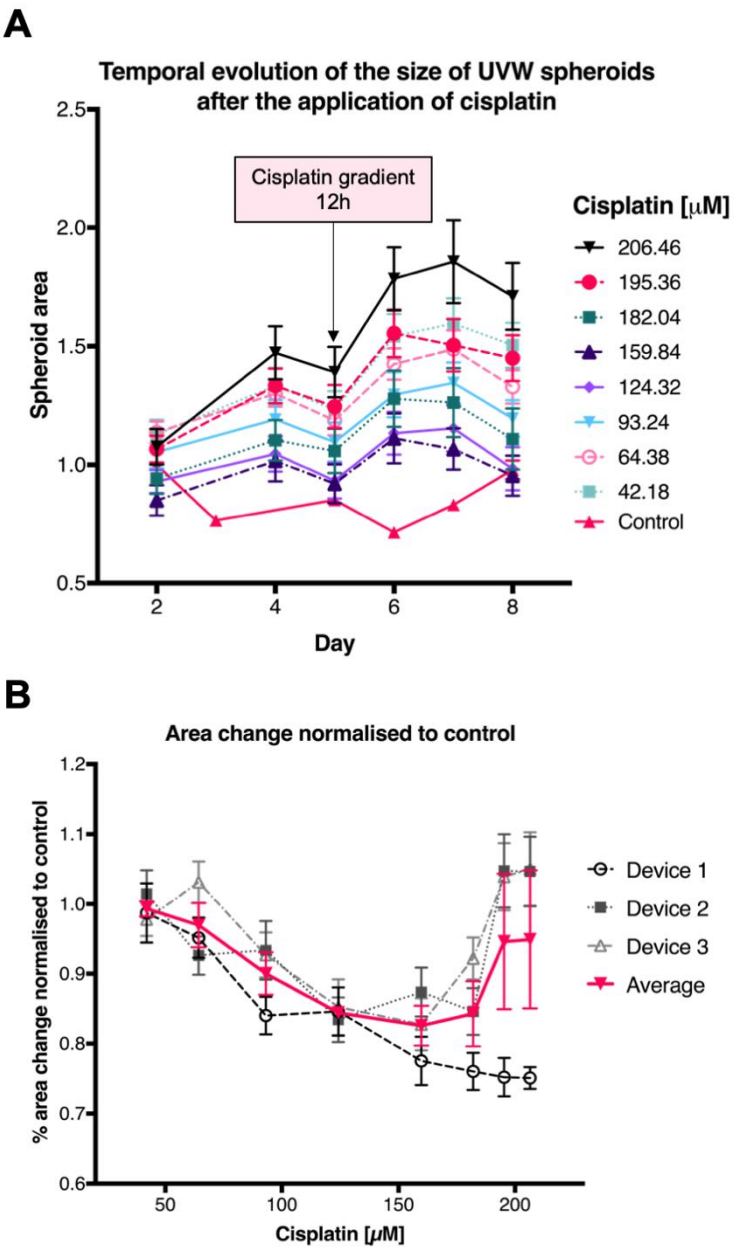

Figure 4.4 Changes in UVW spheroid size after cisplatin incubation

The size of UVW spheroids was recorded every 24-48 hours before and after exposure to a cisplatin concentration gradient (42.18 – 206.46 μM) on day 5 for 12 hours, shown here on the example of device 2. All values represent means of each row of spheroids ± S.E.M. and were normalised to the control. B) The area changes which occurred over the next 72h after drug application (AreaDay8/AreaDay5) was normalised to control. All values represent means ± S.E.M. (n=24 for each device). The variance within each device and between devices at high drug concentrations demonstrates the ambiguity of changes in spheroid areas, which can increase due to growth but also due to disaggregation.

in spheroid area that occurred over the three days in each spheroid was calculated using $Area_{Day8}/Area_{Day5}$ and normalised to the size change seen in a control device (**Figure 4.4B**). In all three devices, the spheroid size decreased in a concentration-dependent manner in rows 4-8 (42.1 -124.3 μM cisplatin). However, for cisplatin concentrations ≥ 159.8 μM the behaviour of the three devices deviated. In device 1, spheroid areas decreased with increasing cisplatin concentrations across the entire concentration range. Whereas in both device 2 and 3, UVW spheroids increased in size for higher cisplatin concentrations ranging from 182.0 – 206.5 μM.

Changes in spheroid size need to be evaluated carefully, since an increase in area could occur due to spheroid growth, but also due to disaggregation, which is frequently a part of cell death. In this device, due to the use of a shear-stress free flow for perfusion of drugs and medium, only few dead cells are washed out of the micro-wells and most dead cells remained in the micro-wells surrounding the intact spheroid. Using methods such as ultra-low adhesion plates or hanging drop plates, individual cells are easily agitated and removed during medium exchanges, and if they remain, they settle at the base of the well, which is not in the same focal plane as the remaining spheroid. Therefore, in this context spheroid size changes should be assessed in combination with additional readouts.

To investigate the origin of the observed size increase at cisplatin concentrations ≥ 159.8 μM in two of the devices, the area change recorded for each spheroid was adjusted for the disaggregation each spheroid had experienced by calculating ΔArea/ΔSF (**Figure 4.5**). By correcting the area change using the change in shape factor, larger shape factor changes occurring due to disaggregation would result in a larger correction of the measured area increase. In a healthy smooth spheroid, where the area change is positive and due to growth, correcting for a small change in shape factor will leave the area change unaffected. This correction reduces the differences between devices at higher concentrations (≥ 159.8 μM), however, the area changes in device 1 for cisplatin concentrations ≥ 159.8 μM still deviated significantly. A discrepancy in spheroid area change between the three devices, especially at higher drug concentrations could occur for several reasons. Firstly, there is the possibility of

dead cells being removed during medium exchange in device 1, where too high of a flow rate could wash out loose dead cells. The loss of dead cells could reduce the spheroid area further and explain the spheroid size changes observed at the three highest cisplatin concentrations. Secondly, experimental data suggests that fringe effects and fluctuations within the wells of each row are more likely to occur in the rows closest to microchannel inlets, namely row 1 -3 (≥ 159.8 µM cisplatin), resulting in fluctuations in readouts. However, in time-lapse experiments using fluorescent calcein gradients (Chapter 3), this error within each row was found to be negligible (<1%).

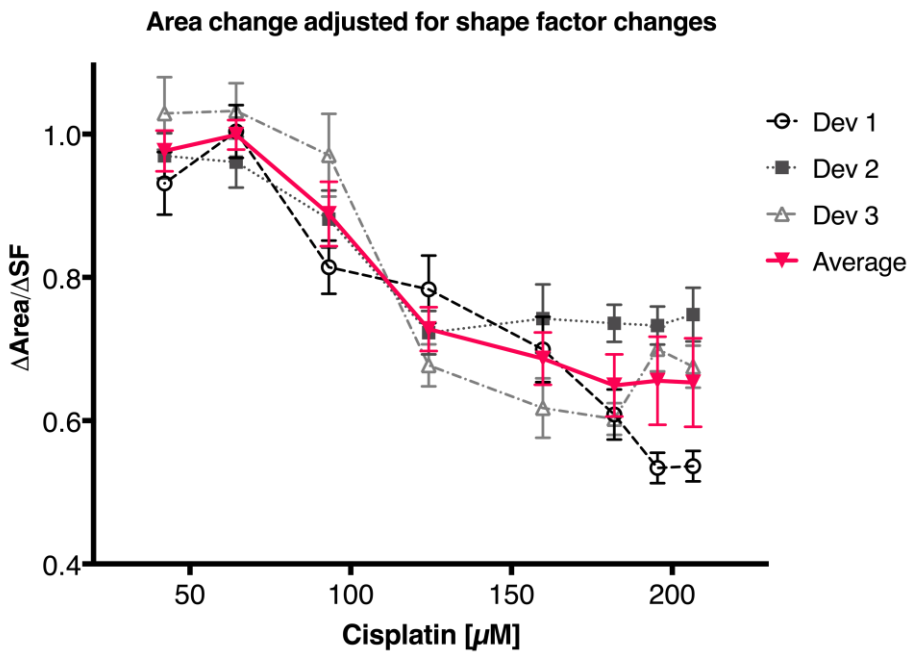

Figure 4.5 Adjustment of UVW spheroid area changes for shape factor changes

ΔArea/ΔSF describes the UVW spheroid size change recorded over the duration of the incubation with cisplatin, after adjustment for the extent of disaggregation which occurred at the same. Values represent means ± S.E.M. (n=24)

4.6 Viability of UVW spheroids after cisplatin incubation

The viable fraction was used as a third parameter to quantify the effect of various cisplatin concentrations on UVW spheroids. The remaining viable fraction (VF) of each spheroid describes the fraction of each spheroid post-treatment, which stained

positively after incubation with the viability dye (FDA), in comparison to its intact size before drug treatment. The viable fraction was calculated using each spheroid's area on day 5 and the FDA-positive area on day 8 as described in Chapter 2 (**Figure 4.6**).

By day 8, increasing cisplatin concentrations had resulted in a concentration-dependent reduction of the viable fraction of UVW spheroids in all three devices. The higher the applied estimated cisplatin concentration, the lower were the observed viable fractions, and for all cisplatin concentrations $\geq$ 64.4 μM the viable fraction was significantly lower ($P<0.0001$) when compared to control. At the highest cisplatin concentration of 206.5 μM, the viable area of the UVW spheroids was reduced to just 18.0 % of the spheroid area on day 5 (**Figure 4.6**). Overall, the effect of the cisplatin gradient on the viable fraction was very similar in all three devices, and the device means, and standard deviation did not differ significantly. Using the concentration-dependent decrease in viable fraction, an EC50 was determined for each device, as well as for the device mean (**Table 4.1**).

Table 4.1 EC50s of cisplatin activity in UVW spheroids obtained from various readouts

EC50s calculated from the shape factor, the viable fraction and the shape factor-corrected area change of UVW spheroids which were exposed to cisplatin for 12 hours and monitored for 3 days.

	SF_{EC50}	VF_{EC50}	$\Delta Area/\Delta SF_{EC50}$
Device 1	147.1	159.8	123.4
Device 2	154.50	129.7	99.0
Device 3	123.7	135.4	110.3
Device mean	141.8	141.6	105.1

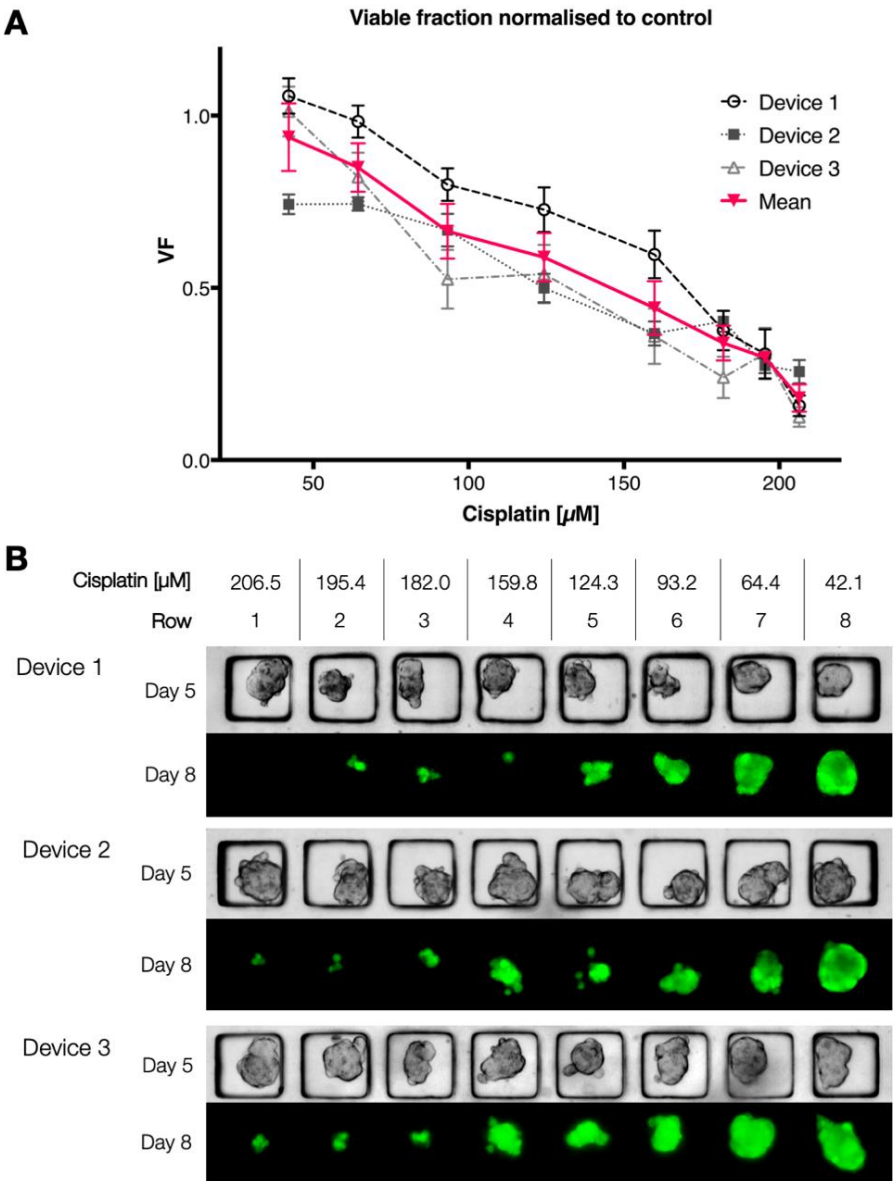

Figure 4.6 Viable fraction of UVW spheroids after exposure to cisplatin in 3 self-generating gradient devices

UVW spheroids were generated in 3 gradient-generating devices and exposed to a concentration gradient of cisplatin to assess the variability between microfluidic devices. A) Viability staining using FDA (live cells) and PI (dead cells) was conducted on day 8, and the remaining viable fraction in response to a range of cisplatin concentration was determined. Values represent means ± S.E.M. (n=24) conducted in 3 gradient-generating devices. B) Representative brightfield images of one column of UVW spheroids from each gradient-generating device were chosen: prior to the application of cisplatin on day 5, and fluorescent images of the FDA-stained remaining area on day 8, which were used to calculate the viable fraction. The FDA-positive area increased in all 3 devices with decreasing cisplatin concentrations along each column of UVW spheroids.

4.7 Combination of multiple parameters of spheroid health

In many studies, the spheroid size, either in form of the diameter, area or volume is used as the primary or only readout of spheroid health to create concentration-response curves and determine drug efficacies. However, since spheroid growth only remains a reliable readout if no significant changes in spheroid morphology occur, a separate descriptor of the shape of each spheroid was introduced (SF). Simultaneous changes in spheroid morphology and size can occur due to disaggregation and cell death, resulting in the dependence of the spheroid size on the spheroid morphology. To correct the impact of disaggregation on the spheroid size, the spheroid growth was adjusted for the extent of disaggregation which occurred over the same time period (**Figure 4.7B**) as described above. **Figure 4.7B** shows the spheroid area growth and the shape factor-adjusted spheroid growth, that were induced by a range of cisplatin concentrations. Both readouts remain near identical with increasing cisplatin concentrations $\leq$ 93.2 μM, but for cisplatin concentrations $\geq$ 124.3 μM the two curves progressively started to deviate, suggesting that with increasing cisplatin doses, the impact of the shape factor on the spheroid area change increased in UVW cells. In contrast to the area change itself, where no sigmoidal curve could be fitted to the data due to the variability at higher drug concentrations, the correction of the area change allowed the fitting of a sigmoidal curve, from which an EC_{50} of 105.1 μM was estimated (**Table 4.1**). The calculation and inclusion of this readout was a part of post-hoc analysis and its validity will need to be investigated further in the future. In order to incorporate this readout permanently in the analysis of spheroids generated in this microfluidic device, the behaviour of different types of cancer spheroids should be assessed to determine how frequently spheroid size changes affect the spheroid shape, and if the new parameter correlates with viability assessment across cell types. Spheroid responses can occur in the form of growth arrest, growth reduction, the induction of various types of cell death (which could affect morphology) or even growth, and the validity of this parameter should be assessed in all of these circumstances before widespread adoption.

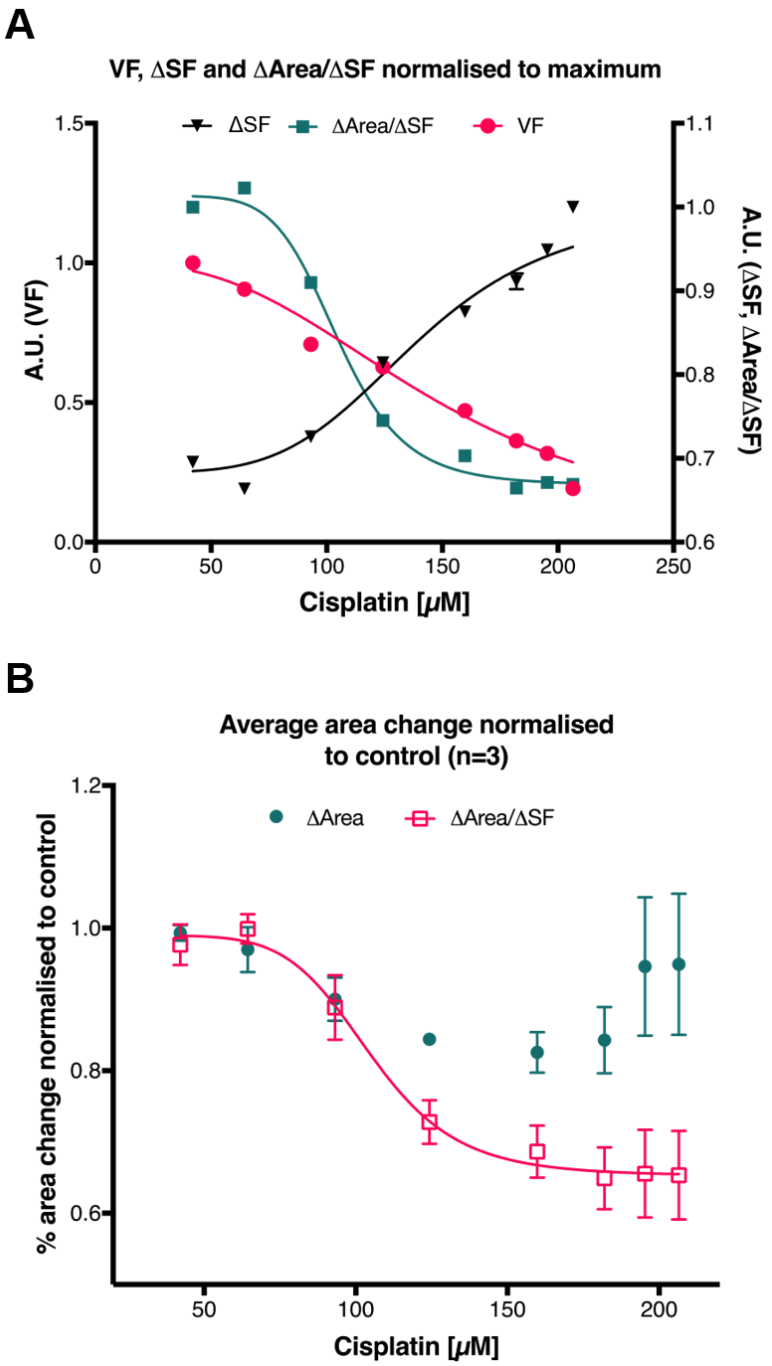

Figure 4.7 Multiple parameters used to determine drug effects on UVW spheroids

A) The mean viable fraction, shape factor changes, and shape factor-corrected area changes obtained from the application of cisplatin gradients were calculated and normalised to the maximum response. Values represent means of 3 devices, which contained 24 spheroids per drug concentration. B) Average area change recorded in three devices and the shape-factor corrected area change, dependent on increasing cisplatin concentrations. Values represent means ± S.E.M.

To further investigate the suitability of the shape factor as a readout for spheroid health, correlation analysis was conducted using Graphpad Prism and Pearson's correlation coefficient. (Thakuri et al., 2016) described the application of Pearson's correlation coefficient for quantification of the correlation between two readouts, which was applied to the shape factor, the area growth, as well as the viable fraction (**Figure 4.7A**). A strong negative correlation was observed between the viable fraction and the shape factor changes, with a correlation index of -0.98, which suggests that as a spheroid's shape factor increases, its viable fractions decreases in a highly correlative manner. The spheroid size change itself showed no correlation with the shape factor (correlation index = -0.30) or the viable fraction (correlation index = 0.34) in UVW spheroids, which is likely due to our observation that a size increase in UVW spheroids is not necessarily caused by proliferation. However, when the shape factor-adjusted area change was compared to the viable fraction, a strong positive correlation (correlation index = 0.94) was found, indicating that the viable fraction increases as the corrected spheroid growth accelerated. As expected, a strong negative correlation of the shape factor-adjusted area changes and the shape factor change was found (correlation index = -0.95), which is due to the equation used to calculate the shape factor-adjusted area change.

4.8 Comparison of drug efficacy data obtained from gradient-generating and single channel micro-well array devices

To further validate whether the correct concentrations of a drug were achieved in the gradient-generating devices, simultaneously, a device which contained just the cell culture channel and $W_{3,4}$ (single-channel channel micro-well array device) was used to grow UVW cell spheroids. These cell culture channels allowed the application of a solution of a fixed cisplatin concentration to the spheroid array. UVW spheroids were treated with cisplatin using the same protocol used for the gradient application (**Figure 4.1A**). After 5 days in culture, the UVW spheroids in each cell culture channel were treated with a different fixed concentration of cisplatin (0, 29.4, 71.5, 101.2,

155.5, 183.7 µM) for 12 hours. After 12 hours, all drug solutions were washed out, and the UVW spheroids were monitored for a further 3 days in culture, when they were stained using PI and FDA to determine cell viability. The brightfield images were processed, analysed, and the mean shape factor changes were plotted in relation to the range of cisplatin concentrations applied in **Figure 4.8B**. Both the concentration-dependent shape factor and viability staining (**Figure 4.8A**) matched the data generated using a cisplatin concentration gradient.

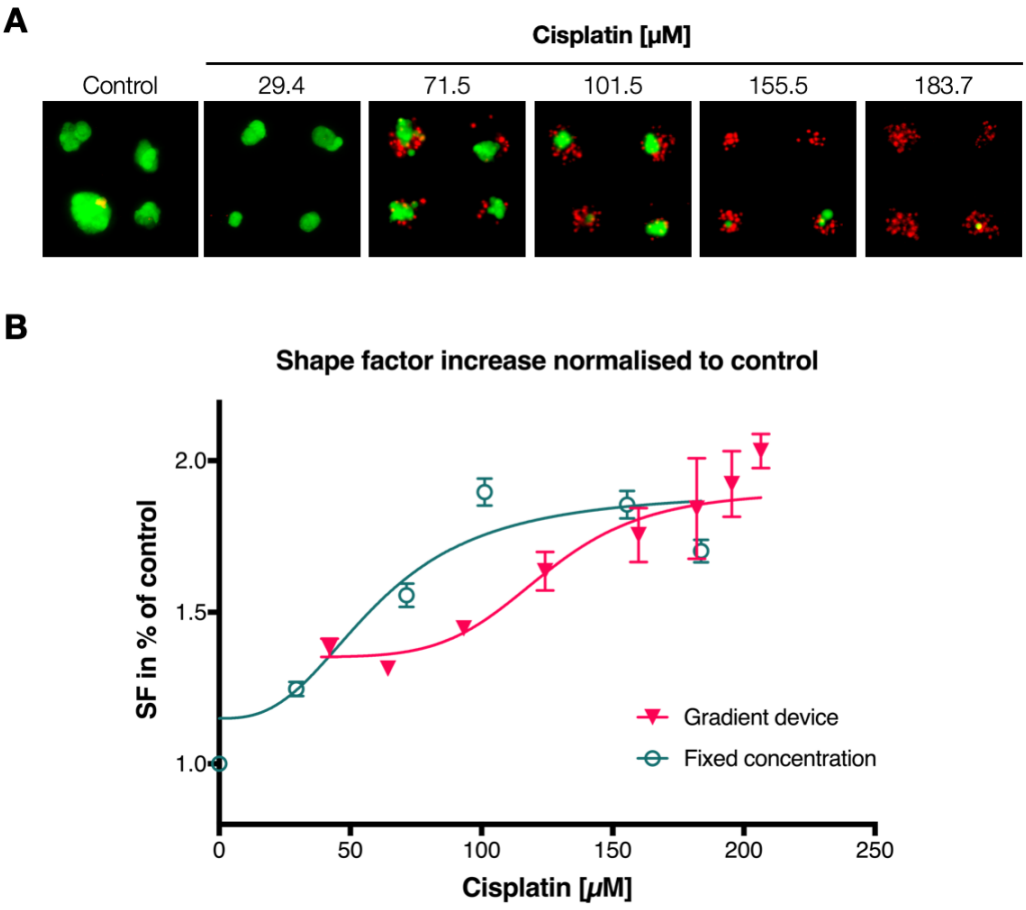

Figure 4.8 Comparison of viable fraction and shape factors of cisplatin-treated UVW spheroids

A) UVW spheroids were treated with fixed concentrations of cisplatin (0, 29.4, 71.5, 101.2, 155.5, 183.7 µM) for 12 hours. Viability staining using PI and FDA was conducted at the end of the experiment and representative images of stained UVW spheroids were chosen. B) The shape factor changes observed after exposure to cisplatin in gradient-generating devices and after application of fixed concentrations were compared and found to be similar.

5 Optimisation of biopsy-derived spheroid generation and culture in microfluidic devices

5.1 Introduction

Due to increasing interest in personalised and precision medicine treatments of cancer, research has turned towards patient-derived tissue in recent years. Patient-derived tissue, either in form of resections or biopsies, provides the advantage of containing a heterogeneous cell population of several cell types, as well as the native extracellular microenvironment, which is thought to provide a more realistic cancer model than cell lines and simple co-cultures. A further aim of this project was to validate the screening capabilities of the microfluidic platform by using biopsy derived 3D tumour models. To achieve this fresh prostate cancer biopsy tissue was expanded in culture to obtain a heterogeneous cancer-cell rich population. These cells were then used to create biopsy-derived spheroids or tumouroids. The terminology around 3D tumour models is still not entirely clear, although publications such as Weiswald et al. have attempted to clearly define and name various spherical cancer models (Weiswald et al., 2015), terms such as tumorospheres, tumoroids and spheroids are still used interchangeably in the literature. However, as per Weiswald et al. spherical tumour models derived from heterogeneous single-cell suspensions of primary tissue could be coined biopsy spheroids, patient-derived spheroids, tumour spheres or tumouroids. These patient-derived 3D models were used to test several drugs, which are commonly used in prostate cancer patients, and to compare their efficacy, as a proof-of-concept screening on primary tissue. The following chapter describes the optimisation of culture conditions required for the generation of biopsy-derived spheroids in the microfluidic platform described in this work.

5.2 Culture requirements of primary prostate tissue

The culture of patient-derived prostate tissue has been carried out in the form of organ culture of human primary prostate tissue for almost 50 years now (Schrodt and

Foreman, 1971; Stonington and Hemmingsen, 1971), and has mainly relied on the use of tissue derived from prostate tumours and benign prostatic hyperplasia (BPH). According to Pretlow et al., (1995) in order to increase the success of prostate organ culture, it was recommended that the resected tissue is immediately placed in cooled saline or culture medium. Despite all efforts, the culture of benign prostate tissue was not successful at the time, and heterogeneous cell populations couldn't be maintained in culture over time (Pretlow et al., 1995). It was reported that prostate explants easily grew out and expanded when cultured in serum-containing medium, while maintaining viable glandular epithelial cells for weeks. Stromal cells on the other hand, atrophied and died during explant culture (Stonington and Hemmingsen, 1971). Since then, the culture of primary prostate tissue has evolved, and is now mainly focused on the maintenance of putative prostate and cancer stem cells in culture. Although the identity and presence of prostate cancer stem cells in prostate tumours remains unclear (Li and Shen, 2019), the culture of primary prostate tissue in conditions which favour stem cells, has yielded promising results in recent years. Growth conditions originally used for the generation of colon organotypic organoid cultures were adapted to include prostate-specific growth factors, such as fibroblast growth factor-10 (FGF10), dihydrotestosterone (DHT) and prostaglandin E2 (PGE2), as well as the ROCK inhibitor Y-27632 and epidermal growth factor (EGF) (Chua et al., 2014; Karthaus et al., 2014; Drost et al., 2016). This resulted in the generation of organotypic structures, of which some recapitulated in vivo prostate morphology, which could be maintained viably in culture for several months (Gao et al., 2014). Several of these studies included the use of serum (Härmä et al., 2010; Chua et al., 2014; Karthaus et al., 2014) and utilised Matrigel as a source of basement membrane extract (BME) at various concentrations to support organoid health. These organoid cultures however did not aim to support the culture of stromal cells, such as fibroblasts, which rely on the growth factors contained in fetal bovine serum. Therefore, in order to achieve the generation of a cancer cell-enriched single-cell suspension, which still contained stromal cells, elements of several studies were incorporated. Initially, the medium composition was adapted from (Chua et al., 2014; Karthaus et

al., 2014), but also included the addition of serum in order to sustain stromal cells. In parallel to organoid culture, patient-derived explant culture of prostate tumours had shown successful maintenance of several cell types within resected tumour tissue for short periods of time, by utilising 10% serum-supplementation (Centenera et al., 2018). By maintaining a heterogeneous cell population throughout the duration of culture, this model would provide similar components to in vivo prostate tumours. The culture conditions for the culture and expansion of the initial biopsy tissue were optimised by S. Patek in Dr Edward's lab, which allowed successful expansion of the biopsy tissue. Once expanded, the biopsy tissue would eventually be dissociated to form a single-cell suspension, which could be seeded into the microfluidic gradient-generating device. In order to allow the formation of patient-derived spheroids from the heterogeneous cell suspension in the microfluidic platform, the appropriate culture conditions were optimised to enhance tumoroid formation. Initially, it was decided to incorporate a form of basement membrane extract (such as Matrigel), since the majority of studies only appeared to show the successful maintenance of patient-derived cancer and cancer stem cells in the presence of matrigel. Although the project did not aim to generate patient-derived organoids, which contain high numbers of stem cells, the maintenance of a cancer and stem cell population amongst other stromal cell types in the patient-derived spheroids was considered crucial, due to their impact on the tumour microenvironment and their role in tumour resistance and recurrence (Li and Shen, 2019). Therefore it was decided to attempt the incorporation of BME at a low percentage (5%), as described by Chua et al. (2014), to enhance the ability of the biopsy-derived cells to aggregate. Additionally, the growth medium was supplemented with serum initially, in order to maintain the resident fibroblast populations in culture over time.

5.3 BME and serum supplementation for the culture of patient-derived spheroids in microfluidic devices

Cells derived from 4 patient biopsies were used for initial tests to determine the ideal conditions used for the generation of tumour-derived spheroids from single cells in the microfluidic platform. Various terms have been used to describe tumour biopsy-derived spheroids, such as “organotypic spheroids”, “primary spheroids”, “tumorospheres” and “tumouroids”, although a universally accepted nomenclature has not been established (Weiswald et al., 2015). For the purpose of this thesis, tumour biopsy-derived spheroids will be referred to as such or as “tumouroids”. The medium used for expansion and subsequent cell culture in microfluidic devices contained all supplements listed in Chapter 2, except for cholera toxin. Additionally, FBS was used to supplement the medium, since the goal was to not just enrich the cancer cell population, but also to maintain a population of heterogeneous cell types. Using serum-supplemented medium without the addition of choleratoxin, three variations of culture conditions were considered for the first four patient biopsies, which involved either the addition of 2.5% or 5% of basement membrane extract (BME) in the form of Matrigel into the culture medium, or the culture in medium alone. All samples were assessed microscopically before the start of each experiment, to confirm that several cell types were present in the expanded biopsy cultures. A single-cell suspension was created, and cells were seeded into microfluidic devices, as described in Chapter 2. Cells of all 4 sample donors (PC01-PC04) formed aggregates within approximately 24 hours (**Figure 5.1**). In most micro-wells a tumoroid formed next to individual cells, of which some but not all integrated into the aggregates by the end of the experiment on day 7 of culture. On day 7, viability staining was conducted with FDA and PI, which showed that the majority of tumoroids were viable and contained only few dead cells (**Figure 5.1**).

In all patient cultures and in all culture conditions, which included the culture in medium alone and medium with the addition of 2.5% and 5% of BME, despite the high degree of viability, the number of the remaining spheroids on day 7 was reduced. The decrease in spheroid numbers was particularly pronounced in biopsy spheroids which

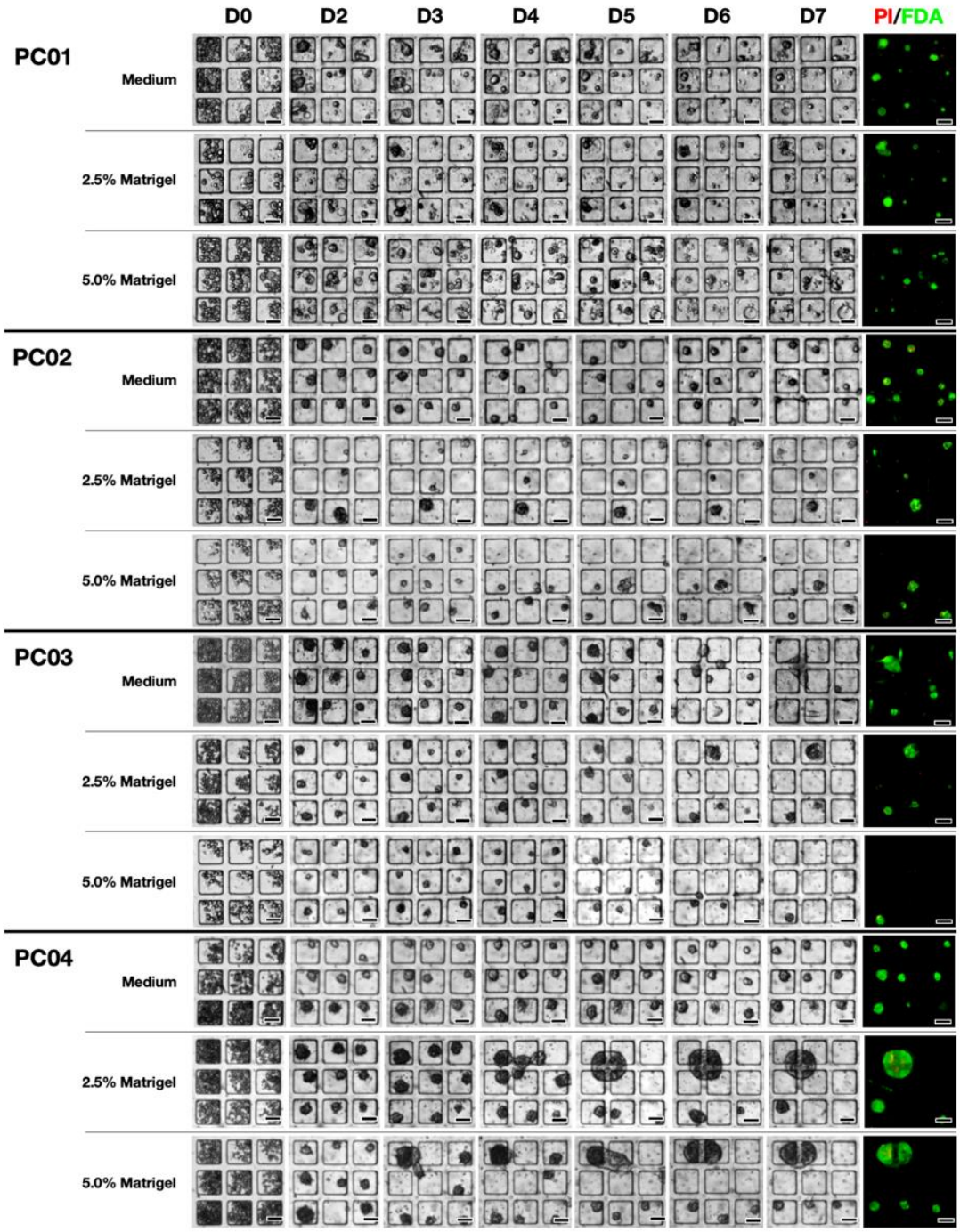

Figure 5.1 Generation of patient-derived spheroids using serum-containing medium and BME supplementation

Cells derived from 4 prostate biopsies (PC01-PC04) were exposed to culture in medium, and medium supplemented with 2.5 and 5% of Matrigel for 7 days, throughout which brightfield images were acquired every 24-48 hours. On day 7 of culture, viability staining was conducted using the fluorescent dyes FDA and PI, and the remaining tumoroids were imaged using fluorescence microscopy. Brightfield and fluorescent images of 9 representative tumoroids of each patient sample and each culture condition are shown at various time points (D0-D7). Scale bars = 100µm

were maintained in 2.5 or 5% of BME in medium (**Figure 5.2**). This appeared to result when individual spheroids from separate micro-wells aggregated together to form large colonies. Additionally, single cells were able to attach to the internal device surface which enabled their migration out of separate micro-wells. This reduced the

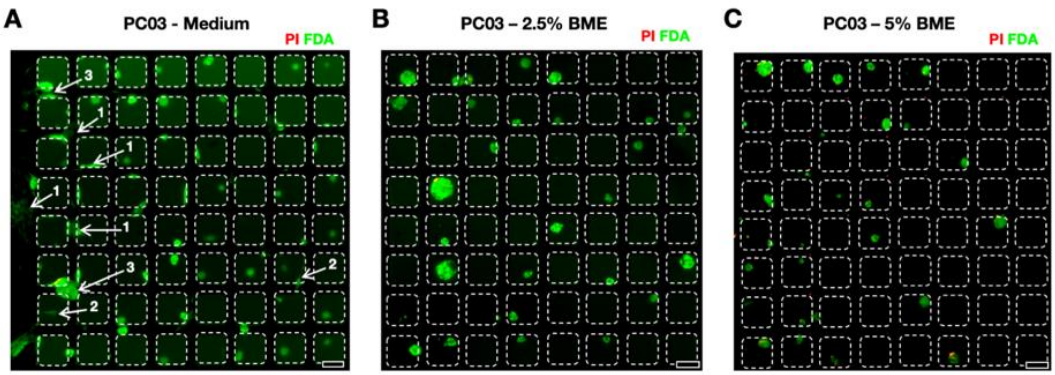

Figure 5.2 The effect of BME supplementation on patient-derived spheroids

A) Viability stain (FDA and PI) of PC03 tumoroids after 7 days in culture with medium, and medium supplemented with 2.5 % BME (B) and 5% BME (C). Arrows display examples of cell morphologies observed: 1 – Flattened cells, 2 - Spindle-shaped cells, 3 – Merging tumoroids. All scale bars = 100µm

number of remaining spheroids available for analysis drastically, effectively reducing the number of remaining tumoroids. The attachment of individual cells and spheroids to the device surface was observed to varying degrees. In the PC03 samples, cells in almost 50% of microwells were found to have attached over time, many displaying a flattened out or spindle-shaped morphology and more than 30% of tumoroids had merged into larger clusters, irrespective of the supplementation with BME (**Figure 5.2A**). However, rising concentrations of BME in the culture environment seemed to affect PC03 cells in two ways: firstly, the addition of BME appeared to reduce the number of cells found attached to the device surface with a flattened out or spindle-shaped morphology (**Figure 5.2B**). Secondly, BME supplementation further increased the number of migrating and merging PC03 tumoroids. **Figure 5.3** shows examples of attached single cells as well as the migration of tumoroids observed in brightfield images over the duration of culture, for which the path of spheroid migration was tracked and plotted as line overlays. This tendency of spheroids to migrate and merge

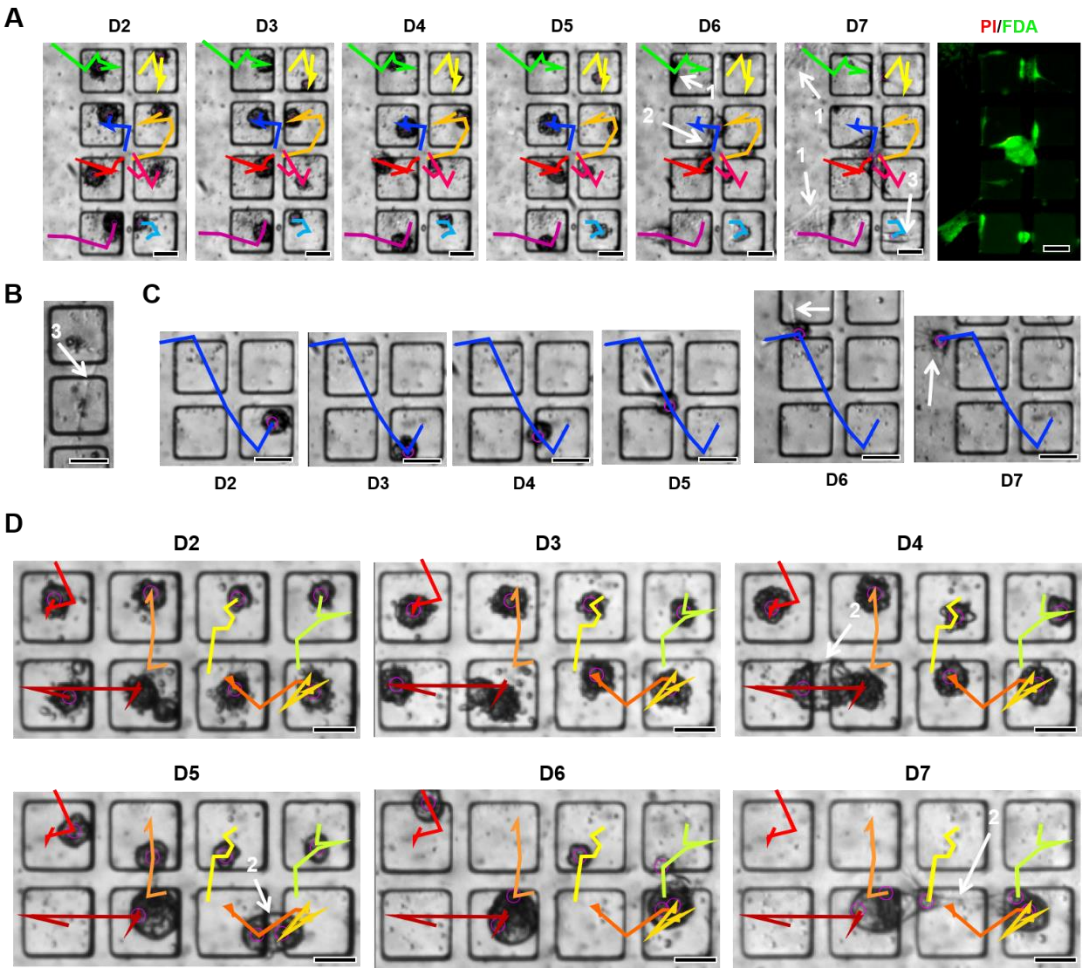

Figure 5.3 Flattened cells and migration of biopsy-derived tumoroids in the presence of BME

A-D) Representative brightfield images of PC03 cells over 7 days in culture, line overlay displays migration tracks over culture duration. A) Brightfield images and fluorescent images after viability stain of PC03 cells over the duration of culture in medium, white arrows display: 1 – Flattened cells, 2 – Merging tumoroids, 3 – Migrating tumoroid. B) PC01 cells migrating across micro-wells on day 6 of culture. C) PC02 tumoroid migrating, attaching and flattening out over 7 days maintained in 2.5% BME, white arrows highlight attachments of spheroid to the device surface. D) PC04 tumoroids migrating and merging over 7 days in culture with 2.5% BME, arrows highlight merging spheroids. All scale bars = 100µm

was also observed in two other patient samples, PC02 and PC04. When maintained in medium, both samples produced distinct compact aggregates, of which a small number (<10%) had migrated out of their individual micro-wells by day 7 (**Figure 5.3C, D**). However, when maintained in 2.5 and 5% Matrigel, the number of cells which flattened out on the device surface and migrating spheroids increased. In fact, cells

derived from the PC04 sample showed the most extreme extent of tumoroid migration and merging (**Figure 5.4**). In the majority of micro-wells in each array of wells, the supplementation with 5% of BME appeared to promote the attachment of tumouroids to the device surface and to other tumoroids, resulting in the formation of a small number of large masses (**Figure 5.4).** Overall, in 3 out of 4 of the patient-derived tumouroid cultures, the addition of BME seemed to result in the exacerbation of cell and spheroid migration. This was not the case for tumouroids generated from PC01. PC01 tumoroids did not aggregate as quickly as the remaining 3 samples, and formed small, looser aggregates, which did not appear to grow or merge to a significant extent. Individual, flattened and attached cells were found in all three culture conditions, but their number was not increased by the addition of BME to the culture medium. Further, although a small number of migrating and merging spheroids were found, the supplementation with BME did not appear to affect this.

In summary, there was little variation in the viability of the tumoroids observed on day 7, independent of culture conditions, although PC01 spheroids showed the least growth, adhesion, migration and a slightly diminished viability in comparison to the other 3 samples. Although single, flattened or spindle-shaped, adhering cells occurred without supplementation of BME, tumoroid merging was increased by the addition of BME in 3 out of the 4 samples, which was an unexpected observation. Previous to these experiments, the migration and merging of tumouroids to the extent as shown in **Figure 5.4** had never been observed in this platform during the culture of cell line-derived spheroids. At the time, this behaviour was attributed to the presence of a significant number of fibroblasts within the population, which could explain the contraction of merged aggregates into a single large one (Figure 5.4). Since the extent of migration and merging observed was highly unusual, future cultures were monitored closely in order to detect and monitor these behaviours. Possible explanations for the increased tumouroid migration and merging will be discussed in **section 5.5**.

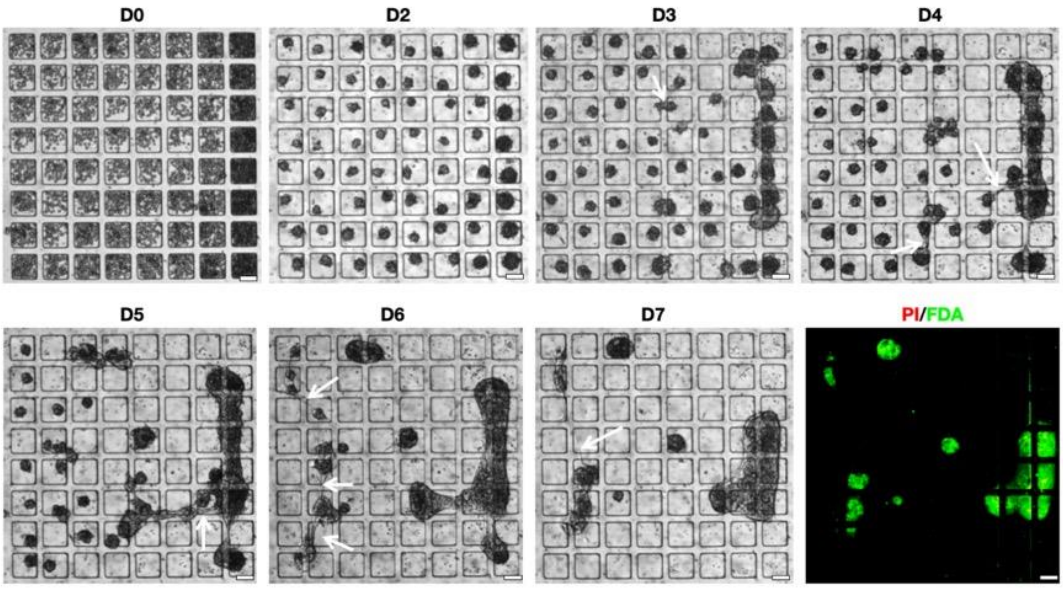

Figure 5.4 Merging of biopsy-derived tumouroids after BME supplementation

PC04 cells were cultured in medium, supplemented with 5% BME, over a period of 7 days. Brightfield images taken every 1-2 days show the formation of tumoroids, cell attachments to the device surface, followed by migrating and merging tumoroids. Viability staining using FDA and PI was conducted on day 7. All scale bars = 100µm

To confirm whether this behaviour was consistent, this experiment was repeated with the passaged cells of each sample that remained in the flask after the first harvesting (P3, passage 3). Unfortunately, the diversity of the P3 culture had declined at this point, and the majority of cells observed in the flask had a distinct fibroblast-like morphology. Most cells were long aligned spindle-shaped cells, and only very few small colonies of cobble-stone-shaped and flattened out epithelial cells remained, in comparison to the original expanded culture. This suggested that the fraction of fibroblasts contained in the initial biopsy had likely proliferated much faster than the cancer cells, and the goal of the generation of a cancer-cell enriched population was not met. The presence of an extensive fibroblast population could explain the large number of attached cells and tumoroids, which appeared to migrate easily and over long distances. When the experiment was repeated using P3 cells, the majority of cells appeared to migrate and cluster to a similar extent as observed in the P2 cells. The behaviour of the cells and tumoroids generated from each patient remained

consistent between the two experiments. As before, supplementation with BME produced an increase in migration and merging as shown above.

The frequent migration and merging of tumoroids had considerable consequences for the analysis and purpose of the microfluidic assay, both in terms of data throughput and difficulties in imaging. In standard conditions, spheroids rest inside the microwells in a similar focal plane, facilitating microscopy and image acquisition. After several days of migration of tumoroids across microwells, along the ceiling and surface of the microfluidic device, the majority of cells were distributed across different focal planes, and several images must be acquired to capture the majority of tumoroids accurately, complicating image analysis and decreasing automation of operation. Therefore, the loss of the majority of trackable spheroids due to migration is not acceptable for the effective operation of the microfluidic assay.

5.4 Effect of serum-free culture medium and choleratoxin on the culture of prostate biopsy-derived tumouroids

Further optimisation of the culture conditions was required to reduce the fibroblast population and the migration of cells and tumoroids within the microfluidic device. In order to reduce the population of fibroblasts, several adaptations were made to the culture medium. Firstly, fetal bovine serum was removed from the culture medium, since it is the main driver that fibroblast proliferation relies on in vitro. Additionally, the changes induced in fibroblasts during serum culture are known to result in the promotion of various processes, such as migration and differentiation (Winkles, 1997; Iyer, 1999), which are not desired in the cultures in these experiments. Secondly, cholera toxin subunit B was added to the culture medium, in order to limit the proliferation of fibroblasts selectively, without toxicity to cancer cells (Eisinger and Marko, 1982; Bennett et al., 1987). In more recent studies involving human tumour samples, cholera toxin has been added routinely to restrict fibroblast proliferation, in order to allow the isolation of near pure cancer cell populations from various types of patient tumours (Kodack et al., 2017; Tomonobu et al., 2019). Lastly, a decision

was made to remove Matrigel supplementation for the duration of the culture of the cells inside the microfluidic devices. Despite the positive effects of Matrigel on the proliferation and outgrowth of primary tissues and explants (Kleinman and Martin, 2005; Chua et al., 2014), even at very low concentrations (2.5 and 5%), this was responsible for the extensive migration and association of tumoroids.

In order to assess the effect of the optimised selective medium, three further prostate biopsy samples were used to test the generation and culture of biopsy-derived tumoroids. The first two samples (PC05 and PC06) were eventually found to have originated from benign prostate disease, while the third (PC07) was confirmed to be prostate cancer, after histopathological examination of the patient biopsies was completed.

5.4.1 Serum-free culture of spheroids generated from benign prostate tissue

The first sample cultured in the new serum-free, BME-free conditions with cholera-toxin was PC05, which resulted in the generation of several morphologies. In all devices, cells adhered to the device surface, although the extent of this varied considerably even within each device channel. For example, the two arrays of tumoroids shown in **Figure 5.5** were found within the same microfluidic device channel and were situated right next to each other. Whereas cells adhered as soon as the first day of culture in array A, in array B the majority of spheroids remained in their individual micro-wells ,and the extent of cell adhesion was less by day 3, at which point viability staining was conducted on several device channels (**Figure 5.5**). All stained devices showed a high degree of viability, with only few dead PI-positive cells observed in each array of tumoroids. By day 3, the majority of individual cells had either aggregated into a solid tumoroid or had started to adhere to the device surface, as shown in the example of **Figure 5.5**. Over the following days, the extent of cell adhesion increased further and cells managed to spread along the walls of the micro-wells,

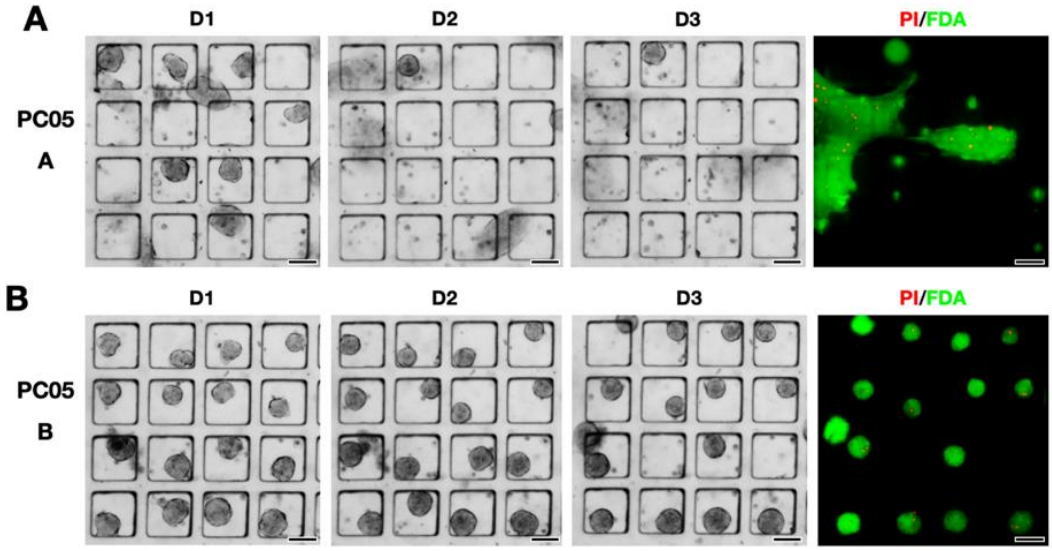

Figure 5.5 Heterogeneous morphologies observed in the same device in serum-free cultures of benign prostate-derived spheroid without BME supplementation

PC05 cells cultured in the presence of cholera toxin and absence of serum for 3 days in a microfluidic device channel which contained four arrays of micro-wells. A) and B) are representative arrays of micro-wells, located adjacent within the device channel. Viability staining using FDA and PI was conducted on day 3. All scale bars = 100µm

attached to the surface of the ceiling of the cell culture channel, and formed far-reaching connections to other tumoroids (**Figure 5.6**). While luminated structures had not developed by day 3, several luminated tumouroids had developed by day 9, when viability staining was conducted (**Figure 5.6.C-E)**.

This experiment was again repeated with the next passage (P3) of outgrown cells from the biopsy tissue, firstly to test if the tumoroid generation was possible again and secondly, if the morphology of the P3 tumoroids would be consistent with the P2 tumoroids. Further, the culture duration was extended, to determine how long the cultured tumoroids would remain viable in the microfluidic device. A large number of the P3 cells of the PC05 sample appeared to aggregate into small round tumoroids during the first 48 hours, although some loose cells remained. However, from day 2 on, again, cells and tumoroids attached to the surface of the micro-wells and migrated and merged for the remaining duration of the experiment. On day 10, viability staining was conducted, which showed that cell viability was somewhat

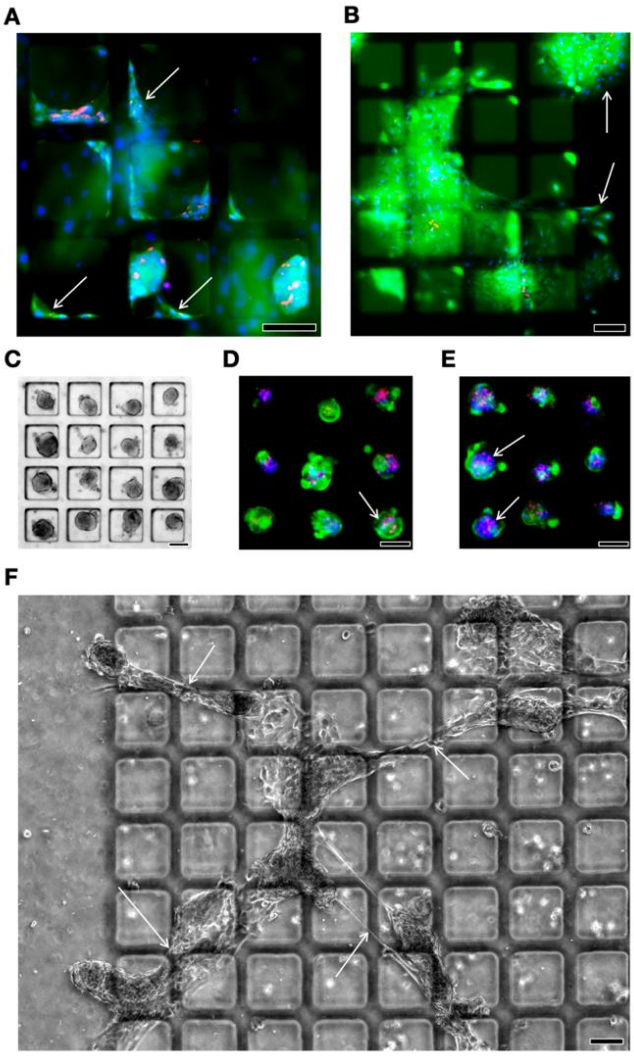

Figure 5.6 Patient-derived spheroids show a variety of morphologies in serum-free culture conditions

PC05 cells cultured in the presence of cholera toxin and absence of serum for 9 days in a microfluidic device, when viability staining using FDA, PI and Hoechst33324 was conducted. A) Viability staining of cells adhering to the walls of the micro-wells (highlighted by white arrows). Faint nuclear stain across the device is due to attached cells on the ceiling of the cell culture channel. B) Viability staining of cells attached to the device ceiling, of which some have flattened out, which are highlighted by white arrows. C) Brightfield image of PC05 tumoroids as observed on day 9. D) Viability staining of solid and luminal (see arrow) PC05 tumoroids on day 9. E) Viability staining of luminal PC05 tumoroids on day 9 (see arrow) F) Phase contrast image of PC05 tumoroids forming far-reaching connections with other tumoroids (see arrows). All scale bars = 100µm

diminished when compared to P2 cells, and large clusters of dead cells were observed within tumoroids (**Figure 5.7**). Further, the number of distinct non-migrating tumoroids was significantly less than in the P2 cells, and the majority of the tumoroids that had formed, appeared solid in viability staining, without the presence of lumen that were found in P2 cells by day 9 **Figure 5.7C-D**. Overall, the heterogeneity between the morphologies observed within the P3 cells of the PC05 sample was reduced, and some formations, such as the luminated tumoroids were not found. The loss of heterogeneity in morphology between the passages suggests that the composition of

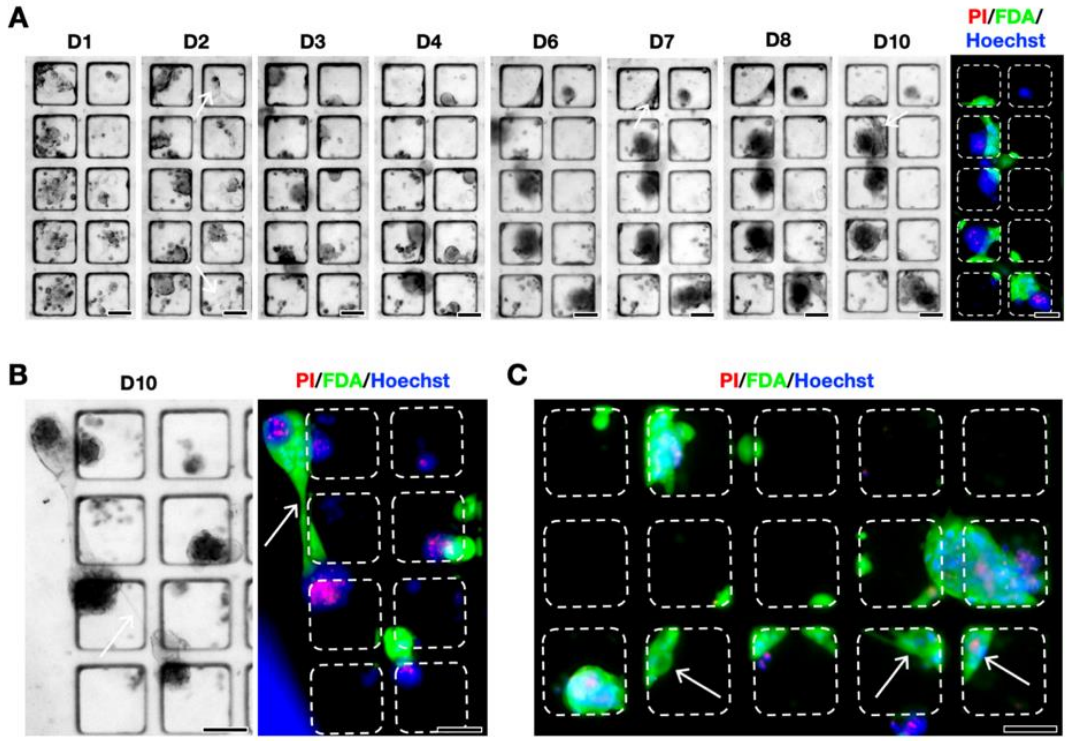

Figure 5.7 Culture of P3 cells derived from biopsies of benign prostate disease in serum-free conditions

Cells of the third passage (P3) of PC05 were used to generate tumoroids in microfluidic devices and were monitored using brightfield imaging throughout the culture duration of 10 days. On day 10 viability staining using FDA, PI and Hoechst33324 (nuclei) was performed. A) Representative brightfield images of tumoroids generated from P3 cells of PC05 are shown over duration of culture, with corresponding fluorescent images of viability staining. B) PC05 tumoroids adhering to micro-well structures, migrating and merging across the array of micro-wells. C) PC05 cells attached to the side walls of the micro-wells and migrating tumoroids. Scale bars = 100µm

the culture likely changed over time. A further reason for this might be found in the original composition of the biopsy sample, as histopathology results later confirmed that the patient (PC05) did not have prostate cancer, but instead a benign growth. Without the presence of cancer cells, which this medium composition aimed to selectively amplify, the cultures mainly consisted of fibroblasts and normal types of prostate cells, such as intermediate cells. Several studies have shown that the propagation of benign prostate tissue is possible using the conditions described here, due to the presence of intermediate cells in healthy prostate tissue (Chua et al., 2014; Gao et al., 2014). However, they also show that the proliferation of benign prostate tissue reduced when compared to the corresponding prostate tumour cells (Gao et al., 2014). Therefore, it is possible that the composition of the P3 cells had shifted towards fibroblasts, explaining the change in morphology observed between the P2 and P3 of PC05. However, in the P3-derived cultures several aggregates containing two distinct separate cell populations were observed within the same micro-well (**Figure 5.7A, B, Figure 5.8B**), which suggests that a number of benign cells were likely maintained in culture, along with the resident fibroblasts. The separation of fibroblast and cancer populations into distinct tumour cell aggregates which are attached to spindle-shaped migrating cells has previously been shown in co-cultures of primary CAF and cancer cells on Matrigel (Pankova et al., 2016).

Cells derived from a second sample (PC06), which originated from benign prostate tissue, were seeded into single-channel micro-well array devices. P2 cells derived from PC06 started to form aggregates in the majority of all micro-wells by day 2. Most micro-wells contained a solid aggregate as well as a number of loose cells. In this case, no cell attachment was observed and no tumoroids were found to migrate and merge. On day 4, viability staining was performed in several devices using FDA, PI and Hoechst33324 (nuclear stain), which showed that small and larger aggregates mostly contained live cells (**Figure 5.8**). On day 10, viability staining was repeated in the remaining devices, however at this point, larger aggregates appeared to have died, although they remained attached to small viable compact aggregates within the same

micro-well (**Figure 5.8B**). By day 10, no adhesion of cells or tumoroids to the device surface was found.

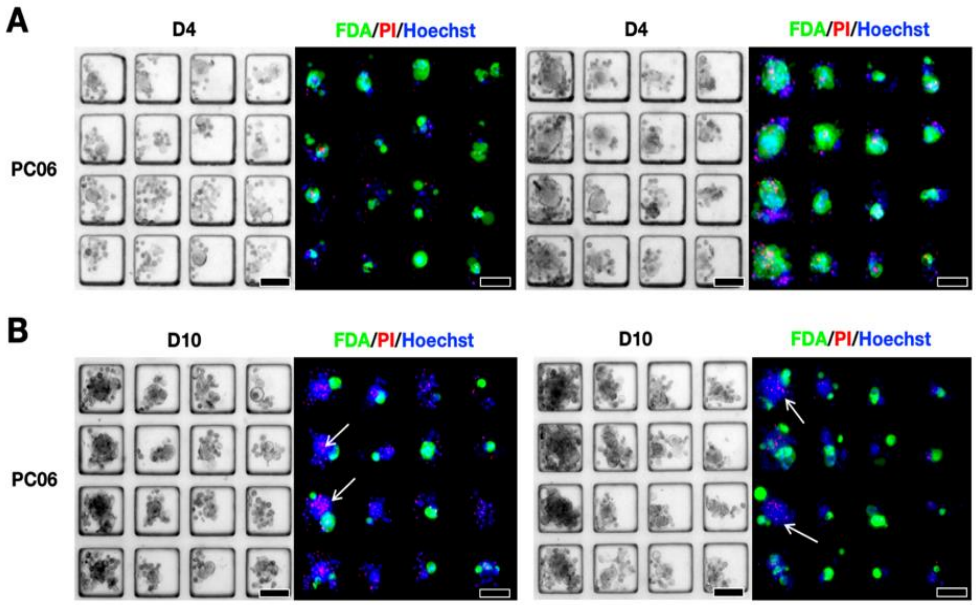

Figure 5.8 Viability and morphology of patient-derived benign tissue spheroids

Cells derived from PC06 were used to generate tumoroids in microfluidic devices Representative brightfield images and fluorescent images after viability staining using FDA, PI and Hoechst33324 on day 4 of culture (A), and on day 10 (B). Arrows highlight dead aggregates. Scale bars = 100µm

5.4.2 Serum-free generation of spheroids from prostate cancer biopsy tissue

A further biopsy sample of PC07-derived cells was received, which were later confirmed to have originated from a prostate tumour. Initial morphological assessment of PC07-derived cells in the flask showed the presence of several different cell types with various morphologies (**Figure 5.9**). A large number of epithelial-like cells were found, which varied in size and were arranged in a honeycomb-shaped pattern (**Figure 5.9A-C**). Present in the same sample were spindle-like cells, which were either interspersed between epithelial cells or interweaved with other spindle-like cells (**Figure 5.9A**), which were most likely fibroblasts. Therefore, in this case the criterium of a heterogeneous cell population enriched for cancer cells, was met.

Once seeded into single-channel micro-well array devices, the majority of cells aggregated into solid or luminal tumoroids of a range of sizes within 3 days of culture in medium free from serum and BME supplementation (**Figure 5.10A)**. Throughout the duration of culture, some aggregates developed a lumen, as shown in **Figure 5.10 A,D,F**, which grew over time. Approximately 30% of tumoroids in micro-wells showed the presence of a lumen, whereas the remaining micro-wells contained solid organoid-like structures or loose cells. The majority of loose cells, which were not attached to an aggregate were determined to be dead cells during viability staining

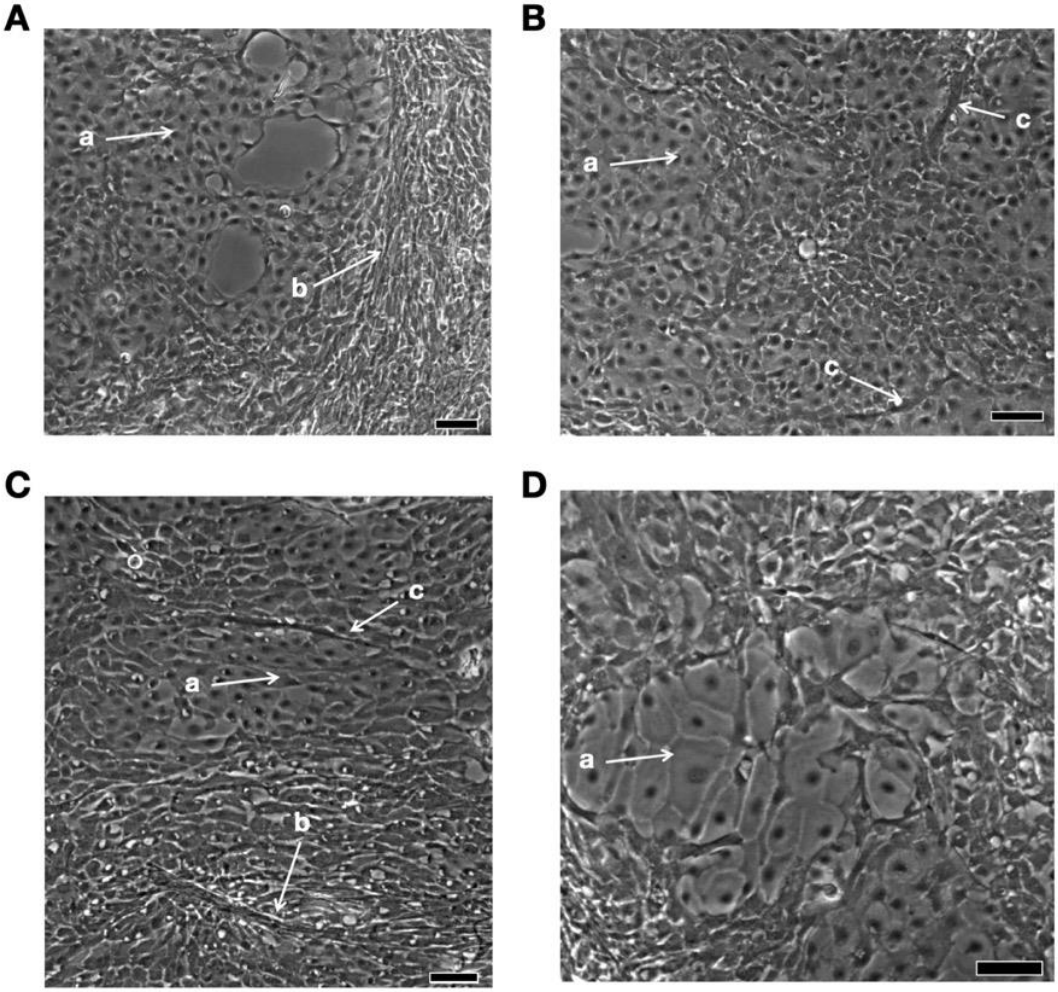

Figure 5.9 Phase contrast images of PC07 biopsy-derived cells in culture on Matrigel.

A-D) PC07-derived cells were expanded in T75 flasks on Matrigel, showing a variety of morphologies, highlighted by white arrows: Polygonal epithelial-like cells arranged in a honeycomb-pattern (a), adjacent to interweaved aggregates of aligned spindle-like cells (b). Individual spindle-like cells were found surrounded by or to surround epithelial-like cells (c). All

conducted on day 7 of culture (**Figure 5.10B**). Cells arranged in acinar-like luminar structures with a thicker outer layer of cells (**Figure 5.10B**), luminar structures with a thin outer layer of cells (**Figure 5.10F**) and solid tumoroids showed positive FDA staining, which indicated good cell viability (**Figure 5.10C**). The formation of luminated structures, similar to acini, is not unusual during the culture of primary prostate cells, due to the glandular nature of the tissue of origin, although the maintenance of the initial tissue morphology usually requires the presence of Matrigel (Chua et al., 2014; Dolega et al., 2015; Pankova et al., 2016).

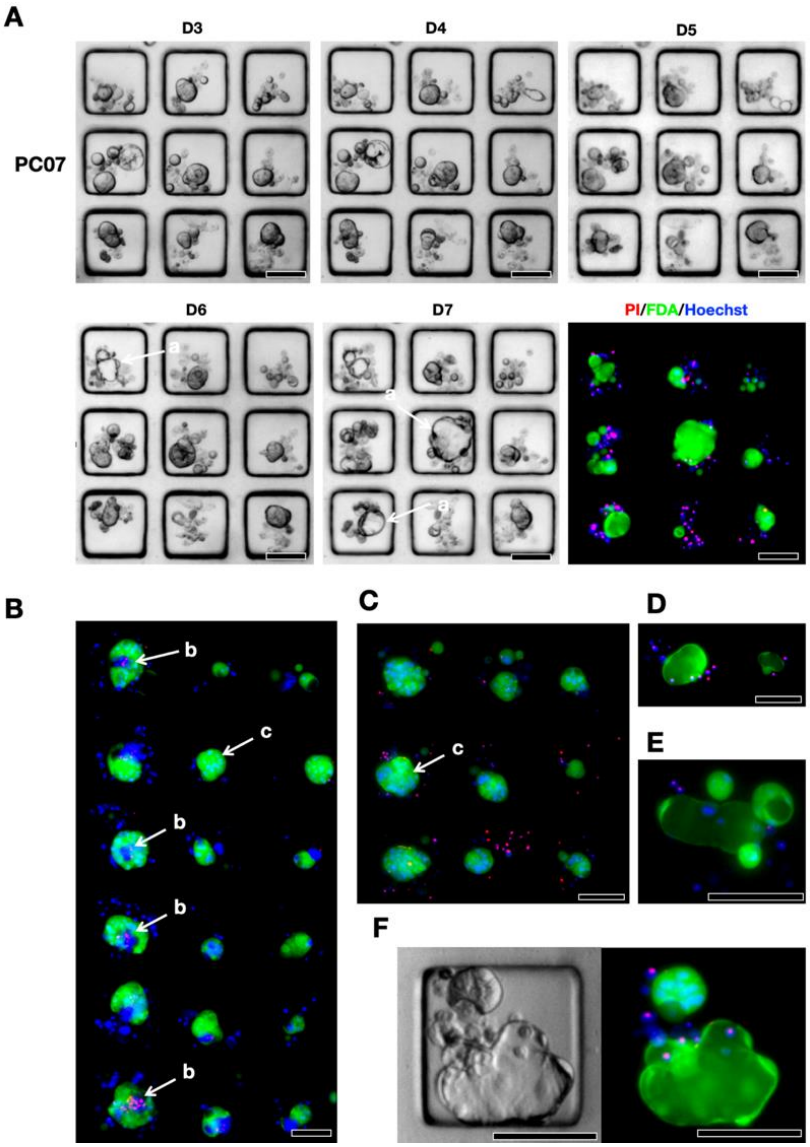

Figure 5.10 Prostate cancer biopsy-derived tumoroids were cultured in serum-free and BME-free conditions in microfluidic devices

PC07-derived cells were cultured in microfluidic device, where A) shows brightfield images of a fixed area within the micro-well array over the culture duration of 7 days, after which viability staining using PI, FDA was conducted with the nuclear stain Hoechst33324. Fluorescent images of viability staining showed B) the presence of lumen within larger aggregates, which were surrounded by a thick layer of cells (b). C) Solid tumoroids were the most commonly aggregate type (c). D-E) Brightfield and fluorescent images of viability staining of aggregates which contained lumen but had not developed a thick outer cell layer. F) Organoid-like tumoroid with a large empty lumen, next to an acinar structure. All scale bars = 100µm

5.5 Summary of preliminary experiments for the optimisation of the generation of tumoroids from prostate biopsy tissue

Out of seven biopsy samples received, four cultures appeared to be dominated by fibroblasts (PC01-PC04), two cultures were determined to have originated from benign disease (PC05 & PC06) and one culture was derived from a diagnosed prostate tumour (PC07). Single-cell suspensions were generated from all seven prostate biopsy samples (PC01-07) and used for the generation of tumoroids in microfluidic devices. Irrespective of culture conditions, all samples generated solid aggregates within 2-3 days, which remained viable for up to 10 days. Aggregates generated from PC06 showed a distinct separation between two spheroidal cell populations in several micro-wells. This separation was visible in brightfield images and fluorescent images and is frequently seen in the co-culture of cancer cells and fibroblasts (Zoetemelk et al., 2019). Only one of the aggregates in each well appeared to remain viable over time (**Figure 5.11A**). Other morphological features of the aggregates generated involved the formation of a lumen, which was seen in PC05 and PC07-derived cells. In tumoroids from both samples, fluorescent images after viability staining suggested the presence of an outer cell layer, which encased a lumen, that was either filled with DNA and dead cells (**Figure 5.11B, C**), or completely empty (**Figure 5.11D**). A summary of the biopsy samples used and the associated morphology of the biopsy-derived spheroids is provided in **Table 5.1**.

Several difficulties were encountered during initial experiments to optimise culture and experimental conditions, such as: 1) the overpopulation of fibroblasts which emerged over time in culture, 2) the adhesion of cells to the microfluidic device, 3) extensive cell and tumoroid migration, sometimes resulting in the merging of tumoroids, and 4) the variations in biopsy samples received.

Fibroblast proliferation appeared to be greatly amplified in cultures PC01-PC04, which were initially maintained in the presence of serum, as well as the growth factors and supplements listed in Chapter 2. In order to reduce the fibroblast population and to allow the establishment of a cancer cell-enriched culture, serum was removed

from the cell culture medium. Furthermore, cholera toxin, a supplement known to limit the proliferation of fibroblasts but not cancer cells, was added to the culture medium. After these changes, fibroblasts still appeared in the cultures, but next to extensive epithelial cell populations (**Figure 5.9**). This suggests that the removal of serum and the addition of choleratoxin aided in the limitation of fibroblast proliferation.

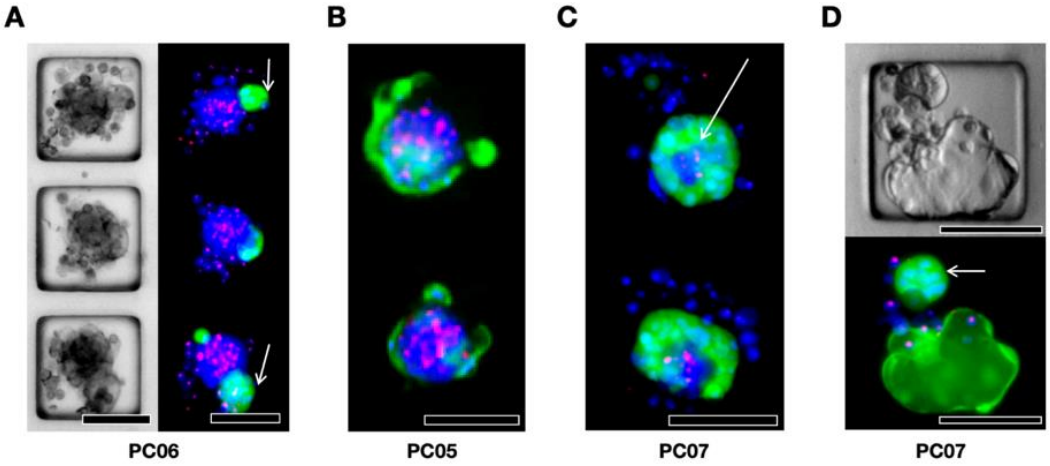

Figure 5.11 Spheroids generated from prostate biopsy tissue demonstrate a morphological variety

A) Tumoroids formed from PC06 cells show distinct separate aggregates (arrows) within the same micro-well, which are shown in brightfield images and after viability staining using PI, FDA and Hoechst33324. B) PC05 cells, when cultured in microfluidic devices, formed aggregates, which appeared luminal with a thin outer cell layer and were filled with DNA and dead cells. C) PC07 cells produced luminal structures with different morphologies. They formed luminal structures, some of which resemble acini (arrow), where thick cell layer surrounds a mostly empty lumen, which contained DNA and dead cells. D) In other micro-wells, PC07 cells grew into organoid-like luminal structures with completely empty lumen (arrow shows acinar structure). All scale bars = 100µm

The adhesion of cells to the device surface, which was seen in four out of the seven samples (PC01-PC05) appeared to be worsened by the addition of a small percentage of BME to the culture medium in PC01-PC04. One possible reason for the increased adhesion seen with BME is the failure of the cell- and protein-repellent Synperonic coating, due to the precipitation of BME onto the surface. Increased adhesion could also be a result of the interaction of the cells in the population with BME. Culturing

primary cells in the presence of BME was previously shown to do induce adhesion as well as migration, which was also found to be increased when PC01-PC04 were cultured with BME, and particularly so in PC04 (**Figure 5.4**).

The migration of individual cells and groups of cells in spheroids was a further problem encountered during preliminary experiments (**Figure 5.3**). It presented problems for the automated imaging of large numbers of tumoroids, due to the migration out of the shared focal plane of each micro-well array. Furthermore, the position of each tumoroid could not be tracked automatically over time, since tumoroids migrated across micro-wells and changed positions in the array. Migration in conjunction with frequent tumoroid merging, reduced the number of tumoroids that could be analysed from each device. Considering the aim of this device, which is to quantitatively assess the effect of cytotoxic agents in biopsy-derived tumoroids, where only few cells are available. In this context, the loss of quantifiable tumoroids to migration and merging had to be avoided. Therefore, we did not continue the use of Matrigel-supplementation for the generation of patient-derived tumoroids. In cultures without Matrigel (PC05-PC07), adhesion of single cells was still seen to a significant extent in tumoroid cultures generated from PC05, but not in the PC06 and PC07.

The migration and merging of tumoroids was an unexpected observation, which was initially attributed to the addition of BME into the culture medium. Fibroblasts, when embedded and cultured within Matrigel have been shown to contract, form vessels and large spheroid-like aggregates. New research involving cancer cell and fibroblast co-cultures within Matrigel has shown that fibroblasts will initially group together and form vessels, which the cancer cells begin to adhere to. Eventually fibroblasts are able to encapsulate any cancer cells within a Matrigel droplet (Méhes et al., 2019; Zhang et al., 2020), which reflects the findings during these experiments. However, it is surprising to observe the same behaviour in the absence of Matrigel embedding, with only 2.5% supplementation or no supplementation at all (PC05). One possible reason for the invasive morphology of the fibroblasts could lie in the medium composition, which included FGF2. FGF2 has been shown to induce migration in breast cancer-associated fibroblasts expressing FGFR1 and 2 (Sumbal and Koledova, 2019).

Table 5.1 Summary of biopsy samples, associated culture conditions and resulting morphologies

Seven prostate biopsies (PC01-PC07) were expanded, disaggregated into single cells and used to generate patient-derived tumoroids, which were exposed to several different culture conditions, with the aim of optimising the culture environment required for the maintenance of a cancer cell-enriched heterogeneous cell population. Several different morphologies were observed in the resulting tumouroids. CT choleratoxin, N.d. not determined

Sample	Source	Culture conditions	Adhesion & migration	Lumen	Separation of cell populations
PC01	n.d.	+ BME + serum - CT	Yes	No	No
PC02	n.d.		Yes	No	No
PC03	n.d.		Yes	No	No
PC04	n.d.		Yes	No	No
PC05	Benign	- serum + CT	Yes	Yes	Yes
PC06	Benign		No	No	Yes
PC07	Prostate cancer		No	Yes, acinar and organoid-like	Yes

The biopsy tissue itself also introduced a number of variables, since the composition of the biopsy-generated tumoroids is affected by variation due to the initial biopsy source (benign vs cancerous tissue), the composition of the biopsy and the effect of the selective medium. In general, prostate biopsies mainly contain epithelial cells, normal and neoplastic, and stromal cells, such as fibroblasts. The biopsy samples of PC01-PC04 contained large numbers of fibroblasts, which could have been a result of the initial composition of the biopsy, or the culture conditions during expansion which included serum and may have amplified fibroblast proliferation. In later cultures a fibroblast population was maintained, but an over-proliferation exceeding the proliferation of cancer cells, was not observed again. This suggests that independent

of the initial biopsy composition, fibroblast proliferation can be controlled with selective medium. In the biopsies of benign disease, PC05 and PC06, other cell types, such as normal prostate epithelial cells were present, which resulted in differing morphologies. Although both biopsies produced solid round tumoroids, a separation of cell populations was observed inside of a large number of micro-wells. For PC05 tumoroids, this presented as round aggregates, in which a thin layer of viable cells surrounded a lumen filled with a dense aggregate of dead cells (**Figure 5.11B**). PC06 on the other hand, showed the formation of two or more attached aggregates, which were discernible in brightfield images as well as in viability staining, where only one of the aggregates remained viable (**Figure 5.11A**). A clear separation between the stromal and epithelial components of cocultures has previously been shown in prostate cancer derived 3D co-cultures, but also other tumour types, such as breast cancer (Pankova et al., 2016; Horman et al., 2017; Zoetemelk et al., 2019). This cellular organisation mimics the tissue organisation in vivo, where ductal compartments of epithelial cells are surrounded by stromal cells (Krušlin et al., 2015). As a result, prostate cancer can be very diffuse and consist of several foci surrounded by healthy tissue (Krušlin et al., 2015). PC07 cells, derived from a prostate tumour, showed the development of acinar and organoid-like structures(**Figure 5.11C,D**) and no indication of an overgrowth of fibroblasts in the culture, which suggests that the selective medium resulted in a cancer cell-enriched heterogeneous cell population. Therefore, the serum-free primary prostate medium supplemented with choleratoxin was determined to be suitable for future tumoroid generation experiments. However, in order to confirm this, further experiments were necessary to determine the composition of the aggregates created from biopsy tissues. RT-qPCR analysis would be conducted after future experiments to confirm the expression of PSA and the presence of cancer cells, using several prostate cancer biomarkers, as described in Chapter2.

6 Drug screening of prostate biopsy-derived tumoroids using a self-generating microfluidic concentration gradient

6.1 Experiment concept

Biopsies of two different prostate cancer patients (PC08 and PC09) were used to generate tumoroids in order to determine the suitability of the microfluidic concentration gradient device for drug efficacy testing of biopsy-derived tumoroids. As described before, initially, both biopsies were expanded for two weeks, after which a single cell suspension was created, and the biopsy-derived cells were seeded into microfluidic devices. Tumoroids were allowed to form for 3 days, after which drug concentration gradients of several drugs were applied for 12 hours. Alongside the experiment in microfluidic devices, RT-qPCR was performed to determine if the expanded sample contained prostate cancer cells, by quantifying the expression of androgen receptors (AR), the prostate-specific androgen (PSA or KLK3) and alpha-methyl-acyl-CoA racemase (AMACR), which are commonly used biomarkers for prostate cancer (Frame et al., 2016). Viability staining was performed at several time points throughout the experiment. Four drugs were chosen for initial proof of principle experiments to: enzalutamide, abiraterone, docetaxel, as well as cisplatin.

Enzalutamide is an orally administered drug which is frequently used in advanced prostate cancer, which acts by inhibiting androgen binding to the androgen receptor (AR) and the translocation of the androgen receptor to the nucleus, as well as the transcription of AR signalling (McCrea et al., 2016; Crona and Whang, 2017). Either alone or in combination with docetaxel, enzalutamide has been shown to improve survival and slow disease progression (Litwin and Tan, 2017). Whilst being well-tolerated, enzalutamide resistance eventually appears to develop in patients, approximately 3.4 months after treatment start (McCrea et al., 2016). In patients, 160 mg enzalutamide is taken orally every day in the form of tablets, which according to pharmacokinetic studies achieves an average maximum plasma concentration of 3.4 µg ml^{-1} after a single dose, although it took approximately 28 days to reach steady state at a peak concentration of 14.5 ± 3.3 µg ml^{-1} (Gibbons et al., 2015). In in vitro studies

assessing the effect of enzalutamide in a 3D context, the administered enzalutamide concentrations ranged from to 5-200 µM (Eder et al., 2016; Hainline et al., 2019; Linxweiler et al., 2019). In this study, enzalutamide concentrations of up to 184 µM were applied to patient-derived spheroids.

Similar to enzalutamide, abiraterone also interferes with the androgen signalling of tumour cells, where it blocks the intra-tumoral and adrenal biosynthesis of androgens, such as testosterone, which can drive tumour growth. The reduction in androgen synthesis results in smaller amounts of circulating androgens to bind to androgen receptors. Abiraterone is frequently used in clinic for the treatment of metastatic prostate cancer, where it has been shown to prolong significantly progression-free survival, however, resistance develops after approximately 4.8 months (McCrea et al., 2016; James et al., 2018). As with enzalutamide, patients take abiraterone daily orally at a dose of 1g. The activity of abiraterone in a 3D in vitro models has only been assessed in a small number of publications, with applied concentrations reaching up to 20 µM (Mosaad et al., 2018; Linxweiler et al., 2019), although research suggests that central androgen inhibition cannot be modelled sufficiently in 3D in vitro models. Interestingly, Mosaad et al. not only showed that concentrations of up to 20 µM did not appear to affect the viability of prostate spheroids and even seemed to enhance the metabolic activity of spheroids, but not monolayers (Mosaad et al., 2018). For this experiment, initially a concentration range of 16-94 µM was chosen for the abiraterone treatment.

Docetaxel is a chemotherapeutic agent of the taxane group, which induces apoptosis in cancer cells by inhibiting microtubule disassembly during mitosis and inhibition of Bcl-2 (Herbst and Khuri, 2003). In clinic, docetaxel was the first drug found to confer a significant survival benefit to patients with metastatic androgen-independent (castration-resistant) prostate cancer (Petrylak et al., 2004; Tannock et al., 2004). To this day, docetaxel is a commonly used treatment for advanced prostate cancer. However, studies indicate that only 50% of patients respond to docetaxel treatment, and resistance is ultimately developed (Hwang, 2012). In patients, docetaxel is usually given intravenously at the start of each treatment cycle, which usually takes 21 days,

with doses ranging from 60-100 mg m^{-2}, which result in plasma concentrations ranging from 5 – 10 µg L^{-1} (Clarke and Rivory, 1999). In vitro toxicity assays conducted on 3D cultures of prostate cancer cell lines showed that cell death can occur at concentrations as low as 10 nM (Chambers et al., 2014), whereas organoids appear to be less sensitive and higher concentrations of up to 10 µM were required to exert cytotoxic effects (Kim et al., 2019). Therefore, a relatively high concentration range of docetaxel was selected, which ranged from 9-107 µM initially.

Cisplatin has cytotoxic effects in many solid tumour types, which it exerts by creating DNA-adducts, that result in the formation of inter- and intra-strand crosslinks. Currently, cisplatin is not indicated for use in patients with prostate cancer. However, in clinical trials of patients with advanced prostate cancer cisplatin only had moderate effects, and only resulted in a PSA response in 20% of unselected patients who received cisplatin monotherapy (Hager et al., 2016). Additionally, cisplatin treatment was associated with significant toxicity, especially in combination with other chemotherapy agents. In the clinic, cisplatin is administered to patients daily intravenously for up to five days per treatment cycle, with 20 mg being the most commonly used dose (Urien and Lokiec, 2004). A pharmacokinetic study of 43 patients showed that cisplatin doses ranging from 20-80 mg resulted in plasma concentrations ranging from 124–2790 ng ml^{-1}, with a mean plasma concentration of 800 ng ml^{-1} (Urien and Lokiec, 2004). In vitro toxicity assays conducted on spheroids derived from two cell lines, in microfluidic devices, that were exposed to cisplatin for 48 hours, demonstrated EC_{so}s of 84 and 75 µM (Ruppen et al., 2014). Additionally, data obtained from earlier experiments using the self-generating gradient device (Chapter 4) showed that UVW cells, although sensitive to cisplatin, had a fairly high EC_{50} of approximately 140 µM after 12 hours of exposure (**Table 4.1)**. As a result of these considerations, cisplatin was initially applied in the following experiment using a concentration gradient ranging from 21-103 µM.

To conclude, in the context of the cytotoxicity testing of prostate cancer-derived tumoroids of PC08 and PC09, cisplatin was unlikely to affect tumoroid growth and viability. As for abiraterone, since its effect in patients is partially due to the reduction

in circulating androgens, the developed in vitro model may not be suitable for the demonstration of the complete mechanism of action of abiraterone. In this tumoroid model, it was expected that only the intra-tumoral androgen synthesis could be modelled and inhibited. The success of abiraterone treatment of the biopsy-derived tumoroids therefore depends on each individual's state of disease progression, and whether intra-tumoral androgen synthesis had started to increase at the time of biopsy. Therefore, it is uncertain if abiraterone treatment could result in the observation of cytotoxic effects in the tumoroids derived from PC08 and PC09. However, both docetaxel and enzalutamide had the potential to inhibit tumour growth and viability in these tumoroids.

6.2 Generation of biopsy-derived spheroids in microfluidic gradient-generating devices for drug efficacy testing

The biopsy tissue of both PC08 & PC09 was initially expanded on Matrigel for 2 weeks, after which morphological assessment of the expanded biopsies confirmed the presence of multiple cell types before cells were harvested from the expanded biopsies. In both expanded biopsies, an outgrowth of spindle-shaped cells, sheets of epithelial-like cells and small clusters of aggregates were observed (**Figure 6.1**).

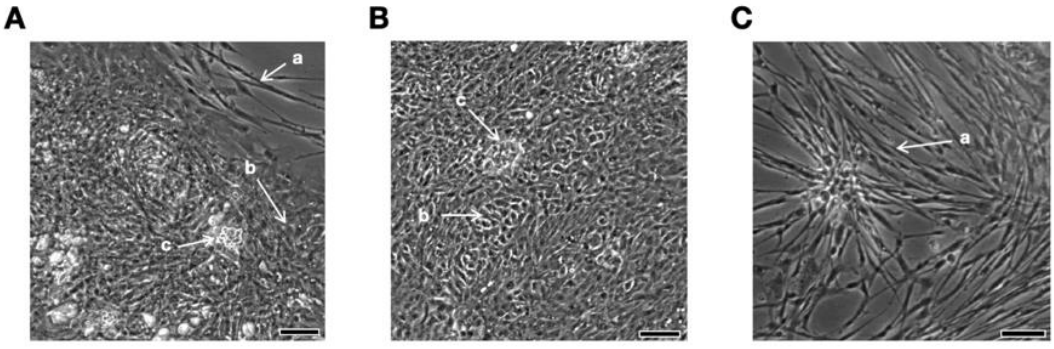

Figure 6.1 Phase contrast images of the expanded biopsy tissue of PC08 for morphological assessment

A-C) Phase contrast images of the expanded PC08 biopsy on the day of passage, showing the presence of several different cell types, such a spindle-shaped cells (a), small clustered cuboidal or polygonal cells growing in a single sheet or in multiple layers (b), and the formation of three-dimensional tumoroid-like aggregates. Scale bars = 100µm

A single-cell suspension was generated from both biopsies, which was seeded into gradient-generating microfluidic devices for drug efficacy testing. The number of devices that could be seeded depended on the outgrowth and expansion of each biopsy. Cells derived from PC08 were seeded into 22 gradient generating devices (of two different micro-well sizes, 150 and 250 µm), whereas PC09 cells were seeded into 13 devices. All tumoroids were monitored every 24 hours by brightfield microscopy, which showed that 24 hours after seeding, solid, smooth aggregates had formed inside all micro-wells, where they were maintained for up to 12 days (**Figure 6.2A**).

Over the duration of culture, the majority of PC08 tumoroids in control conditions started to develop a complex glandular morphology, and lumen formation was observed as early as day 9 of culture. On day 3 of culture, before the tumoroids were exposed to drugs, viability staining of a control device showed compact solid viable tumoroids, with only few lumen present (**Figure 6.2B**). By day 12 viable tumoroids were present in almost all micro-wells and more than 50% of tumoroids contained lumen or protrusions of proliferating cells, which were observed in brightfield and fluorescent images (**Figure 6.2**). These images were processed, analysed and the size and shape change of every tumoroid was determined over the duration of culture. The area of PC08-derived tumoroids increased steadily from day 3 onwards and by day 12 the area of tumoroids in control conditions had increased by 35.9% (**Figure 6.3A**). During this area growth, the spheroid shape factor of the PC08 tumoroids initially remained unchanged until day 8, however by day 12, the shape factor had increased significantly (**Figure 6.3**). A size increase in combination with an increasing shape factor coincides with the observation of the increasing development of tumoroids with complex morphology over time.

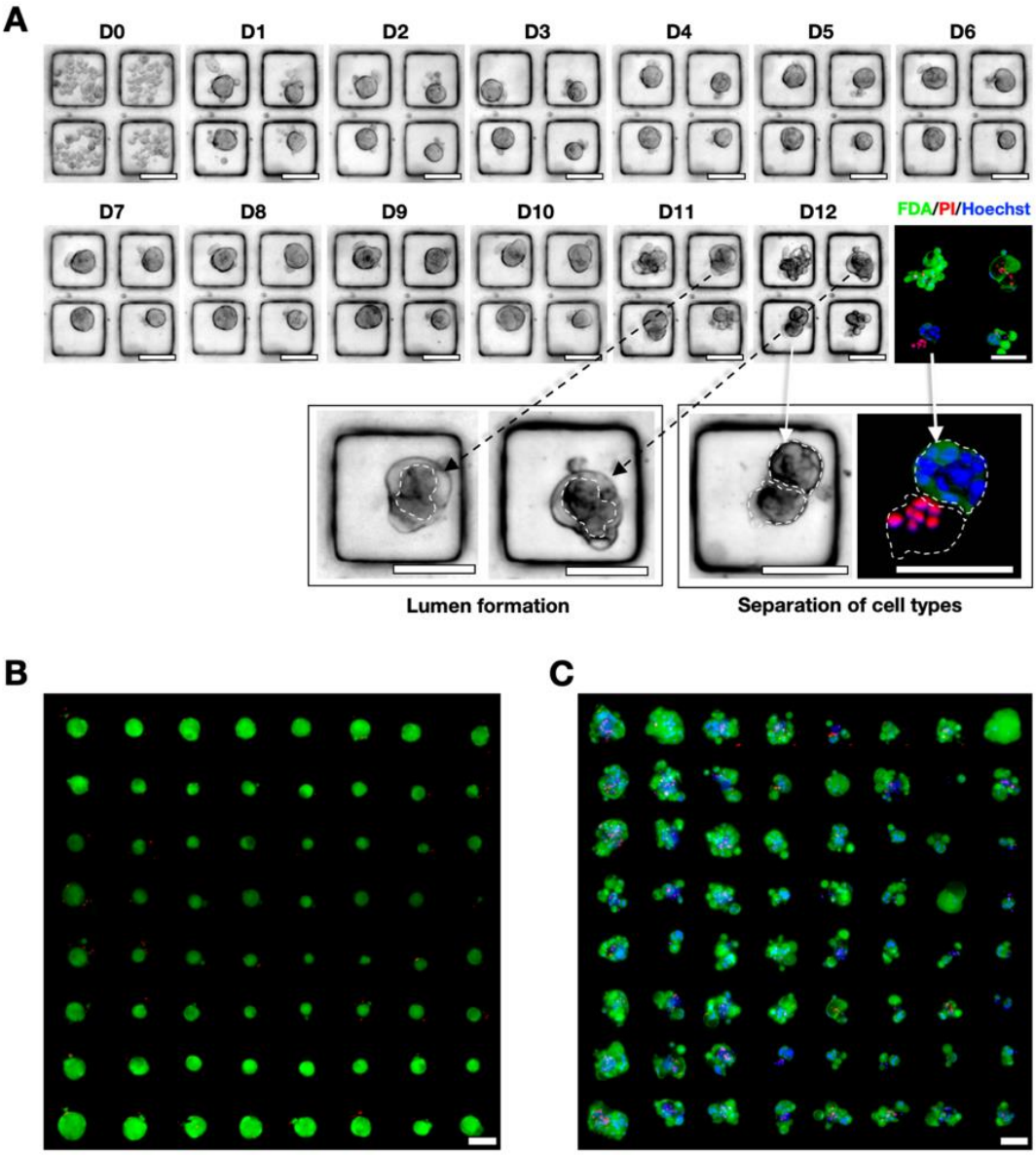

Figure 6.2 Prostate biopsy-derived tumoroids were monitored in culture for 12 days

A) Brightfield images of PC08-derived tumoroids in control conditions over 12 days of culture in a microfluidic gradient-generating device. Viability staining was conducted on day12 using PI, FDA and Hoechst. B) Viability stain (FDA & PI) of PC-08 derived tumoroids on day 3 of culture. C) Viability stain (FDA, PI & Hoechst33324) of PC-08 derived tumoroids on day 12 of culture, which show extensive formation of lumen and cell protrusions. All scale bars = 100µm

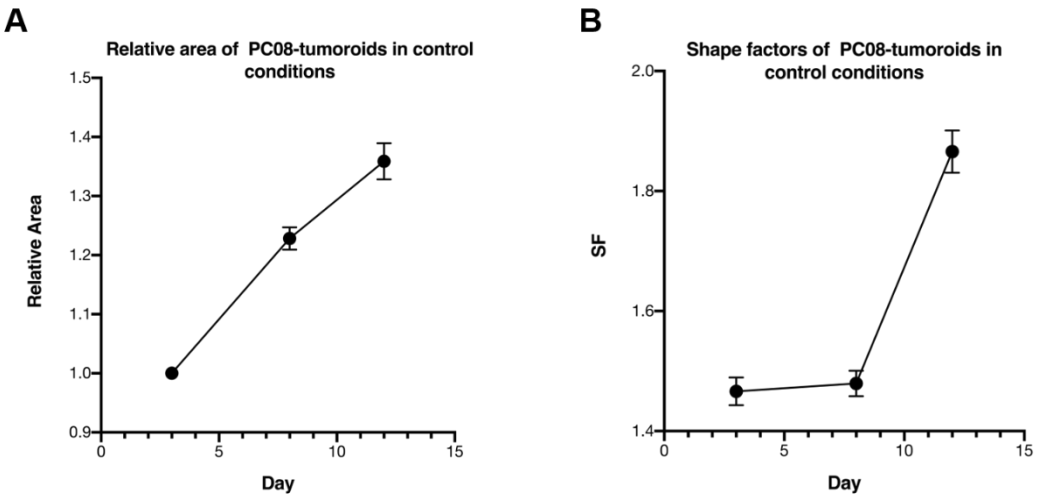

Figure 6.3 Size and shape changes of biopsy-derived tumoroids

PC08 cells were used to form tumoroids, which were cultured in control conditions for 12 days. A) Tumoroid areas were normalized to areas on day 3 of culture and expressed as relative areas for the culture duration of 12 days. B) The shape factors of control tumoroids were determined over the duration of culture. All values represent means ± S.E.M with n≥188

6.3 Repeated incubation of biopsy-derived tumoroids with drug concentration gradients

For tumoroids generated from PC08 the aim was to mimic fractionated chemotherapy as it occurs in clinic, and therefore tumoroids were incubated with all drugs repeatedly. On two days (day 3 and on day 8) a drug concentration gradient of either enzalutamide, abiraterone, docetaxel or cisplatin was applied to PC08 tumoroids (in triplicates) for 12 hours. On day 3, drug concentration gradients of the selected drugs (14-92µM enzalutamide, 16.2-93.8µM abiraterone, 8.9-108.8µM docetaxel, 21.1-103.2µM cisplatin) were applied to the PC08 tumoroid arrays for 12 hours, after which the drug solutions were washed off to prevent cross-contamination. The tumoroid growth and morphology were monitored daily using brightfield microscopy. On day 8, one set of replicate devices of each applied drug gradient was stained using FDA and PI, to assess the effect of the first drug concentration application, which showed that aggregates in all micro-wells at all drug concentrations were highly viable (**Figure 6.4**).

Since none of the four agents had shown any cytotoxic effects on PC08 tumoroids by then, the applied drug concentrations were doubled for the second drug gradient application on day 8 of culture. On day 8 of culture, the remaining devices were exposed to the drug concentration gradients (29.4-183.7µM enzalutamide, 32.5-187.5µM abiraterone, 17.8-217.6µM docetaxel, 42.2-206.5µM cisplatin) for a second time for 12h. After the incubation with the four drugs was completed, all drug solutions were washed off and once again, the tumoroid arrays were monitored daily using brightfield microscopy (**Figure 6.5A**). These images showed that PC08

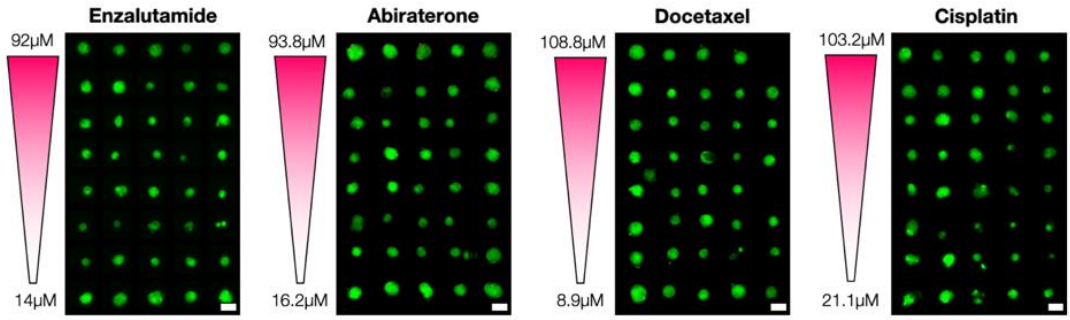

Figure 6.4 PC08-derived tumoroids were exposed to drug concentration gradients of four drugs

PC08-derived tumoroids were incubated with drug concentration gradients of 14-92µM enzalutamide, 16.2-93.8µM abiraterone, 8.9-108.8µM docetaxel and 21.1-103.2µM cisplatin for 12 hours on day 3 of culture. On day 8 viability staining was conducted using FDA (green) and PI (red) to assess the effect of the drug exposure on tumoroid viability. This demonstrated almost 100% cell viability in all treatment conditions across all concentrations. All scale bars=100µm

tumoroids exposed to a gradient of enzalutamide continued to grow from the first application on day 3 until day 8, across the entire enzalutamide concentration range that was applied (**Figure 6.5A**). After the application of the second enzalutamide gradient on day 8, several loose cells start to appear in micro-wells next to tumoroids in all device rows and across all concentrations from day 9 onward. Tumoroids appeared to continue to grow moderately after day 8 until approximately day 10, when the growth in size stagnated. From day 11 of culture the branching and complexity of PC08 tumoroids increased across the entire enzalutamide concentration range. Viability staining on day 12 confirmed that the majority of tumoroids were highly viable

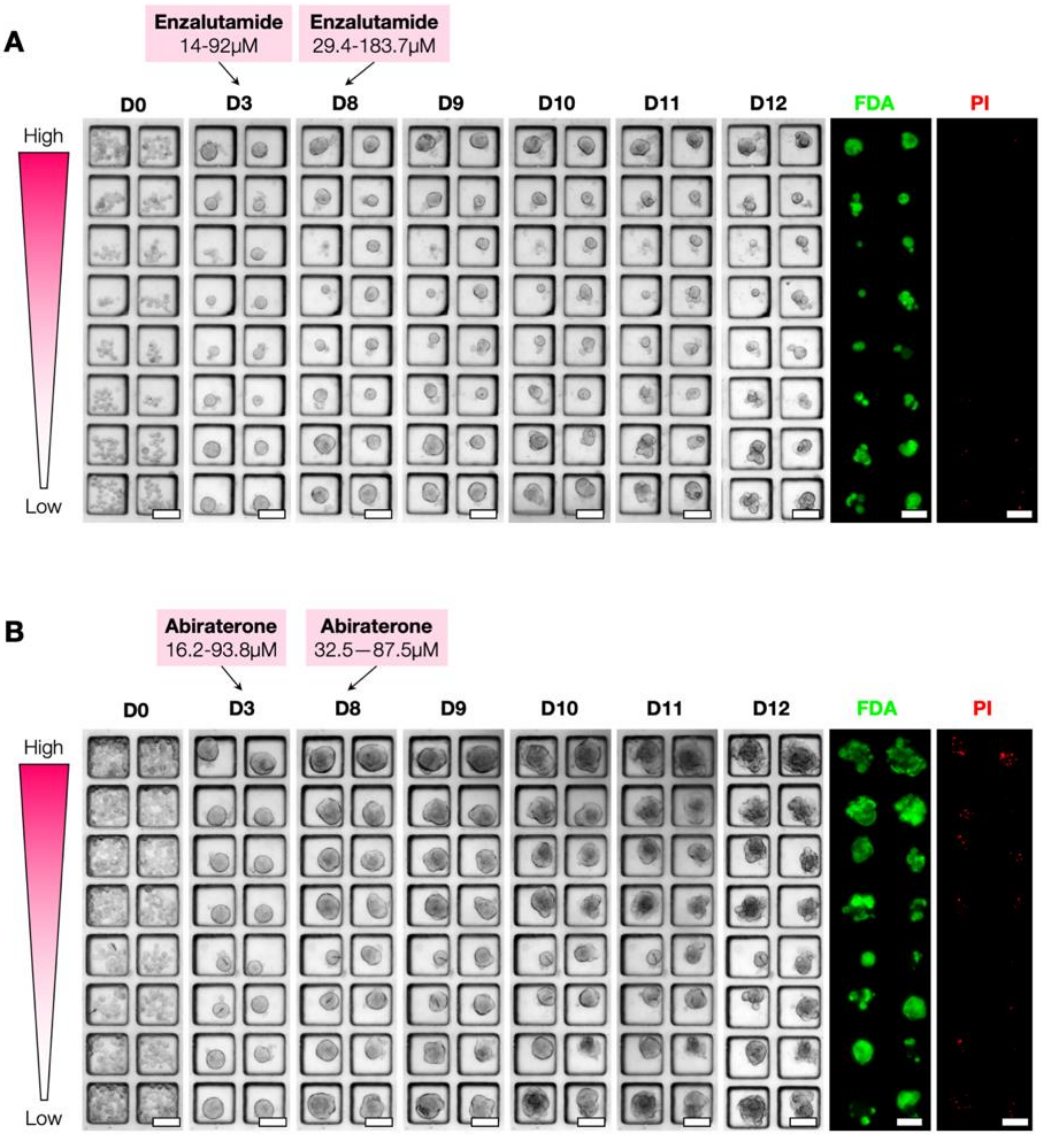

Figure 6.5 PC08-derived tumoroids were repeatedly exposed drug concentration gradients of enzalutamide and abiraterone

PC08-derived tumoroids were exposed drug concentration gradients repeatedly (on day 3 and day 8), after which viability staining using FDA and PI was performed on day 12. Representative brightfield images are shown of A) PC08-derived tumoroids after the incubation of with a concentration gradient of enzalutamide (first application range:14-92µM, second application: 29.3-183.7µM) throughout the course of the experiment. B) Representative brightfield and fluorescent images of PC08-tumoroids after repeated exposure to a gradient of abiraterone (first application: 16.2-93.8µM, second application:32.5-87.5µM). All scale bars=100µm

and only few dead cells were present. No concentration-dependent changes were observed as an effect of enzalutamide treatment of PC08 tumoroids (**Figure 6.5A**).

Brightfield images showed, that when PC08 tumoroids were exposed to abiraterone concentrations for the first time on day 3, tumoroid growth continued until day 8, independent of device row and the received abiraterone concentration (range of 16.2-93.8µM abiraterone, **Figure 6.5B**). This tumoroid growth continued after the second abiraterone gradient application on day 8, with twice the concentration used during the first application (range of 32.5-187.5µM abiraterone). In all rows, irrespective of received drug concentration, tumoroids grew visibly in size and complexity. Lumen and tumoroid protrusions developed relatively frequently from day 10 of culture in almost all device rows. Viability staining on day 12 confirmed that abiraterone had no significant cytotoxic effect on the tumoroids, and no concentration-dependent changes were observed (**Figure 6.5B**).

PC08 tumoroids exposed to a cisplatin concentration gradient (21.1-103.2µM cisplatin) on day 3 of culture appeared to continue to grow until day 8, even at the highest concentration applied (103.2µM cisplatin = 1st Row, **Figure 6.6A**). On day 8, the remaining PC08 tumoroids were exposed to a second cisplatin concentration gradient (17.8-217.6µM cisplatin), and brightfield images showed that tumoroids across the entire concentration range continued to grow in size until day 10. From day 10 until day 12, several single loose cells appear, while tumoroid size appears to stay constant. Many developed lumen and protrusions, irrespective of the applied cisplatin concentration. Viability staining on day 12 showed the presence of a small number of dead cells across the higher end of cisplatin concentration range applied (17.8-217.6µM cisplatin), while viable tumoroids remained in almost all micro-wells, but no clear concentration-dependent effect was discernible (**Figure 6.6A**).

PC08 tumoroids exposed to a docetaxel concentration gradient (8.9-108.8µM docetaxel) on day 3 showed continued growth until day 8 across the entire concentration range. Several loose cells were found in the three rows with the highest docetaxel concentrations (**Figure 6.6B**). On day 8, the second docetaxel concentration gradient (17.8-217.6µM docetaxel) was administered to the tumoroid arrays, from day 9 on

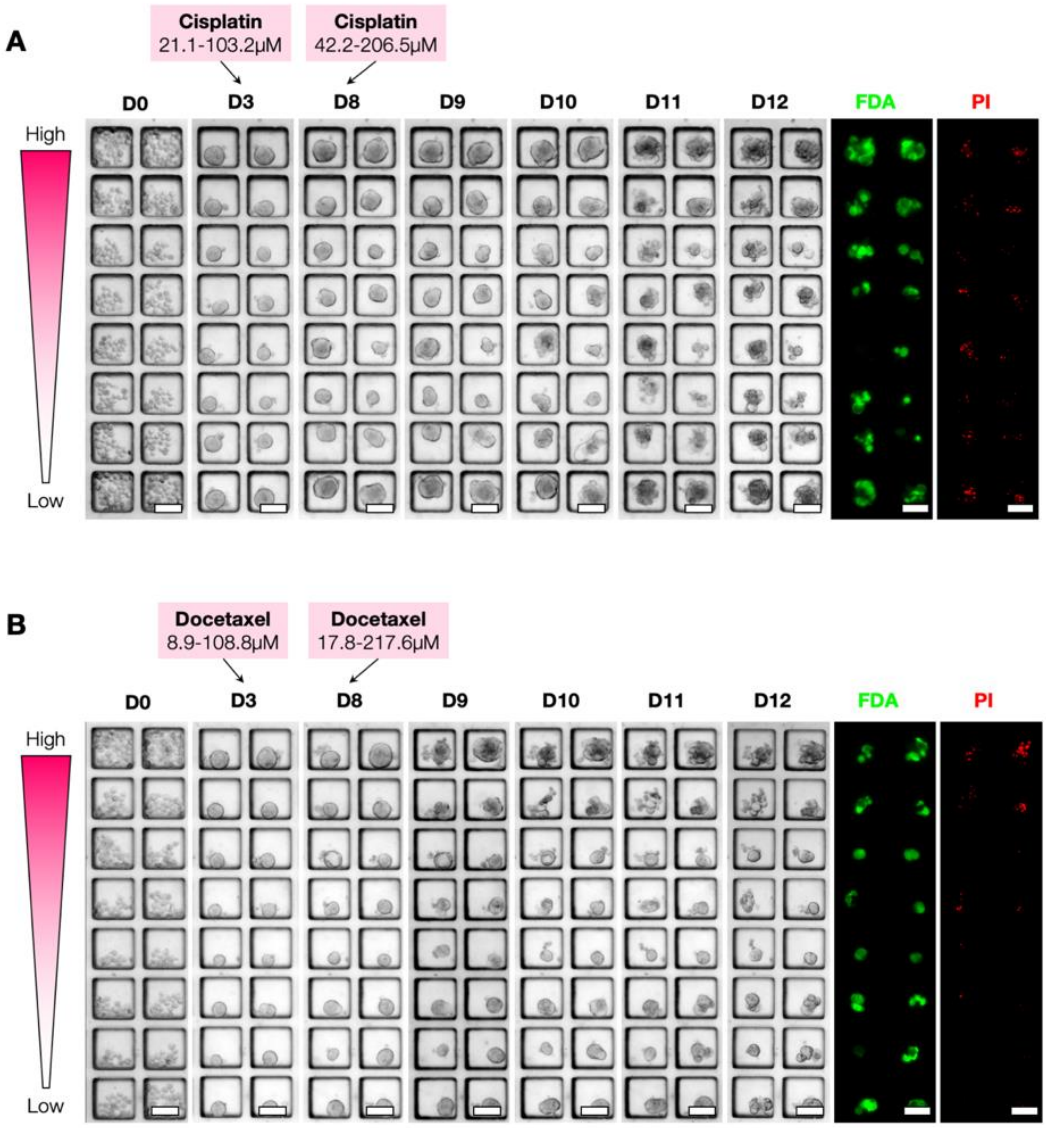

Figure 6.6 PC08-derived tumour spheroids were exposed to drug concentration gradients of cisplatin and docetaxel

PC08-derived tumoroids were incubated with drug concentration gradients repeatedly, (on day 3 and day 8), after which viability staining using FDA and PI was performed on day 12. Representative brightfield images are shown of A) PC08-derived tumoroids after the incubation with a concentration gradient of cisplatin (first application range: 21.1-103.2µM, second application: 42.2-206.5µM) throughout the course of the experiment. B) Representative brightfield and fluorescent images of PC08-tumoroids after repeated exposure to a gradient of docetaxel (first application: 8.9-108.8µM, second application: 17.8-217.6µM). All scale bars=100µm

brightfield images showed beginning tumoroid disaggregation in the 2 rows with the highest concentration. After the second gradient application, tumoroid growth

continues until day 10 in the rows with lower concentrations, but tumoroid size decreased in the rows of the three highest docetaxel concentrations from day 10 onward (**Figure 6.6B**). Viability staining on day 12 showed the presence of small compact viable tumoroids in almost all micro-wells, while the intensity and area of PI staining increased in the rows at the high end of the docetaxel concentration range (**Figure 6.6B**).

There appeared to be a moderate concentration-dependent effect of the second docetaxel concentration gradient on tumoroid integrity, size and viability. To confirm this observation, brightfield images were processed and extent of disaggregation was quantified. Monitoring the tumoroid shape factor before, during and after the repeated incubation with a docetaxel gradient, showed that the first application of the docetaxel had no significant effect on the shape factors of PC08 tumoroids (**Figure 6.7A**). Except for a transient, but significant ($p=0.049$), increase in SF on day 4 in the device row which received the highest concentration of docetaxel (Row 1=108.8µM docetaxel), tumoroid shape factors in all remaining device rows continued to decrease until day 8. On day 8, the second docetaxel gradient (17.8-217.6µM) was applied, which resulted in a significant increase ($p<0.001$) in shape factors of tumoroids in rows with docetaxel concentrations $\geq$ 122.1µM. The increase in shape factors was dependent on the docetaxel concentration applied (**Figure 6.7B**), which resulted in an $EC50_{PC08\text{-}SF\text{-}docetaxel}$=149.2µM. Further, on day 12 the remaining viable fraction of docetaxel-treated PC08 tumoroids was determined, which showed a concentration-dependent decrease in viability with increasing docetaxel concentrations and suggested an $EC50_{PC\text{-}VF\text{-}docetaxel}$=210.9µM (**Figure 6.7C, D**). None of the other drugs appeared to have had a detrimental effect on PC08-derived tumoroids at the concentration ranges applied. In order to test the robustness of the drug concentrations and the protocol used with PC08 tumoroids, the increased drug concentrations were tested on one further set of patient-derived tumoroids, PC09.

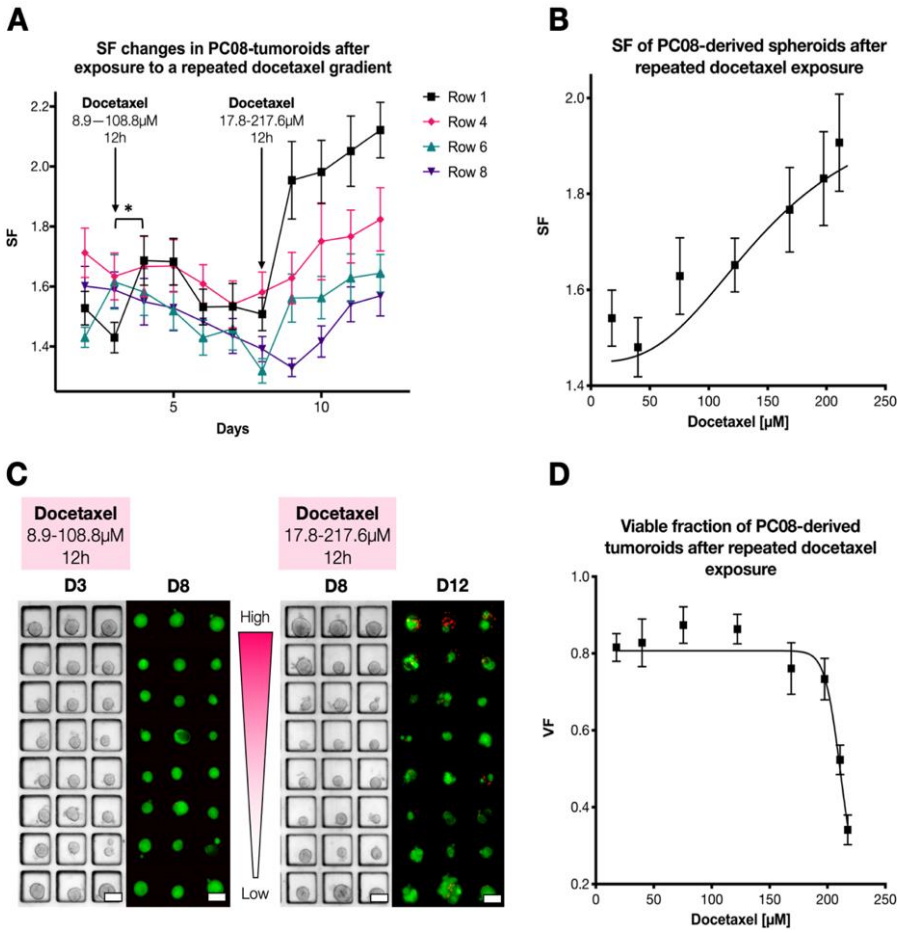

Figure 6.7 Results of repeated exposure of PC08 tumoroids to a docetaxel concentration gradient.

A) The evolution in the shape factor changes over time was obtained by calculating the mean shape factor of each row of tumoroids, for each day of the culture. For simplicity rows 1, 4, 6, and 8 are shown (Row 1=217.56µM, Row 2=210.9µM, Row 3= 197.6µM, Row 4=168.7µM, Row 5=122.1µM, Row 6=75.48µM, Row 7=39.9µM, Row 8=17.8µM). *Represent $p<0.05$. (B) The repeated application of a docetaxel concentration gradient resulted in a concentration-dependent increase in shape factor and an EC50 of 149.2µM was established. C) Representative images of PC08 tumoroids before and after the first and second application of a docetaxel concentration gradient. After the first exposure to a docetaxel gradient, viability was unaffected. When PC08 tumoroids were exposed to a higher docetaxel gradient for a second time, a concentration-dependent reduction in viability was observed. D) The application of the second docetaxel concentration gradient on day 8 resulted in a reduction of the mean remaining viable tumoroid fraction in each device row with an EC50 of 210.9µM. All values are means ±S.E.M. Scale bars=100µM

6.4 Application of a single drug concentration gradient to biopsy-derived tumour spheroids

After morphological assessment of the expanded biopsy, PC09-derived cells were seeded into 13 devices (both 150 and 250µm-micro-well size), where cells were allowed to aggregate and grow for 3 days. On day 3, concentration gradients of several drugs were applied to the arrays of micro-wells for 12 hours, such as docetaxel (17.8µM-217.6µM docetaxel) and enzalutamide (±DHT, 29.4-183.7µM), while several devices were used as controls for the culture with DHT, without DHT and in the presence of the vehicle (DMSO). After 12 hours of drug incubation, the drug treatments were washed off and tumoroids were continuously monitored using brightfield microscopy until day 8, when viability staining was conducted. The majority of PC09 tumoroids were solid aggregates, although lumen formation did occur increasingly in tumoroids towards the end of the culture duration (**Figure 6.8**). Out of all treatments applied, only the docetaxel concentration gradient appeared to affect tumoroid health in a concentration-dependent manner. In the rows at the higher end of the docetaxel range applied (17.8-217.6µM), a decrease in tumoroid size and increasing disaggregation were observed (**Figure 6.8A**). Viability staining showed an increasing number of PI-stained cells in the two rows which received the highest docetaxel concentrations (Row 1 and 2). These observations were confirmed when the tumoroid shape was quantified over the duration of culture, which showed that the docetaxel concentration gradient had resulted in a concentration-dependent increase in tumoroid shape factors, resulting in an $EC50_{PC09\_SF\_docetaxel}$=163.7µM (**Figure 6.9A**), which was very similar to the EC50 established in PC08.

When an enzalutamide concentration gradient (29.4-183.7µM) was applied to the array of PC09-tumoroids in the absence of DHT, tumoroid growth continued across the entire concentration range after day 3 of culture (**Figure 6.8B**). Only very limited tumoroid disaggregation was observed, which was consistent across the entire concentration range. Quantitative analysis of the PC09 tumoroid shape over the duration of culture showed that the enzalutamide concentration range applied did not affect the mor-phology of PC09 tumoroids (**Figure 6.9A**). These results were consistent with

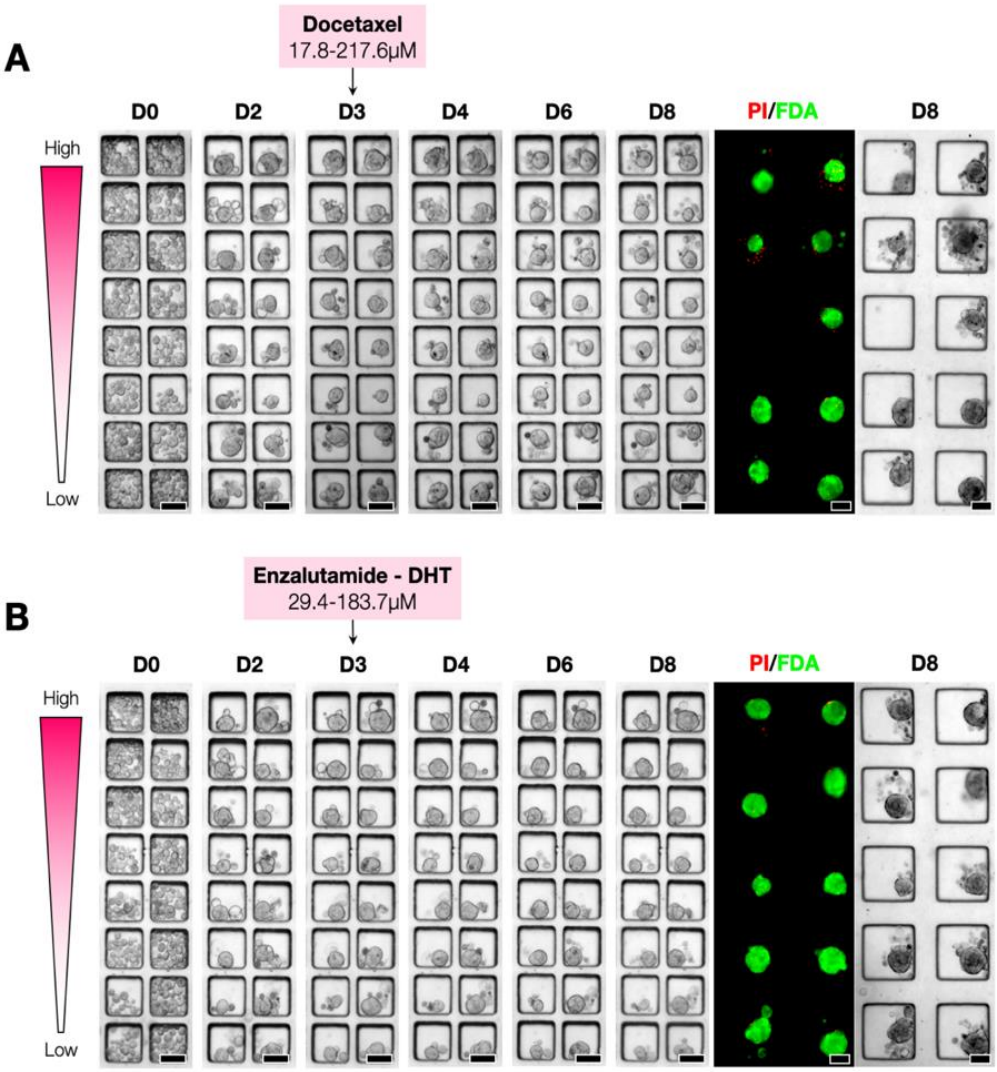

Figure 6.8 Representative brightfield images of PC09-tumoroids before and after the incubation with a drug concentration gradient on day 3 of culture.

On day 8 of culture, viability staining using PI and FDA was performed. A) PC09-tumoroids, which were exposed to a docetaxel concentration gradient (12.8-217.6µM) on day 3 for 12 hours. A gradual decrease in tumoroid size in row 1-3 combined with increasing disaggregation, is visible in brightfield images. Viability staining was conducted on day 8 in devices with 250µm-micro-wells, which showed the presence of dead cells in row 1 and 2. but not rows 4 and 5. B) PC09-spheroids were culture in the absence of DHT for 3 days, after which a enzalutamide concentration gradient (29.4-183.7µM) was applied for 12 hours. This did not appear to affect tumoroid growth and morphology. Viability staining conducted on day 8, showed that tumoroids were equally viable across the entire enzalutamide concentration range. All scale bars = 100µm

the application of an enzalutamide concentration gradient in the presence of DHT. In fact, the effect of DHT in the culture medium on the shape factor of PC09-tumoroids was quantified, and no significant difference in tumoroid shape was found (**Figure 6.9B**).

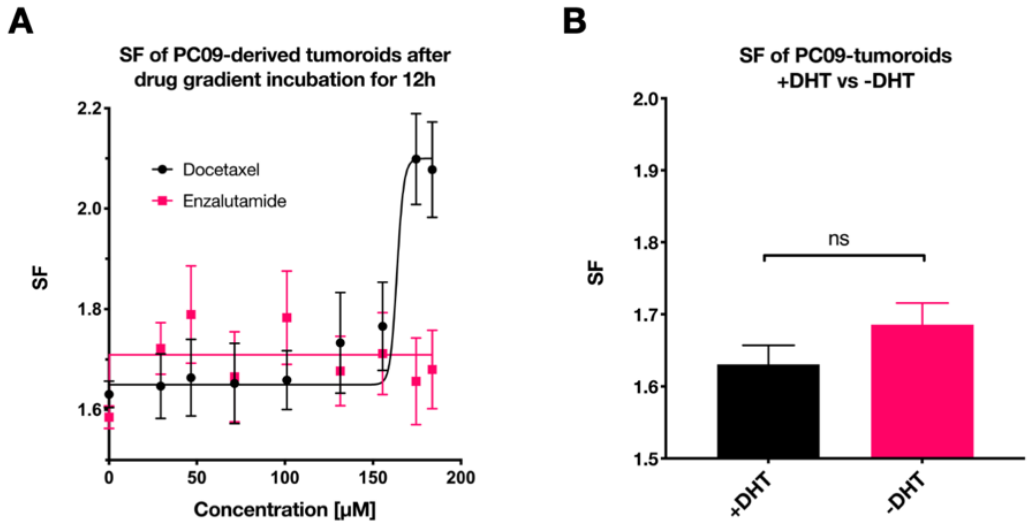

Figure 6.9 Drug concentration- dependent changes in spheroid shape

A) Quantitative analysis of PC09-tumoroid shape changes which had occurred by day 8 of culture, after the application of a concentration gradient of enzalutamide or docetaxel on day 3. A concentration-dependent increase in disaggregation and SF was induced by docetaxel, which resulted in an EC50 of 163.7µM, whereas the enzalutamide concentration range applied did not affect the SF of PC09-tumoroids. B) Control PC09-tumoroids were cultured in the presence (+DHT) and absence (-DHT) of DHT for the duration of culture. SF quantification on day 8 shows that SF of PC09-tumoroids do not differ significantly, independent of DHT supplementation. All values are means of device rows ± S.E.M.

To summarise, biopsy-derived tumoroids generated from both PC08 and PC09, were unaffected by the incubation with the androgen receptor inhibitor enzalutamide for 12 hours. Docetaxel on the other hand, affected tumoroid shape and viability in tumoroids generated from both patients with EC_{50}s of 149.2µM (PC08) and 163.7µM (PC09). All experiments were conducted in duplicates (PC09) or triplicates (PC08), using 150µm- and 250µm-microwells, which confirmed these results.

As a positive control, LNCaP spheroids, which were cultured alongside the biopsy-derived tumoroids, were exposed to a docetaxel concentration gradient (12.8-217.6µM) using the same schedule as for biopsy-derived spheroids (**Figure 6.10**). In response to the incubation with a range of docetaxel concentrations for 12 hours, LNCaP spheroids continued to grow in size from day 3 until day 8 in Rows 5-8, which corresponded to a docetaxel concentration range of 122.1-12.8µM (**Figure 6.10)**. At docetaxel concentrations ≥ 168.7µM, LNCaP spheroids appeared to decrease in size, but remained as viable compact aggregates when viability staining was conducted on day 8 ((**Figure 6.10**). The observed changes in shape factor and the remaining viable fraction were used to generate concentration response curves, which were compared to the results obtained from PC09 patient-derived tumoroids (**Figure 6.11**). LNCaP spheroids displayed a similar docetaxel concentration-dependent decrease in viable fraction, resulting in an $EC_{50\_LNCaP\_Doc}$=183.2µM, similar to the $EC_{50\_PC09\_Doc}$=163.7µM of PC09-derived tumoroids (**Figure 6.11A**). However, whereas the viability of LNCaP and PC09-derived spheroids decreased to a similar extent, LNCaP spheroids did not exhibit a concentration-dependent increase in shape factor,

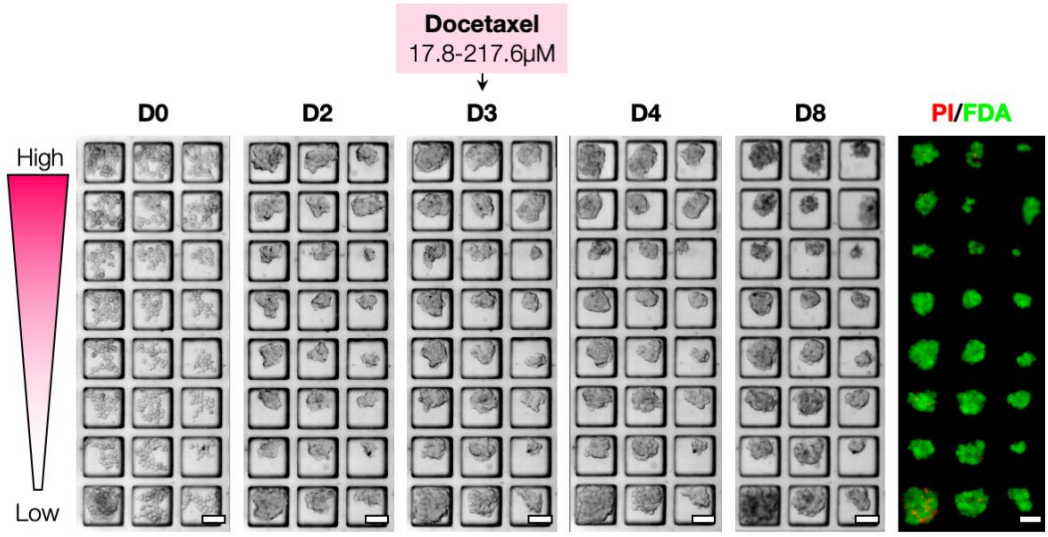

Figure 6.10 LNCaP spheroids were incubated with a docetaxel concentration gradient

LNCaP spheroids were exposed to a docetaxel concentration gradient (12.8-217.6µM) in the same manner as the patient-derived spheroids. Viability staining was conducted on day 8 of culture using PI and FDA. Scale bars = 100 µm

and disaggregation did not occur across the entire docetaxel concentration range (12.8-217.6µM, **Figure 6.11B**). This demonstrates the heterogeneity of morphologies

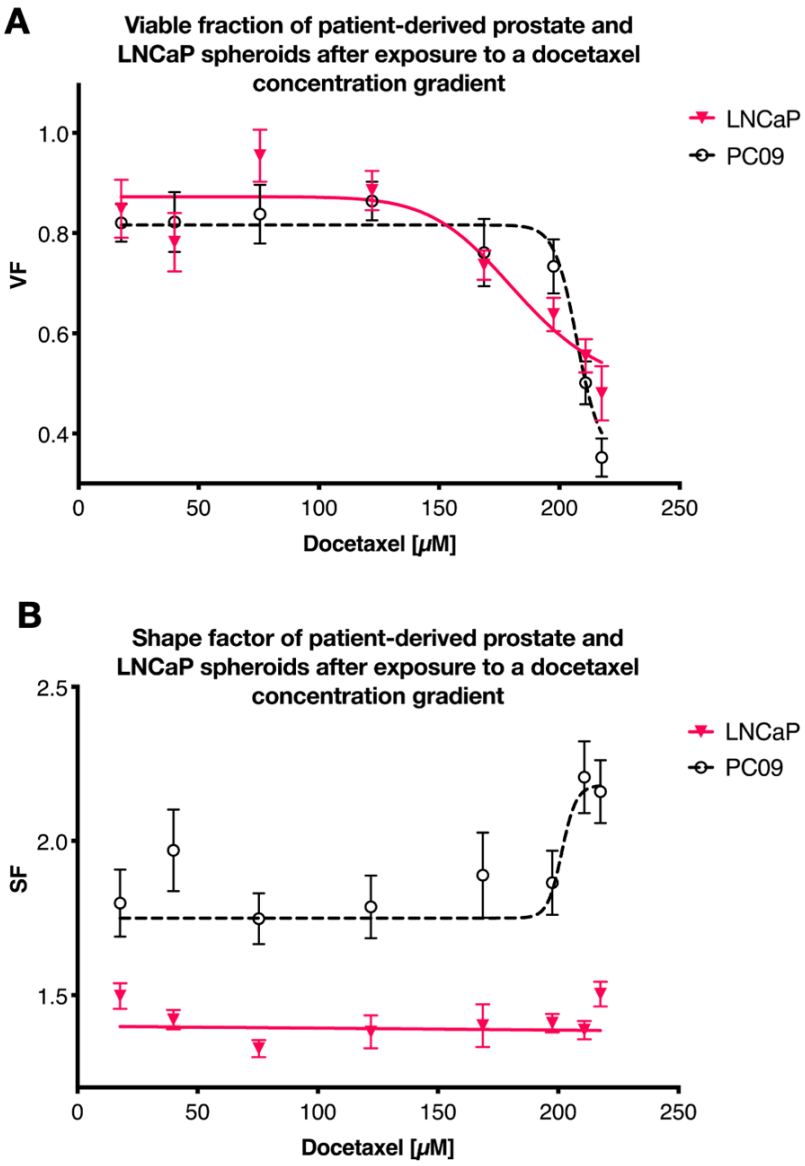

Figure 6.11 Viable fraction and shape factors of LNCaP spheroids in comparison with primary prostate tumoroids

Alongside PC09-derived tumoroids, LNCaP cells were used to generate spheroids, which were incubated with a docetaxel concentration gradient (12.8-217.6µM) in the same manner as the patient-derived spheroids. Viability staining was conducted on day 8 of culture for both PC09 and LNCaP spheroids. A) Viable fraction of PC09-derived biopsy spheroids and LNCaP spheroids after exposure to a docetaxel concentration gradient for 12h. B) Shape factors of PC09 and LNCaP spheroids after a 12h incubation with a docetaxel concentration gradient.

and shape factors between cell types, such as the generally lower shape factor and rounder nature of LNCaP spheroids in comparison to the primary spheroids, which requires the use of several readouts to provide meaningful comparison between different cell types.

6.5 RT q-PCR analysis to confirm presence of prostate cancer cells

To determine if the expanded cell populations of PC08 and PC09 contained prostate cancer cells, RT q-PCR was conducted to quantify and confirm the presence of prostate cancer biomarkers, such as AR, PSA and AMACR. PNT2 cells, an immortalised cell line generated normal prostate tissue, were used as a reference cell line for all samples, with ActinB serving as a housekeeping gene. As a positive control, the expression of all 3 biomarkers was assessed in LNCaP cells, which were originally derived from the metastatic site of a prostate cancer patient. As expected, LNCaP cells expressed higher levels of ARs, KLK3 (PSA) and AMACR than PNT2 cells (**Figure 6.12**). PC08 showed the highest expression of androgen receptors of the samples tested, which was similar to AR expression in LNCaP. Whereas the relative expression of ARs was significantly lower in PC09. Nonetheless, all 3 samples tested expressed PSA (encoded by the KLK3 gene) to varying degrees. The highest levels of PSA were found in LNCaP cells, which served as a control, while PC08 and PC09 expressed smaller amounts of PSA. AMACR was used as a third marker to identify prostate cancer cells, and was found to be expressed similarly in all 3 samples and no significant difference in AMACR expression was found between LNCaP, PC08 and PC09 cells (**Figure 6.12**).

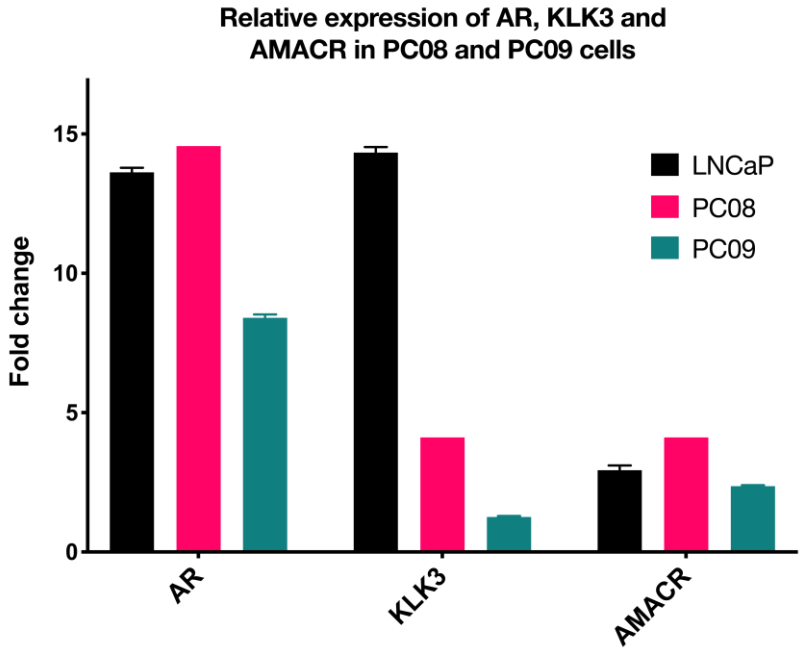

Figure 6.12 Quantitative analysis of the expression of prostate cancer biomarkers

Quantitative expression analysis of AR, KLK3 and AMACR using RT q-PCR was conducted on LNCaP cells, which served as a positive control, the patient-derived cells PC08 and PC09, and PNT2 cells, which were used as a reference group. ActinB was used as a housekeeping gene. All values represent fold change ± standard error

7 Discussion and conclusion

The aim of the work presented in this thesis was the development of a microfluidic platform and associated protocols for drug screening on 3D, physiologically relevant tumour models, allowing statistically meaningful quantitative comparison of drug efficacies in patient-derived tumoroids. The following sections will discuss the main results and implications of this work, as well as potential future opportunities for platform development and applications.

7.1 A novel device for maximised drug efficacy testing of biopsy-derived tumoroids

A review of the relevant literature in chapter 1 showed the increasing shift towards the utilisation of patient-derived tissue in drug discovery and for personalised medicine applications. The use of fresh tumour tissue has the advantage of retaining several elements of the tumour microenvironment, such as the presence of multiple cell types, e.g. fibroblasts, cancer associated fibroblasts, and cancer cells, whilst simultaneously preserving a degree of intra-tumoral heterogeneity, which is a particularly important aspect of prostate cancer, contributing to treatment resistance (Tolkach and Kristiansen, 2018; Yadav et al., 2018). However, the most commonly used drug screening technologies, such as ultra-low adhesion and hanging drop plates, require a large number of cells or volume of tissue for the screening of solid tumours in a 3D environment, for the purpose of precision medicine applications. Tumour resections, which could provide a large number of cells, are often not feasible. Hence, biopsy-derived tissue is used for ex vivo drug screening, which can contain as little as 500.000 cells (Rajer and Kmet, 2005).

Microfluidic technologies offer the opportunity of precise spatial and temporal control over the culture microenvironment, whilst requiring reduced amounts of reagents and cells. While several approaches have shown promising results (Lee et al., 2014; Ma et al., 2015; Ruppen et al., 2015; Akay et al., 2018; Eduati et al., 2018), many still require the use of tubing and fluid actuation equipment (Eduati et al., 2018), and

other specialised equipment, which is not easily accessible or compatible with up-scaling. Akay et al. (2018) presented a microfluidic platform which contained a gradient generator that was capable of generating a 7-point concentration response curve from patient-derived glioblastoma spheroids, with 9-11 replicates for each concentration. However, only 3 devices could be filled for each patient in the study, providing three concentration response curves (Akay et al., 2018). Ruppen et al. demonstrated the ability of their microfluidic platform to test the efficacy of one drug treatment (cisplatin) in patient-derived tumour cells and pericytes individually, as well as in co-culture, demonstrating pericyte-mediated resistance (Ruppen et al., 2015). However, the use of fairly large spheroids resulted in a reduced number of possible tested conditions and only 32 wells with spheroids could be generated for each patient.

The small number of available cells in biopsies, in combination with the need for highest possible number of drug conditions tested, means that some assays using microfluidic technologies have achieved extensive drug screens in patient-derived cells in a 3D context (Ma et al., 2015). However, in order to achieve a screens of this size from biopsy tissue, the cell number in each replicate had to be reduced greatly (e.g. 10 cells per well), which came at the cost of losing cell-to-cell contact and spheroid formation (Ma et al., 2015). The culture of patient-derived tumour cells in alginate beads resulted in a similar loss of cell-to-cell contact, and the screened cells had not formed 3-dimensional tumoroids (Lee et al., 2014). Individual cells suspended in a matrix lack the gas and concentration gradients, extensive cell-to-cell contact, and the heterogeneity of metabolic activity and proliferation observed in spheroids and tumoroids, which mimic the in vivo tumour more accurately than monolayer cultures. These studies, though extensive in scale and extremely efficient, demonstrate that increasing the throughput of a patient-tissue screening assay can result in reduced physiological relevance of the tumour model employed. Although the mentioned studies have extensively improved on previous patient tissue screening in monolayers (Burstein et al., 2011), by enabling patient-derived tissue screening in a 3D context (Ruppen et al., 2015; Akay et al., 2018) or by maximising the number of possible

drug screens (Lee et al., 2014; Ma et al., 2015; Eduati et al., 2018), there remains an unmet need for a platform can accomplish both. There remains a need for a platform which can easily generate and culture spheroids from patient biopsies and provide drug efficacy screening of as many compounds as possible, without the use of extensive specialised equipment. This would not only enable the screening of patient tissue for treatment-guidance in a precision medicine context, but could also allow increased use of patient-derived tissue in drug discovery, adaptive clinical trials and could provide efficient testing of combinatorial drug treatments.

Therefore, this thesis aimed to provide a microfluidic solution and protocols for the in vitro screening of anticancer agents in biopsy-derived tumouroids, which maximises the number of possible quantitative readouts of drug efficacy. In fact, up to 22 different conditions could be tested in the gradient-generating device from a single patient biopsy, creating spheroid numbers equivalent to 32 96-well plates (described in detail in section 7.6). Chapter 3 described the design and operation of this proposed microfluidic platform, which resulted in the consistent on-chip generation and culture of hundreds of spheroids contained in micro-wells. In Chapter 4, we describe how a reproducible drug concentration gradient could be applied to an array of tumour spheroids, resulting in the generation of concentration-response curves with eight different concentrations and up to 24 replicates, from each individual gradient-generating device. Chapter 5 then described the optimisation of culture conditions in the microfluidic devices for the generation of tumoroids from patient-derived biopsy tissues and their culture. The microfluidic platform designed in this thesis was then applied to the screening of tumoroids derived from two prostate cancer patient biopsies in chapter 6, the results of which were published in Scientific Reports (Mulholland et al., 2018). From two patient biopsies, we generated thousands of tumoroids, which were successfully exposed to several anticancer drug gradients for drug efficacy testing. This presents a significant improvement in throughput in comparison to other microfluidic devices which are able to screen patient-derived cells in a 3D environment (Akay et al., 2018). Most importantly, the increase in throughput achieved using this novel platform, did not necessitate the use of a less

physiologically relevant 2D tumour model. Using the microfluidic platform presented here, the number of possible drug efficacy tests on patient-derived tumour cells could be maximised, while retaining physiological relevance through the use of 3D tumour models. Additionally, the screening of thousands of patient-derived tumouroids in microfluidic devices was conducted entirely without the use of external actuation or other specialised equipment. The effects of drug exposure could then be quantified in a label-free manner (shape factor, size) as well as by end-point analysis (viability staining). Label-free readouts, which can be generated at any time point throughout drug screening assays, offer the opportunity to maximise the information which can be obtained from biopsy-derived spheroids, without necessitating the use of cytotoxic end-point measurements. In parallel with drug efficacy testing of the patient-derived spheroids, gene expression analysis confirmed the presence of cancer cells and intact androgen receptors in the biopsy samples. These results will be discussed hereafter in more detail, with a focus on future work and opportunities for this platform.

7.2 The generation of a stable and repeatable microfluidic compound concentration gradient

A microfluidic platform was developed to create a system which could screen a large number of spheroids using a microfluidic concentration gradient, without the use of external actuation equipment. Open wells were chosen in favour of syringe pumps for the generation of fluid flow, due of the ease of operation by micropipette, cost and complexity of operation and the lack of tubing-related errors. Additionally, open wells would allow potential future upscaling to a 96-well plate format, accessible to multi-channel pipettes and robotic dispensing. However, evaporation is a common issue with open reservoirs, which is why particular attention was paid to the minimisation and monitoring of evaporation in the device. We demonstrated how a carefully designed microfluidic network could utilise hydrostatic pressure gradients, in order to establish a stable compound concentration gradient across an array of

microwells (Chapter 3, **Figure 3.11**). Experimental data obtained from timelapse experiments using the fluorophore calcein to generate a concentration gradient, showed that such concentration gradient took approximately 1 hour to establish, and remained stable for a further 12-16 hours. This experimental fluorescent concentration gradient closely matched the FEM simulation conducted, to estimate the convective and diffusive behaviour of calcein in the microfluidic device (Chapter 3, **Figure 3.10**).

However, since most anticancer compounds are non-fluorescent and cannot be visualised using fluorescent microscopy, it was important to find a way to assure that the expected concentration gradient had formed. The validated numerical model described in Chapter 3 (**Equation 8,9**) described the evolution of fluid volume in all reservoirs over time. This meant that during experiments, the volumes contained in each reservoir could be measured and compared to the predicted volumes at that time point, to decide if the correct concentration gradient pattern had formed. Therefore, in all experiments using the microfluidic concentration gradient to apply drugs, once the concentration gradient application was complete after 12 hours, the remaining fluid volumes in all open reservoirs were measured. If the volumes in the reservoirs differed from the value predicted by the FEM-simulation by more than 10%, it was assumed that a gradient had not formed as expected and the experiment was discarded. This test was used to determine if any external factors that had not been considered in the simulation, such as a liquid meniscus and evaporation, had affected the device. We attempted to limit evaporation by keeping all microfluidic devices in a humidified incubator (humidity > 95% at 37.5 °C), surrounded by humidifying fluid reservoirs.

Once a gradient is established, our FEM simulation estimated that in a worst-case scenario, a deviation of approximately 10% could occur in the concentration gradient pattern over 24 hours. Deviations could occur due to variations in temperature and due to small differences between the manually created device reservoirs, which could affect the filling height. In experiments using calcein, minor variations in concentration occurred across the microwells of each row due to fringe effects at the

edges of the microwell array (**Figure 3.9**). The deviation between microwells of the same row was most pronounced in Row 1 and 2 of the microwell array and amounted to a deviation of less than 1%. This could be corrected by further optimising the geometry of the device, for example by widening the array of micro-channels, or by reducing the width of the micro-well array. However, to avoid the impact of these variations in the existing platform, the spheroids in the first and last 3 columns, which were most affected by the fringe effects, were excluded from analysis. Due to the potential impact of external factors such as evaporation and liquid absorption into PDMS, a 13-hour window was chosen for the application of drugs the patient-derived tumoroids in chapter 5, which allowed 1 hour for the establishment and 12 hours of sustained exposure to the drug concentration gradient. Both evaporation and liquid absorption into the PDMS could be reduced by the replacement of PDMS as a material with a hard plastic such as polystyrene, produced by injection-moulding, which could significantly extend the stability and duration of the microfluidic concentration gradient.

Despite these disadvantages, PDMS is the predominant polymer used in microfluidic research and prototyping due to its chemical properties and its biocompatibility. PDMS possesses high optical clarity, which enables microscopy applications, its gas permeability and high porosity to liquids. This permeability allows for oxygen and carbon dioxide gas exchange throughout the device, which enables live cell experiments and cell cultures on chips (Halldorsson et al., 2014). Additionally, PDMS is relatively inexpensive and quick to manufacture, which has led to its widespread adoption in microfluidic device proto-typing and manufacturing (Halldorsson et al., 2014). However, PDMS is also known to have a high degree of permeability for small hydrophobic molecules, which can be absorbed into the bulk PDMS over time (Wang et al., 2012). In the context of functional toxicity assays conducted in this thesis, drug absorption into PDMS could reduce the drug concentrations applied to spheroids and result in a deviation of the applied microfluidic concentration gradient from the simulation established in Chapter 3. Wang et al. 2012 quantified the PDMS absorption of a number of drugs, which demonstrated that drugs with a log P value of > 2.62 can

be subject to absorption into PDMS devices, whereas drugs with a log P < 2.47 showed minimal absorption (Wang et al., 2012). The log P values of cisplatin and calcein are below 0 (ALOGPS), which suggest that they shouldn't be subject to diffusion into PDMS. However, enzalutamide, docetaxel and abiraterone possess log P values estimated to be > 2.62, suggesting that drug absorption into PDMS is a possibility. The impact of drug absorption into PDMS may be limited to some extent in the self-generating concentration gradient devices, because a continuous flow is present, which refreshes the drug solution throughout the experiment. Additionally, the absorption of small hydrophobic drugs can be limited using certain PDMS surface coatings (Gomez-Sjoberg et al., 2010; Gökaltun et al., 2019), however the effect of the specific coating used in this thesis on the absorption of small molecule drugs is not known. In order to avoid the potential issue of PDMS drug absorption, future versions of this device should be manufactured from a different substrate, such as polystyrene, which shows little to no absorption of molecules. However, hard plastics such as polystyrene have very low gas permeability, which means that gas transport within a hard plastic device would only occur through the liquid in the form of diffusion. As a result, the microfluidic device design reported here would have to be adjusted, which would involve shortening micro-channels and further miniaturisation, in order to guarantee sufficient gas exchange in the platform to support on-chip cell cultures.

In this project the main purpose of the microfluidic concentration gradient is the efficient generation of concentration response curves, but it is also a flexible and versatile tool, since a gradient could be re-established at any point in time. This allows its application to a number of treatment regimens used in patients, which can then be mimicked on chip, such as fractionated chemotherapy, as described in Chapter 6 (**Figure 6.7**). Further, if the concentration gradient is immediately re-established after 12 hours, the duration of the drug concentration could be extended to achieve longer incubation periods (e.g. 24h). In summary, the microfluidic platform described here is capable of generating reproducible, stable concentration gradients, which can be modelled and predicted using the analytical solution and FEM simulation described in Chapter 3.

7.3 Drug efficacy testing using a microfluidic concentration gradient

In Chapter 4, it was demonstrated how a microfluidic concentration gradient of cisplatin could be used to perform drug efficacy testing on spheroids formed from cell lines in the platform designed in this thesis. The data obtained from the screen performed using a concentration gradient of cisplatin was validated by comparison with devices which had been incubated with fixed cisplatin concentrations (**Figure 4.8**). Since the original aim was to screen patient-derived spheroids in the device, the platform was applied to cytotoxicity testing of prostate patient-biopsy derived tumoroids (Chapter 6, **Figure 6.7, Figure 6.8**), which allowed the quantitative comparison of drug efficacies in tumoroids obtained from 2 patients.

The microfluidic concentration gradient established in the device, produces compound concentrations spanning two orders of magnitude (e.g. 17.8-217.6µM docetaxel, **Figure 6.7**), which corresponds to approximately 10% to 90% of the concentration of the applied drug solution. Drug screening in monolayers usually covers a concentration range of 5 orders of magnitude, in order to be able to obtain a concentration-response curve irrespective of each drug's efficacy. For the drug screening of tumour spheroids however, a smaller concentration range is usually sufficient, since the literature suggests that spheroids derived from cell lines or primary tissue tend to be vastly less sensitive to chemotherapeutic compounds than cells cultured in monolayers (Melissaridou et al., 2019). Therefore, a reduced concentration range is adequate in the context of screening tumour spheroids. However, if a larger concentration range would be required, an additional device could be used, applying the same drug at a concentration range which is magnitudes higher or lower, while providing eight concentration points per device with up to 24 replicates. This represents a potentially significant trade-off in the number of possible treatments that can be tested in tumoroids derived from biopsies. Using this microfluidic platform, up to 22 gradient-generating devices could be filled per patient biopsy, enabling quantitative efficacy testing of up to 21 drugs (while at least one device remains as a control), which presents an improvement in throughout even compared to other microfluidic platforms used to screen patient-derived spheroids (Ruppen et al., 2015; Akay et al.,

2018). Reducing the number of potential drug efficacy tests in order to generate a larger concentration range of a drug is unlikely to add additional value, assuming that sufficiently high drug concentrations are used during screening. The drug concentration ranges used in this thesis for docetaxel, enzalutamide and cisplatin were comparable to previous studies, which had suggested resistance to lower concentrations in spheroids, and several documented reduced efficacy in 3D cultures when compared to monolayers (Godugu et al., 2013; Ruppen et al., 2014, 2015; Baek et al., 2016; Melissaridou et al., 2019). Further, in the context of precision medicine, it becomes a priority to establish 'hits', the drug or drug combination which is the most effective, or which drugs have no effect, in order to inform on the treatment best suited to the patient's tumour. Therefore, it becomes a priority to maximise the number of possible treatment regimens which can be modelled, in order to identify hits, rather than the identification of an EC_{50} value.

Since the platform has the capability of producing a range of spheroid sizes (**Figure 3.12**), it has the potential to detect spheroid size-dependent drug effects (Tanenbaum et al., 2017). Larger spheroids appear to be more resistant to chemotherapeutic agents than smaller spheroids, which is likely due to the presence of a drug concentration gradient within a spheroids and the variation in relative drug penetration of the spheroid, but could also involve the presence of necrotic and hypoxic cells in spheroids larger than 500-600 micron (Friedrich et al., 2009). Beyond the range of spheroid sizes generated within each device, the size of the spheroids generated could also be controlled by the utilisation of larger micro-wells. Although the majority of experiments presented here were conducted in microwells of 150µm width, both patient biopsy drug screens in Chapter 6 were also conducted in microwells of 250µm size to account for larger spheroids. These experiments confirmed the observations made in micro-wells of 150µm size and no difference in chemosensitivity was found between the two spheroid size ranges. Due to the current design of the device, the area which contains the microwell array was fixed and could harbour an array of eight rows and 30 columns of 150µm sized wells, which resulted in the formation of 240 spheroids. In order to fit 250µm microwells into the micro-well

array area, the number of micro-wells had to be reduced to five rows of 17 microwells, forming 85 tumouroids with up to 13 replicates per drug concentration applied. This again presents a trade-off between the number of replicates and points generated on a concentration-response curve, and the spheroid size required for the tumour model, which could be an important factor when studying drug effects. Considering the mechanisms of action of the applied drugs can inform on the size of 3D tumour model required to demonstrate the drug's mechanism of action, which can identify if the trade-off of fewer replicates and fewer drugs tested is acceptable. For example, in order to test the efficacy of a drug which targets hypoxic cells, spheroids containing hypoxic cells larger than 500-600µm would be required to be able to demonstrate a drug's efficacy. In this context, the trade-offs associated with using larger spheroids are acceptable, because they represent a more physiologically relevant tumour model, which is required to be able to demonstrate the effect of a hypoxia-targeting drug.

In order to accommodate a larger number of micro-wells, increase the points on the concentration-response curve or to further increase the size of microwells to more than 500µm, the device could be adapted by increasing the width of the cell culture channel. Depending on the application of the device, the trade-offs of using larger spheroids have to be weighed against the benefits which they provide, in order to determine if the use of spheroids larger than 200µm in diameter is justified. However, in the context of drug efficacy testing of patient-derived spheroids for the purpose of precision medicine, this trade-off is not acceptable, since the anticancer drugs tested target proliferating cells, which are represented in tumour models of less than 200µm diameter, and the maximisation of possible drug screens remains a priority.

7.4 Drug screening of heterogeneous cell populations derived from prostate cancer biopsies

A proof-of concept screen was conducted on tumoroids derived from two patients' biopsies, in order to quantify the efficacy of a range of drugs (Chapter 6). The

heterogeneous nature of the tissue obtained from tumour biopsy provides the advantage of maintaining a more realistic tumour microenvironment with several resident cell types (cancer cells, normal prostate cells, fibroblasts and cancer associated fibroblasts). However, biopsy tissue presents several challenges, since the number of cancer cells within each biopsy can vary depending on the biopsy location relative to the tumour. Additionally, the different cell types contained in every biopsy proliferate at different rates. Depending on the original quantities of all cell types present, this can result in the overgrowth of the fibroblast population (Neal et al., 2018), which occurred in 4 out of the 9 prostate biopsy cultures conducted during this project. In order to selectively enrich the cell population for epithelial cancer cells, several supplements were used to promote epithelial cell proliferation, such as FGF10 (Memarzadeh et al., 2007). Both DHT and PGE2 are required for the development of the prostate in vivo and the enhanced proliferation of prostate cancer cells (Gleave et al., 2020). Additionally, after initial tests which had resulted in an overgrowth of fibroblasts, choleratoxin was added to the medium, in order to selectively reduce the growth of fibroblasts (Hollenberg and Cuatrecasas, 1973; Eisinger and Marko, 1982). This appeared to be successful, since biopsy cultures with choleratoxin continued to show the presence of fibroblasts, but their numbers were greatly reduced, and overgrowth of the fibroblasts was prevented.

In order to confirm the presence of cancer cells in the biopsy-derived tumoroids which had been exposed to several anticancer agents, RT-qPCR was conducted in parallel (**Figure 6.12**). Results showed that androgen receptors were present in both biopsy populations to an extent comparable to LNCaP cells. In comparison to benign PNT2 cells, an increased expression of PSA (KLK3) was determined for both biopsy cultures. The expression of the cancer cell marker AMACR was found to be consistent between the two biopsy cultures (PC08 & PC09) and the LNCaP cancer cell line. This suggests that both tumour biopsy cultures contained a significant cancer cell population, which produced intact androgen receptors capable of the expression of PSA as a result of androgen stimulation.

However, despite the presence of seemingly functional androgen receptors in the prostate cancer cells in culture, the non-steroidal androgen receptor inhibitor enzalutamide had no inhibitory effect on the proliferation and viability of biopsy-derived tumoroids from either patient PC08 or PC09 (**Figure 6.8**A). Studies conducted on prostate cancer derived organoids showed that enzalutamide frequently failed to affect proliferation of prostate organoids and organoid formation for a number of reasons (Chua et al., 2014; Gao et al., 2014). Structural changes in the androgen receptor and specific splice variants have been identified which lead to enzalutamide resistance and AR activation upon binding of enzalutamide (Golshayan and Antonarakis, 2013; Joseph et al., 2013; McCrea et al., 2016). In the clinic, approximately 60% of patients show a response after enzalutamide treatment initially, although resistance emerges after approximately 3.4 months and de novo resistance can be observed (Beer et al., 2014; McCrea et al., 2016). Additionally, the presence of fibroblasts in the two biopsy cultures might contribute to the resistance observed to enzalutamide, cisplatin and abiraterone, by conferring a certain degree of chemotherapy protection, which has been demonstrated in in several cancer types (Paraiso and Smalley, 2013; Onion et al., 2016). Enzalutamide and anti-androgen resistance in prostate cancer specifically has been linked to the presence of cancer-associated fibroblasts, which modify the response of prostate cancer cells (Eder et al., 2016). However, since it has been shown that patient-derived organoids of the same cancer type, and even the same tumour, can display a large variety of possible drug responses (Gao et al., 2014) and only two patient biopsies were screened, no larger assumptions or conclusions could be made. Although beyond the scope of this project, the data presented here showed that cancer cells could be maintained in culture in the presence of fibroblasts, which suggests the application of the device for the investigation of fibroblast-mediated drug resistance.

Additionally, while patient-derived tissues have shown great predictive value (Vlachogiannis et al., 2018; Phan et al., 2019), the general difficulty of translating in vitro data established from in vitro functional assays of patient-derived tissues into patient-relevant data still remains, and no universal method exists to directly

translate in vitro EC_{50}s into a target dose for patients. This translation has to be considered carefully for each drug, depending on its absorption, distribution, metabolism and excretion in humans, which affect drug efficacy in human, but not in in vitro models. In this thesis, this was considered initially when choosing drug concentration ranges to be tested on biopsy-derived spheroids, and later once EC_{50}s had been determined experimentally. The chosen testing concentrations for each drug had to be high enough to affect the viability and growth of tumoroids to a measurable extent, if the cancer cells in question were sensitive to a specific drug. This was complicated by the fact that 3D cultures are frequently more resistant than corresponding monolayer cultures (Melissaridou et al., 2019), and by the presence of fibroblasts within the population, which could confer protection to cancer cells in the tumouroids (Eder et al., 2016). Additionally, the consequences of choosing a testing drug concentration range below the therapeutic threshold, would mean that no efficacy data could then be produced from the sample tissue. A further consideration for the drug screening of prostate-biopsy derived spheroids in this thesis was the incubation period of 12 hours, which is shorter than incubation periods used in publications that report drug efficacy data obtained in cell lines, where exposure typically ranges from 24-72 hours (Kogashiwa et al., 2010; Chambers et al., 2014). Therefore, to compensate for the known resistance of 3D tumoroids and the short incubation period, relatively high drug concentration ranges were selected for the drug screening of the patient-derived tumouroids, as described in **Section 6.1**. Tumouroids generated from both biopsies showed a response in the form of diminished viability to only one of the tested drugs, which was docetaxel. Two concentration response curves could be fitted to the data, and EC_{50}s of 149.2µM (PC08) and 163.7µM (PC09) were established. The concentration response curves showed a concentration dependent increase in disaggregation and a reduction in viability. However, the EC_{50}s established here exceed the docetaxel plasma concentrations that can be achieved safely in human patients during treatments (5-10 µg L^{-1}, Clarke and Rivory, 1999), and as such have limited translational value. The efficacy data generated during this project for both patient

biopsies and LNCaP cells, suggests a limited sensitivity of the PC08 and PC09 tumouroids to docetaxel, which could be the result of non-specific toxicity.

7.5 Heterogeneous biopsy-derived spheroids as physiologically relevant tumour models

In this study, patient-derived prostate biopsies were expanded and then dissociated into a single-cell suspension, which was used to generate 3D patient-derived spheroids. The advantage of the approach used here is the maintenance of several cell types which are originally found in the tumour, mimicking the cellular diversity of in vivo tumour tissue, which can contribute to tumour progression and drug resistance. Using this approach, the tumour ECM and original tissue configuration was not maintained, which could be a disadvantage if the maintenance of resident immune cells was required for immunotherapy testing, or the screening of drugs targeting matrix proteins. However, for functional assays for application in precision medicine, 3D tumour models generated from patient-derived single cell suspensions have been shown in several studies to predict clinical responses with an accuracy of more than 80% (Halfter et al., 2016; Halfter and Mayer, 2017).

For applications which require the maintenance of all resident cells in their native tissue organisation, including the tumour ECM, tissue fragment and tissue slice can be created from patient tumour tissue, as described in Chapter 1. Nagourney et al. (2012) and Jung et al. (2013) both showed the use of tumour fragments for precision medicine and tested a small number of drugs, 16 and 11 respectively, on these patient-derived tumour fragments. The results of these screens were highly predictive and the assay-guided therapy of patients resulted in a significant improvement in patient outcomes (Nagourney et al., 2012; Jung et al., 2013).

A further study by Karekla et al., which used large tumour fragments of approximately 500µm size, was able to show that the fragment tissue response to cisplatin correlated with patient survival. Additionally, laser ablation could be used to visualise the spatial distribution of cisplatin in the tissue fragment, which in combination with

immunohistochemistry assays revealed which cells had taken up cisplatin throughout the tumour. Recent studies have shown that even resident immune cells can be maintained in tumour fragment cultures, which can be used for personalised screening of immunotherapy drugs, such as checkpoint inhibitors (Jenkins et al., 2018). However, due to the large size of tumour fragments, the number of possible drug screens is extremely limited, which reduces their applicability to large screens for precision medicine. The benefits of using large tumour fragments are mainly connected to the maintenance of most resident cells and the ECM, which allows the screening of immunomodulatory drugs, and can provide considerable insights into drug mechanisms. Additionally, explant culture allow the assessment of drug penetration of tumour tissue, while maintaining a high degree of physiological relevance (Karekla et al., 2017; Centenera et al., 2018). A different approach to the drug screening of intact patient tissue is the use of tissue slices of approximately 300µm thickness, which can be maintained in culture viably for several days (Martin et al., 2019). Similar to fragments, these slices maintain the intratumoural heterogeneity of cells and the tissue architecture, providing a physiologically relevant model for drug and immunotherapy efficacy testing. However, assays involving tissue slices are limited by the decline in viability of the tissue slices, which is eventually observed in most cultures, due to the lack of vascularisation and the extensive damage resulting from microtome or vibratome slicing. As a result, drug screening assays of patient-derived tissue slices usually do not exceed a culture duration of 3 days, which limits the effects of drugs that can be observed in vitro to immediate toxicity, whereas growth-inhibiting or enhancing effects cannot be observed.

However, the need for physiologically relevant tumour models utilising patient tissue remains, especially for the efficacy testing of immunotherapies, EMT- or ECM-targeting drugs and mechanistic studies. For these applications, primary tumour slice and fragment cultures remain an invaluable model, which reflects inter- and intratumoural heterogeneity, while maintains the tumour microenvironment of the parent tumour. However, the lack of long-term viability and the small number of drug screens which can be performed on fragments and slices, still necessitates the use of

other patient-derived tumour models for large screens for precision medicine. Despite the lack of the native ECM and immune cells, tumouroids derived from suspensions of patient tumours are capable of producing predictive results in functional assays of anticancer drugs, whilst enabling a larger number of drug assays to be conducted (Halfter and Mayer, 2017). Therefore, unless the presence of resident immune cells or the ECM is required for the application of the model, spheroids derived from single cell suspension can explore a larger number of possible drug treatments for use in precision medicine.

The device reported here could also be applied to the screening of patient-derived tumour fragments for essays which require the presence of resident immune cells., In its current design, the microfluidic device reported here could accommodate tumour fragments of up to 100µm size, which could be applied to the testing of immune checkpoint inhibitor drugs that act on resident immune cells. Further, the device could easily be adapted by increasing the depth of the central cell culture channel to trap tumour fragments larger than 200 µm, for drug efficacy testing using the microfluidic concentration gradient.

7.6 Advantages of miniaturisation using microfluidic technologies

The miniaturisation of cytotoxicity assays performed in ultra-low adhesion conditions, which resulted in the design of the microfluidic device described in this work, had several benefits. Firstly, a reduced number of cells and reagents was required for the generation and culture of a large number of spheroids, when compared to 96-well plates and other microfluidic platforms (Ruppen et al., 2015). Further, in order to seed spheroids in all 240 microwells of one microfluidic device, only 4 pipetting steps had to be conducted to fill the micro-well array. In order to generate the same number of spheroids in an ultra-low adhesion 96-well plate, at least 240 pipetting steps would have to be performed to generate the same number of spheroids. If the biopsy-screen of PC08, which allowed the seeding of 22 devices, was conducted using conventional ultra-low adhesion 96-well plates, an equivalent of 32 96-well plates would have to be seeded in order to provide a similar number of tested conditions and replicates. Irrespective of the cost of ultra-low adhesion plates, the entirety of

the biopsy-drug screens was conducted simultaneously and by a single person. In order to perform a screening assay of the same size, using 32 96-well plates, robotic dispensing would be required.

Additionally, the miniaturisation of the micro-well array allows a reduction in the number of images which needed to be acquired in order to monitor spheroid size and morphology over time. The field of view used for spheroid imaging allowed the capture of 64 150µm-micro-wells per image, which resulted in the acquisition of 792 images for the example of the drug efficacy testing of PC08-derived tumoroids. If conducted in 96-well plates, daily brightfield imaging of every tumoroid would require the acquisition of 36864 images over the duration of the experiment, and over 3000 images per day of culture. Understandably, this is not feasible in most laboratory environments which do not have extensive automated equipment. The microfluidic platform developed in chapter 3 demonstrated a significant improvement in throughput, ease of operation and efficient use of limited cell material. Using this microfluidic platform, up to 22 conditions could be screened using microfluidic concentration gradients, which exceeds the number of possible screens reported in other publications, due to the efficient use of cellular material and miniaturisation (Nagourney et al., 2012; Ruppen et al., 2015; Akay et al., 2018).

7.7 Label-free readouts provide advantages

In all experiments conducted for this work, spheroids were monitored every 24-48 hours using brightfield microscopy. This initially allowed the quantification of each spheroid's size over time, and the spheroid size change observed during an experiment, which is frequently used as a measure of drug efficacy. However, it is not reliable when the integrity of a spheroid is compromised and disaggregation occurs (Patra et al., 2016). In order to increase the amount of information obtained from brightfield images of tumour spheroids, the label-free readout of the shape factor was established. The shape factor is a label-free non-destructive measure of spheroid health, and easily calculated using each spheroid's area and perimeter length (Kelm

et al., 2003; De Wever et al., 2010; Estrada et al., 2015; Zanoni et al., 2016). Using cell line derived spheroids, as well as patient-derived tumoroids, we demonstrated the suitability of the shape factor as a sensitive indicator of a spheroid's response to a drug, which can add additional value to brightfield images acquired. Since the calculation of the shape factor does not require the application of a label or dye, which would be an end-point-measurement, it provides an entirely non-destructive readout of spheroid health by quantifying disaggregation. If dyes were used to assess spheroid or tumouroid viability every 24 hours, a screen would require one device of each treatment condition to be stained and terminated every day, which would limit the number of possible screens in the context of precision medicine.

The importance of a frequent assessment of tumouroid integrity is highlighted in Chapter 6 (**Figure 6.7**), where the first application of a repeated docetaxel concentration gradient resulted only in a transient increase in shape factor by day 4 in the row of PC08-tumoroids containing the highest concentration of docetaxel (108.8µM). However, by day 8, the viability was consistent across the entire docetaxel concentration range applied and no concentration-dependent change in shape factor was detected. If viability staining was the only available readout for the efficacy of the applied docetaxel concentration gradient, no adverse effect on the spheroids could have been detected. Further, the example of **Figure 6.7** in Chapter 6 shows that tumoroid disaggregation continued to increase for 3 days following the second docetaxel gradient application. This highlights how the choice of the day for end-point analysis could affect the concentration-response curve and IC50 obtained, and as a consequence, a suitable day for end-point analysis needs to be determined carefully.

These examples demonstrate the added value of just one additional phenotypic descriptor, the spheroid shape, as an early indicator for disaggregation, when combined with measurements of spheroid size and viability. Härmä et al. (2014) showed how extensive phenotypic screening using brightfield imagines in combination with additional phenotypic descriptors such as intensity, organoid wall thickness, lumen size, and the shape and length of outgrowing protrusions could be used to generate a

multiparametric profile of spheroid drug responses. This study utilised 21 phenotypic descriptors of certain spheroid and tumoroid features in an extensive computing effort. By considering 21 different readouts in the analysis, a detailed drug response profile could be created for each drug's effect on the parameters (Härmä et al. (2014). Multiparametric profiles are sensitive to dynamic changes in tumour spheroids, such as invasion and differentiation, which result in changes in morphology. And while viability assessment or the measurement of cell death remains one of the most important readouts of cancer cell killing, the detection of other morphological changes, such as the loss of organoid lumens or a decrease in invasive behaviour, could indicate drug effects beyond cytotoxicity. As such, utilising phenotypic descriptors in multiparametric analysis, the drug effects on processes such as invasion and differentiation can be quantified, which captures a more complete picture of complex drug responses. In the future, further descriptors of spheroid morphology, such as intensity, hollowness, and the number of attached aggregates could be incorporated into the Matlab analysis software developed for this project, to better quantify the changes observed in the patient-derived tumoroids, such as lumen formation, protrusion and aggregates of several spheroids.

The importance of the incorporation of several readouts for the assessment of drug effects was demonstrated in Chapter 6 (**Figure 6.8**), where it was shown that patient-derived tumoroids (PC09) did not decrease in size in response to a docetaxel concentration gradient, but showed a concentration dependent increase in shape factor, indicating decreasing roundness and increasing disaggregation. LNCaP spheroids on the other hand, did not show any changes in spheroid shape, but decreased in size after incubation with a docetaxel gradient (**Figure 6.10**). Finally, viability staining showed that spheroid viability was similarly affected in both types of spheroids, which shows that neither spheroid size on its own, nor the spheroid shape factor can serve as a single readout to describe the effect of docetaxel for both types of spheroids. Therefore, the incorporation of multiparametric readouts of dynamic phenotypic changes could be used to mitigate the risks of misinterpreting drug effects based on single readouts.

7.8 Conclusion and future work

Due to the lack of better models and protocols, there is an ongoing need for rapid and predictive ways to profile patient tumours, in order to stratify patients appropriately and provide precision medicine solutions. However, a large amount of anticancer therapy testing relies on animal models and the expansion of patient-derived tissue within animals to create patient-derived xenografts (PDX). In order to generate patient-derived xenografts, patient-derived tumour cells are implanted into an immunodeficient nude mice (Pauli et al., 2017). Both animal studies as well as PDX-derived in vitro essays are resource-intensive and require a lot of time and expertise. The microfluidic platform developed in this work and the associated protocols offer a new solution for medium- to large-throughput anticancer agent screening of 3D tumoroids generated from patient-derived biopsy tissue. We anticipate applications of the platform presented here in the screening of biopsy tissue, which contains a very small number of cells, such as fine needle aspirates, which could aid precision medicine, adaptive clinical trials and drug discovery efforts. Additionally, since patient-derived cells appeared to form organoid-like aggregates in the microfluidic platform in suspension cultures without BME, it is conceivable that the benefits of efficient drug screening using this platform could be applied to the screening of patient-derived organoids. This could take the form of suspension culture utilising a small concentration of BME, or could be in the form of a solid matrix that can be introduced into the platform, which is currently being developed.

Further, the easy application of a single drug concentration gradient to an array of tumoroids, suggests the applicability of our technology to combinatorial drug screening, which is currently being developed using this platform. Despite the prevalence of combination therapy treatments in clinic and in vitro, the combinatorial drug screening of patient derived tumoroids remains challenging, due to the large number of cells required. By combining drug concentration gradients in several ways, it is possible to obtain spheroid responses across a large part of a drug combination matrix. Beyond combination therapy screening of two or more anticancer compounds, it is

conceivable that our system could improve and enable extensive screening of combination chemo- and radiotherapy, as well as cell-based immunotherapy in patient-derived tissue, offering a novel strategy for personalised medicine.

8 References

Akay, M., Hite, J., Avci, N.G., Fan, Y., Akay, Y., Lu, G., et al. (2018). Drug Screening of Human GBM Spheroids in Brain Cancer Chip. Scientific Reports *8*: 1–9.

Aref, A.R., Huang, R.Y.J., Yu, W., Chua, K.N., Sun, W., Tu, T.Y., et al. (2013). Screening therapeutic EMT blocking agents in a three-dimensional microenvironment. Integrative Biology (United Kingdom) *5*: 381–389.

Ashley, E.A. (2016). Towards precision medicine. Nature Reviews Genetics *17*: 507–522.

Aubrey, B.J., Strasser, A., and Kelly, G.L. (2016). Tumor-suppressor functions of the TP53 pathway. Cold Spring Harbor Perspectives in Medicine *6*:.

Baek, N., Seo, O.W., Lee, J., Hulme, J., and An, S.S.A. (2016). Real-time monitoring of cisplatin cytotoxicity on three-dimensional spheroid tumor cells. Drug Design, Development and Therapy *10*: 2155–2165.

Balkwill, F.R., Capasso, M., and Hagemann, T. (2012). The tumor microenvironment at a glance. Journal of Cell Science *125*: 5591–5596.

Beebe, D.J., Mensing, G. a, and Walker, G.M. (2002). Physics and applications of microfluidics in biology. In Annual Review of Biomedical Engineering, pp 261–86.

Beer, T.M., Armstrong, A.J., Rathkopf, D.E., Loriot, Y., Sternberg, C.N., Higano, C.S., et al. (2014). Enzalutamide in Metastatic Prostate Cancer before Chemotherapy. New England Journal of Medicine *371*: 424–433.

Bennett, D.C., Cooper, P.J., and Hart, I.R. (1987). A line of non-tumorigenic mouse melanocytes, syngeneic with the B16 melanoma and requiring a tumour promoter for growth. International Journal of Cancer *39*: 414–418.

Benton, G., Arnaoutova, I., George, J., Kleinman, H.K., and Koblinski, J. (2014). Matrigel: From discovery and ECM mimicry to assays and models for cancer research. Advanced Drug Delivery Reviews.

Benton, G., Kleinman, H.K., George, J., and Arnaoutova, I. (2011). Multiple uses of basement membrane-like matrix (BME/Matrigel) in vitro and in vivo with cancer cells. International Journal of Cancer *128*: 1751–1757.

Binnewies, M., Roberts, E.W., Kersten, K., Chan, V., Fearon, D.F., Merad, M., et al. (2018). Understanding the tumor immune microenvironment (TIME) for effective therapy. Nature Medicine *24*: 541–550.

Bissell, M.J., Rizki, A., and Mian, I.S. (2003). Tissue architecture: The ultimate regulator of breast epithelial function. Current Opinion in Cell Biology *15*: 753–762.

Boumber, Y. (2018). Tumor mutational burden (TMB) as a biomarker of response to immunotherapy in small cell lung cancer. Journal of Thoracic Disease *10*: 4689–4693.

Boyd, A. Livingstone, L. E. Wilson, M. (2000). Dose-response relationship for radiation-induced mutations at micro- and minisatellite loci in human somatic cells in culture. International Journal of Radiation Biology *76*: 169–176.

Bozic, I., Antal, T., Ohtsuki, H., Carter, H., Kim, D., Chen, S., et al. (2010). Accumulation of driver and passenger mutations during tumor progression. Proceedings of the National Academy of Sciences *107*: 18545–18550.

Breslin, S., and O'Driscoll, L. (2013). Three-dimensional cell culture: the missing link in drug discovery. Drug Discovery Today *18*: 240–9.

Brody, J.P., Yager, P., Goldstein, R.E., and Austin, R.H. (1996). Biotechnology at low Reynolds numbers. Biophysical Journal *71*: 3430–41.

Brown, J.M., and Giaccia, A.J. (1998). The unique physiology of solid tumors: opportunities (and problems) for cancer therapy. Cancer Research *58*: 1408–16.

Burstein, H.J., Mangu, P.B., Somerfield, M.R., Schrag, D., Samson, D., Holt, L., et al. (2011). American Society of Clinical Oncology clinical practice guideline update on the Use of chemotherapy sensitivity and resistance assays. Journal of Clinical Oncology

29: 3328–3330.

Butera, G., Pacchiana, R., and Donadelli, M. (2018). Autocrine mechanisms of cancer chemoresistance. Seminars in Cell and Developmental Biology *78*: 3–12.

Campisi, J. (2013). Aging, cellular senescence, and cancer. Annual Review of Physiology *75*: 685–705.

Carmeliet, P., and Jain, R.K. (2000). Angiogenesis in cancer and other diseases. Nature *407*: 249–57.

Carnero, A., and Lleonart, M. (2016). The hypoxic microenvironment: A determinant of cancer stem cell evolution. Inside the Cell *1*: 96–105.

Cassidy, J.W., Caldas, C., and Bruna, A. (2015). Maintaining tumor heterogeneity in patient-derived tumor xenografts. Cancer Research *75*: 2963–2968.

Centenera, M.M., Hickey, T.E., Jindal, S., Ryan, N.K., Ravindranathan, P., Mohammed, H., et al. (2018). A patient-derived explant (PDE) model of hormone-dependent cancer. Molecular Oncology *12*: 1608–1622.

Chambers, K.F., Mosaad, E.M.O., Russell, P.J., Clements, J. a., and Doran, M.R. (2014). 3D Cultures of Prostate Cancer Cells Cultured in a Novel High-Throughput Culture Platform Are More Resistant to Chemotherapeutics Compared to Cells Cultured in Monolayer. PLoS ONE *9*: e111029.

Chen, X., and Song, E. (2019). Turning foes to friends: targeting cancer-associated fibroblasts. Nature Reviews Drug Discovery *18*: 99–115.

Cheng, Y.-H., Chen, Y.-C., Brien, R., and Yoon, E. (2016). Scaling and Automation of High-Throughput Single-Cell-Derived Tumor Sphere Assay Chip. Lab Chip 15–17.

Cheung-Ong, K., Giaever, G., and Nislow, C. (2013). DNA-Damaging Agents in Cancer Chemotherapy: Serendipity and Chemical Biology. Chemistry & Biology *20*: 648–659.

Chou, T.C. (2010). Drug combination studies and their synergy quantification using the chou-talalay method. Cancer Research *70*: 440–446.

Chua, C.W., Shibata, M., Lei, M., Toivanen, R., Barlow, L.J., Bergren, S.K., et al. (2014).

Single luminal epithelial progenitors can generate prostate organoids in culture. Nature Cell Biology *16*: 951–61, 1–4.

Cioffi, M., Moretti, M., Manbachi, A., Chung, B.G., Khademhosseini, A., and Dubini, G. (2010). A computational and experimental study inside microfluidic systems: the role of shear stress and flow recirculation in cell docking. Biomedical Microdevices *12*: 619–626.

Clarke, S.J., and Rivory, L.P. (1999). Clinical pharmacokinetics of docetaxel. Clinical Pharmacokinetics *36*: 99–114.

Crona, D.J., and Whang, Y.E. (2017). Androgen receptor-dependent and -independent mechanisms involved in prostate cancer therapy resistance. Cancers *9*:.

Crusz, S.M., and Balkwill, F.R. (2015). Inflammation and cancer: Advances and new agents. Nature Reviews Clinical Oncology *12*: 584–596.

Dalmau, E., Armengol-Alonso, A., Muñoz, M., and Seguí-Palmer, M.Á. (2014). Current status of hormone therapy in patients with hormone receptor positive (HR+) advanced breast cancer. Breast *23*: 710–720.

Dehm, S.M., and Tindall, D.J. (2005). Regulation of androgen receptor signaling in prostate cancer. Expert Review of Anticancer Therapy *5*: 63–74.

Dhiman, N., Kingshott, P., Sumer, H., Sharma, C.S., and Rath, S.N. (2019). On-Chip Anticancer Drug Screening – Recent Progress in Microfluidic Platforms to Address Challenges in Chemotherapy. Biosensors and Bioelectronics.

Dienstmann, R., Jang, I.S., Bot, B., Friend, S., and Guinney, J. (2015). Database of genomic biomarkers for cancer drugs and clinical targetability in solid tumors. Cancer Discovery *5*: 118–123.

Dijkstra, K.K., Cattaneo, C.M., Weeber, F., Chalabi, M., Haar, J. van de, Fanchi, L.F., et al. (2018). Generation of Tumor-Reactive T Cells by Co-culture of Peripheral Blood Lymphocytes and Tumor Organoids. Cell *174*: 1586-1598.e12.

DiMasi, J.A., Grabowski, H.G., and Hansen, R.W. (2016). Innovation in the pharmaceutical industry: New estimates of R&D costs. Journal of Health Economics

47: 20–33.

Dobrolecki, L.E., Airhart, S.D., Alferez, D.G., Aparicio, S., Behbod, F., Bentires-Alj, M., et al. (2016). Patient-derived xenograft (PDX) models in basic and translational breast cancer research. Cancer and Metastasis Reviews *35*: 547–573.

Dolega, M.E., Abeille, F., Picollet-D'hahan, N., and Gidrol, X. (2015). Controlled 3D culture in Matrigel microbeads to analyze clonal acinar development. Biomaterials *52*: 347–357.

Dongre, A., and Weinberg, R.A. (2019). New insights into the mechanisms of epithelial–mesenchymal transition and implications for cancer. Nature Reviews Molecular Cell Biology *20*: 69–84.

Dougan, M., Dranoff, G., and Dougan, S.K. (2019). Cancer Immunotherapy: Beyond Checkpoint Blockade. Annual Review of Cancer Biology *3*: 55–75.

Dracham, C.B., Shankar, A., and Madan, R. (2018). Radiation induced secondary malignancies: A review article. Radiation Oncology Journal *36*: 85–94.

Drost, J., and Clevers, H. (2018). Organoids in cancer research. Nature Reviews Cancer *18*: 407–418.

Drost, J., Karthaus, W.R., Gao, D., Driehuis, E., Sawyers, C.L., Chen, Y., et al. (2016). Organoid culture systems for prostate epithelial and cancer tissue. Nature Protocols *11*: 347–358.

Duda, D.G., Duyverman, A.M.M.J., Kohno, M., Snuderl, M., Steller, E.J.A., Fukumura, D., et al. (2010). Malignant cells facilitate lung metastasis by bringing their own soil. Proceedings of the National Academy of Sciences of the United States of America *107*: 21677–21682.

Duffy, D.C., McDonald, J.C., Schueller, O.J.A., and Whitesides, G.M. (1998). Rapid Prototyping of Microfluidic Systems in Poly(dimethylsiloxane). Analytical Chemistry *70*: 4974–4984.

Eder, T., Weber, A., Neuwirt, H., Grünbacher, G., Ploner, C., Klocker, H., et al. (2016). Cancer-associated fibroblastsmodify the response of prostate cancer cells to

androgen and anti-androgens in three-dimensional spheroid culture. International Journal of Molecular Sciences *17*: 1–15.

Eduati, F., Utharala, R., Madhavan, D., Neumann, U.P., Longerich, T., Cramer, T., et al. (2018). A microfluidics platform for combinatorial drug screening on cancer biopsies. Nature Communications *9*:.

Eisinger, M., and Marko, O. (1982). Selective proliferation of normal human melanocytes in vitro in the presence of phorbol ester and cholera toxin. Proceedings of the National Academy of Sciences *79*: 2018–2022.

Estrada, M.F., Rebelo, S.P., Davies, E.J., Pinto, M.T., Pereira, H., Santo, V.E., et al. (2015). Modelling the tumour microenvironment in long-term microencapsulated 3D co-cultures recapitulates phenotypic features of disease progression. Biomaterials.

Fan, Y., Nguyen, D.T., Akay, Y., Xu, F., and Akay, M. (2016). Engineering a Brain Cancer Chip for High-throughput Drug Screening. Scientific Reports *6*: 25062.

Fanale, D., Maragliano, R., Bazan, V., and Russo, A. (2017). Caretakers and Gatekeepers. ELS 1–10.

Fares, J., Fares, M.Y., Khachfe, H.H., Salhab, H.A., and Fares, Y. (2020). Molecular principles of metastasis: a hallmark of cancer revisited. Signal Transduction and Targeted Therapy *5*:.

Farkona, S., Diamandis, E.P., and Blasutig, I.M. (2016). Cancer immunotherapy: The beginning of the end of cancer? BMC Medicine *14*: 1–18.

Fatehullah, A., Tan, S.H., and Barker, N. (2016). Organoids as an in vitro model of human development and disease. Nature Cell Biology *18*: 246–254.

Ferreira, L.P., Gaspar, V.M., and Mano, J.F. (2018). Design of spherically structured 3D in vitro tumor models -Advances and prospects. Acta Biomaterialia *75*: 11–34.

Frame, F.M., Pellacani, D., Collins, A.T., and Maitland, N.J. (2016). Harvesting human prostate tissue material and culturing primary prostate epithelial cells. Methods in Molecular Biology *1443*: 181–201.

Frey, D.M., Droeser, R.A., Viehl, C.T., Zlobec, I., Lugli, A., Zingg, U., et al. (2010). High frequency of tumor-infiltrating FOXP3+ regulatory T cells predicts improved survival in mismatch repair-proficient colorectal cancer patients. International Journal of Cancer *126*: 2635–2643.

Frey, O., Misun, P.M., Fluri, D. a, Hengstler, J.G., and Hierlemann, A. (2014). Reconfigurable microfluidic hanging drop network for multi-tissue interaction and analysis. Nature Communications *5*: 4250.

Fridman, W.H., Pagès, F., Sautès-Fridman, C., and Galon, J. (2012). The immune contexture in human tumours: impact on clinical outcome. Nature Reviews Cancer *12*: 298–306.

Friedman, A.A., Letai, A., Fisher, D.E., and Flaherty, K.T. (2015). Precision medicine for cancer with next-generation functional diagnostics. Nature Reviews Cancer *15*: 747–756.

Friedrich, J., Seidel, C., Ebner, R., and Kunz-Schughart, L. a (2009). Spheroid-based drug screen: considerations and practical approach. Nature Protocols *4*: 309–324.

Frimat, J.-P., Sisnaiske, J., Subbiah, S., Menne, H., Godoy, P., Lampen, P., et al. (2010). The network formation assay: a spatially standardized neurite outgrowth analytical display for neurotoxicity screening. Lab on a Chip *10*: 701–709.

Galluzzi, L., Buqué, A., Kepp, O., Zitvogel, L., and Kroemer, G. (2017). Immunogenic cell death in cancer and infectious disease. Nature Reviews Immunology *17*: 97–111.

Gao, D., Vela, I., Sboner, A., Iaquinta, P.J., Karthaus, W.R., Gopalan, A., et al. (2014). Organoid Cultures Derived from Patients with Advanced Prostate Cancer. Cell *159*: 176–187.

Gascoigne, K.E., and Taylor, S.S. (2009). How do anti-mitotic drugs kill cancer cells? Journal of Cell Science *122*: 2579–2585.

Gatenby, R.A., and Gillies, R.J. (2004). Why do cancers have high aerobic glycolysis? Nature Reviews Cancer *4*: 891–899.

Ghebranious, N., and Donehower, L.A. (1998). Mouse models in tumor suppression.

Oncogene *17*: 3385–3400.

Gibbons, J.A., Ouatas, T., Krauwinkel, W., Ohtsu, Y., Walt, J.S. van der, Beddo, V., et al. (2015). Clinical Pharmacokinetic Studies of Enzalutamide. Clinical Pharmacokinetics *54*: 1043–1055.

Gieniec, K.A., Butler, L.M., Worthley, D.L., and Woods, S.L. (2019). Cancer-associated fibroblasts—heroes or villains? British Journal of Cancer *121*: 293–302.

Gitlin, L., Schulze, P., and Belder, D. (2009). Rapid replication of master structures by double casting with PDMS. Lab on a Chip *9*: 3000.

Gleave, A.M., Ci, X., Lin, D., and Wang, Y. (2020). A synopsis of prostate organoid methodologies, applications, and limitations. Prostate *80*: 518–526.

Godugu, C., Patel, A.R., Desai, U., Andey, T., Sams, A., and Singh, M. (2013). AlgiMatrix™ Based 3D Cell Culture System as an In-Vitro Tumor Model for Anticancer Studies. PLoS ONE *8*:.

Gökaltun, A., Kang, Y.B. (Abraham), Yarmush, M.L., Usta, O.B., and Asatekin, A. (2019). Simple Surface Modification of Poly(dimethylsiloxane) via Surface Segregating Smart Polymers for Biomicrofluidics. Scientific Reports *9*: 1–14.

Golshayan, A.R., and Antonarakis, E.S. (2013). Enzalutamide: an evidence-based review of its use in the treatment of prostate cancer. Core Evidence *8*: 27–35.

Gomez-Sjoberg, R., Leyrat, A.A., Houseman, B.T., Shokat, K., and Quake, S.R. (2010). Biocompatibility and Reduced Drug Absorption of Sol−Gel-Treated Poly(dimethyl siloxane) for Microfluidic Cell Culture Applications. Analytical Chemistry *82*: 8954–8960.

Gracz, A.D., Williamson, I.A., Roche, K.C., Johnston, M.J., Wang, F., Wang, Y., et al. (2015). A high-throughput platform for stem cell niche co-cultures and downstream gene expression analysis. Nat Cell Biol *17*: 340–349.

Griffith, L.G., and Swartz, M.A. (2006). Capturing complex 3D tissue physiology in vitro. Nature Reviews Molecular Cell Biology *7*: 211–224.

Griguolo, G., Pascual, T., Dieci, M.V., Guarneri, V., and Prat, A. (2019). Interaction of host immunity with HER2-targeted treatment and tumor heterogeneity in HER2-positive breast cancer. Journal for ImmunoTherapy of Cancer *7*: 1–14.

Groebe, K., Erz, S., and Mueller-Klieser, W. (1994). Glucose diffusion coefficients determined from concentration profiles in EMT6 tumor spheroids incubated in radioactively labeled L-glucose. Advances in Experimental Medicine and Biology *361*: 619–625.

Groot, J.F. De, Fuller, G., Kumar, A.J., Piao, Y., Eterovic, K., Ji, Y., et al. (2010). Tumor invasion after treatment of glioblastoma with bevacizumab: Radiographic and pathologic correlation in humans and mice. Neuro-Oncology *12*: 233–242.

Grundy, T.J., Leon, E. De, Griffin, K.R., Stringer, B.W., Day, B.W., Fabry, B., et al. (2016). Differential response of patient-derived primary glioblastoma cells to environmental stiffness. Scientific Reports *6*: 23353.

Hafner, A., Bulyk, M.L., Jambhekar, A., and Lahav, G. (2019). The multiple mechanisms that regulate p53 activity and cell fate. Nature Reviews Molecular Cell Biology *20*: 199–210.

Hager, S., Ackermann, C.J., Joerger, M., Gillessen, S., and Omlin, A. (2016). Anti-tumour activity of platinum compounds in advanced prostate cancer-a systematic literature review. Annals of Oncology *27*: 975–984.

Hainline, K.M., Gu, F., Handley, J.F., Tian, Y.F., Wu, Y., Wet, L. de, et al. (2019). Self-Assembling Peptide Gels for 3D Prostate Cancer Spheroid Culture. Macromolecular Bioscience *19*: 1800249.

Halfter, K., Hoffmann, O., Ditsch, N., Ahne, M., Arnold, F., Paepke, S., et al. (2016). Testing chemotherapy efficacy in HER2 negative breast cancer using patient-derived spheroids. Journal of Translational Medicine *14*: 1–14.

Halfter, K., and Mayer, B. (2017). Bringing 3D tumor models to the clinic – predictive value for personalized medicine. Biotechnology Journal *12*: 1–16.

Halldorsson, S., Lucumi, E., Gómez-Sjöberg, R., and Fleming, R.M.T. (2014).

Advantages and challenges of microfluidic cell culture in polydimethylsiloxane devices. Biosensors & Bioelectronics *63C*: 218–231.

Han, C., Zhang, Q., Ma, R., Xie, L., Qiu, T., Wang, L., et al. (2010). Integration of single oocyte trapping, in vitro fertilization and embryo culture in a microwell-structured microfluidic device. Lab on a Chip *10*: 2848.

Hanahan, D., and Coussens, L.M. (2012). Accessories to the Crime: Functions of Cells Recruited to the Tumor Microenvironment. Cancer Cell *21*: 309–322.

Hanahan, D., and Weinberg, R. a. (2000). The hallmarks of cancer. Cell *100*: 57–70.

Hanahan, D., and Weinberg, R.A. (2011). Hallmarks of Cancer: The Next Generation. Cell *144*: 646–674.

Härmä, V., Schukov, H.P., Happonen, A., Ahonen, I., Virtanen, J., Siitari, H., et al. (2014). Quantification of dynamic morphological drug responses in 3D organotypic cell cultures by automated image analysis. PLoS ONE *9*:.

Härmä, V., Virtanen, J., Mäkelä, R., Happonen, A., Mpindi, J.P., Knuuttila, M., et al. (2010). A comprehensive panel of three-dimensional models for studies of prostate cancer growth, invasion and drug responses. PLoS ONE *5*:.

Herbst, R.S., and Khuri, F.R. (2003). Mode of action of docetaxel – a basis for combination with novel anticancer agents. Cancer Treatment Reviews *29*: 407–415.

Higashiyama, M., Oda, K., Okami, J., Maeda, J., Kodama, K., Takami, K., et al. (2008). In vitro-chemosensitivity test using the collagen gel droplet embedded culture drug test (cd-dst) for malignant pleural mesothelioma: Possibility of clinical application. Annals of Thoracic and Cardiovascular Surgery *14*: 355–362.

Hollenberg, M.D., and Cuatrecasas, P. (1973). Epidermal growth factor: receptors in human fibroblasts and modulation of action by cholera toxin. Proceedings of the National Academy of Sciences of the United States of America *70*: 2964–8.

Holton, A.B., Sinatra, F.L., Kreahling, J., Conway, A.J., Landis, D.A., and Altiok, S. (2017). Microfluidic Biopsy Trapping Device for the Real-Time Monitoring of Tumor Microenvironment. PLOS ONE *12*: e0169797.

Horman, S.R., To, J., Lamb, J., Zoll, J.H., Leonetti, N., Tu, B., et al. (2017). Functional profiling of microtumors to identify cancer associated fibroblast-derived drug targets. Oncotarget *8*: 99913–99930.

Howes, A.L., Richardson, R.D., Finlay, D., and Vuori, K. (2014). 3-Dimensional Culture Systems for Anti-Cancer Compound Profiling and High-Throughput Screening Reveal Increases in EGFR Inhibitor-Mediated Cytotoxicity Compared to Monolayer Culture Systems. PloS One *9*: e108283.

Hwang, C. (2012). Overcoming docetaxel resistance in prostate cancer: A perspective review. Therapeutic Advances in Medical Oncology *4*: 329–340.

Iyer, V.R. (1999). The Transcriptional Program in the Response of Human Fibroblasts to Serum. Science *283*: 83–87.

James, A., Vincent, B., Sivadas, A., and Pavithran, K. (2018). A study on the clinical outcome of abiraterone acetate in castration resistant prostate cancer patients. International Journal of Hematology-Oncology and Stem Cell Research *12*: 4–7.

Jenkins, R.W., Aref, A.R., Lizotte, P.H., Ivanova, E., Stinson, S., Zhou, C.W., et al. (2018). Ex vivo profiling of PD-1 blockade using organotypic tumor spheroids. Cancer Discovery *8*: 196–215.

Jorgensen, J.H., and Ferraro, M.J. (2009). Antimicrobial Susceptibility Testing: A Review of General Principles and Contemporary Practices. Clinical Infectious Diseases *49*: 1749–1755.

Joseph, J.D., Lu, N., Qian, J., Sensintaffar, J., Shao, G., Brigham, D., et al. (2013). A clinically relevant androgen receptor mutation confers resistance to second-generation antiandrogens enzalutamide and ARN-509. Cancer Discovery *3*: 1020–1029.

Jung, P.S., Kim, D.Y., Kim, M.B., Lee, S.W., Kim, J.H., Kim, Y.M., et al. (2013). Progression-free survival is accurately predicted in patients treated with chemotherapy for epithelial ovarian cancer by the histoculture drug response assay in a prospective correlative clinical trial at a single institution. Anticancer Research

33: 1029–1034.

Junttila, M.R., and Sauvage, F.J. De (2013). Influence of tumour micro-environment heterogeneity on therapeutic response. Nature *501*: 346–354.

Karekla, E., Liao, W.J., Sharp, B., Pugh, J., Reid, H., Quesne, J. Le, et al. (2017). Ex Vivo explant cultures of non-small cell lung carcinoma enable evaluation of primary tumor responses to anticancer therapy. Cancer Research *77*: 2029–2039.

Karthaus, W.R., Iaquinta, P.J., Drost, J., Gracanin, A., Boxtel, R. van, Wongvipat, J., et al. (2014). Identification of Multipotent Luminal Progenitor Cells in Human Prostate Organoid Cultures. Cell *159*: 163–175.

Kelm, J.M., Timmins, N.E., Brown, C.J., Fussenegger, M., and Nielsen, L.K. (2003). Method for generation of homogeneous multicellular tumor spheroids applicable to a wide variety of cell types. Biotechnology and Bioengineering *83*: 173–180.

Kim, H., Phung, Y., and Ho, M. (2012). Changes in global gene expression associated with 3D structure of tumors: An ex vivo matrix-free mesothelioma spheroid model. PLoS ONE *7*:.

Kim, M., Mun, H., Sung, C.O., Cho, E.J., Jeon, H.J., Chun, S.M., et al. (2019). Patient-derived lung cancer organoids as in vitro cancer models for therapeutic screening. Nature Communications *10*:.

Kim, R., Emi, M., and Tanabe, K. (2007). Cancer immunoediting from immune surveillance to immune escape. Immunology *121*: 1–14.

Kim, S., Kim, H.J., and Jeon, N.L. (2010). Biological applications of microfluidic gradient devices. Integrative Biology *2*: 584.

Kleinman, H.K., and Martin, G.R. (2005). Matrigel: Basement membrane matrix with biological activity. Seminars in Cancer Biology *15*: 378–386.

Kodack, D.P., Farago, A.F., Dastur, A., Held, M.A., Dardaei, L., Friboulet, L., et al. (2017). Primary Patient-Derived Cancer Cells and Their Potential for Personalized Cancer Patient Care. Cell Reports *21*: 3298–3309.

Kogashiwa, Y., Sakurai, H., Kimura, T., and Kohno, N. (2010). Docetaxel suppresses invasiveness of head and neck cancer cells in vitro. Cancer Science *101*: 1382–1386.

Kolstad, P. (1968). Intercapillary distance, oxygen tension and local recurrence in cervix cancer. Scandinavian Journal of Clinical and Laboratory Investigation *21*: 145–157.

König, L., Mairinger, F.D., Hoffmann, O., Bittner, A.K., Schmid, K.W., Kimmig, R., et al. (2019). Dissimilar patterns of tumor-infiltrating immune cells at the invasive tumor front and tumor center are associated with response to neoadjuvant chemotherapy in primary breast cancer. BMC Cancer *19*: 1–13.

Konkel, J.E., Zhang, D., Zanvit, P., Chia, C., Zangarle-Murray, T., Jin, W., et al. (2017). Transforming Growth Factor-β Signaling in Regulatory T Cells Controls T Helper-17 Cells and Tissue-Specific Immune Responses. Immunity *46*: 660–674.

Kostarelos, K., Emfietzoglou, D., Papakostas, A., Yang, W.-H., Ballangrud, Å.M., and Sgouros, G. (2005). Engineering Lipid Vesicles of Enhanced Intratumoral Transport Capabilities: Correlating Liposome Characteristics with Penetration into Human Prostate Tumor Spheroids. Journal of Liposome Research *15*: 15–27.

Kross, K.W., Heimdal, J.H., Olsnes, C., Olofsson, J., and Aarstad, H.J. (2008). Co-culture of head and neck squamous cell carcinoma spheroids with autologous monocytes predicts prognosis. Scandinavian Journal of Immunology *67*: 392–399.

Krušlin, B., Ulamec, M., and Tomas, D. (2015). Prostate cancer stroma: An important factor in cancer growth and progression. Bosnian Journal of Basic Medical Sciences *15*: 1–8.

Kunz-Schughart, L. a, Freyer, J.P., Hofstaedter, F., and Ebner, R. (2004). The use of 3-D cultures for high-throughput screening: the multicellular spheroid model. Journal of Biomolecular Screening : The Official Journal of the Society for Biomolecular Screening *9*: 273–285.

Kwapiszewska, K., Michalczuk, A., Rybka, M., Kwapiszewski, R., and Brzózka, Z. (2014). A microfluidic-based platform for tumour spheroid culture, monitoring and drug

screening. Lab on a Chip *14*: 2096–104.

Lancaster, M.A., and Huch, M. (2019). Disease modelling in human organoids. DMM Disease Models and Mechanisms *12*:.

Landberg, G., Fitzpatrick, P., Isakson, P., Jonasson, E., Karlsson, J., Larsson, E., et al. (2020). Patient-derived scaffolds uncover breast cancer promoting properties of the microenvironment. Biomaterials *235*: 119705.

Laperrousaz, B., Porte, S., Gerbaud, S., Härmä, V., Kermarrec, F., Hourtane, V., et al. (2018). Direct transfection of clonal organoids in Matrigel microbeads: A promising approach toward organoid-based genetic screens. Nucleic Acids Research *46*:.

Lawler, S.E., Speranza, M.C., Cho, C.F., and Chiocca, E.A. (2017). Oncolytic viruses in cancer treatment a review. JAMA Oncology *3*: 841–849.

Lazzari, G., Nicolas, V., Matsusaki, M., Akashi, M., Couvreur, P., and Mura, S. (2018). Multicellular spheroid based on a triple co-culture: A novel 3D model to mimic pancreatic tumor complexity. Acta Biomaterialia *78*: 296–307.

Lee, D.W., Choi, Y.S., Seo, Y.J., Lee, M.Y., Jeon, S.Y., Ku, B., et al. (2014). High-throughput screening (HTS) of anticancer drug efficacy on a micropillar/microwell chip platform. Analytical Chemistry *86*: 535–542.

Leffers, N., Gooden, M.J.M., Jong, R.A. De, Hoogeboom, B.N., Hoor, K.A. Ten, Hollema, H., et al. (2009). Prognostic significance of tumor-infiltrating T-lymphocytes in primary and metastatic lesions of advanced stage ovarian cancer. Cancer Immunology, Immunotherapy *58*: 449–459.

Li, J.J., and Shen, M.M. (2019). Prostate stem cells and cancer stem cells. Cold Spring Harbor Perspectives in Medicine *9*: 1–16.

Liberti, M. V., and Locasale, J.W. (2016). The Warburg Effect: How Does it Benefit Cancer Cells? Trends in Biochemical Sciences *41*: 211–218.

Lim, W., and Park, S. (2018). A Microfluidic Spheroid Culture Device with a Concentration Gradient Generator for High-Throughput Screening of Drug Efficacy. Molecules *23*: 3355.

Linxweiler, J., Hammer, M., Muhs, S., Kohn, M., Pryalukhin, A., Veith, C., et al. (2019). Patient-derived, three-dimensional spheroid cultures provide a versatile translational model for the study of organ-confined prostate cancer. Journal of Cancer Research and Clinical Oncology *145*: 551–559.

Lipinski, M.M., and Jacks, T. (1999). The retinoblastoma gene family in differentiation and development. Oncogene *18*: 7873–7882.

Litwin, M.S., and Tan, H.J. (2017). The diagnosis and treatment of prostate cancer: A review. JAMA - Journal of the American Medical Association *317*: 2532–2542.

Ma, W.Y., Hsiung, L.C., Wang, C.H., Chiang, C.L., Lin, C.H., Huang, C.S., et al. (2015). A Novel 96well-formatted Micro-gap Plate Enabling Drug Response Profiling on Primary Tumour Samples. Scientific Reports *5*: 1–9.

Macdonald, V. (2009). Chemotherapy: Managing side effects and safe handling. Canadian Veterinary Journal *50*: 665–668.

Majety, M., Pradel, L.P., Gies, M., and Ries, C.H. (2015). Fibroblasts influence survival and therapeutic response in a 3D co-culture model. PLoS ONE *10*: 1–18.

Majumder, B., Baraneedharan, U., Thiyagarajan, S., Radhakrishnan, P., Narasimhan, H., Dhandapani, M., et al. (2015). Predicting clinical response to anticancer drugs using an ex vivo platform that captures tumour heterogeneity. Nature Communications *6*:.

Malhotra, V., and Perry, M.C. (2003). Classical Chemotherapy: Mechanisms, Toxicities and the Therapeutc Window. Cancer Biology & Therapy *2*: 1–3.

Martin, S.Z., Wagner, D.C., Hörner, N., Horst, D., Lang, H., Tagscherer, K.E., et al. (2019). Ex vivo tissue slice culture system to measure drug-response rates of hepatic metastatic colorectal cancer. BMC Cancer *19*: 1–14.

Martinez, M., and Moon, E.K. (2019). CAR T cells for solid tumors: New strategies for finding, infiltrating, and surviving in the tumor microenvironment. Frontiers in Immunology *10*: 1–21.

McCrea, E., Sissung, T.M., Price, D.K., Chau, C.H., and Figg, W.D. (2016). Androgen

receptor variation affects prostate cancer progression and drug resistance. Pharmacological Research *114*: 152–162.

McDonald, J.C., and Whitesides, G.M. (2002). Poly(dimethylsiloxane) as a Material for Fabricating Microfluidic Devices. Accounts of Chemical Research *35*: 491–499.

Medler, T.R., Cotechini, T., and Coussens, L.M. (2015). Immune Response to Cancer Therapy: Mounting an Effective Antitumor Response and Mechanisms of Resistance. Trends in Cancer *1*: 66–75.

Méhes, E., Biri-Kovács, B., Isai, D.G., Gulyás, M., Nyitray, L., and Czirók, A. (2019). Matrigel patterning reflects multicellular contractility. PLoS Computational Biology *15*: 1–28.

Mehling, M., and Tay, S. (2014). Microfluidic cell culture. Current Opinion in Biotechnology *25*: 95–102.

Melissaridou, S., Wiechec, E., Magan, M., Jain, M.V., Chung, M.K., Farnebo, L., et al. (2019). The effect of 2D and 3D cell cultures on treatment response, EMT profile and stem cell features in head and neck cancer 11 Medical and Health Sciences 1112 Oncology and Carcinogenesis. Cancer Cell International *19*: 1–10.

Memarzadeh, S., Xin, L., Mulholland, D.J., Mansukhani, A., Wu, H., Teitell, M.A., et al. (2007). Enhanced Paracrine FGF10 Expression Promotes Formation of Multifocal Prostate Adenocarcinoma and an Increase in Epithelial Androgen Receptor. Cancer Cell *12*: 572–585.

Minotti, G., Menna, P., Salvatorelli, E., Cairo, G., and Gianni, L. (2004). Anthracyclines: Molecular advances and pharmacologie developments in antitumor activity and cardiotoxicity. Pharmacological Reviews *56*: 185–229.

Mosaad, E.O., Chambers, K.F., Futrega, K., Clements, J.A., and Doran, M.R. (2018). The Microwell-mesh: A high-throughput 3D prostate cancer spheroid and drug-testing platform. Scientific Reports *8*: 1–12.

Mulholland, T., McAllister, M., Patek, S., Flint, D., Underwood, M., Sim, A., et al. (2018). Drug screening of biopsy-derived spheroids using a self-generated

microfluidic concentration gradient. Scientific Reports *8*: 14672.

Murata, M. (2018). Inflammation and cancer. Environmental Health and Preventive Medicine *23*:.

Nagourney, R.A., Blitzer, J.B., Shuman, R.L., Asciuto, T.J., Deo, E.A., Paulsen, M., et al. (2012). Functional profiling to select chemotherapy in untreated, advanced or metastatic non-small cell lung cancer. Anticancer Research *32*: 4453–4460.

Neal, J.T., Li, X., Zhu, J., Giangarra, V., Grzeskowiak, C.L., Ju, J., et al. (2018). Organoid Modeling of the Tumor Immune Microenvironment. Cell *175*: 1972-1988.e16.

Nebbioso, A., Tambaro, F.P., Dell'Aversana, C., and Altucci, L. (2018). Cancer epigenetics: Moving forward. PLoS Genetics *14*: 1–25.

Nelson, C.M., and Bissell, M.J. (2006). Of extracellular matrix, scaffolds, and signaling: tissue architecture regulates development, homeostasis, and cancer. Annual Review of Cell and Developmental Biology *22*: 287–309.

O'Donnell, J.S., Teng, M.W.L., and Smyth, M.J. (2019). Cancer immunoediting and resistance to T cell-based immunotherapy. Nature Reviews Clinical Oncology *16*: 151–167.

Oh, K.W., Lee, K., Ahn, B., and Furlani, E.P. (2012). Design of pressure-driven microfluidic networks using electric circuit analogy. Lab Chip *12*: 515–545.

Okamoto, K., and Seimiya, H. (2019). Revisiting Telomere Shortening in Cancer. Cells *8*: 107.

Onion, D., Argent, R.H., Reece-Smith, A.M., Craze, M.L., Pineda, R.G., Clarke, P.A., et al. (2016). 3-Dimensional Patient-Derived Lung Cancer Assays Reveal Resistance to Standards-of-Care Promoted by Stromal Cells but Sensitivity to Histone Deacetylase Inhibitors. Molecular Cancer Therapeutics *15*: 753–763.

Ooft, S.N., Weeber, F., Dijkstra, K.K., McLean, C.M., Kaing, S., Werkhoven, E. van, et al. (2019). Patient-derived organoids can predict response to chemotherapy in metastatic colorectal cancer patients. Science Translational Medicine *11*: eaay2574.

Pampaloni, F., Reynaud, E.G., and Stelzer, E.H.K. (2007). The third dimension bridges the gap between cell culture and live tissue. Nature Reviews. Molecular Cell Biology *8*: 839–845.

Pankova, D., Chen, Y., Terajima, M., Schliekelman, M.J., Baird, B.N., Fahrenholtz, M., et al. (2016). Cancer-associated fibroblasts induce a collagen cross-link switch in tumor stroma. Molecular Cancer Research *14*: 287–295.

Papapetrou, E.P. (2016). Patient-derived induced pluripotent stem cells in cancer research and precision oncology. Nature Medicine *22*: 1392–1401.

Paraiso, K.H.T., and Smalley, K.S.M. (2013). Fibroblast-mediated drug resistance in cancer. Biochemical Pharmacology *85*: 1033–1041.

Patra, B., Chen, Y.-H., Peng, C.-C., Lin, S.-C., Lee, C.-H., and Tung, Y.-C. (2013). A microfluidic device for uniform-sized cell spheroids formation, culture, harvesting and flow cytometry analysis. Biomicrofluidics *7*: 054114.

Patra, B., Peng, C.-C., Liao, W.-H., Lee, C.-H., and Tung, Y.-C. (2016). Drug testing and flow cytometry analysis on a large number of uniform sized tumor spheroids using a microfluidic device. Scientific Reports *6*: 21061.

Pauli, C., Hopkins, B.D., Prandi, D., Shaw, R., Fedrizzi, T., Sboner, A., et al. (2017). Personalized in vitro and in vivo cancer models to guide precision medicine. Cancer Discovery *7*: 462–477.

Payne, S.R., and Kemp, C.J. (2005). Tumor suppressor genetics. Carcinogenesis *26*: 2031–2045.

Pearson, G.W. (2019). Control of Invasion by Epithelial-to-Mesenchymal Transition Programs during Metastasis. Journal of Clinical Medicine *8*: 646.

Petrylak, D.P., Tangen, C.M., Hussain, M.H.A., Lara, P.N., Jones, J.A., Taplin, M.E., et al. (2004). Docetaxel and estramustine compared with mitoxantrone and prednisone for advanced refractory prostate cancer. New England Journal of Medicine *351*: 1513–1520.

Pfeffer, C.M., and Singh, A.T.K. (2018). Apoptosis: A target for anticancer therapy.

International Journal of Molecular Sciences *19*:.

Phan, N., Hong, J.J., Tofig, B., Mapua, M., Elashoff, D., Moatamed, N.A., et al. (2019). A simple high-throughput approach identifies actionable drug sensitivities in patient-derived tumor organoids. Communications Biology *2*: 78.

Pinto, A.C., Ades, F., Azambuja, E. de, and Piccart-Gebhart, M. (2013). Trastuzumab for patients with HER2 positive breast cancer: Delivery, duration and combination therapies. Breast *22*: S152–S155.

Powley, I.R., Patel, M., Miles, G., Pringle, H., Howells, L., Thomas, A., et al. (2020). Patient-derived explants (PDEs) as a powerful preclinical platform for anti-cancer drug and biomarker discovery. British Journal of Cancer *122*: 735–744.

Pretlow, T.G., Yang, B., and Pretlow, T.P. (1995). Organ culture of benign, aging, and hyperplastic human prostate. Microscopy Research and Technique *30*: 271–281.

Quail, D.F., and Joyce, J.A. (2013). Microenvironmental regulation of tumor progression and metastasis. Nature Medicine *19*: 1423–1437.

Quaresma, M., Coleman, M.P., and Rachet, B. (2015). 40-year trends in an index of survival for all cancers combined and survival adjusted for age and sex for each cancer in England and Wales, 1971-2011: A population-based study. The Lancet *385*: 1206–1218.

Rajer, M., and Kmet, M. (2005). Quantitative analysis of fine needle aspiration biopsy samples. Radiology and Oncology *39*: 269–272.

Ribatti, D. (2017). A revisited concept: Contact inhibition of growth. From cell biology to malignancy. Experimental Cell Research *359*: 17–19.

Richards, Z., McCray, T., Marsili, J., Zenner, M.L., Manlucu, J.T., Garcia, J., et al. (2019). Prostate Stroma Increases the Viability and Maintains the Branching Phenotype of Human Prostate Organoids. IScience *12*: 304–317.

Riffle, S., Pandey, R.N., Albert, M., and Hegde, R.S. (2017). Linking hypoxia, DNA damage and proliferation in multicellular tumor spheroids. BMC Cancer *17*: 338.

Robertson, G., Bushell, T.J., and Zagnoni, M. (2014). Chemically induced synaptic activity between mixed primary hippocampal co-cultures in a microfluidic system. Integrative Biology *6*: 636–644.

Roos, W.P., Thomas, A.D., and Kaina, B. (2016). DNA damage and the balance between survival and death in cancer biology. Nature Reviews Cancer *16*: 20–33.

Ruoslahti, E. (2002). Specialization of tumour vasculature. Nature Reviews Cancer *2*: 83–90.

Ruppen, J., Cortes-Dericks, L., Marconi, E., Karoubi, G., Schmid, R. a, Peng, R., et al. (2014). A microfluidic platform for chemoresistive testing of multicellular pleural cancer spheroids. Lab on a Chip *14*: 1198–205.

Ruppen, J., Wildhaber, F.D., Strub, C., Hall, S.R.R., Geiser, T., Schmid, R. a., et al. (2015). Towards personalized medicine: chemosensitivity assays of patient lung cancer cell spheroids in a perfused microfluidic platform. Lab Chip *15*: 3076–3085.

Sachs, N., and Clevers, H. (2014). Organoid cultures for the analysis of cancer phenotypes. Current Opinion in Genetics & Development *24*: 68–73.

Sackmann, E.K., Fulton, A.L., and Beebe, D.J. (2014). The present and future role of microfluidics in biomedical research. Nature *507*: 181–9.

Sakai, Y., Hattori, K., Yanagawa, F., Sugiura, S., Kanamori, T., and Nakazawa, K. (2014). Detachably assembled microfluidic device for perfusion culture and post-culture analysis of a spheroid array. Biotechnology Journal *9*: 971–979.

Sanjabi, S., Oh, S.A., and Li, M.O. (2017). Regulation of the immune response by TGF-β: From conception to autoimmunity and infection. Cold Spring Harbor Perspectives in Biology *9*: 1–34.

Schindelin, J., Arganda-Carreras, I., Frise, E., Kaynig, V., Longair, M., Pietzsch, T., et al. (2012). Fiji: an open-source platform for biological-image analysis. Nature Methods *9*: 676–682.

Schirrmacher, V. (2019). From chemotherapy to biological therapy: A review of novel concepts to reduce the side effects of systemic cancer treatment (Review).

International Journal of Oncology *54*: 407–419.

Schmidts, A., and Maus, M. V. (2018). Making CAR T cells a solid option for solid tumors. Frontiers in Immunology *9*: 1–10.

Schrodt, G.R., and Foreman, C.D. (1971). In vitro maintenance of human hyperplastic prostate tissue. Investigative Urology.

Seebacher, N.A., Stacy, A.E., Porter, G.M., and Merlot, A.M. (2019). Clinical development of targeted and immune based anti-cancer therapies (Journal of Experimental & Clinical Cancer Research).

Shuford, S., Wilhelm, C., Rayner, M., Elrod, A., Millard, M., Mattingly, C., et al. (2019). Prospective Validation of an Ex Vivo, Patient-Derived 3D Spheroid Model for Response Predictions in Newly Diagnosed Ovarian Cancer. Scientific Reports *9*: 1–13.

Siddik, Z.H. (2003). Cisplatin: mode of cytotoxic action and molecular basis of resistance. Oncogene *22*: 7265–79.

Snider, J.W., Datta, N.R., and Vujaskovic, Z. (2016). Hyperthermia and radiotherapy in bladder cancer. International Journal of Hyperthermia *32*: 398–406.

Steinmetz, M.O., and Prota, A.E. (2018). Microtubule-Targeting Agents: Strategies To Hijack the Cytoskeleton. Trends in Cell Biology *28*: 776–792.

Stonington, O.G., and Hemmingsen, H. (1971). Culture of Cells as a Monolayer Derived from the Epithelium of the Human Prostate: A New Cell Growth Technique. Journal of Urology *106*: 393–400.

Suarez-Carmona, M., Lesage, J., Cataldo, D., and Gilles, C. (2017). EMT and inflammation: inseparable actors of cancer progression. Molecular Oncology *11*: 805–823.

Sumbal, J., and Koledova, Z. (2019). FGF signaling in mammary gland fibroblasts regulates multiple fibroblast functions and mammary epithelial morphogenesis. Development (Cambridge) *146*:.

Sung, K.K.E., and Beebe, D.D.J. (2014). Microfluidic 3D models of cancer. Advanced

Drug Delivery Reviews 1–11.

Tan, M.E., Li, J., Xu, H.E., Melcher, K., and Yong, E. (2015). Androgen receptor: structure, role in prostate cancer and drug discovery. Acta Pharmacologica Sinica *36*: 3–23.

Tanenbaum, L.M., Mantzavinou, A., Subramanyam, K.S., Carmen, M.G. del, and Cima, M.J. (2017). Ovarian cancer spheroid shrinkage following continuous exposure to cisplatin is a function of spheroid diameter. Gynecologic Oncology *146*: 161–169.

Tannock, I.F., Wit, R. De, Berry, W.R., Horti, J., Pluzanska, A., Chi, K.N., et al. (2004). Docetaxel plus prednisone or mitoxantrone plus prednisone for advanced prostate cancer. New England Journal of Medicine *351*: 1502–1512.

Teng, M.W.L., Swann, J.B., Koebel, C.M., Schreiber, R.D., and Smyth, M.J. (2008). Immune-mediated dormancy: an equilibrium with cancer. Journal of Leukocyte Biology *84*: 988–993.

Thakuri, P.S., Ham, S.L., Luker, G.D., and Tavana, H. (2016). Multiparametric Analysis of Oncology Drug Screening with Aqueous Two-Phase Tumor Spheroids. Molecular Pharmaceutics *13*: 3724–3735.

Thoma, C.R., Zimmermann, M., Agarkova, I., Kelm, J.M., and Krek, W. (2014). 3D cell culture systems modeling tumor growth determinants in cancer target discovery. Advanced Drug Delivery Reviews *69–70*: 29–41.

Tolkach, Y., and Kristiansen, G. (2018). The Heterogeneity of Prostate Cancer: A Practical Approach. Pathobiology *85*: 108–116.

Tomonobu, N., Kinoshita, R., Sumardika, I.W., Chen, Y., Inoue, Y., Yamauchi, A., et al. (2019). Convenient methodology for extraction and subsequent selective propagation of mouse melanocytes in culture from adult mouse skin tissue. Biochemistry and Biophysics Reports *18*: 100619.

Tropmann, A., Tanguy, L., Koltay, P., Zengerle, R., and Riegger, L. (2012). Completely Superhydrophobic PDMS Surfaces for Microfluidics. Langmuir *28*: 8292–8295.

Tsui, J.H., Lee, W., Pun, S.H., Kim, J., and Kim, D. (2013). Microfluidics-assisted in vitro

drug screening and carrier production. Advanced Drug Delivery Reviews *65*: 1575–1588.

Tung, Y.-C., Lee, C.-H., and Patra, B. (2016). Microfluidic device for cell spheroid culture and analysis.

Urien, S., and Lokiec, F. (2004). Population pharmacokinetics of total and unbound plasma cisplatin in adult patients. British Journal of Clinical Pharmacology *57*: 756–763.

Vaira, V., Fedele, G., Pyne, S., Fasoli, E., Zadra, G., Bailey, D., et al. (2010). Preclinical model of organotypic culture for pharmacodynamic profiling of human tumors. Proceedings of the National Academy of Sciences of the United States of America *107*: 8352–8356.

Valente, K.P., Khetani, S., Kolahchi, A.R., Sanati-Nezhad, A., Suleman, A., and Akbari, M. (2017). Microfluidic technologies for anticancer drug studies. Drug Discovery Today *22*: 1654–1670.

Vazquez, A., Kamphorst, J.J., Markert, E.K., Schug, Z.T., Tardito, S., and Gottlieb, E. (2016). Cancer metabolism at a glance. Journal of Cell Science *129*: 3367–3373.

Viallard, C., and Larrivée, B. (2017). Tumor angiogenesis and vascular normalization: alternative therapeutic targets. Angiogenesis *20*: 409–426.

Vlachogiannis, G., Hedayat, S., Vatsiou, A., Jamin, Y., Fernández-Mateos, J., Khan, K., et al. (2018). Patient-derived organoids model treatment response of metastatic gastrointestinal cancers. Science *359*: 920–926.

Voskoglou-Nomikos, T., Pater, J.L., and Seymour, L. (2003). Clinical predictive value of the in vitro cell line, human xenograft, and mouse allograft preclinical cancer models. Clinical Cancer Research *9*: 4227–4239.

Wagner, M., and Koyasu, S. (2019). Cancer Immunoediting by Innate Lymphoid Cells. Trends in Immunology *40*: 415–430.

Wang, D., and Lippard, S.J. (2005). Cellular processing of platinum anticancer drugs. Nature Reviews Drug Discovery *4*: 307–320.

Wang, J.D., Douville, N.J., Takayama, S., and ElSayed, M. (2012). Quantitative analysis of molecular absorption into PDMS microfluidic channels. Annals of Biomedical Engineering *40*: 1862–73.

Weiswald, L.-B., Bellet, D., and Dangles-Marie, V. (2015). Spherical Cancer Models in Tumor Biology. Neoplasia (New York, N.Y.) *17*: 1–15.

Welker, L., Akkan, R., Holz, O., Schultz, H., and Magnussen, H. (2007). Diagnostic outcome of two different CT-guided fine needle biopsy procedures. Diagnostic Pathology *2*: 31.

Wetering, M. van de, Francies, H.E., Francis, J.M., Bounova, G., Iorio, F., Pronk, A., et al. (2015). Prospective Derivation of a Living Organoid Biobank of Colorectal Cancer Patients. Cell *161*: 933–945.

Wever, O. De, Hendrix, A., Boeck, A. De, Westbroek, W., Braems, G., Emami, S., et al. (2010). Modeling and quantification of cancer cell invasion through collagen type I matrices. The International Journal of Developmental Biology *54*: 887–896.

Wilson, W.R., and Hay, M.P. (2011). Targeting hypoxia in cancer therapy. Nature Reviews Cancer *11*: 393–410.

Winkles, J.A. (1997). Serum- and Polypeptide Growth Factor-Inducible Gene Expression in Mouse Fibroblasts (Elsevier Masson SAS).

Wong, R.S.Y. (2011). Apoptosis in cancer: From pathogenesis to treatment. Journal of Experimental and Clinical Cancer Research *30*: 87.

Yadav, S.S., Stockert, J.A., Hackert, V., Yadav, K.K., and Tewari, A.K. (2018). Intratumor heterogeneity in prostate cancer. Urologic Oncology: Seminars and Original Investigations *36*: 349–360.

Zanoni, M., Piccinini, F., Arienti, C., Zamagni, A., Santi, S., Polico, R., et al. (2016). 3D tumor spheroid models for in vitro therapeutic screening: a systematic approach to enhance the biological relevance of data obtained. Scientific Reports *6*: 19103.

Zhang, Y., Jiang, B., and Lee, M.H. (2020). A novel 3d model for visualization and tracking of fibroblast-guided directional cancer cell migration. Biology *9*: 1–13.

Zhang, Y.L., Li, J., Mo, H.Y., Qiu, F., Zheng, L.M., Qian, C.N., et al. (2010). Different subsets of tumor infiltrating lymphocytes correlate with NPC progression in different ways. Molecular Cancer *9*: 1–11.

Zoetemelk, M., Rausch, M., Colin, D.J., Dormond, O., and Nowak-Sliwinska, P. (2019). Short-term 3D culture systems of various complexity for treatment optimization of colorectal carcinoma. Scientific Reports *9*: 1–14.

Zong, W.X., Rabinowitz, J.D., and White, E. (2016). Mitochondria and Cancer. Molecular Cell *61*: 667–676.

Zugazagoitia, J., Guedes, C., Ponce, S., Ferrer, I., Molina-Pinelo, S., and Paz-Ares, L. (2016). Current Challenges in Cancer Treatment. Clinical Therapeutics *38*: 1551–1566.

Websites:

https://www.who.int/news-room/fact-sheets/detail/cancer

Accessed on 16th May 2020

https://www.cancerresearchuk.org/health-professional/cancer-statistics/incidence#heading-Zero

Accessed on 16th May 2020

https://www.cancerresearchuk.org/health-professional/cancer-statistics/risk

Accessed on 16th May 2020

https://www.cancerresearchuk.org/health-professional/cancer-statistics/incidence/common-cancers-compared#heading-Zero

Accessed on 30th April 2020

https://www.cancerresearchuk.org/health-professional/cancer-statistics/mortality#heading-One

Accessed 16th May 2020